MIT
International Center for
Air Transportation

Development of low-thrust solid rocket motors for small, fast aircraft propulsion

Matthew T. Vernacchia and R. John Hansman

This report is based on the Doctoral Dissertation of Matthew T. Vernacchia submitted to the Department of Aeronautics and Astronautics in partial fulfillment of the requirements for the degree of Doctor of Philosophy at the Massachusetts Institute of Technology.

The work presented in this report was also conducted in collaboration with the members of the Doctoral Committee:
Prof. R. John Hansman (Chair)
Prof. Paulo Lozano
Prof. Ahmed Ghoniem

Report No. ICAT-2020-04
May 2020

MIT International Center for Air Transportation (ICAT)
Department of Aeronautics & Astronautics
Massachusetts Institute of Technology
Cambridge, MA 02139 USA

Development of low-thrust solid rocket motors for small, fast aircraft propulsion

by

Matthew T. Vernacchia and R. John Hansman

Abstract

Small, uncrewed aerial vehicles (UAVs) are expanding the capabilities of aircraft systems. However, a gap exists in the size and capability of aircraft: no small aircraft are capable of sustained fast flight. A small, fast aircraft requires a propulsion system which is both miniature and high-power, requirements which current UAV propulsion technologies do not meet. Solid propellant rocket motors could be used, but must be re-engineered to operate at much lower thrust and for much longer burn times than conventional small solid rocket motors. This imposes unique demands on the motor and propellant.

This work investigates technological challenges of small, low-thrust solid rocket motors: slow-burn solid propellants, motors which have low thrust relative to their size (and thus have low chamber pressure), thermal protection for the motor case, and small nozzles which can withstand long burn times. Slow-burn propellants were developed using ammonium perchlorate oxidizer and the burn rate suppressant oxamide. By varying the amount of oxamide (from 0-20%), burn rates from $4\,\mathrm{mm\,s^{-1}}$ to $1\,\mathrm{mm\,s^{-1}}$ (at 1 MPa) were achieved. Using these propellants, a low-thrust motor successfully operated at a (thrust / burn area) ratio 10 times less than that of typical solid rocket motors. This motor can provide 5–10 N of thrust for 1-3 minutes. An ablative thermal protection liner was tested in these firings. Despite the long burn time, only a few millimeters of ablative are needed. A new ceramic-insulated nozzle was demonstrated on this motor. The nozzle has a small throat diameter (only a few millimeters) and can operate in thermal steady-state. Models were developed for the propellant burn rate, motor design, heat transfer within the motor and nozzle, and for thermal stresses in the nozzle insulation.

This work shows that small, low-thrust solid motors are feasible, by demonstrating these key technologies in a prototype motor. Further, the experimental results and models will enable engineers to design and predict the performance of solid rocket motors for small, fast aircraft. By providing insight into the physics of these motors, this thesis may help to enable a new option for aircraft propulsion.

Contents

1 Introduction **11**

1.1 Motivation: the small and fast aircraft capability gap 11

1.2 Example concept for a small, fast aircraft 13

1.3 Technology challenges for small, fast aircraft propulsion 16

1.4 Overview of this thesis 18

2 Overview of solid propellant rockets **19**

2.1 Typical practices for solid rocket motors 19

2.2 Solid rocket motor overview 21

2.2.1 Thrust, chamber pressure and propellant burn rate 21

2.2.2 Relation of motor efficiency to aircraft range 24

2.2.3 Rocket motor performance parameters 25

2.3 Solid propellant overview 31

2.3.1 Composition of composite propellants 32

2.3.2 Combustion of composite propellants 34

2.3.3 Solid propellant properties 35

3 Low-thrust solid rocket motors for aircraft propulsion **39**

3.1 The thrust/burn area ratio 40

3.1.1 Relation of the thrust/burn area ratio to motor design 40

3.1.2 Relation of the thrust/burn area ratio to trajectory and fuselage 41

3.2 Lower limit on thrust 43

4 Slow-burn solid propellant **49**

4.1 Slow-burn propellants based on ammonium nitrate 50

4.2 Slow-burn propellants based on ammonium perchlorate and oxamide . 50

4.2.1 Reducing burn rate with larger AP particles 50

4.2.2 Reducing burn rate with burn rate suppressants (oxamide) . . 51

4.2.3 Previous measurements of oxamide's effect on burn rate 54

4.2.4 Model of oxamide's effect on burn rate 56

5 Propellant characterization **59**

5.1 Propellant family used in this work 59

5.1.1 Propellant ingredients 60

5.1.2 No metal fuel for small, low-thrust motors 63

5.2 Combustion simulation 64

5.3 Methods and equipment for propellant characterization 66

5.3.1 Strand burner apparatus 66

5.3.2 Soot measurement methods 72

5.4 Results: burn rate 74

5.4.1 Strand burner burn rate measurements 74

5.4.2 Comparison to other studies of the effect of oxamide on burn rate 78

5.5 Results: minimum burn pressure 80

5.6 Results: soot in combustion products 81

5.7 Conclusions regarding propellant development 83

6 Motor case design and materials considerations **85**

6.1 Motor case design considerations 86

6.1.1 Baseline motor case design 88

6.1.2 Motor axial taper 90

6.1.3 Manufacturing 91

6.2 Material selection 92

6.2.1 Material selection for tension-loaded structures 95
6.2.2 Material selection for bending-loaded structures 96
6.2.3 Other material selection considerations 98
6.2.4 Material recommendations 98

7 Research motor testing **99**
7.1 Propellant mixing and casting 99
7.2 Research motor 100
7.2.1 Test facility 101
7.2.2 Research motor design 102
7.3 Research motor instrumentation 108
7.3.1 Chamber pressure 108
7.3.2 Thrust 110
7.3.3 Case temperature 116
7.3.4 Cameras 116
7.3.5 Data logger 116
7.4 Motor testing results 117
7.4.1 Thrust and chamber pressure measurements 117
7.4.2 Research motor burn rate measurements 120
7.4.3 Operation at low thrust/burn area ratio 125
7.4.4 Characteristic velocity measurements 125
7.4.5 Thrust coefficient measurements 128
7.4.6 Nozzle clogging 129
7.4.7 Pressure spikes 136

8 Motor case thermal protection **139**
8.1 Ablative materials for thermal protection 141
8.2 Thermal protection used in this work 142
8.3 Models of heat transfer to the motor case 144
8.3.1 Heat flux to the inner wall 144

8.3.2 Heat flux through the thermal protection layers 155
8.3.3 Hot gas energy loss 160
8.4 Ablation and char depth in the research motor 163
8.4.1 Char depth measurements 163
8.4.2 Char depth fits 167
8.4.3 Alterations in char structure due to inhibitor layer 169
8.4.4 Effects of acceleration and vibration on char 170
8.4.5 Liner buckling 171
8.5 Heat transfer and liner effectiveness measurements in the research motor 173
8.5.1 Case temperature and heat flux measurements 173
8.5.2 Hot gas energy loss measurements 178
8.6 Recommendations for further thermal protection development 181
8.6.1 Design recommendations 181
8.6.2 Experiment recommendations 181
8.6.3 Modeling recommendations 182

9 Nozzle mechanical and thermal design 185
9.1 Design challenges for small, long-burn-time nozzles 185
9.1.1 Conventional nozzle thermal design techniques 187
9.1.2 Small, long-burn time nozzles with steady-state ceramic insulation 196
9.2 Nozzle heat transfer boundary conditions 198
9.2.1 Internal hot gas thermal boundary 198
9.2.2 External thermal boundary 214
9.3 Nozzle thermal simulation 215
9.3.1 Model description 216
9.3.2 Prediction of nozzle shell temperatures in flight conditions . . 217
9.4 Nozzle testing 219
9.4.1 Comparison of shell temperature measurements to thermal model 220

9.4.2 Damage to boron nitride nozzle insert 222
9.5 Recommendations for further nozzle development 225
9.5.1 Nozzle testing and modeling recommendations 225
9.5.2 Nozzle design recommendations: base diameter trade-offs . . . 225

10 Ceramic nozzle insulation **229**
10.1 Thermal stress issues in ceramic insulators 230
10.1.1 Example of failure due to thermal stress 231
10.1.2 The thermal shock resistance parameter for comparing materials 233
10.1.3 Thermal shock resistance of common engineering ceramics . . 234
10.2 Cellular ceramic insulation 236
10.3 Modeling thermal stresses and heat transfer in cellular ceramic insulation 237
10.3.1 Honeycomb mechanics theory 237
10.3.2 Finite element model of thermal stresses 242
10.3.3 Thermal conductivity of ceramic honeycomb insulation 249
10.4 Producing cellular ceramic insulation 252
10.4.1 Effect of sintering process on material properties of fused silica 253
10.5 Nozzle insert material 254
10.6 Tests of the ceramic insulation 257
10.6.1 Torch test method for preliminary evaluation of nozzle materials 257
10.6.2 Failed tests with graphite nozzle inserts 258
10.6.3 Successful test with boron nitride insert 262
10.7 Recommendations for further ceramic insulation development 262

11 Conclusion **265**

A Methods of estimating burn rate from motor firings **269**
A.1 Method 1: average burn rate and n-averaged chamber pressure 270
A.2 Method 2: c^*-based burn rate 271
A.3 Fitting the pressure trace 271

B Nozzle deposit SEM images and EDS maps **273**

Chapter 1

Introduction

1.1 Motivation: the small and fast aircraft capability gap

A gap exists in the size and capability of flight vehicles: no small vehicles are capable of sustained level flight at high speed. The small and fast gap is illustrated by fig. 1-1, which plots the speed and size of some U.S. military aircraft. Speed and mass are plotted on logarithmic axes, so that a variety of aircraft, from tiny uncrewed aerial vehicles (UAVs) to fighter jets, can be included in a single plot. Broad categories of air vehicles are indicated as gray patches. This figure focuses on aircraft which can sustain flight for a duration of a few minutes or more (although a few shorter-duration missiles are included). Longer flight duration enables more interesting missions.

There is a gap which the existing aircraft classes do not cover [1] : small, fast aircraft with speed above $100\,\mathrm{m\,s^{-1}}$ and mass below $10\,\mathrm{kg}$. This undeveloped regime appears in the upper left of fig. 1-1. Small, fast aircraft in this regime would be useful for many valuable missions. This thesis is part of a research effort by MIT and its partners to develop a new class of small, fast aircraft.

One significant challenge for small, fast aircraft is that current propulsion systems

[1] Some small hobby rockets, sounding rockets and munitions do have speeds and masses in this range. However, they have very brief flight times.

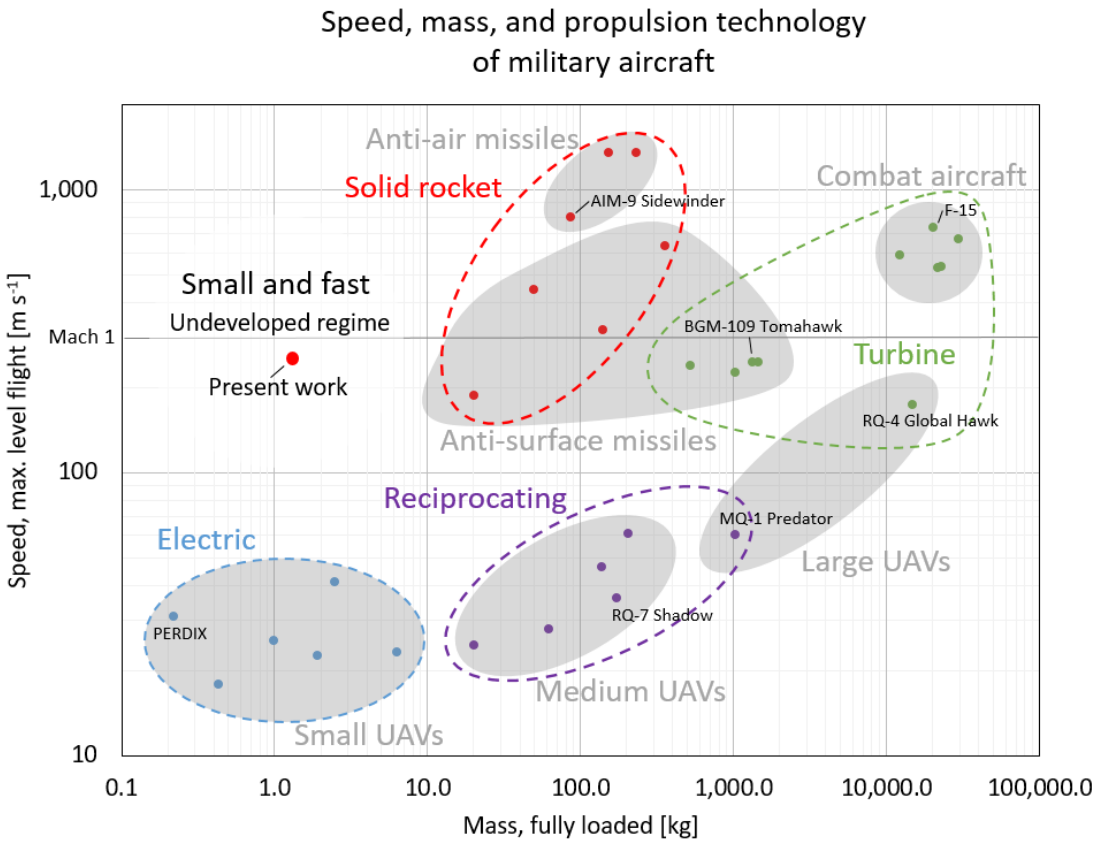

Figure 1-1: The speed vs. size design space currently lacks small, fast aircraft. The mass axis uses maximum takeoff mass for aircraft, and launch mass (incl. payload and propellant) for missiles. Data from [36, 37, 78, 1, 80, 92].

do not fit the power needed for high-speed flight into a small package. The focus of this thesis is to address this propulsion need by developing a new class of miniature slow-burn solid rocket motors.

First, let us briefly examine the current landscape of air vehicle propulsion. Four major propulsion technologies are used in the contemporary air vehicles listed in fig. 1-1:

1. *Electric motors / propellers*, which are used almost exclusively on small UAVs with low flight speeds,

2. *Reciprocating engines / propellers*, which are used on medium to large UAVs with flight speeds up to $70\,\mathrm{m\,s^{-1}}$,

3. *Turbine engines*, which are used on large, fast combat aircraft, cruise missiles, and UAVs, and

4. *Solid rockets*, which are used on fast, medium-sized missiles.

The speed and size regimes in which these technologies have been applied are shown in fig. 1-1. Of these technologies, only the turbine engine or the solid rocket motor appear to be technically feasible for small, fast aircraft. The solid rocket motor was selected as the propulsion technology for this investigation due to its high specific power and low mechanical complexity.

Small, fast aircraft have different thrust and endurance requirements than typical applications of solid rocket motors: the rocket motor must deliver a low thrust level (just enough to counter drag) for a few minutes. In contrast, typical solid rockets are optimized to deliver their impulse quickly, either to catch up with a target (i.e. tactical missiles) or reduce gravity losses (i.e. sounding rockets and launch vehicles). Most small (kilogram-scale) solid rocket motors only burn for a few seconds, not the few minutes desired here. Further, motors for small aircraft have thrust levels which are unusually low, even relative to the size of the motor. The (thrust / burn area) ratio is a measure of thrust relative to motor size; these motors have (thrust / burn area) ratio 1/10th that of typical solid rocket motors. Adapting solid rockets to the needs of small aircraft motivates the development of slow-burning solid propellants and a compact, long-burn-time rocket motor.

The following section presents an example design for a small, fast aircraft using rocket propulsion. The contribution of this thesis is to identify and solve technology challenges for these aircraft's propulsion systems. These challenges and contributions are introduced in section 1.3.

1.2 Example concept for a small, fast aircraft

This section introduces an example design for a small, fast aircraft using rocket propulsion. This aircraft concept, called 'Firefly', is a representative example from

the middle of the unexplored region shown in fig. 1-1. The Firefly aircraft serves as a reference case for many of the issues examined in this thesis.

The design goals of the Firefly vehicle concept are:

1. Cruise at Mach 0.8, after dropping from a host aircraft at an altitude of 10 km.
2. Fit in a 70 mm × 70 mm × 480 mm bounding box, when stowed before drop.
3. Maximize range and endurance, ideally providing several minutes of powered flight.

Firefly is a deployable UAV; it is designed to launch from a larger host aircraft in transonic flight, as illustrated in fig. 1-2. After launch, Firefly would unfold its wing and tails, stabilize, then ignite its rocket motor for powered flight. The nominal mission is steady level cruise (powered flight) at Mach 0.8 and 10 km altitude. After motor burnout, the vehicle would glide for some time.

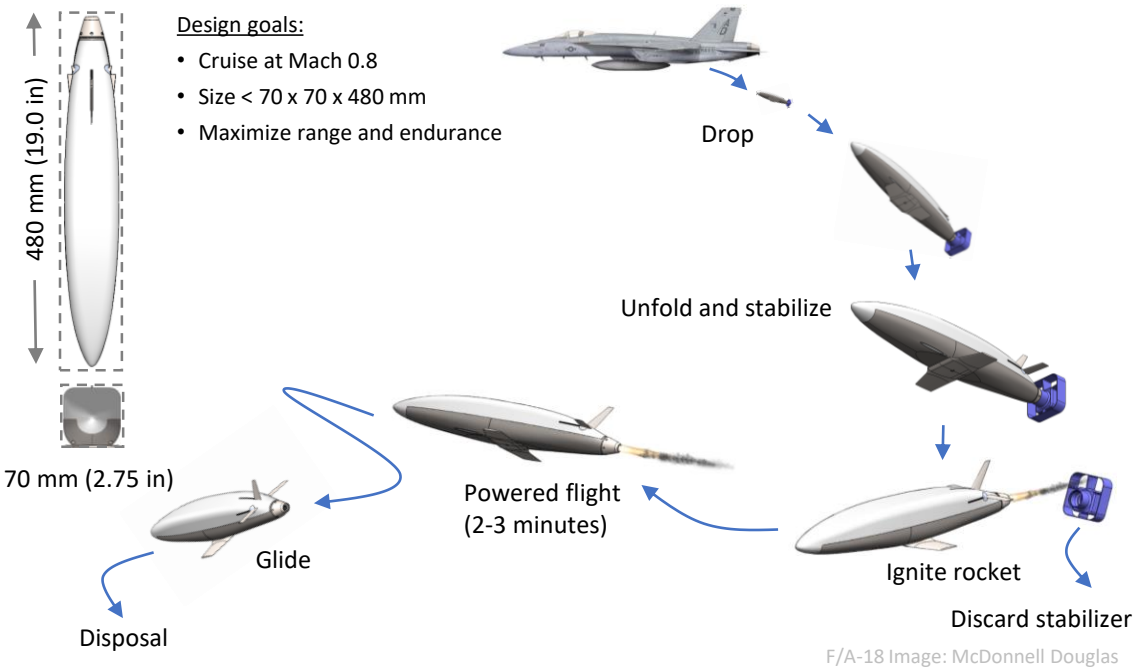

Figure 1-2: The nominal mission considered in this work is air-launch at 10 km altitude, followed by powered cruise at Mach 0.8.

A baseline reference design for Firefly is shown in fig. 1-3. The aircraft's fuselage is 460 mm long. The motor case, made of titanium alloy, is the primary structure of

the fuselage. The motor case is filled with solid propellant (pink). The propellant burns from the aft end towards the front. As the propellant burns, the inside of the motor case would be exposed to hot combustion gas; to avoid this, an ablative material (black) lines the inside of the motor case. The ablative liner protects the motor case from hot combustion gas. The ablative is thicker at the aft of the motor, where it is exposed to hot combustion gas for a longer time. A wing is attached to the motor case; the wing rotates about a pivot to fold and fit into the deployment canister. The control surfaces also fold. The fuselage is configured with the payload mounted in front of the motor, and the motor has a circular cross section.

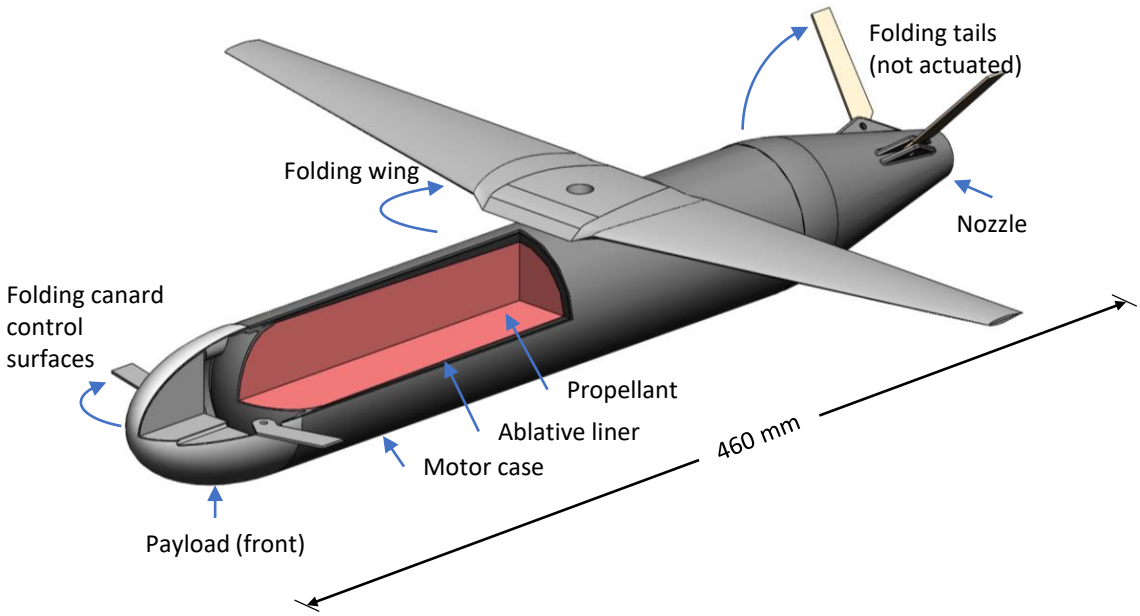

Figure 1-3: Baseline design of a small, fast aircraft with rocket propulsion.

The baseline design presented here is version 3 of the Firefly design. An earlier design iteration (version 1) was presented in the author's MS thesis [89].

1.3 Technology challenges for small, fast aircraft propulsion

Solid rocket motors for small, fast aircraft propulsion operate at much lower thrust and for much longer burn times than conventional small solid rocket motors. This imposes unique demands on the motor and the propellant. The propellant must burn slowly and be able to operate at unusually low chamber pressures. The propellant burn rate should be adjustable[2], so that a single propellant 'family' can accommodate a range of mission and aircraft concepts. The motor case design is coupled to the fuselage and propellant grain design. The motor case must store as much propellant as possible and also provide mounting locations for the payload and control surfaces which will not get too hot. The inside of the motor case requires thermal protection from 1500–2200 K combustion gas for a few minutes. The thermal protection layers must be thin to minimize the use of valuable volume within the small motor. The nozzle is so small that conventional thermal designs will not work for the long burn time. It requires novel applications of insulating materials which tolerate extreme temperatures and thermal stresses.

This thesis investigates these technical challenges and solution options. A family of slow-burn propellants was developed, two motor case configurations were investigated, and a novel ceramic-insulated nozzle was designed. Experiments were conducted to characterize the propellant, demonstrate a low thrust motor, measure ablation in the context of this motor, and test new nozzle designs and materials. Models were developed for the propellant burn rate, motor design, heat transfer within the motor and nozzle, and for thermal stresses in the nozzle insulation.

The results of this work advance the key technologies needed for small, slow-burn rocket motors. Specifically, the contributions of this thesis are:

1. *For the design of small, low-thrust motors*, this thesis identifies unusually low (thrust / burn area) ratio as a key challenge, shows that low (thrust / burn

[2]at the time of manufacture

area) requires slow-burn propellant and low chamber pressure, and quantifies the lower limits on the (thrust / burn area) ratio.

2. *For slow-burn propellants*, this thesis quantifies the effect of oxamide (a burn rate suppressant) on burn rate. Oxamide was previously known as a burn rate suppressant, but previous work in the open literature did not include burn rate measurements at conditions relevant to this work (high oxamide contents of 10-20% and low pressures of 0.1–2 MPa), and did not provide a quantitative model of oxamide's effect on burn rate. This thesis presents new measurements for the burn rates of propellants with up to 20% oxamide content, and a model of oxamide's effect on burn rate.

3. *For the operation of small, low-thrust motors*, this thesis demonstrates motor operation at low (thrust / burn area), and identifies low c^* and C_F efficiencies (of about 85%) as intrinsic features of small, low-thrust motors. Also, nozzle clogging and pressure spikes are identified as technical risks.

4. *For motor case thermal protection*, this thesis measures ablation and models heat transfer under the unusual conditions of these motors. It was discovered that combustion gas primarily transfers heat to the walls by radiation, and that the combustion gas is cooled significantly by this heat loss. These are unusual phenomena which occur due to the motor's small size and low thrust.

5. *For the nozzle*, this thesis identifies the thermal challenges posed by small size and long burn time and presents a novel ceramic-insulated nozzle for small, long-burn motors. The ceramic-insulated nozzle design is supported by modeling and demonstration in a motor firing.

The experimental results and models enable engineers to design and predict the performance of solid rocket motors for small, fast aircraft. It is hoped that this thesis will help unlock a new option for aircraft propulsion by providing insight into the physics of these motors.

1.4 Overview of this thesis

Chapter 2 provides an overview of rocket motor and solid propellant technology. The body of this thesis is then arranged around the technical challenges described above. The lower limit on a motor's thrust, and the performance of low-thrust motors are discussed in chapter 3. Theory and experimental work on slow-burn propellants are presented in chapters 4 and 5. Options for motor case and fuselage design are explored in chapter 6. Test firings of a research motor are reported in chapter 7. The design, modeling and testing of the motor case's thermal protection is described in chapter 8. Finally, the nozzle and its ceramic insulation are discussed in chapters 9 and 10.

Chapter 2

Overview of solid propellant rockets

2.1 Typical practices for solid rocket motors

Solid propellant rockets have a long history, and in the last half-century advances in science and industrial practices have enabled solid rocket motors to be a reliable and performant solution for space launchers and missiles. The first black powder rockets were fielded by the Chinese (13th century), the India kingdom of Mysore (18th century) and the British (19th century) [53]. Double base propellants [1] were developed in the late 1800s and early 1900s [90]. They are still used in some military applications requiring low smoke, but have largely been superseded by higher-performance composite propellants [77]. Composite propellants consist of particles of solid oxidizer bound by a polymer fuel matrix. The first castable composite propellants were developed at Caltech's Guggenheim Aeronautical Laboratory (which would later form the Jet Propulsion Laboratory, JPL) in 1942 [34]. Three companies with ties to JPL – Aerojet General Corporation, Thiokol Chemical Corporation, and United Technology Corporation – made major advances in the following years [34]. By the 1970s, the now-standard combination of hydroxyl-terminated polybutadiene (HTPB) binder and ammonium perchlorate (AP) oxidizer had been developed, and

[1] Double base propellants consist of solid nitrocellulose gelatinized with a liquid energetic nitrate ester, usually nitroglycerin [43].

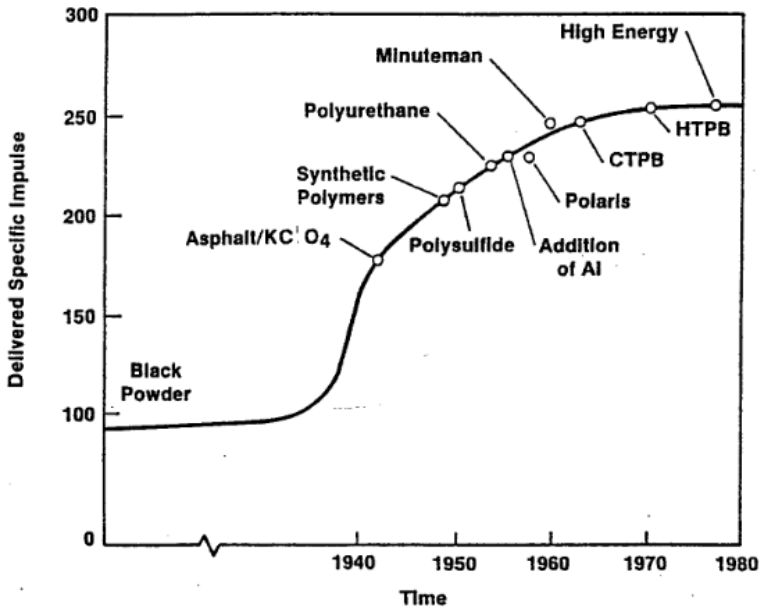

Figure 2-1: Solid propellant performance history. Reprinted from [86].

solid propellants reached a high level of performance (see fig. 2-1). Major advances in nozzle and motor case design were also made, mostly due to advances in materials. Parallel solid propulsion work was also undertaken in France and the former Soviet Union, although the Russians have not used solid propulsion in as many strategic or space applications as the United States. In the US today, the major solid propulsion enterprises are Aerojet Rocketdyne and Northrop Grumman Innovation Systems (formerly Orbital ATK) [87].

Throughout this history, best practices have been accumulated for the safe and reliable development, production and operation of solid rocket motors. Much of this knowledge is proprietary (or classified), but useful resources are available in the open literature. As with most things relating to rocketry, *Rocket Propulsion Elements* [77] is the standard introductory reference. *Solid Rocket Propulsion Technology* by Alain Davenas [19] and *Propellants and Explosives* by Naminosuke Kubota [43] provide more details.

Low-thrust motors and slow-burn solid propellants are somewhat neglected areas of research. To the author's knowledge, no solid rocket motors have been designed

with the low thrust, small size and long burn time achieved in this work.

2.2 Solid rocket motor overview

Solid propellant rocket motors store propellant as a solid grain within the combustion chamber. When the motor is ignited, the surfaces of the propellant grain burn and produce hot gas, which is expelled from the chamber through a nozzle to produce thrust. The main components of the motor are illustrated in fig. 2-2.

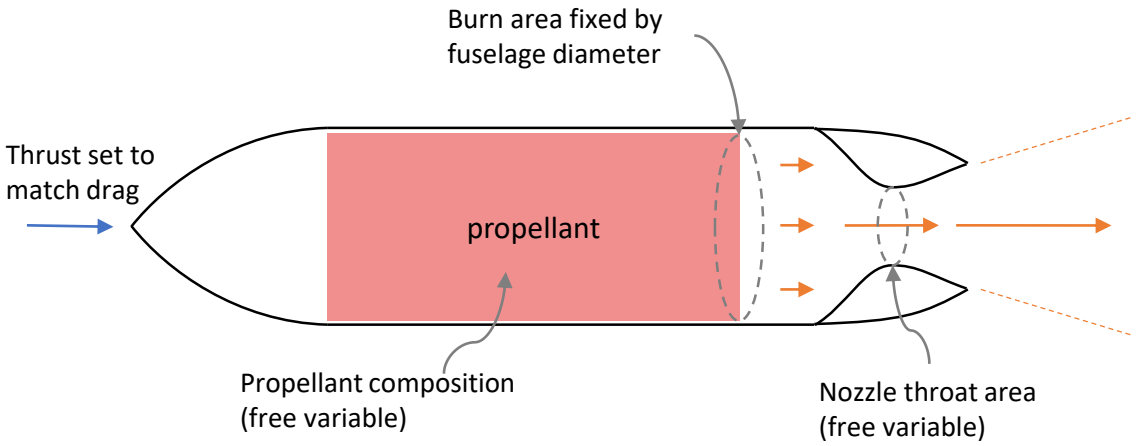

Figure 2-2: In designing an end-burn motor, the propellant composition and throat area are the free variables used to set the thrust and chamber pressure.

2.2.1 Thrust, chamber pressure and propellant burn rate

The motor is designed to produce some required amount of thrust – in this case, to match the drag on the aircraft. The thrust depends on the mass flow rate of propellant. However, the flow of propellant into the combustion chamber cannot be regulated – all of the propellant is loaded into the combustion chamber when the motor is assembled. Instead, the mass flow rate and thrust depend on how quickly the propellant burns (burn rate), and how large a surface area of propellant

is burning (burn area). The burn area is fixed by the motor diameter for an end-burn motor[2]. The burn rate depends on the propellant composition and the pressure in the combustion chamber. The nozzle throat area helps set the chamber pressure. Thus, the propellant composition and throat area are the free variables for the design of an end-burn motor.

The chamber pressure and mass flow are set by an equilibrium between the nozzle mass flow and the combustion mass flow. This equilibrium is illustrated in fig. 2-3. The nozzle mass flow increases linearly with pressure and is shown as a black dashed line. If the nozzle throat area were smaller, the slope of this line would be shallower. The combustion mass flow (for a typical, fast-burn propellant) is shown as an orange curve. The combustion mass flow increases with pressure, but the trend is sub-linear[3]. At some pressure, the combustion is equal to the nozzle mass flow – this is a stable equilibrium pressure at which the motor will operate. A slow-burn propellant will yield a lower combustion mass flow (blue curve) and will cause the motor to operate at a lower chamber pressure (if the nozzle throat area is held constant).

By adding different amounts of burn rate suppressant, a designer can adjust the burn rate of the propellant and set the thrust of the motor. For the very low thrust levels needed here, the motor will need a slow-burn propellant and a low chamber pressure. Thus, slow burn propellants are important to this work. Chapter 4 describes how the burn rate can be reduced, and chapter 5 describes the characterization of a family of slow-burn propellants.

In addition to using a slow-burn propellant, the burn rate and thrust are reduced by designing the motor to operate at a lower chamber pressure. Thus, the motors in this work have low chamber pressure. However, the chamber pressure cannot be too

[2]An end-burn motor burns a solid propellant grain from the nozzle end towards the forward end. Alternatively, a core-burn motor burns a hollow propellant grain from the core outwards. End burn motors are used in this work to give low thrust and long burn time. Core-burn motors give higher thrust, and are the more common design in other applications.

[3]For stable motor operation, the combustion mass flow must increase sub-linearly with chamber pressure. If the combustion mass flow increased super-linearly with chamber pressure, the equilibrium in fig. 2-3 would be unstable. In this case, the motor would not operate at a stable equilibrium pressure – it would either extinguish itself or explode. See Sutton and Biblarz [77], Example 12-1.

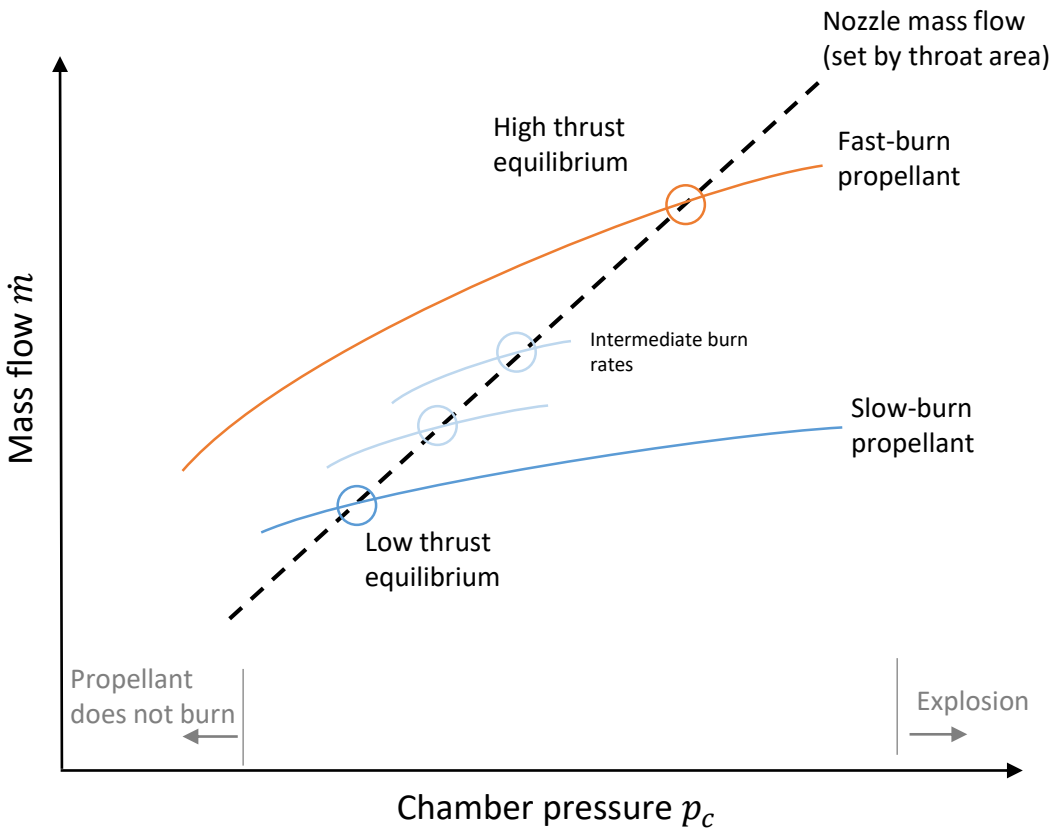

Figure 2-3: The chamber pressure and mass flow are set by an equilibrium between the nozzle mass flow and the combustion mass flow. A slower burning propellant causes the motor to operate at a lower chamber pressure, lower mass flow and lower thrust.

low: for some propellants there is a minimum pressure below which the propellant will not burn. This sets a lower limit on the (thrust / burn area) ratio the motor can achieve, and is discussed further in chapter 3.

Mathematically, the (equilibrium) chamber pressure is:

$$p_c = \frac{A_b}{A_t} \rho_s c^* r(p_c) \tag{2.1}$$

where A_b is the burn area, A_t is the throat area, ρ_s is the propellant density, c^* is the characteristic velocity of the propellant (see section 2.2.3.3) and $r(p_c)$ is the pressure-dependent burn rate of the propellant (with dimensions of velocity). ρ_s, c^* and r depend on the propellant composition.

The thrust force of the motor is:

$$F = C_F\left(\frac{p_e}{p_c}, \frac{p_a}{p_c}, \gamma\right) A_t p_c \tag{2.2}$$

where $C_F\left(\frac{p_e}{p_c}, \frac{p_a}{p_c}, \gamma\right)$ is the thrust coefficient, a dimensionless parameter which depends on the expansion of gas through the nozzle (see section 2.2.3.2).

2.2.2 Relation of motor efficiency to aircraft range

In addition to providing the required thrust, the motor should be efficient so that the aircraft has long range. An aircraft with longer range is desirable, as it can perform more missions.

The Breguet range equation predicts the powered-flight range $R_{powered}$ of an aircraft in steady, level flight:

$$R_{powered} = v_{cruise}\frac{L}{D}\ln\left(\frac{m_{init}}{m_{final}}\right) I_{sp} \tag{2.3}$$

where v_{cruise} is the (constant) flight speed, L/D is the aircraft's lift to drag ratio (at v_{cruise}), m_{init} is the initial mass (with propellant) and m_{final} is the final mass (after all propellant has been burned). I_{sp} is the specific impulse, which measures the 'fuel efficiency' of the propulsion system (and has units of seconds).

Aircraft which fly at a high altitude, like the Firefly concept, have a significant glide range in addition to the powered flight range. Depending on the mission, the extra glide range may or may not be useful.

To have long range, the aircraft should have high L/D (good aerodynamic design), high m_{init}/m_{final} (good structural design), and high I_{sp} (an efficient motor). Specific impulse is defined and discussed in the following section. The mass ratio depends somewhat on the motor case design, which is discussed in chapter 6.

2.2.3 Rocket motor performance parameters

This section describes three important performance metrics for rocket motors: the specific impulse I_{sp}, thrust coefficient C_F, and characteristic velocity c^*. Specific impulse measures the 'fuel efficiency' of the motor, and depends on both C_F and c^*. The thrust coefficient measures the effectiveness of the nozzle, and depends primarily on the nozzle pressure ratio. The characteristic velocity measures the 'energetic-ness' of propellant combustion, and depends primarily on the combustion gas temperature. These parameters are used in almost all rocket propulsion literature; details and derivations can be found in Sutton and Biblarz [77], chapter 3.

The 'ideal' values of all three parameters can be calculated from the theory of isentropic, 1-dimensional channel flow through a nozzle. For a particular motor, the actual values of these parameters are measured in motor firing experiments. The measured values are less than the ideal values due to inefficiencies. The ideal formulas and measurement techniques for each parameter are discussed below.

2.2.3.1 Specific impulse

The 'fuel efficiency' of the motor is measured by the specific impulse, I_{sp}:

$$I_{sp} \equiv \frac{1}{g_0}\frac{F}{\dot{m}} = \frac{1}{g_0} C_F c^* \tag{2.4}$$

For historical reasons, specific impulse is normalized by the constant $g_0 \equiv 9.806\,65\,\mathrm{m\,s^{-2}}$, and has units of seconds. Typical values for solid-propellant rocket motors are 150–270 s (see fig. 2-1). The right-most term in eq. (2.4) shows that specific impulse is the product of nozzle effectiveness (measured by C_F, section 2.2.3.2) and propellant 'energetic-ness' (measured by c^*, section 2.2.3.3).

Higher specific impulse increases the range R of a rocket-powered vehicle:

- For steady level flight, the Breguet range equation predicts that $R \sim I_{sp}$

- For ballistic trajectories [4], $R \sim I_{sp}^2$

It is desirable to design an efficient motor with high I_{sp}.

Ideal formula The ideal specific impulse is calculated as:

$$I_{sp,ideal} = \frac{1}{g_0} C_{F,ideal} c^*_{ideal} \tag{2.5}$$

where $C_{F,ideal}$ is given by eq. (2.11) and c^*_{ideal} by eq. (2.14). If the nozzle exit pressure (p_e) is equal to the ambient pressure (matched expansion), then:

$$I_{sp,ideal} = \frac{1}{g_0} \sqrt{\frac{2\gamma}{\gamma - 1} \frac{\mathcal{R} T_c}{\mathcal{M}} \left[1 - \left(\frac{p_e}{p_c} \right)^{(\gamma-1)/\gamma} \right]} \tag{2.6}$$

where $\mathcal{R}$ is the universal gas constant, T_c is the exhaust gas temperature, $\mathcal{M}$ is the exhaust gas molar mass and γ is the exhaust gas ratio of specific heats. To have high I_{sp}, the exhaust gas should be hot, the exhaust gas molar mass should be low, and the chamber pressure should be high (relative to the exit pressure).

Experimental measurement The actual specific impulse is determined by measuring the thrust and mass flow rate, and using eq. (2.4). For solid rocket motors, it is often difficult to measure the instantaneous mass flow rate, so the time-averaged specific impulse is used [5]:

$$\langle I_{sp,meas} \rangle = \frac{1}{g_0 m_p} \int_{t_{start}}^{t_{end}} F dt \tag{2.7}$$

where $\int_{t_{start}}^{t_{end}} F dt$ is the total impulse, and $m_p = \int_{t_{start}}^{t_{end}} \dot{m} dt$ is the total mass of propellant burned between t_{start} and t_{end}.

[4] For a ballistic trajectory (ignoring drag) $R \sim v_0^2 \approx (\Delta v)^2$, where v_0 is the velocity at burnout and Δv is the change in velocity delivered by the rocket motor. The Tsiolkovsky rocket equation states that $\Delta v \sim I_{sp}$.

[5] This definition of $\langle I_{sp,meas} \rangle$ is equal to $\left(\int_{t_{start}}^{t_{end}} I_{sp} \dot{m} dt \right) / \left(\int_{t_{start}}^{t_{end}} \dot{m} dt \right)$, i.e. the time-average of I_{sp} weighted by the mass flow at each time.

Efficiency The specific impulse efficiency $\zeta_{I_{sp}}$ is the ratio of the measured and ideal specific impulse:

$$\zeta_{I_{sp}} = \frac{I_{sp,meas}}{I_{sp,ideal}} \tag{2.8}$$

where $I_{sp,ideal}$ is calculated using the actual ambient pressure at which the motor was fired.

The specific impulse efficiency is the product of the thrust coefficient efficiency (which will be defined in eq. (2.12)) and characteristic velocity efficiency (eq. (2.16)):

$$\zeta_{I_{sp}} = \zeta_{C_F}\zeta_{c^*} \tag{2.9}$$

The specific impulse efficiency $\zeta_{I_{sp}}$ is always less than 1, and losses are due to inefficiencies in nozzle expansion ($\zeta_{C_F} < 1$) and inefficiencies in combustion ($\zeta_{c^*} < 1$). Characterizing these inefficiencies is important to accurately predict the performance of the motor and the range of the vehicle.

2.2.3.2 Thrust coefficient

The thrust coefficient C_F is a dimensionless parameter which represents the effectiveness of the nozzle expansion process. It is defined as:

$$C_F \equiv \frac{F}{A_t p_c} \tag{2.10}$$

The thrust coefficient ranges from about 0.8 to 1.9 for typical rockets [77]; higher values are preferred.

Ideal formula The thrust coefficient depends on the chamber pressure p_c, exit pressure p_e, ambient pressure p_a, nozzle expansion ratio A_e/A_t, and exhaust gas

ratio of specific heats γ. For an ideal nozzle:

$$C_{F,ideal} = \sqrt{\frac{2\gamma^2}{\gamma-1}\left(\frac{2}{\gamma+1}\right)^{(\gamma+1)/(\gamma-1)}\left[1-\left(\frac{p_e}{p_c}\right)^{(\gamma-1)/\gamma}\right]} + \frac{p_e - p_a}{p_c}\frac{A_e}{A_t} \qquad (2.11)$$

The parameters on the right-hand side are not independent: the nozzle pressure ratio p_c/p_e is set by the nozzle expansion ratio A_e/A_t.

For a given p_c, C_F is maximized when $p_e = p_a$, a condition known as matched expansion. Often, the nozzle expansion ratio A_e/A_t is chosen so that p_e will equal the ambient pressure at the expected operating altitude.

For the motor designs in this work, it is assumed that the nozzle expansion ratio is always chosen to give matched expansion at the nominal chamber pressure. Thus, p_e is fixed to equal p_a, and A_e/A_t is set by the choice of p_c. Further, γ is set by the propellant chemistry, and does not depend on the motor design. Under these assumptions, p_c is the only free variable in determining C_F, and one can think of C_F as a function primarily of p_c, $C_F(p_c)$.

Assuming the nozzle is always designed for matched expansion, C_F increases monotonically with p_c (fig. 2-4); thus higher chamber pressures are desirable. Low thrust motors (which operate at low chamber pressure) will have low C_F.

Note that C_F does not depend on the temperature of the combustion gas. Thus, C_F represents the contribution of nozzle expansion to specific impulse, whereas c^* (which *does* depend on T_c, see section 2.2.3.3) represents the contribution of combustion to specific impulse. Together, $I_{sp} = C_F c^*/g_0$.

Experimental measurement In motor firings, C_F is determined by measuring the thrust, chamber pressure and throat area, and using eq. (2.10).

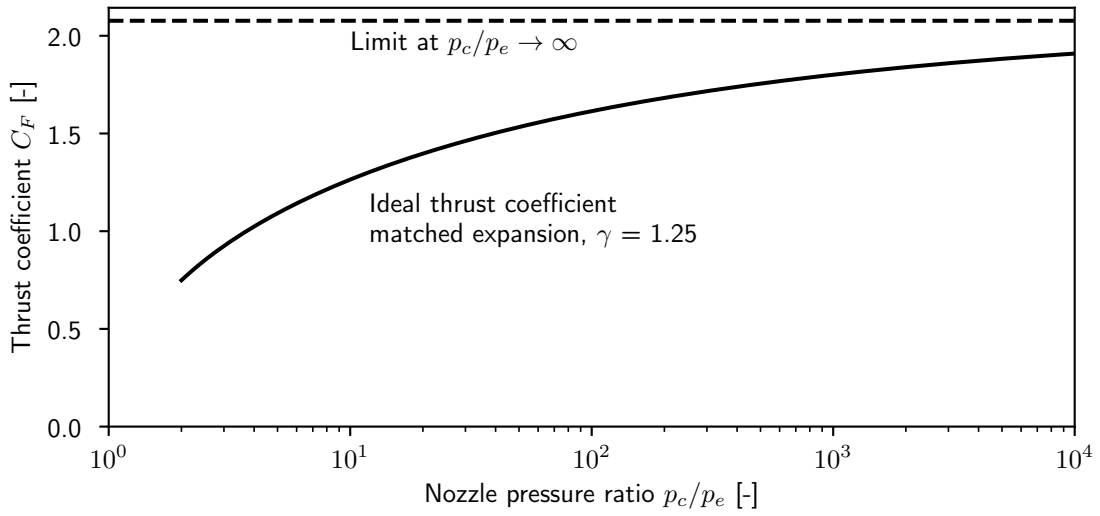

Figure 2-4: The thrust coefficient is higher if the chamber pressure p_c is high relative to the nozzle exit pressure p_e.

Efficiency The C_F efficiency ζ_{C_F} is the ratio of the measured and ideal thrust coefficients:

$$\zeta_{C_F} = \frac{C_{F,meas}}{C_{F,ideal}} \tag{2.12}$$

The efficiency is less than 1, and in well designed nozzles it will be > 0.90 [77]. Reasons for reduced efficiency include:

- *Divergence losses* - a non-axial component of the nozzle exit velocity will reduce thrust and reduce C_F. The nozzles in this work use a conical exit with 15° half angle; for this geometry the divergence losses are 1.7%.

- *Viscous losses* - viscous forces in the nozzle reduce the exit velocity. This is a more severe problem for smaller nozzles with lower Reynolds numbers.

- *Multi-phase flow* - solid particles in the exhaust reduce C_F. The propellants used in this work produce about 2% by mass solid soot in the exhaust gas.

- *Nozzle obstructions or surface damage* - solid deposits obstructing the gas flow

through the nozzle or damage to the nozzle surfaces will increase losses in the nozzle.

A representative value of ζ_{C_F} can be measured from motor firings, and then used as a correction factor for similar nozzles.

2.2.3.3 Characteristic velocity

Characteristic velocity, c^*, measures the propellant combustion process's contribution to specific impulse. The characteristic velocity c^* is defined as:

$$c^* \equiv \frac{A_t p_c}{\dot{m}} \tag{2.13}$$

For typical solid propellants, c^* is between 1200 and 1600 $\mathrm{m\,s^{-1}}$ [77]. Higher values are desirable.

Ideal formula The ideal value of c^* is [77]:

$$c^*_{ideal} = \sqrt{\frac{\mathcal{R}T_c}{\gamma\mathcal{M}}} \left(\frac{\gamma+1}{2}\right)^{\frac{1}{2}(\frac{\gamma+1}{\gamma-1})} \tag{2.14}$$

where $\mathcal{R}$ is the universal gas constant, $\mathcal{M}$ is the exhaust gas molar mass, and T_c is the (stagnation) temperature at the nozzle inlet. Note that c^* is proportional to $\sqrt{T_c}$; c^* is higher for hotter-burning, more energetic propellants. Also, the ideal value of c^* does *not* depend on the chamber pressure or nozzle expansion process. Thus, c^* is a figure of merit for the propellant and combustion process.

Experimental measurement The actual value of c^* is measured in motor firing experiments. Characteristic velocity can be measured from $A_t p_c/\dot{m}$ (the right-hand side of eq. (2.13)). However, measuring the instantaneous mass flow rate in solid rocket motors is difficult. If instantaneous $\dot{m}$ measurements are not available (as in this work), the time-averaged characteristic velocity can be used instead. It is

defined as [6]:

$$\langle c^*_{meas} \rangle = \frac{A_t}{m_p} \int_{t_{start}}^{t_{end}} p_c(t) dt \tag{2.15}$$

Efficiency The departure of the actual value of c^* from the ideal value is measured by the c^* efficiency, ζ_{c^*}:

$$\zeta_{c^*} \equiv \frac{c^*_{meas}}{c^*_{ideal}} \tag{2.16}$$

The actual characteristic velocity is less than the ideal value because:

- *Incomplete combustion* reduces c^*.
- *Heat loss* to the ablative liner and motor case reduces c^*.

The actual c^* is typically 90-99% of the theoretical value, but the exact value is hard to predict. Thus, the actual c^* must be measured in a motor under realistic conditions. A typical value of ζ_{c^*} can be found from these results and used as a correction factor in the design of similar motors.

2.3 Solid propellant overview

A solid propellant contains both fuel and oxidizer mixed together. This is different from most other combustion systems, where the fuel and oxidizer are only mixed just before combustion (e.g. internal combustion engines, torches, liquid bi-propellant rocket engines). This poses a chemistry challenge: the propellant ingredients must react energetically with each other, but also be safely stored and handled while mixed together. A propellant must also not ignite when exposed to mechanical shock, heat or electrostatic discharges during handling. Finally, because the propellant burn rate

[6] This definition of $\langle c^*_{meas} \rangle$ is equal to $\left(\int_{t_{start}}^{t_{end}} c^* \dot{m} dt\right) / \left(\int_{t_{start}}^{t_{end}} \dot{m} dt\right)$, i.e. the time-average of c^* weighted by the mass flow at each time.

determines the motor's chamber pressure and thrust, the propellant must burn at a stable and predictable rate.

Composite propellants are heterogeneous mixtures of a crystalline oxidizer, a polymer binder, and possibly a metal fuel. The solid oxidizer and binder do not react with each other at room temperature, but when heated decompose (gasify) and undergo energetic gas-phase reactions. Ammonium perchlorate composite propellant (APCP) is the most-used composite propellant (e.g. the Space Shuttle's Reusable Solid Rocket Motor, Orbital ATK's Star motor series [60]). APCP is energetic (up to 270 seconds of specific impulse [77]), is resistant to accidental ignition, and will burn stably in a properly designed motor.

2.3.1 Composition of composite propellants

Composite propellants contain a solid oxidizer and (optionally) a powdered metal fuel, held together by a rubber-like binder (fig. 2-5). Usually, the solid oxidizer is ammonium perchlorate (NH_4ClO_4), although in some propellants other oxygen-rich salts are used (e.g ammonium nitrate, NH_4NO_3). Ammonium perchlorate is a crystalline solid, which is divided into small particles (10–500 µm) and dispersed though the propellant. During combustion, the solid oxidizer decomposes to produce an oxygen-rich gas. A polymer matrix, the binder, binds the oxidizer particles together, giving the propellant mechanical strength. Hydroxyl-terminated polybutadiene (HTPB) is a typical binder. The binder serves as a fuel, giving off hydrocarbon vapors during combustion. Additional fuel may be added as hot-burning metal powder dispersed in the binder.

During propellant mixing, the other ingredients are added to the binder while the binder is in a liquid form, making a slurry. A curative is then added to cross-link the binder into a solid, solidifying the propellant. After the curative is mixed in, the propellant must be cast into the correct shape before the propellant solidifies (usually this takes a few hours).

Other minor ingredients can be included in the propellant. Bonding agents (e.g.

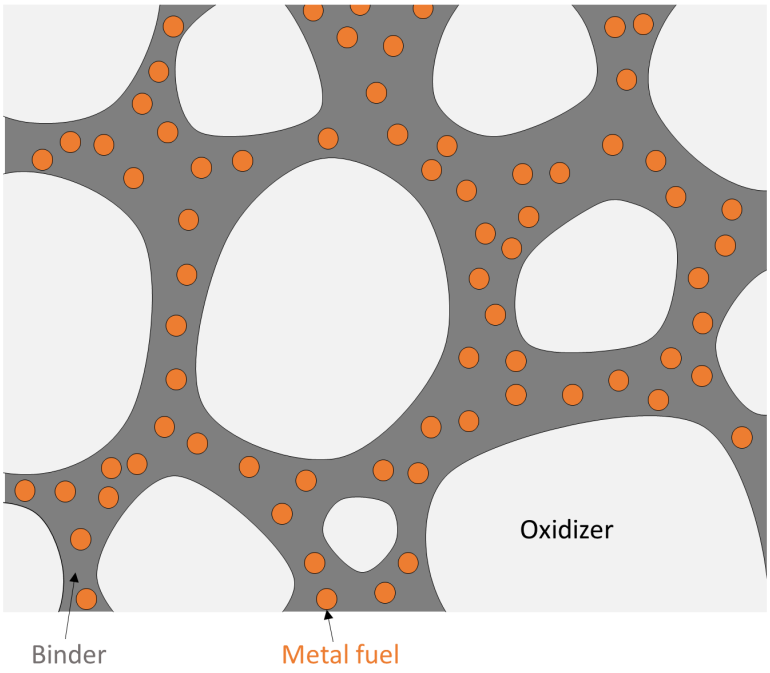

Figure 2-5: A composite propellant consists of crystalline oxidizer particles, and possibly a metal fuel powder, dispersed in a polymer binder.

HX-752) promote better adhesion between the oxidizer particles and the binder, improving mechanical properties and stabilizing combustion. Antioxidants (e.g. CAO-5) improve the shelf life of the propellant. Plasticizers (e.g. IDP) make mixing and casting easier by improving the rheological properties of the propellant slurry. Burn rate suppressants (e.g. oxamide) or catalysts (e.g. Fe_2O_3) can be added to modify the propellant's burn rate.

Some propellants include an opacifier to make the propellant opaque and emissive. During combustion heat is transfered to the solid propellant by radiation. For good combustion, the propellant must be opaque so that the (infrared) radiation is absorbed at the burning surface, not deeper into the solid. If a large amount of metal fuel is used, this will make the propellant opaque. Propellants without metal fuel

often used carbon powder as an opacifier [51].

2.3.2 Combustion of composite propellants

The combustion process of a composite propellant has many steps, and the flame structure is complex (fig. 2-6). Although the propellant is a solid, important reactions, including combustion of the fuel with the oxidizer, occur in the gas phase. A set of flames hover over the surface of the burning propellant. These flames transfer heat to the propellant surface, causing its solid components to decompose into gases. The gaseous decomposition products contain fuel vapor and oxidizing species, which supply the flames with reactants.

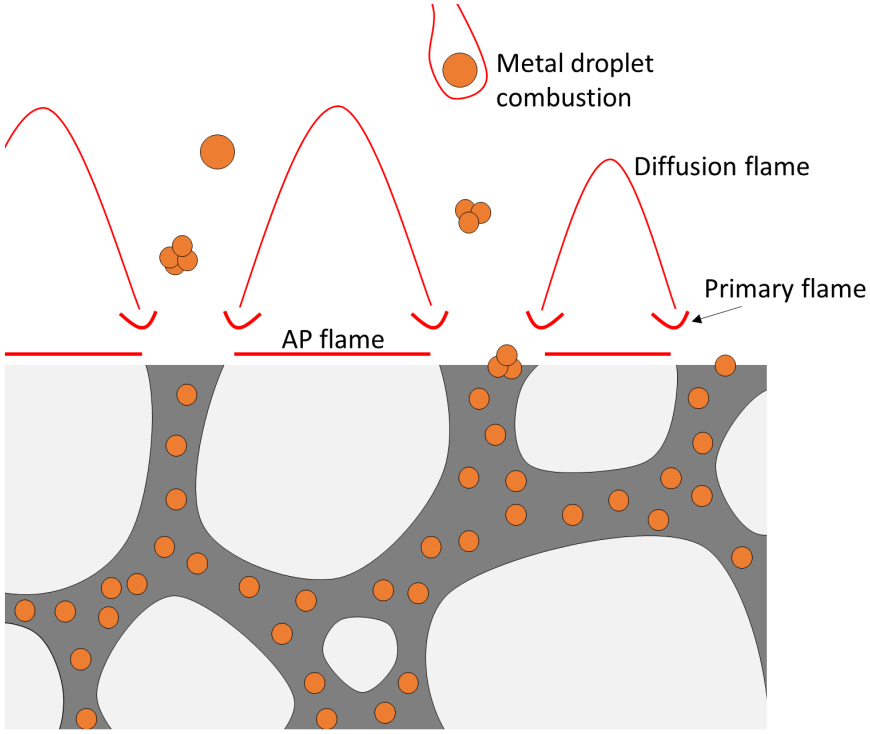

Figure 2-6: The typical flame structure of composite propellant combustion. Heat from the flames decomposes the ammonium perchlorate and binder, which in turn supply oxidizing (AP) and fuel (binder) gases to the flames. Based on figures in [46, 66].

This flame structure causes the propellant to burn faster at higher pressures. At higher pressures, the gas phase is denser, causing reactions and diffusion to proceed more quickly. This moves the flame structure closer to the surface. The closer flames and denser conducting medium enhance heat transfer to the surface, which drives more decomposition, increasing the burn rate.

Although the dependence of burn rate on pressure is complicated, it can be empirically described by fitting a simple power law to experimental data (see section 2.3.3.2). The dependence of burn rate on pressure is important because it determines the chamber pressure and thrust of a solid rocket motor (recall section 2.2).

2.3.3 Solid propellant properties

This section defines several important properties of solid propellant. These include the solid density ρ_s and pressure-dependent burn rate $r(p_c)$ which were introduced in section 2.2 and are necessary to determine the equilibrium chamber pressure of a motor. Typical techniques for predicting and measuring these properties are also discussed.

2.3.3.1 Solid propellant density

The ideal density of the solid propellant is the weighted average of the densities of the propellant ingredients. The actual density of the propellant can be determined by weighing a sample of known volume. The actual density will be less than the ideal density if there are voids in the propellant.

2.3.3.2 Pressure-dependent burn rate

The pressure dependence of the propellant burn rate is typically modeled with Vieille's formula:

$$r(p_c) = ap_c^n \tag{2.17}$$

where n is the dimensionless burn rate exponent, and a is the burn rate coefficient, which has dimensions of [velocity (pressure)$^{-n}$]. For stable operation in a motor, the propellant burn rate must increase sub-linearly with pressure, i.e. $n < 1$. For typical composite propellants, n is between 0.2 and 0.5 [77].

a and n are model parameters which must be determined experimentally. These can be measured by:

- Burning small strands of propellant at a controlled pressure in a 'Strand Burner' apparatus. Using several samples of the same propellant, the burn rate can be measured at several pressures. Then, values for a and n can be fit to this data.

- Firing the propellant in a motor with known A_b and A_t, and measuring the time to burn the propellant and the chamber pressure. a and n can be fit to data from one or several firings, depending on the details of the experiment.

The Strand Burner experiment is easier to repeat over a range of chamber pressures, but the motor firing gives a more accurate prediction of what the burn rate will be in a similar motor. Both techniques are used in this work.

The burn rate also has a (weaker) dependence on the initial temperature of the propellant grain [77]. This was not measured in this work. All burn rate measurements in this work were at an initial temperature of 15–25 °C.

2.3.3.3 Minimum burn pressure

For some propellants, there is a minimum pressure below which the propellant will not burn. When oxamide is added to reduce the burn rate, the minimum burn pressure increases with oxamide content. The minimum burn pressure puts a lower limit on chamber pressure. As discussed in chapter 3, this has important implications for motor and vehicle design, setting a minimum feasible thrust for the motor.

2.3.3.4 Combustion gas ratio of specific heats

The expansion of the exhaust gas through the nozzle depends on the gas's ratio of specific heats, γ. Thus it is important to quantify γ for the gas.

The ratio of specific heats is predicted by combustion equilibrium software [65]. The ratio of specific heats will change slightly as the gas expands through the nozzle. The values presented here are for the chamber (stagnation) conditions; assuming the gas properties are 'frozen' at the chamber conditions is a good approximation for small nozzles [77].

The numerical predictions of γ are generally quite good [77], and measuring γ in the motor would be difficult, thus no empirical data for γ is presented in this work.

2.3.3.5 Other properties

Other properties of the propellant, e.g. mechanical properties, aging, thermal expansion, sensitivity to accidental ignition, etc., are also important for other aspects of solid rocket motor design. However, these other properties were not measured in this work.

Chapter 3

Low-thrust solid rocket motors for aircraft propulsion

The design of slow-burn solid rocket motors for aircraft propulsion is coupled to the fuselage configuration and the desired trajectory. The motor's thrust is set by the trajectory, and its burn area is set by the fuselage diameter. Inconveniently, the required thrust level is very low compared to the required burn area. The challenge of these slow-burn motors is not low thrust itself, but low thrust relative to the burn area.

The low (thrust / burn area) ratio is an unusual feature of motors meant to propel an aircraft in steady, level flight. Typical solid rocket motors are designed to accelerate a vehicle quickly, either to catch up with a target (i.e. tactical missiles) or to reduce gravity losses (i.e. sounding rockets and launch vehicles). Most development efforts have focused on high thrust motors with high-energy, faster burning propellants. Operation at low thrust, in contrast, is a somewhat neglected area of research.

The thrust and burn area constraints of UAV propulsion require a slow-burn propellant. This motivated the development of a family of slow-burn propellants, which is discussed in chapter 4 and chapter 5. As will be shown in this chapter, even with slow-burn propellant, the efficiency of the motor (I_{sp}) is reduced by operating

at such a low thrust/burn area ratio.

3.1 The thrust/burn area ratio

This section introduces the thrust/burn area ratio, F/A_b, as a parameter for motor design. This parameter is seldom used in the propulsion literature. However, it is helpful for the design of slow-burn motors for aircraft propulsion because it provides a link between the motor design, fuselage configuration, and trajectory.

For the motors considered here, thrust and burn area are fixed by the aircraft and trajectory design. For steady, level flight the thrust is fixed to match the drag on the aircraft at cruise speed. For an end-burn motor which fills the fuselage, the burn area is set by the fuselage diameter.

For the reference Firefly mission (cruise at Mach 0.8, 10 km altitude), these considerations set a F/A_b ratio which is 1/10th the value of typical solid rocket motors. In fact, the required F/A_b is very close to the lower limit at which the propellant can operate.

3.1.1 Relation of the thrust/burn area ratio to motor design

To derive the relation of F/A_b to the other motor design parameters, we start with two equations (see section 2.2): 1) thrust:

$$F = p_c A_t C_F(p_c) \tag{3.1}$$

and 2) mass flow equilibrium:

$$\dot{m} = \underbrace{\frac{p_c A_t}{c^*}}_{\text{nozzle}} = \underbrace{A_b r \rho_s = A_b (a p_c^n) \rho_s}_{\text{combustion}} \tag{3.2}$$

Motor	Application	Thrust [N]	Burn area [m^2]	F/A_b [kPa]
First Stage, Minuteman	Missile booster	865 581	24.84	34.8
Orbus-6	Upper stage	76 394	2.52	30.3
STAR 27	Upper stage	26 732	0.89	30.1
Cesaroni P38-6G Classic	Hobby	325.3	0.0204	15.9
Cesaroni P38-2G Classic	Hobby	125.1	0.0068	18.4

Table 3.1: Different solid rocket motors, with a wide range of sizes and applications, all operate at similar F/A_b. Thrust and burn area are average values over the burn time. All these motors use ammonium perchlorate composite propellant. Data from [77, 13].

Combining the two equations gives:

$$\frac{F}{A_b} = p_c^n C_F(p_c) c^* a \rho_s \tag{3.3}$$

The F/A_b ratio depends on the chamber pressure and the properties of the propellant (n, c^*, a and ρ_s). F/A_b does not depend on the size of the motor. In fact, table 3.1 shows that several motors, which differ in size (total impulse) by five orders of magnitude, have similar values of F/A_b, all between 15 kPa and 35 kPa.

3.1.2 Relation of the thrust/burn area ratio to trajectory and fuselage

The ratio F/A_b is related to the trajectory. In steady, level flight:

$$F = D = qC_D S_{ref} \tag{3.4}$$

where q is the dynamic pressure, C_D is the drag coefficient, and S_{ref} is the drag reference area. For the purposes of this chapter, we will take S_{ref} to be the forward-projected area of the fuselage.

Dividing both sides of eq. (3.4) by A_b gives:

$$\frac{F}{A_b} = qC_D \left(\frac{S_{ref}}{A_b} \right) \tag{3.5}$$

Thus, F/A_b is proportional to the dynamic pressure, and to the ratio of drag reference area over burn area. q depends on the trajectory, and S_{ref}/A_b depends on how the motor is configured within the fuselage. For an end-burn motor, A_b is the transverse section area of the propellant grain. S_{ref} will be slightly larger, due to the ablative liner and case wall which surround the propellant (fig. 3-1). Thus, for end-burn motors, S_{ref}/A_b will be slightly greater than one. For the baseline design shown in fig. 1-3, $S_{ref}/A_b = 1.2$.

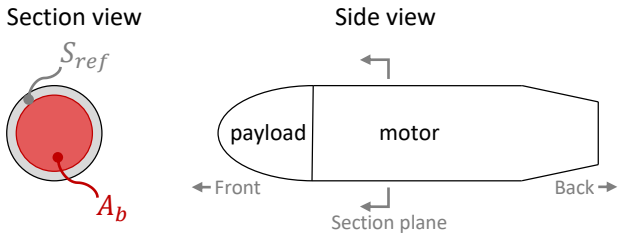

Figure 3-1: The fuselage frontal reference area S_{ref} (shaded gray) is only slightly larger than the propellant burn area A_b (shaded red).

S_{ref}/A_b is only weakly dependent on the size of the vehicle. If the fuselage diameter were increased, S_{ref}/A_b would be closer to 1 – the burn area would increase, but the thickness of the ablative would not change.

Thus, the three terms on the right-hand side of eq. (3.5) (q, C_D, and S_{ref}/A_b), are set by the trajectory and fuselage configuration. Together, they set a required value for the motor's F/A_b. As will be shown below, this value is inconveniently low.

Consider the F/A_b required by eq. (3.5) for the example Firefly mission (Mach 0.8, 10 km altitude). At Mach 0.8 and 10 km altitude, the dynamic pressure is $q = 12$ kPa. At Mach 0.8, C_D might be about 0.2, depending on the size of the wings and tails. As discussed above, $S_{ref}/A_b = 1.2$. The desired F/A_b for steady, level flight is about 2.9 kPa.

This value is much lower than the typical values presented in table 3.1. In fact, it is almost at the lower limit of F/A_b that can be achieved, even with slow-burn propellants.

3.2 Lower limit on thrust

There is a lower limit on F/A_b below which a propellant cannot operate. Thus, there is a lower limit on the thrust of an end-burn motor (if the motor diameter is fixed). This is primarily because the motor must have a very low chamber pressure to achieve low F/A_b, but below some minimum pressure the propellant will not burn. Even with slow-burn propellants, F/A_b ratios less than about 2 kPa are not feasible. As will be shown below, there is also a performance penalty to operating at low F/A_b: the specific impulse is less if the motor is made to operate a lower F/A_b.

The preceding sections showed that the example Firefly mission requires an end-burn motor which operates a F/A_b which is much lower than that of typical motors. Some parameters of the motor design need to be changed to operate at low F/A_b. Revisiting eq. (3.3), note that p_c^n and $C_F(p_c)$ both decrease monotonically with decreasing p_c:

$$\frac{F}{A_b} = \underbrace{p_c^n C_F(p_c)}_{\text{pressure-dependent}} \quad c^* a \rho_s \tag{3.6}$$

The remaining variables, $c^* a \rho_s$, depend only on the propellant composition, not pressure. Thus, to make F/A_b small, the motor must operate at low p_c and use a slow-burn propellant with low a.

However, operating at low p_c reduces C_F and I_{sp} (because the nozzle expansion is less efficient when the pressure ratio across the nozzle is lower). Also, each propellant has a minimum pressure below which it will not burn.

This trend is illustrated in fig. 3-2 for several different propellants. Three propellants are from the family of ammonium perchlorate (AP) propellants developed

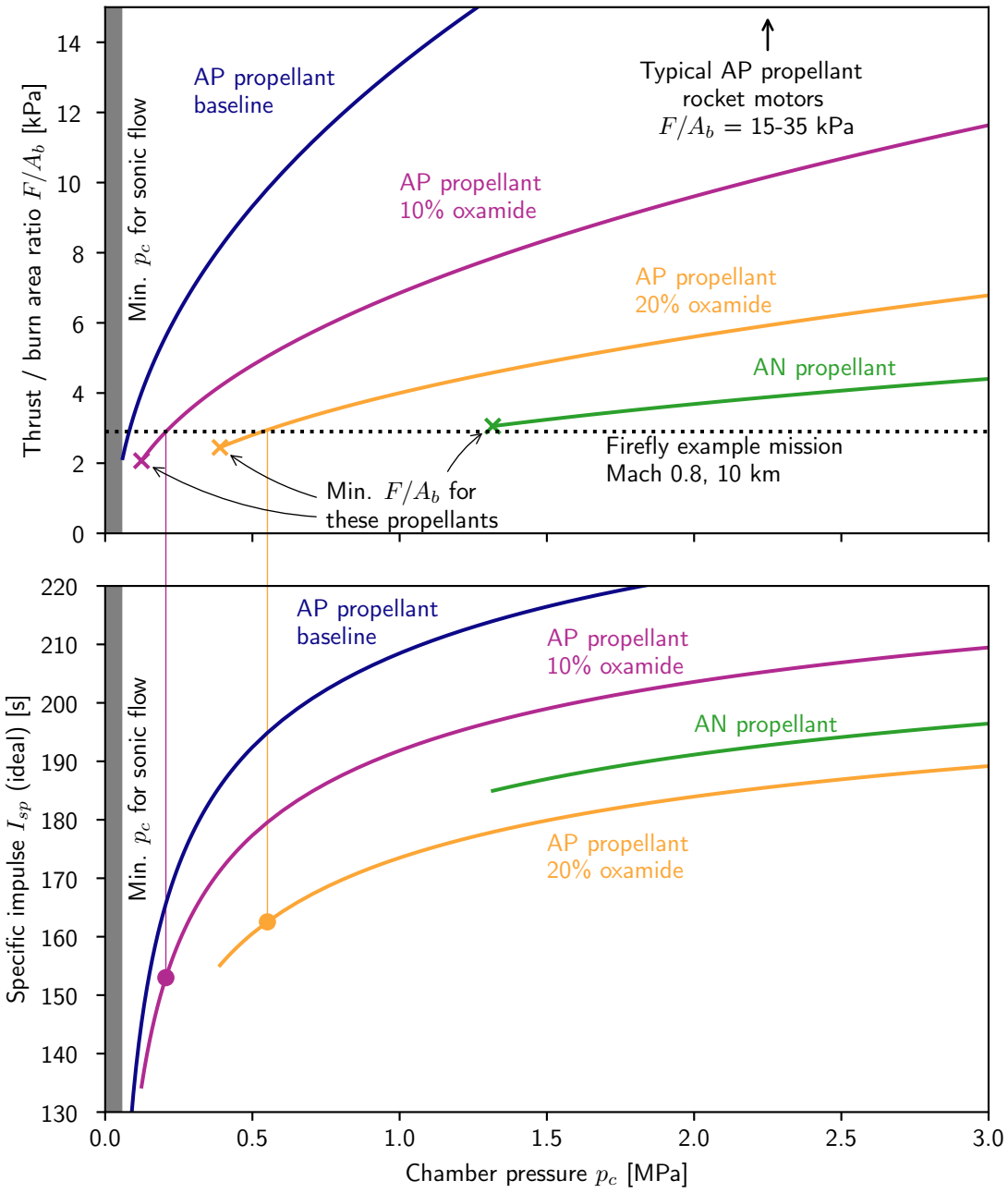

Figure 3-2: Operating at lower F/A_b requires low chamber pressure and reduces specific impulse. At some minimum F/A_b, each propellant reaches its minimum burn pressure (marked with 'x'). Lower F/A_b is infeasible for that propellant.

in this work. In these propellants, the burn rate is set by the amount of oxamide (a burn rate suppressant). The baseline AP propellant (blue curve) burns fastest, the

10% oxamide propellant (pink curve) has an intermediate burn rate, and the 20% oxamide propellant (orange curve) burns slower. For comparison, an ammonium nitrate (AN) propellant (green curve) is also included. Using AN oxidizer is a different way to make a slow burning propellant (see chapter 4).

The curves show F/A_b (top plot) and specific impulse (bottom plot) versus chamber pressure. The relation between F/A_b and p_c is calculated using eq. (3.3) and propellant burn rate data measured in this work[1]. Specific impulse is calculated using the *ideal* 1d nozzle model, assuming matched expansion to an ambient pressure of 30 kPa. These plots help to find a propellant and chamber pressure which meet a mission's F/A_b requirement, while keeping I_{sp} as high as possible.

For each propellant, reducing chamber pressure reduces F/A_b (top plot). However, the chamber pressure cannot be less than the propellant's minimum burn pressure; this sets a lower limit on F/A_b for that propellant. The minimum combustion pressures for each propellant are marked with an 'x' in the top plot [2].

Although the AN propellant has the slowest burn rate, the AP+oxamide propellants can operate at lower F/A_b because they have lower minimum combustion pressures. The 10% oxamide propellant can provide an F/A_b down to 2.1 kPa. Interestingly, the slower-burning propellants (AP+20% oxamide and AN) have *higher* minimum F/A_b – although they are slower-burning, their minimum burn pressures are much higher.

For each propellant, operating at lower chamber pressure reduces the specific impulse (bottom plot). As the exit pressure is always expanded to ambient (30 kPa), lower p_c reduces the nozzle pressure ratio, lowering I_{sp}. At a given chamber pressure, cooler-burning propellants give lower I_{sp}.[3]

Looking across the top plot, notice that at a given F/A_b, the slower-burning pro-

[1]For the AN propellant, a, n are from Sutton and Biblarz [77] table 13-10 and the minimum burn pressure is from Vernacchia [89].

[2]The AP baseline propellant curve is not marked with an 'x' because the minimum p_c to choke the nozzle flow is higher than the minimum burn pressure of this propellant.

[3]For the AP+oxamide propellants, adding more oxamide reduces the flame temperature and decreases c^* (the effects of oxamide on combustion will be discussed further in chapter 4).

pellants can operate at a higher chamber pressure. The F/A_b required for the Firefly reference mission (Mach 0.8, 10 km altitude) is about 2.9 kPa and is marked on the top plot with a black dotted line. This is barely within the limits of the AP+oxamide propellants. The AN propellant cannot achieve this F/A_b – the required p_c is so low that it would not burn. At this F/A_b, the baseline AP propellant would need such a low p_c that the nozzle flow would barely reach sonic velocity, and the specific impulse would be abysmal (< 130 s).

The 10% and 20% oxamide propellants can operate at the example mission F/A_b. For the 10% oxamide propellant, the motor would operate at $p_c = 0.21$ MPa and $I_{sp,ideal} = 153$ s; for the 20% oxamide propellant, $p_c = 0.55$ MPa and $I_{sp,ideal} = 163$ s. These operating points are marked with dots on the bottom plot.

The effects of F/A_b on specific impulse are summarized in fig. 3-3. This plot shows the same data as fig. 3-2, but plotted as I_{sp} versus F/A_b. Generally, lower F/A_b reduces specific impulse, and slower-burning propellants give higher specific impulse at a given F/A_b.

For $F/A_b > 3.1$ kPa, the AN propellant can operate and has slightly higher specific impulse than the AP+oxamide propellant (fig. 3-3). However, the AN propellant is less dense (1480 kg m^{-3} vs. 1600 kg m^{-3}) so less propellant mass can fit in the motor. Also, for $F/A_b > 4$ kPa, the AN propellant requires high (> 3 MPa) chamber pressures (fig. 3-2, top plot), which entail a heavy motor case. In contrast, the AP+oxamide propellant family can be used for a wide range of F/A_b. Thus, the AP+oxamide propellant family is preferred for this work.

These specific impulse values (e.g. $I_{sp,ideal} = 153$ s for the example mission with AP+10% oxamide propellant) are unusually low for modern solid rocket motors ($I_{sp} > 250$ s is achievable). Further, small, low-thrust motors have low c^* and C_F efficiencies (as will be discussed in later chapters). These inefficiencies reduce the delivered I_{sp} to about 110 s. Despite this low I_{sp}, an aircraft propelled by such a motor can have a powered flight range of 50–100 km, which is useful for many missions.

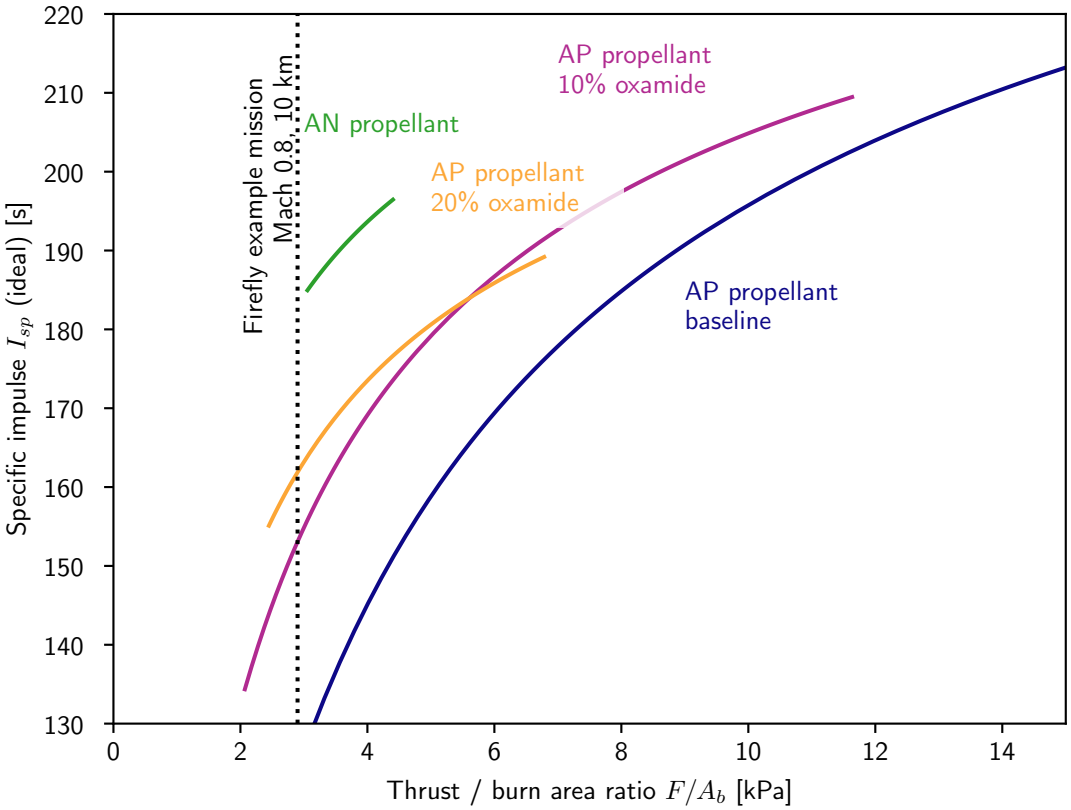

Figure 3-3: Operating at lower F/A_b reduces specific impulse. Slower-burning propellants usually give higher specific impulse at a given F/A_b.

Chapter 4

Slow-burn solid propellant

Slow-burn propellants are necessary for small, low-thrust motors. Three routes to achieve a slow-burn propellant are: 1) change to an inherently slower-burning oxidizer, 2) use a larger oxidizer particle size, or 3) add a burn rate suppressant to the propellant. This work employs large oxidizer particles and a burn rate suppressant (oxamide).

Slow-burn solid propellants are a somewhat neglected area of research. Most new propellant development efforts in recent decades have focused on high-energy, faster-burning propellants, as these are desirable in most space and military applications [43, 77]. Slow burn propellants are only desirable in niche applications such as gas generators [77].

This chapter describes the physical mechanisms by which large AP particles and oxamide reduce the burn rate, and reviews the (sparse) literature which has been published about oxamide in recent decades. A novel model of oxamide's effect on propellant burn rate is also presented.

4.1 Slow-burn propellants based on ammonium nitrate

Ammonium nitrate composite propellants are used for some slow-burn applications [77], but were not used in this work. This section reviews some of the drawbacks of ammonium nitrate propellants.

Substituting ammonium nitrate (AN, NH_4NO_3) for ammonium perchlorate as the oxidizer reduces the propellant burn rate. AN burns cooler and has slower decomposition kinetics than AP [43]. However, AN based propellants have issues with performance, processing and storage. AN is a less effective oxidizer than AP (lower oxygen balance), so it requires a higher solids loading (difficult to mix) and achieves a lower specific impulse at the same chamber pressure. Further, AN is very hygroscopic, and has poor temperature stability in storage [43].

4.2 Slow-burn propellants based on ammonium perchlorate and oxamide

The focus of this propellant development work has been a family of slow-burn ammonium perchlorate propellants. These achieve a slow burn rate by using large AP particles and a burn rate suppressant, oxamide. The burn rate of the propellant can be tailored by altering the oxamide content.

4.2.1 Reducing burn rate with larger AP particles

Increasing the AP particle size decreases the burn rate of AP composite propellants. A larger AP particle size increases the distance which the AP and binder decomposition products must diffuse to mix. This moves the diffusion flame farther from the propellant surface, decreasing heat feedback to the surface, and thus decreasing the burn rate [28]. This effect saturates at very small or large sizes, where the burn rate

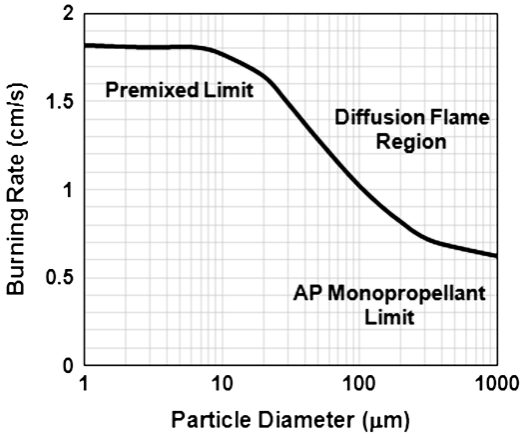

Figure 4-1: Increased AP particle size decreases the burn rate of AP composite propellant. The data in this figure are from detailed numerical simulations of the combustion process. Reprinted from [28].

approaches the premixed limit and the AP monopropellant burn rate, respectively (fig. 4-1).

However, using large AP particle size alone does not make the propellant burn rate slow enough. Also, AP particle size is not a convenient mechanism for tailoring the burn rate, as only a few particle size blends are commercially available.

4.2.2 Reducing burn rate with burn rate suppressants (oxamide)

To reduce the burn rate further, a burn rate suppressant is introduced as a minor ingredient in the propellant formulation. Burn rate tailoring is easily achieved by varying the amount of burn rate suppressant. Oxamide is the most notable of the burn rate suppressants, but others, including melamine, urea, and azodicarbonamide, are used [84, 25]. A suppressant can reduce the burn rate of a propellant by at least 50% [25, 43].

Although burn rate suppressants are widely known, they are a neglected area of research. The chemical thermodynamics and burn rate effects of these propellants were still being measured in the 2010s, mostly by Trache et al. [84, 85] in Algeria and

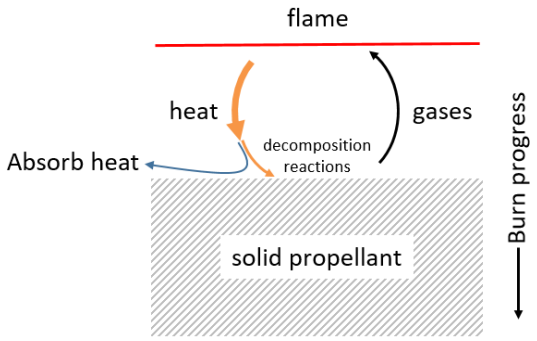

Figure 4-2: It is believed that coolants reduce the burn rate by absorbing heat at the surface of the propellant, which slows the condensed phase decomposition reactions.

Italy and Ghorpade et al. [25] and Parhi et al. [61, 62] in India . This author's MS thesis [89] proposed the first[1] quantitative model for the dependence of burn rate on oxamide content.

These burn rate suppressants act as coolants [11]. Coolants remove heat from the surface of the burning propellant, which reduces the surface temperature (fig. 4-2). The rates of the surface decomposition reactions are temperature dependent, so cooling the surface decreases its decomposition rate. Decreasing the decomposition rate reduces the mass flux available to the gas-phase flame structure, and decreases the burn rate.

At the surface of the burning propellant, suppressants decompose endothermically, and do so at a lower temperature than the other propellant ingredients [84, 25]. There are two possible routes by which this may provide a cooling effect. First, the energy consumed by suppressant decomposition increases the heat required to decompose a unit volume of solid propellant. Second, the injection of relatively cool suppressant product gases into the boundary layer above the propellant surface may reduce heat transfer.

The coolant effect of oxamide is examined in fig. 4-3. The left plot shows thermal gravimetric analysis (TGA), which measures the mass loss of a sample as it decomposes while heated. The right plot shows differential scanning calorimetry (DSC),

[1] at least in the open literature

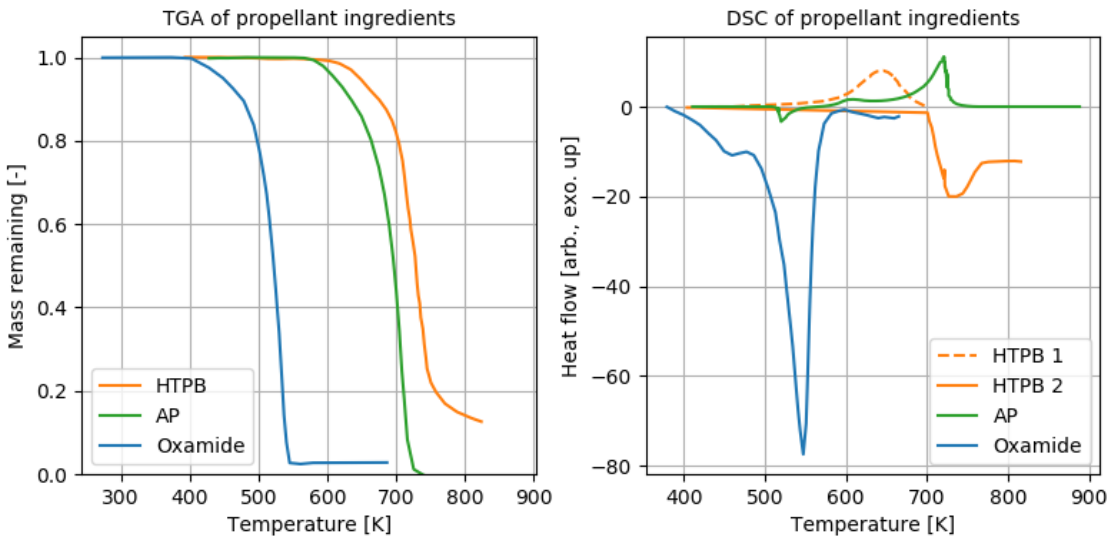

Figure 4-3: Oxamide decomposes at a lower temperature and more endothermically than other propellant ingredients (AP and HTPB). Data from [81, 43, 84].

which measures the heat released/absorbed by reactions in a sample as it is heated. Exothermic reactions have positive heat flow, endothermic reactions have negative heat flow. The DSC data are scaled so the area under the DSC curves is proportional to the specific heat of the decomposition reaction. Compared to the HTPB binder and AP oxidizer (orange and green curves), oxamide (blue curves) decomposes at a lower temperature, and its decomposition is much more endothermic (more negative on the right DSC plot).

The data in fig. 4-3 were collected on the individual propellant ingredients, in experiments performed by other researchers (HTPB data from [81], AP data from [43], oxamide data from [84]). The data do not capture possible interactions between the ingredients during heating. Also, these data were taken at heating rates much lower than those of combustion [2].

More recently, in 2018, Trache et al. performed calorimetry experiments on (mixed) samples of oxamide-doped composite propellant [85]. This study provided further

[2]The HTPB data contain an exothermic cyclization reaction around 650 K (orange dashed curve). This reaction occurs at the low heating rates used to collect these data, but its kinetics are so slow that it does not occur in propellant combustion [81].

evidence that oxamide suppresses the condensed phase decomposition of the propellant.

4.2.3 Previous measurements of oxamide's effect on burn rate

Although oxamide is widely known to be an effective burn rate suppressant for composite propellants [77], there are few quantitative reports of its effect on burn rate in the open literature. Only a few suitable sources were found:

1. Parhi et al. [61, 62] describe the development of an oxamide-suppressed AP composite propellant. This propellant was developed for a slow-burn solid rocket booster used by the Indian Space Research Organization (ISRO). The propellant burn rate was measured in a strand burner and in ballistic evaluation motors. Oxamide concentrations of 0, 1, 2, 3 and 4% were tested. The propellant formula is stated in [61] as 84% AP, 11.18% HTPB and 4% oxamide [3]. The burn rates were measured at pressures between 1 and 4 MPa. These experiments are more comparable to the present work than Ghorpade et al. [25] or Trache et al. [84], as the propellant composition and test pressures are similar.

2. Jeenu, Pinumalla, and Deepak [38] report burn rates for 0% and 3% oxamide propellants in large (750–12 000 kg) test motors [4]. The baseline propellant is 68% AP, 18% Al, and 14% binder (HTPB). The motor chamber pressures were 1.6–3.3 MPa. Jeenu et al.'s work was performed in the same ISRO facility as Parhi et al.

3. Ghorpade et al. [25] reports strand burner experiments on composite propellants with oxamide (and several other burn rate suppressants). These data

[3] A later (2018) paper [62] references aluminum in the propellant. However, the I_{sp} reported in [61] is consistent with the no-metal formula. Perhaps a decision was made to add metal between the 2015 and 2018 publications?

[4] Jeenu et al. also present burn rate tests on smaller 35 mm × 40 mm specimens of propellant.

were collected at a much higher pressure (5–9 MPa) than the pressures considered in this work. It also used a metalized propellant (60% AP, 20% binder, 10% Al, and 10% oxamide).

4. Trache et al. [84] measured the burn rate of 0.5% and 3% oxamide propellants in a strand burner. The baseline propellant was 68% AP, 14% binder (HTPB), and 18% Al. Pressures of 0.5–7 MPa were used. Trache's data have more scatter than the other data, and have few trials (only three strand tests per propellant).

Burn rate data from these studies are plotted in fig. 4-4. To compare burn rate data from different studies, which used different baseline propellants, the burn rate data are shown in terms of the burn rate multiplier ϕ_{om}. ϕ_{om} is the ratio of the propellant burn rate with oxamide to the burn rate of that study's baseline, no-oxamide propellant (at the same pressure).

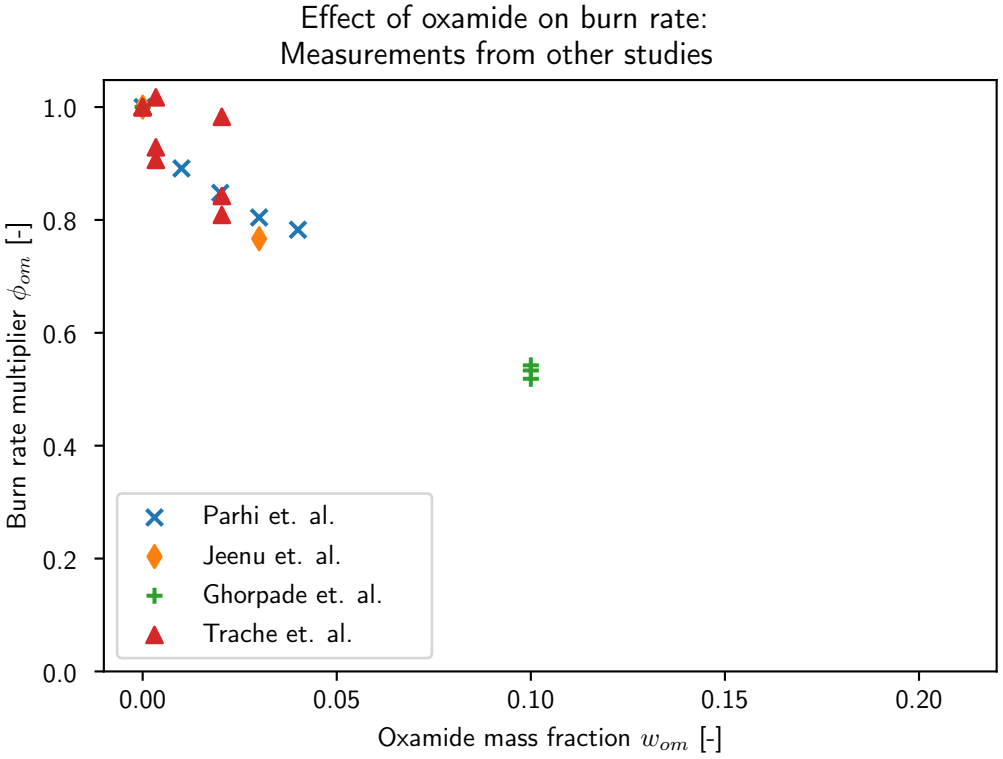

Figure 4-4: Various measurements of the effect of oxamide on propellant burn rate.

The highest oxamide content tested in the literature was 10%. At this oxamide content, the burn rate was halved ($\phi_{om} = 0.5$).

4.2.4 Model of oxamide's effect on burn rate

Vernacchia [89] proposed a quantitative model predicting the reduction in burn rate that will occur from introducing a given concentration of oxamide into a propellant. To the author's knowledge, no other research has yet proposed such a model. Use of this model would significantly reduce the experimental effort of tailoring the burn rate of a propellant for a particular application. This predictive capacity would enhance the utility of oxamide as a design tool for slow-burning solid propellants.

This theory is derived by applying the conservation of energy and mass to a control volume containing the decomposing surface of the propellant. It assumes that the presence of oxamide 1) reduces the heat flux into the surface, by diluting and cooling the gas-phase flame and 2) increases the energy required to decompose a unit mass of solid propellant. The full derivation is presented in Vernacchia [89], section 2.6.

This theory predicts that the burn rate multiplier ϕ_{om} due to the addition of oxamide is:

$$\phi_{om} = \frac{1 - w_{om}}{1 + \lambda w_{om}} \tag{4.1}$$

where w_{om} is the mass fraction of oxamide in the propellant, and λ is a dimensionless parameter. λ can be predicted from thermochemical data, which suggest it is about 7 for typical AP composite propellants [89]. The burn rate with oxamide is then $r_{om}(p_c) = \phi_{om}(w_{om}) r_0(p_c)$, where $r_0(p_c)$ is the burn rate without oxamide.

In terms of the burn rate coefficient, a, the model is:

$$a = a_0 \frac{1 - w_{om}}{1 + \lambda w_{om}} \tag{4.2}$$

where a_0 is the burn rate coefficient with no oxamide. It is assumed that the burn

rate exponent n does not vary with oxamide content.

One of the contributions of this work is to validate this model with additional burn rate data (see section 5.4).

Chapter 5

Propellant characterization

Accurate modeling and design of a motor requires characterization of the propellant, particularly empirical characterization of the burn rate as a function of pressure. To this end, a family of several slow burn AP+HTPB+oxamide propellants were developed and characterized. Ideal combustion gas properties were computed with chemical equilibrium software. The burn rate was measured as a function of pressure and oxamide content, in both a strand burner and a research motor. Both strand burner and motor burn rate data are well-fit by the oxamide model presented in section 4.2.4. The burn rate data and model also agree with loosely comparable data available in the open literature (see section 5.4.2).

These propellant data provide the foundation for the motor analysis presented in chapter 3. It is vital to this project's ongoing motor development work with these slow-burn propellants.

5.1 Propellant family used in this work

This work used a family of ammonium perchlorate (AP) composite propellants, which use large AP particle sizes and the burn rate suppressant oxamide to achieve a slow burn rate. The amount of oxamide in the propellant can be varied to achieve a variety of burn rates. Propellants with oxamide mass fractions of 0%, 5%, 10%, 13%

and 20% were mixed and tested; the burn rate is reduced by a factor of four over this range of oxamide content.

A family of propellants with tailorable burn rate enables flexibility in adjusting the propellant and motor for different missions. Propellants with different burn rates are also necessary for some motor configurations (i.e. a tapered motor with varying burn area).

5.1.1 Propellant ingredients

This propellant family is based on a standard ammonium perchlorate composite propellant with no metal fuel. The "base" propellant consists of 80% AP and 20% HTPB-based binder. In the propellants which contain oxamide, the ratio of AP to binder is kept at 4:1. The mass ratio of each binder ingredient to HTPB resin is the same in all the propellants (except the 20% oxamide propellant [1]). The composition of the baseline (0% oxamide) propellant is listed in Table 5.1, and the 10% oxamide propellant is listed in Table 5.2.

Two AP particle size distributions were used in this work:

- '400/200 micron blend': a blend of 400 µm diameter rounded particles, 200 µm diameter rounded particles, and finer ground particles.
- '400 micron blend': a blend of 400 µm diameter rounded particles and finer ground particles.

The use of large (400 µm) AP particles reduces the propellant burn rate. A blend including finer ground particles enables higher solids loading by increasing the packing density of the AP particles [77].

Propellants with 0%, 10% and 13% oxamide were made with the '400/200 micron blend' AP. Propellants with 5% and 20% oxamide were made with the '400

[1]For the 20% oxamide propellant, the binder was slightly modified, with the carbon powder opacifier content reduced to 0.2%. The objective of this modification was to reduce amount of soot in the combustion products.

Purpose	Ingredient	Mass fraction [%]	
Binder			20.00
Resin	Hydroxyl-terminated polybutadiene	10.98	
Binding agent	HX-752	0.27	
Anti-oxidant	CAO-5	0.11	
Curative	Modified MDI	1.72	
Plasticizer	Isodecyl pelargonate	4.72	
Opacifier	Carbon powder	2.20	
Oxidizer			80.00
	Ammonium perchlorate	80.00	

Table 5.1: The baseline AP propellant

micron blend' AP. Both AP blends were coated with tricalcium phosphate (anti-caking agent) by the manufacturer [2].

The binder is primarily hydroxyl-terminated polybutadiene (HTPB). The HTPB resin had a molar mass of $2800\,\mathrm{g\,mol^{-1}}$. It is cross linked with Modified MDI (a diphenyl methane diisocyanate). The HTPB resin was purchased pre-mixed with CAO-5 (anti-oxidant) and HX752 (bonding agent). Isodecyl pelargonate (IDP, plasticizer), and graphite powder (opacifier) are added to the binder [3].

The oxamide (burn rate suppressant) was purchased as a powder [4]; the stated purity was $> 98\%$. The oxamide tended to clump during storage, so it was ground in a ball mill shortly before use.

Most of the propellants used approximately 2% by mass graphite powder as the opacifier. To reduce the amount of soot in the exhaust, a lower graphite power content of 0.2% was tried in the 20% oxamide propellant. The formulation of this propellant is listed in table 5.3.

[2]The AP blends were purchased from RCS Rocket Motor Components, Inc. of Cedar City, Utah.

[3]All of the binder chemicals, except the graphite powder, were purchased from RCS Rocket Motor Components, Inc.

[4]from Alfa Aesar of Ward Hill, Massachusetts

Purpose		Ingredient	Mass fraction [%]
Binder			18.00
	Resin	Hydroxyl-terminated Polybutadiene	9.88
	Binding agent	HX-752	0.24
	Anti-oxidant	CAO-5	0.09
	Curative	Modified MDI	1.55
	Plasticizer	Isodecyl pelargonate	4.25
	Opacifier	Carbon powder	1.98
Oxidizer			72.00
		Ammonium perchlorate	72.00
Burn rate suppressant			10.00
		Oxamide	10.00

Table 5.2: The 10% oxamide propellant

Purpose		Ingredient	Mass fraction [%]
Binder			16.00
	Resin	Hydroxyl-terminated Polybutadiene	9.74
	Binding agent	HX-752	0.24
	Anti-oxidant	CAO-5	0.09
	Curative	Modified MDI	1.53
	Plasticizer	Isodecyl pelargonate	4.19
	Opacifier	Carbon powder	0.21
Oxidizer			64.00
		Ammonium perchlorate	64.00
Burn rate suppressant			20.00
		Oxamide	20.00

Table 5.3: The 20% oxamide propellant, with reduced carbon powder content.

5.1.2 No metal fuel for small, low-thrust motors

This work used a simple propellant without metal fuel, because the typical advantages of metal fuel are not valid for very small motors. The goal of metal fuel is to increase specific impulse by raising the combustion temperature (recall that $I_{sp} \sim \sqrt{T_c}$). However, metal fuel also produces solid or liquid particles in the exhaust, which make the nozzle expansion less efficient. The inefficiencies occur because the momentum and temperature of the condensed phase particles lag behind those of the gas. In motors with large nozzles, the gas takes a long time to flow through the nozzle, the particle lag is minor, and the loss of nozzle efficiency is small. In large motors, adding metal fuel improves specific impulse, and is a standard practice. For example, the propellant used in the Space Shuttle's Reusable Solid Rocket Motors contained 16% aluminum powder (by mass) [39].

With small nozzles, the gas accelerates through the nozzle in little time, the particle lag is severe, and the loss of nozzle efficiency is large. For very small nozzles, it is likely that including metal fuel would not improve specific impulse. Figure 5-1 shows that the I_{sp}-maximizing metal fuel content is lower for smaller nozzles. The motors considered in this work have nozzle throat diameters of only a few millimeters; thus no metal fuel is used.

There were a few other motivations for excluding the metal fuel:

1. Reducing the number of ingredients simplifies the propellant.

2. Metal fuel increases smoke production; smoke is not desirable in some applications as it makes the vehicle more visible.

3. Metal fuel increases the flame temperature, which requires a thicker ablative liner inside the motor case. This reduces the volume of propellant in a given motor case size.

4. Additional condensed-phase material in the combustion products could contribute to nozzle clogging.

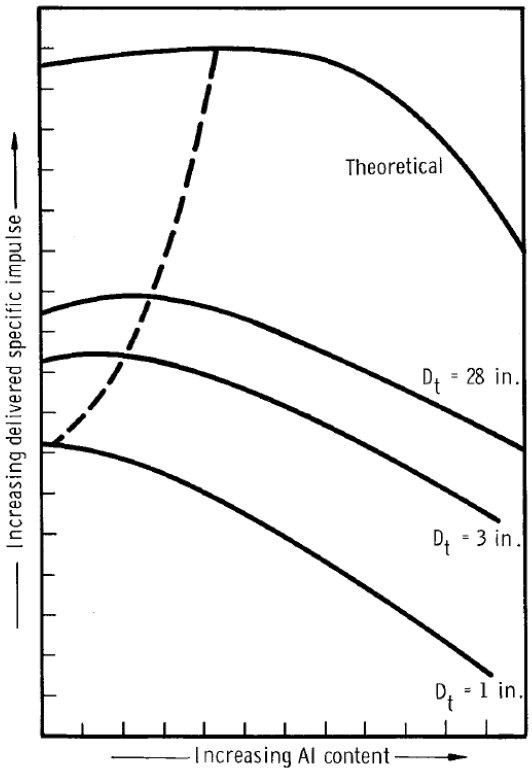

Figure 5-1: For smaller nozzles (smaller throat diameter D_t), the I_{sp}-maximizing metal fuel (Al) content is lower. The solid curves show I_{sp} vs. Al content for different nozzle sizes; the dashed curve connects the maxima of the solid curves. Reprinted from [75].

5.2 Combustion simulation

Combustion simulations (chemical equilibrium calculations) were performed on this family of propellants to predict how the properties of the combustion gas would vary with oxamide content. Figure 5-2 shows the variation in 1) the ideal properties of the combustion gas and 2) the solid density versus oxamide content. The ideal combustion gas properties were computed with the *Rocket Propulsion Analysis* (RPA) combustion equilibrium software [65] [5].

As expected, the flame temperature and characteristic velocity decrease when more oxamide is added to the propellant. Oxamide decomposes endothermically,

[5]Katya Bezugla performed the *Rocket Propulsion Analysis* runs and tabulated the data as an undergraduate researcher on the project.

so the oxamide consumes energy that would otherwise appear as thermal energy in the combustion products. However, the decrease in c^* is much smaller than the decrease in burn rate. Adding 20% oxamide decreases the burn rate by 75%, but only decreases c^* by 16%.

Adding oxamide causes minor variations in the combustion gas ratio of specific heats (γ) and the solid propellant density (ρ_s). These are not large enough to be important to motor performance.

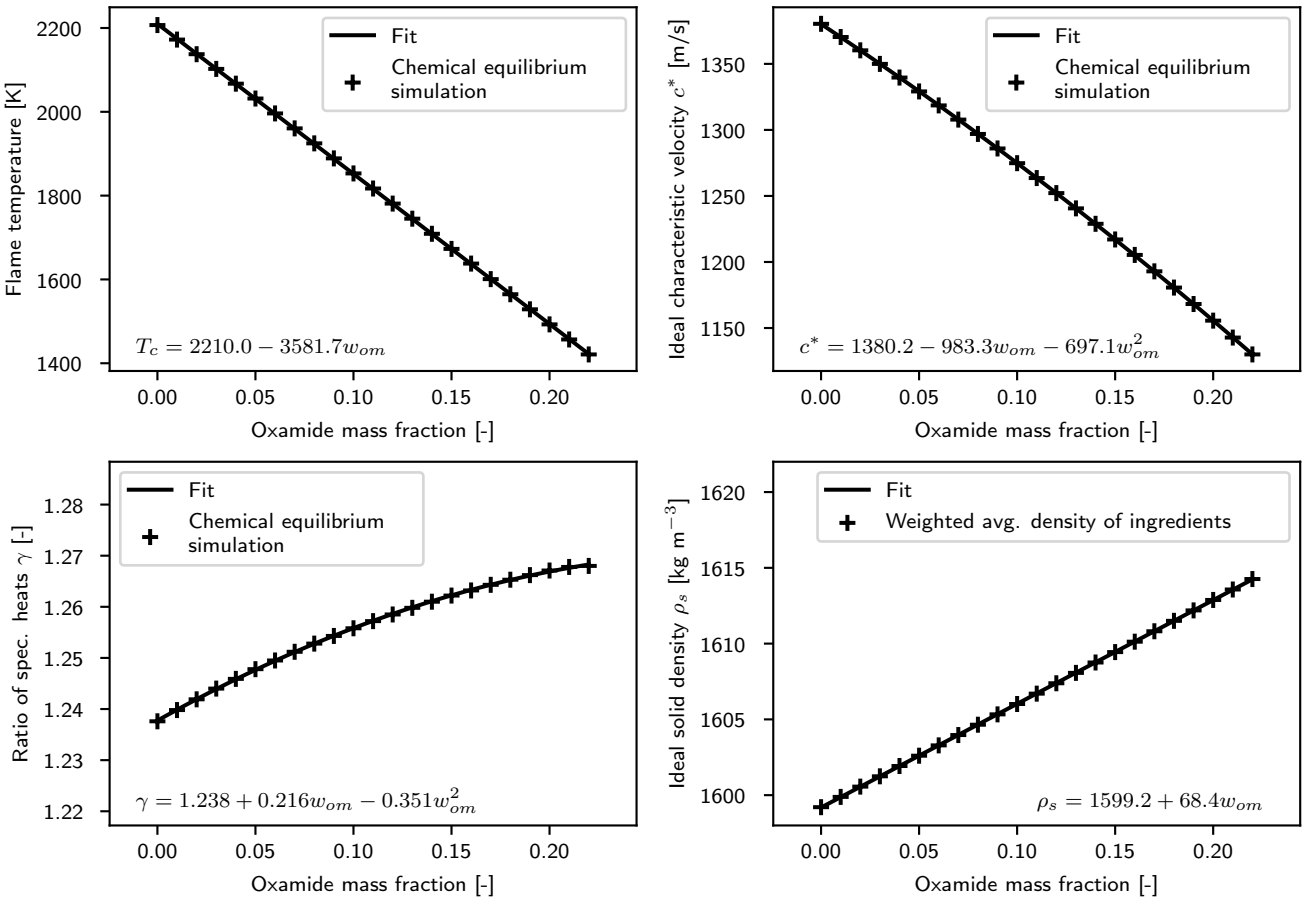

Figure 5-2: The ideal flame temperature, characteristic velocity, ratio of specific heats, and solid density of the propellant.

5.3 Methods and equipment for propellant characterization

5.3.1 Strand burner apparatus

A set of burn rate measurements were performed in a strand burner, which burns small samples ("strands") of solid propellant at a controlled pressure. Several samples of each propellant were burned at different pressures; this process was repeated for 5 different propellants (0%, 5%, 10%, 13% and 20% oxamide content). These data allow insight into how the burn rate varies with both pressure and oxamide content. A custom strand burner device was designed and built for this work.

When propellant batches were mixed (see section 7.1), propellant samples were taken for testing in the strand burner. The samples of propellant were cast into glass tubes (9.7 mm ID x 90.5 mm long). A special machine was built to extrude the propellant into the glass tubes. After filling, the propellant was left to cure in the tubes.

Each propellant-filled sample tube was connected to a pressurized plenum. The propellant was ignited by a small piece of starter propellant, which was itself ignited by a 6 W blue laser. The burn rate was measured by video, and the pressure was recorded with a pressure transducer. Further details on the design and operation of the strand burner are presented below in sections 5.3.1.1 and 5.3.1.2.

5.3.1.1 Strand burner mechanical design

The strand burner has four subsystems, which are illustrated in fig. 5-3:

1. The sample holder (shown in red in fig. 5-3) holds the propellant sample and the laser igniter. The sample is contained in a quartz glass tube, which allows for optical observation of the flame front.

2. The plenum (shown in gray) collects combustion gases from the burning propellant sample. Gas is vented from the plenum through the backpressure regulator.

A large plenum smooths out variations in pressure, and allows solid particles to settle out before reaching the backpressure regulator.

3. The backpressure regulator (shown in green) maintains the desired pressure in the plenum by venting gas if the pressure exceeds the set-point. The backpressure regulator is sensitive to clogging, so it is place on the far side of the plenum (to allow solid particles to settle out of the flow) and is protected by a filter.

4. A pressure sensor (shown in cyan, model PX119-600AI from Omega Engineering) measures the pressure in the plenum.

A camera is set up to record the progress of the flame front through the sample. An analog to digital converter and computer record the plenum pressure and the laser current.

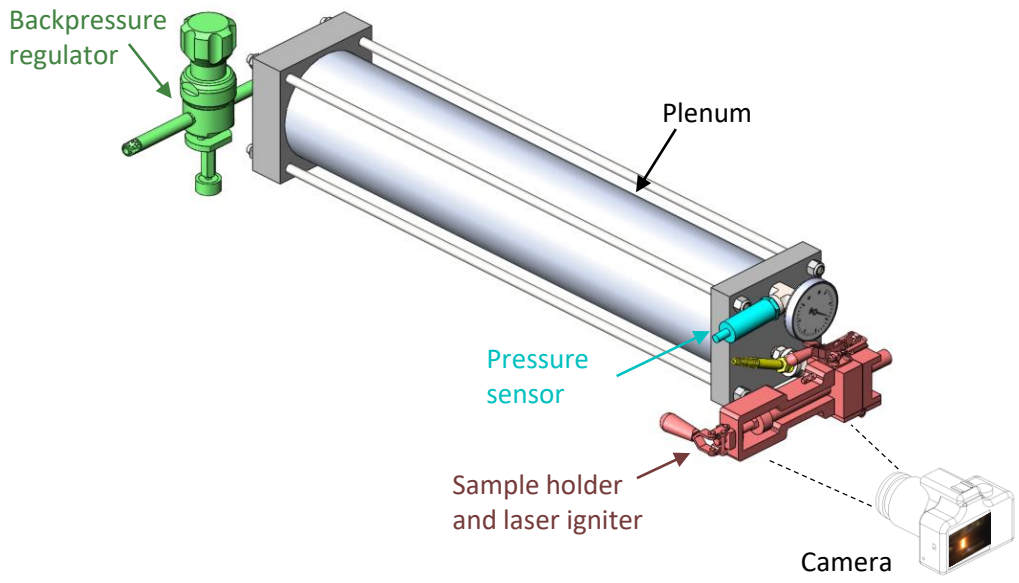

Figure 5-3: Samples of propellant are burned at a controlled pressure in the strand burner's sample holder. The plenum and backpressure regulator help control the pressure.

The sample holder is the most mechanically complex part of the strand burner,

and is detailed in fig. 5-4. The purpose of the sample holder is to hold the propellant sample in alignment with the laser, and to create a sealed, pressurized path from the propellant sample to the plenum.

The sample holder has two sets of moving parts:

1. A toggle which retracts to allow the propellant sample to be removed and replaced, and

2. A door which opens to allow the laser window to be cleaned.

The internal components of the sample holder are shown in cross section in fig. 5-4(a). The laser beam path is shown in blue. At the right end of the beam path is the laser, and at the left end is the right face of the propellant sample. A quartz glass window is placed in the middle of the beam path; it protects the laser from the combustion gases and seals the pressurized volume. A second passage joins the beam path passage at a right angle (into the page); this connects to the plenum. The propellant sample is contained in a quartz glass sample tube. The right end of the sample tube is inserted a few millimeters into the beam path passage, and the left end is held in place by a toggle clamp. O-ring face seals are used at both ends of the sample tube and on the door.

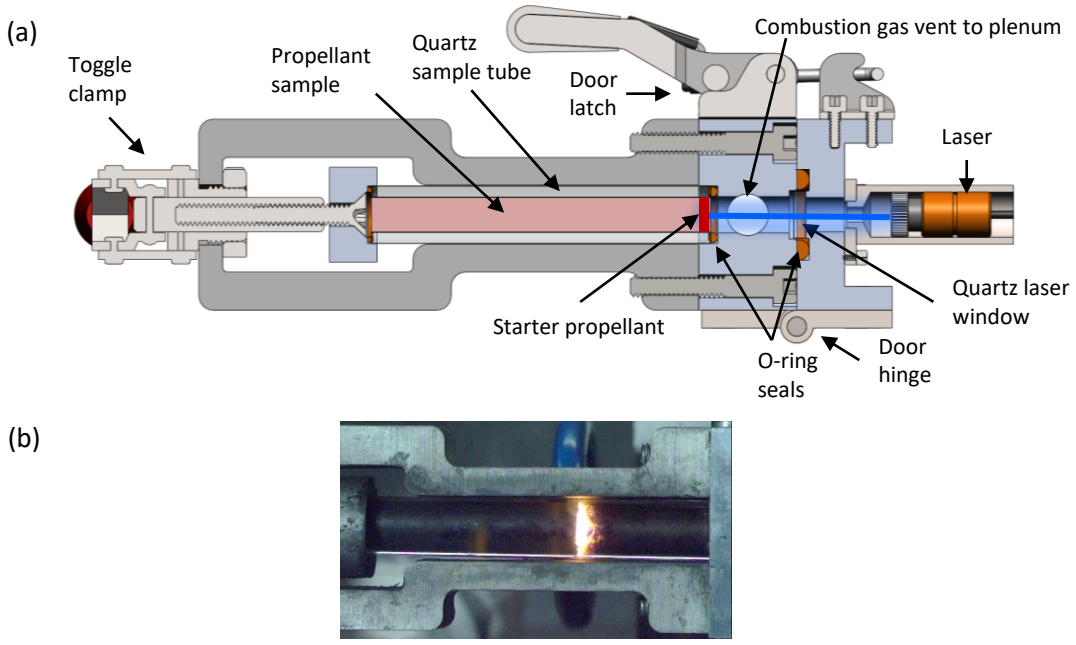

Figure 5-4: (a) the strand burner's sample holder (shown in cross section) connects a sample tube to the pressurized plenum and ignites the propellant sample with a laser. (b) A propellant sample burning in the sample holder.

5.3.1.2 Strand burner measurement procedure

A small piece (0.1 g) of fast-burning starter propellant[6] is placed in the right end of the sample tube. The starter propellant is ignited by the laser beam. It quickly burns up and ignites the 'main' propellant sample. Then, the flame front progresses along the sample from right to left. An example image of the flame front is shown in fig. 5-4(b).

The burn rate of each strand was measured by video. Figure 5-5 shows a sequence of video frames of a burning propellant sample. The first frame shows a blue/purple glow from the laser light igniting the starter propellant. The subsequent frames show the flame front progressing along the strand. The burn length of the samples is 82.2 mm (90.5 mm quartz tube length, minus room for the starter propellant). The time to burn the propellant sample was determined via a frame-by-frame review of the video (the video was recorded at 250 frames per second). The sample of propellant

[6]Cesaroni Technologies 'Classic' propellant.

shown in fig. 5-5 burned in 57.80 s, so the measured burn rate was $1.42\,\mathrm{mm\,s^{-1}}$.

For each propellant formulation, several (4 to 10) strands were burned at different pressures, and their burn rates recorded. Then, the burn rate parameters a and n were fit to these (pressure, burn rate) points using a non-linear least squares algorithm[7].

[7]The `lmfit` python package was used to perform the fits.

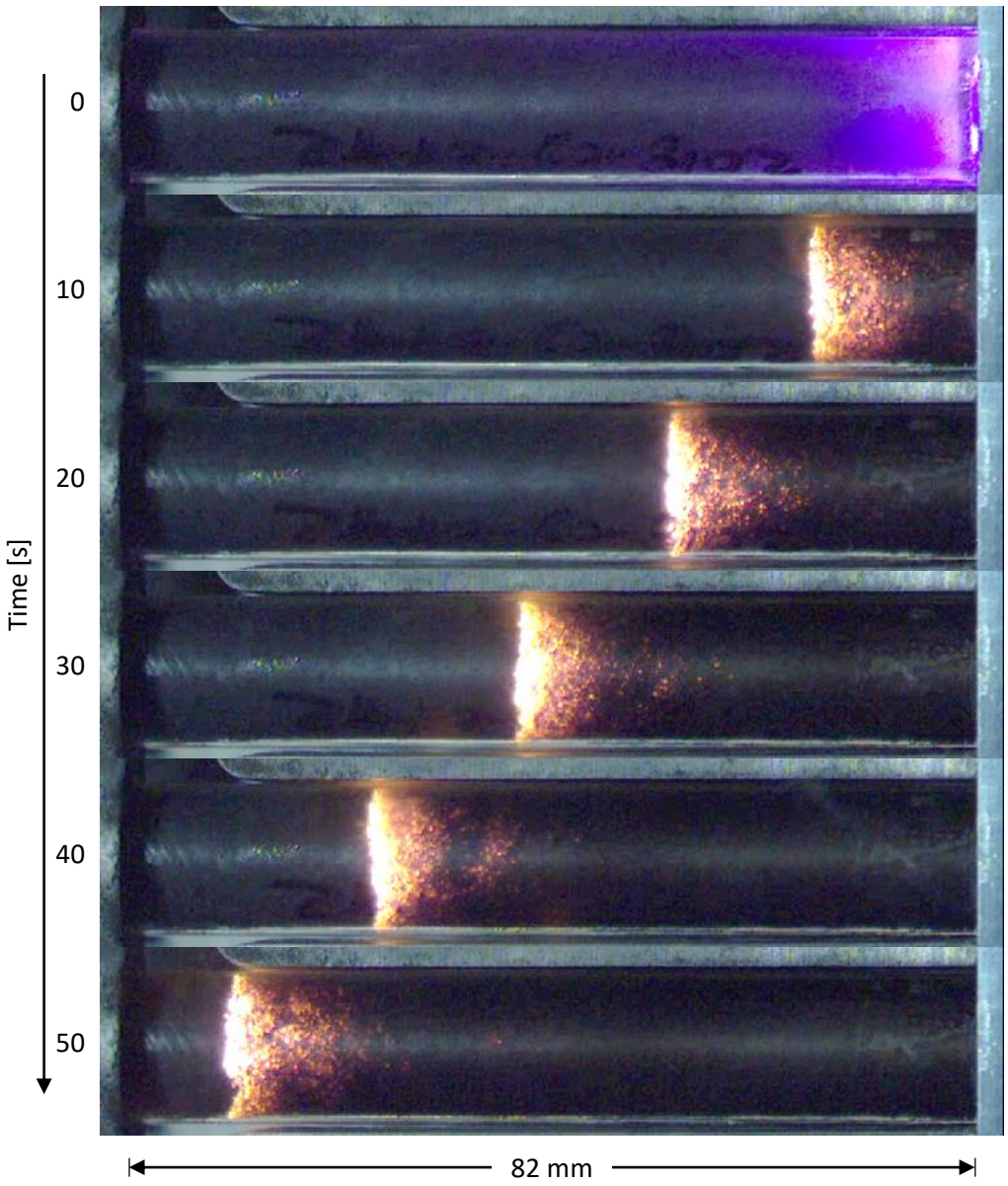

Figure 5-5: Video frames from burning a strand of 13% oxamide propellant at a pressure of 0.52 MPa. The propellant burn rate was measured to be 1.42 mm s^{-1}.

5.3.2 Soot measurement methods

This section describes measurements of the amount of soot in the combustion products.

The amount of soot is important because it influences the transfer of heat from the combustion gas to the ablative liner of the motor case (heat transfer to the ablative liner is described further in section 8.3.1). This heat transfer is undesirable, because it cools the combustion gas (reducing c^*) and causes the ablative liner to ablate more quickly. The heat transfer to the liner is mostly due to radiation from soot particles in the combustion gas. If there is more soot, the gas will be more emissive and the heat flux to the liner will be higher.

Estimating the amount of soot in the combustion gas is necessary to model the radiative heat transfer from the combustion gas to the liner. It is difficult to accurately simulate the amount of soot in the combustion products, so the amount of soot needed to be characterized experimentally.

To quantify the amount of soot produced by propellant combustion, samples of propellant were burned in a glass container, and the soot left in the container was collected and weighted.

The propellant samples were approximately 5 g in mass and cuboid-shaped. The 5% oxamide propellant was used.

The container was a Pyrex glass dish covered with a fiberglass cloth lid. The container was made from glass to avoid reactions with hydrochloric acid in the combustion gas [8]. A 19 mm hole was cut into the fiberglass lid to admit the tip of a propane blowtorch which was used to ignite the propellant.

After all components were weighted, the propellant was placed in the dish and the fiberglass lid was secured over the dish with stainless steel wire. The torch was then placed into the hole in the lid. The torch was mounted on a stand with a remote

[8] Before conducting this experiment, we attempted to measure the soot which had accumulated in the Strand Burner's plenum. However, the soot in the Strand Burner was mixed with a large amount of white-ish material. The Strand Burner plenum is made from aluminum alloy. The white-ish material is probably Al_2O_3 and $AlCl_3$, products of aluminum corrosion by hydrochloric acid.

trigger. Figure 5-6 shows the complete setup just before burning.

The torch was fired (by remote control) for about 1 s to ignite the propellant. The propellant then burned for about 15 s at ambient pressure (about 100 kPa). Some amount of soot escaped through and around the torch, so the collected soot mass is slightly less than the true amount of soot produced.

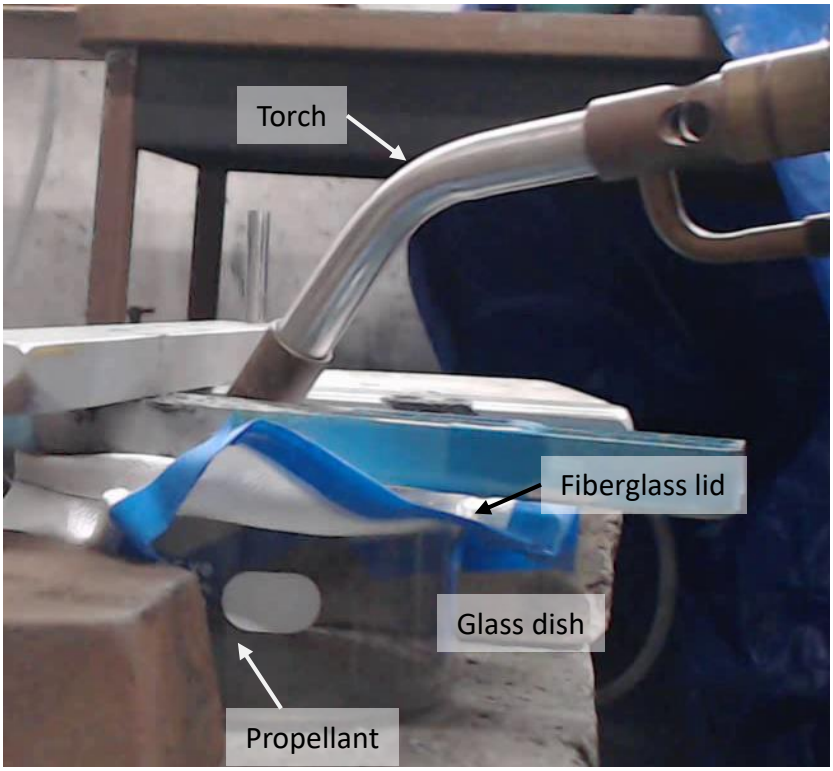

Figure 5-6: The soot collection setup before burning.

After the dish cooled, the soot from the inside of the lid and dish was carefully brushed into a weighing tray and weighted. Figure 5-7 shows the soot collected in one trial, side-by-side with a propellant sample. The soot is black in color an appears to be made of carbon (as expected).

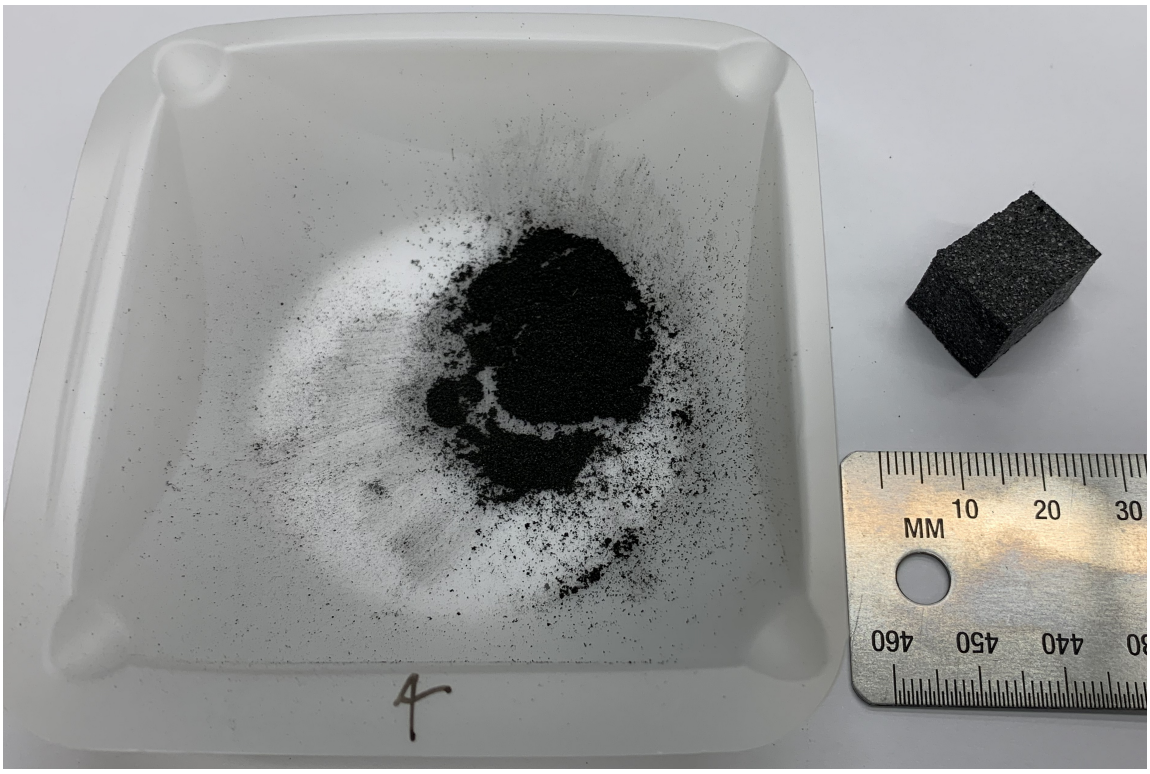

Figure 5-7: A propellant sample (right) and the soot collected from burning a similar propellant sample (left).

5.4 Results: burn rate

5.4.1 Strand burner burn rate measurements

The burn rate vs. pressure measurements from the strand burner are presented in fig. 5-8. Each propellant formulation is shown in a different color. For AP particle size, the 0%, 10% and 13% oxamide propellants used the '400/200 micron blend'. The 5% and 20% oxamide propellants used the '400 micron blend' and thus had a larger average AP particle size.

Each point is the burn rate and pressure for a particular strand burner sample. The horizontal error bars show how much the strand burner pressure varied during the burn [9].

[9]The pressure control system has some dead-band, so the pressure in the strand burner varies slightly while a sample burns.

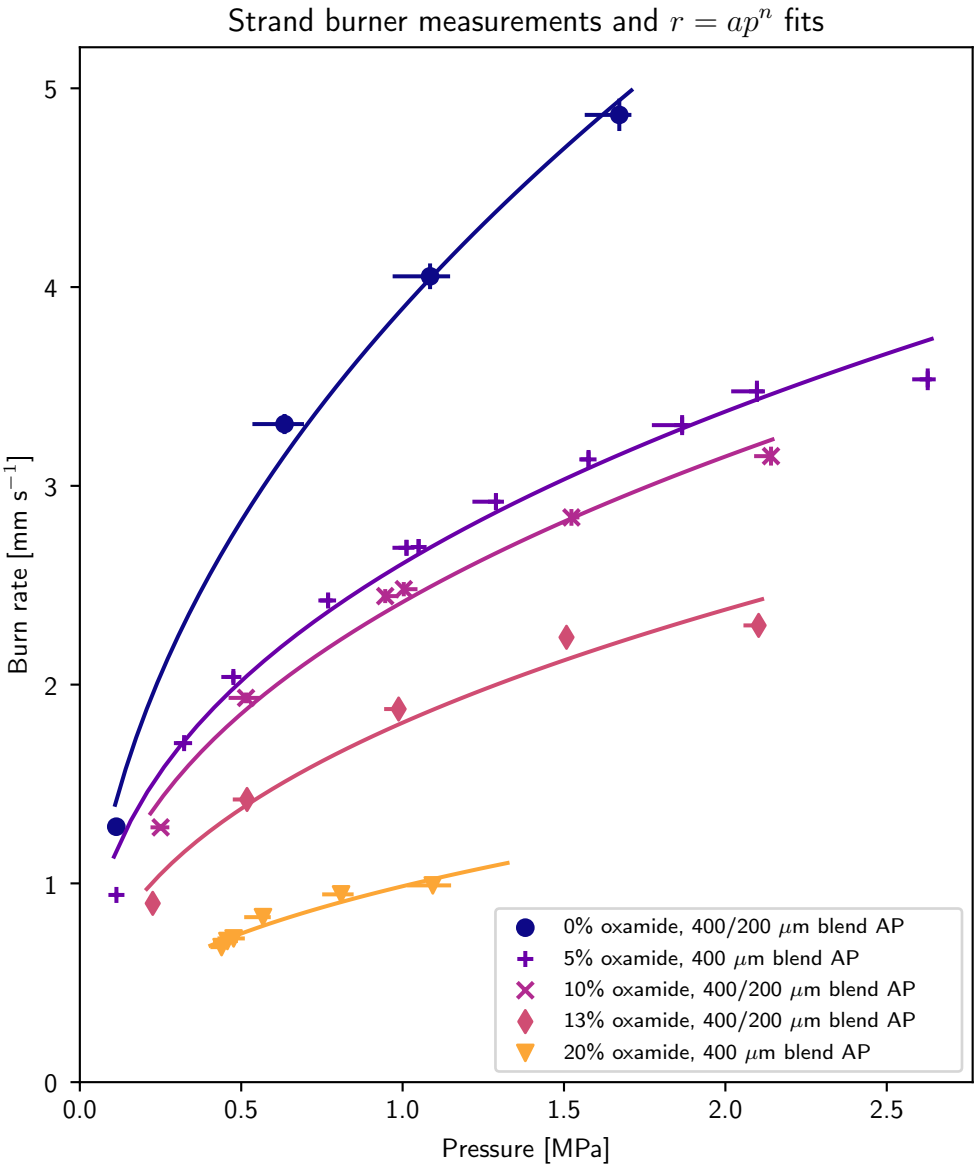

Figure 5-8: Strand burner experiments measured the burn rate of each propellant at several pressures. A Vieille model ($r = ap^n$) was fit to the measurements from each propellant. The horizontal error bars show the minimum and maximum pressure during the experiment. The vertical error bars show uncertainty in the strand length and burn time (in some cases they are smaller than the markers).

The standard burn rate fitting method is Vieille's formula, $r = ap^n$, with a and n as free parameters. A separate $r = ap^n$ fit was performed for each propellant (curves in fig. 5-8). Within each propellant, the burn rate is higher at higher pressures. Between propellants, propellants with more oxamide burn more slowly at a given pressure.

The a, n values from each propellant are plotted in fig. 5-9. The fit values of a and n are shown as colored points, and the 95% confidence intervals from the Vieille fit are shown with error bars. As expected, the burn rate coefficient a is lower for propellants with more oxamide.

A model of $a(w_{om})$ was fit to these points. This model was introduced in section 4.2.4; its functional form is:

$$a = a_0 \frac{1 - w_{om}}{1 + \lambda w_{om}} \tag{5.1}$$

Two different fits were made for the two different AP particle sizes: '400/200 micron blend' and '400 micron blend'. The fits were allowed to have different a_0 values, but constrained to have the same λ value. A nonlinear least squares method[10] was used to solve the fits. In the top subplot of fig. 5-9, the $a(w_{om})$ model for the '400/200 micron blend' AP is shown as a solid curve, and the model for the '400 micron blend' AP is shown as a dashed curve. Each point is connected to its model by a gray line. The burn rate coefficient is lower for the propellants with '400 micron blend' AP because larger AP particles reduce the burn rate (recall section 4.2.1).

The burn rate exponent n is shown in the bottom plot of fig. 5-9. n does not show significant variations with oxamide content. For all propellants, the error bars on n overlap with the mean value of $n = 0.402$. Thus, the models used later in this work assume that n does not vary with oxamide content.

[10]Implemented in the python package `lmfit` [57].

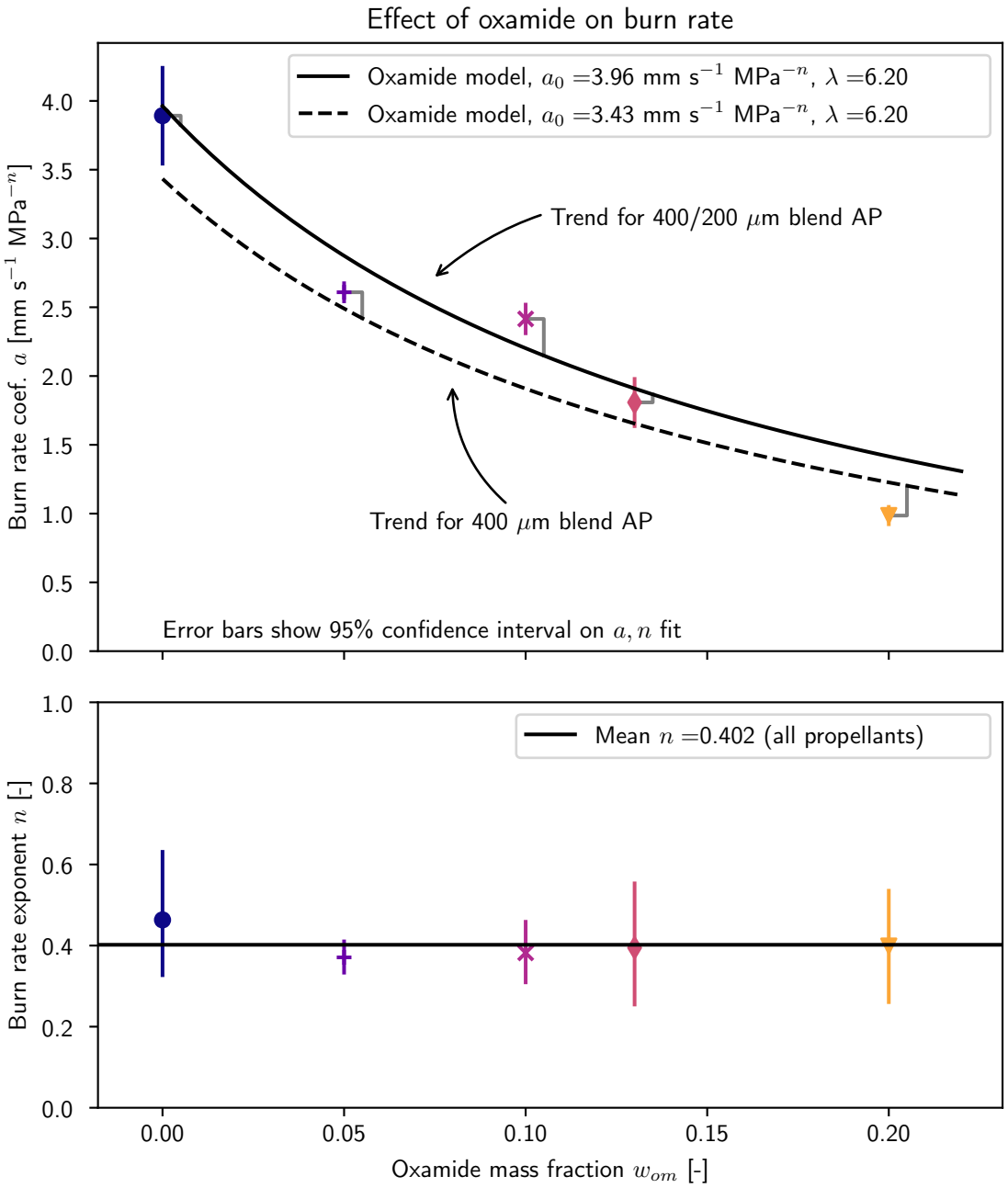

Figure 5-9: The burn rate coefficient a decreases with oxamide content, whereas the exponent n is roughly constant. Each point on these plots represents a fit from fig. 5-8.

5.4.2 Comparison to other studies of the effect of oxamide on burn rate

The effect of oxamide on burn rate measured in this work agrees with measurements from other studies. A comparison is shown in fig. 5-10. Data from this work are shown in black; other studies in gray. To compare burn rate data from different studies, which used different baseline propellants, the burn rate data are shown in terms of the burn rate multiplier ϕ_{om}. ϕ_{om} is the ratio of the propellant burn rate with oxamide to the burn rate of that study's baseline, no-oxamide propellant (at the same pressure).

The other studies had different propellant formulations and test pressures than this work. In all these propellants, oxamide was *substituted* for AP. This is different from this work, which 'diluted' all the ingredients, and kept the ratio of AP to binder constant when oxamide was added (see section 5.1). Also, some of the other propellants contained metal fuel, whereas the propellants in this work did not. Some of the other burn rate experiments were conducted at higher pressures, whereas relatively low pressures were used in this work (0.1–2.5 MPa). The other studies are described further in section 4.2.3.

Despite the various propellant formulations and test pressures, all the ϕ_{om} data cluster around the oxamide model presented in this work. All of the burn rate exponent data clusters around $n = 0.4$.

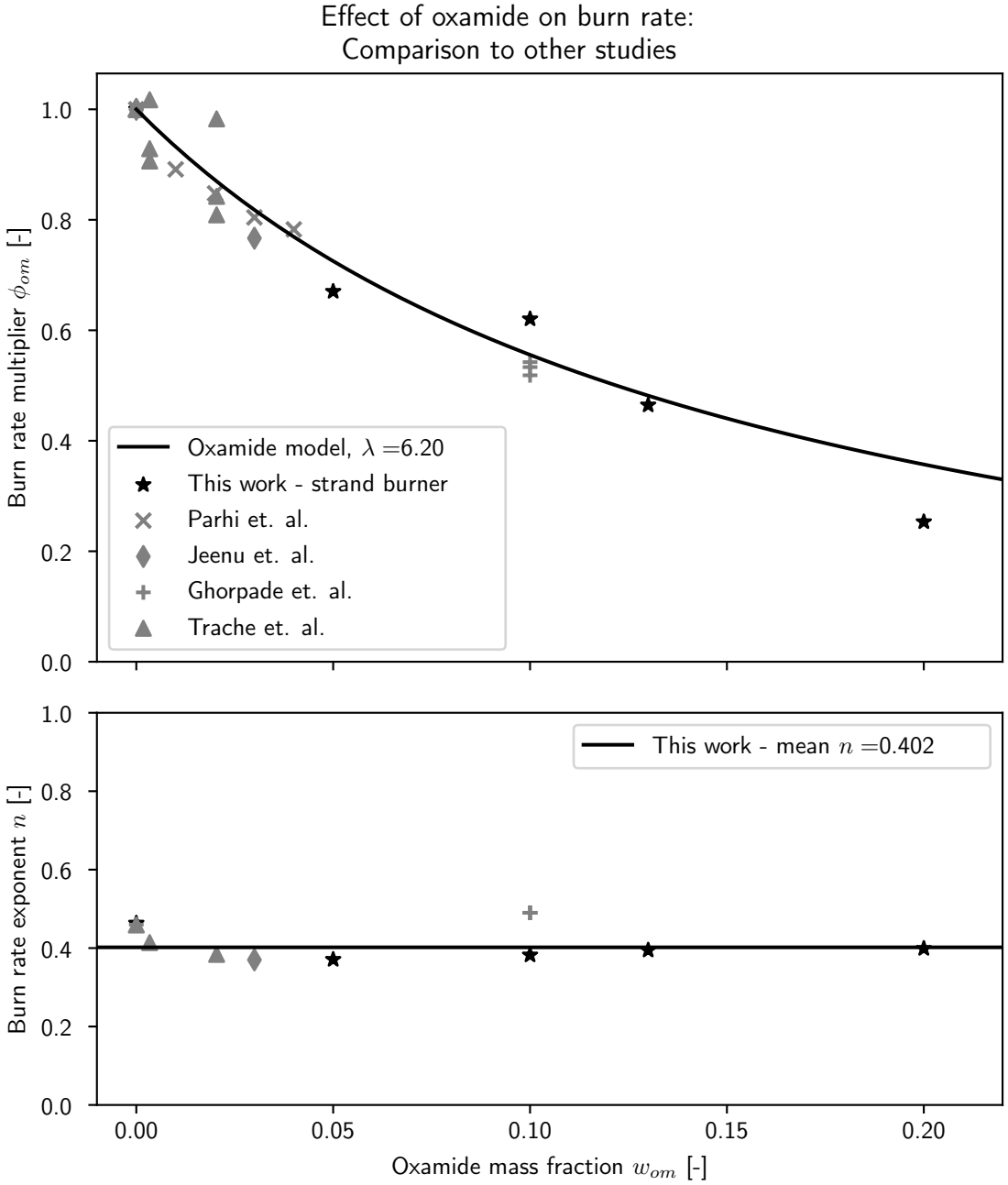

Figure 5-10: Various assessments of the effect of oxamide on propellant burn rate. The oxamide model (black curve) and strand burner data (black stars) from this work agree with measurements from other studies (gray marks).

5.5 Results: minimum burn pressure

For each propellant, there is a minimum pressure below which it will not burn. As discussed in chapter 3, the minimum burn pressure sets a lower limit on the thrust at which a motor can operate. It is not possible to predict the minimum burn pressure from first principles, so experimental characterization is necessary.

The minimum burn pressure was investigated with the strand burner (fig. 5-11). For each propellant formulation, we do not know the minimum burn pressure exactly, but do have lower and upper limits from the strand burner. The lower limit is the highest pressure at which a strand burner sample would not burn. The upper limit is the lowest pressure at which a strand burner sample ignited and burned. In these strand burner experiments, we first attempted to ignite each formulation at atmospheric pressure (0.1 MPa). If the sample did not ignite, we then attempted to ignite it incrementally higher pressures until it did ignite. The 0 and 5% oxamide propellants burned at atmospheric pressure. The 10% and 13% oxamide propellants did not burn at atmospheric pressure but did burn at 0.2 MPa. The 20% oxamide propellants did not burn until the pressure was raised to 0.4 MPa.

A simple quadratic fit (black line) is shown with the data. This fit should be regarded with some skepticism as there is no theoretical basis for the relationship to be quadratic.

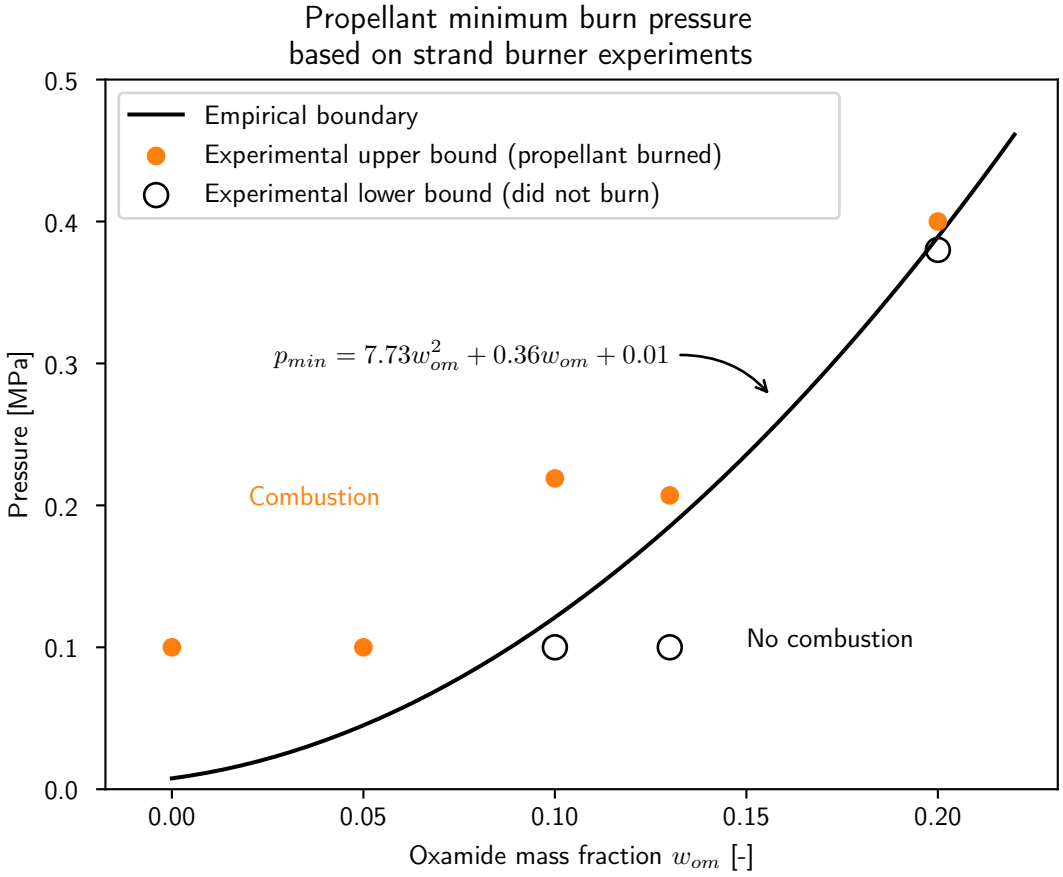

Figure 5-11: The minimum burn pressure is the minimum pressure at which the propellant will sustain combustion; it increases with oxamide content.

5.6 Results: soot in combustion products

Soot measurements were performed on three samples of the 5% oxamide propellant. The masses of the propellant samples and collected soot are listed in table 5.4. The soot mass was $1.35\% \pm 0.24\%$ of the propellant mass.

These numbers are a lower bound on the soot produced in the experiment, as not all of the soot could be collected. Some of the soot escaped around the torch tip or through the torch itself.

There was some unaccounted-for deposition of mass on the fiberglass lids. The fiberglass lids were found to be 0.1–0.2 g heavier after burning the propellant, brushing off the soot, and drying under vacuum for 30 minutes. Vacuum drying rules out

Trial	Propellant mass [gram]	Soot mass collected [gram]	Soot mass fraction [%]
2	5.79	0.0883	1.53
3	5.41	0.0806	1.49
4	5.03	0.0527	1.05

Table 5.4: The average soot mass collected in these experiments was $1.35\% \pm 0.24\%$ of the propellant mass. Trial 1 is not included because a rip in the fiberglass cover allowed a large amount of soot to escape in this trial.

water from the combustion gas as the source of the extra mass. The source of the extra mass is not known.

The soot mass fraction may depend on combustion pressure and oxamide mass fraction. These tests were at ambient pressure and used 5% oxamide propellant. It is not known if more or less soot would be produced at higher pressures or with more oxamide.

The propellant contained about 2% carbon powder by mass as an opacifier. Thus, it is likely that the soot in the combustion products is mostly the remaining, unreacted opacifier powder.

It may be possible to reduce the soot concentration in the combustion products by using less opacifier. This would reduce the radiative heat transfer from the combustion gas to the ablative liner, which is desirable. A propellant (the 20% oxamide propellant) was made with 0.2% carbon powder. However, the soot production of this propellant could not be measured. The propellant would not burn at atmospheric pressure, due to its high oxamide content. The soot testing rig could only measure the soot production of propellants which burn at atmospheric pressure. A soot mass fraction of 2% is assumed in the heat transfer analysis in this thesis (chapter 8). This is higher than the average soot collected in these experiments (1.35%), as some soot escaped and was not collected. The 2% value is chosen to match the amount of carbon powder opacifier used in most of the propellant batches. In some of the heat transfer analysis, results are also presented for a lower soot content, which may be representative of the propellant with reduced carbon powder.

5.7 Conclusions regarding propellant development

A family of slow-burn propellants, which are suitable for use in low-thrust rocket motors, have been developed and characterized. The completed work demonstrates a sufficient solution to the propellant needs of this project. The author believes that the range of oxamide contents tested in this work, 0-20%, brackets the range of oxamide contents which would be useful in low thrust motors.

Further, the above results inform the following recommendations for future slow-burn propellants:

- *Less soot* – most propellants in this work contained 2% carbon powder (by mass) as an opacifier, and its combustion products also contain about 2% carbon soot. Reducing the amount of soot in the combustion gas will decrease heat transfer to the motor case, which is beneficial. In one batch of propellant, the opacifier content was reduced to 0.2% without adversely affecting the combustion behavior. Future propellants should use a carbon powder content of 0.2% to give less soot.

- *Larger AP particles* – most propellants in this work used the '400/200 micron blend' AP. Instead, using a '400 micron blend' AP gives a slower burning propellant. Two propellants in this work did use the larger AP blend, and did burn more slowly. Future propellants should also use the '400 micron blend' AP.

Chapter 6

Motor case design and materials considerations

A good motor case and fuselage design has low drag, low mass, and a large propellant volume. This increases the range of the aircraft. To have large propellant volume and low drag, the motor case should be long and slender. To have large propellant volume and low mass, the motor case should be made from high specific strength materials and have an efficient structure. Further, the motor case must withstand internal pressure loads, and be manufactured at an acceptable cost.

The motor case design is described in section 6.1. Its shape is a circular cylinder. The motor case is fairly typical and mostly follows standard design practices (e.g. NASA SP-8025 [74]).

Section 6.2 discusses material options for the motor case. Titanium alloy Ti-6Al-4V is a good choice; its high specific strength results in a lightweight structure. This alloy can be produced via additive manufacturing to enable complex case designs. For simpler case designs, other manufacturing options (e.g. drawn tube) are available and may be less expensive.

6.1 Motor case design considerations

Once the propellant ignites, the motor case is filled with hot, pressurized gas. This drives the major design considerations for the motor case: pressure loads and case temperature (fig. 6-1).

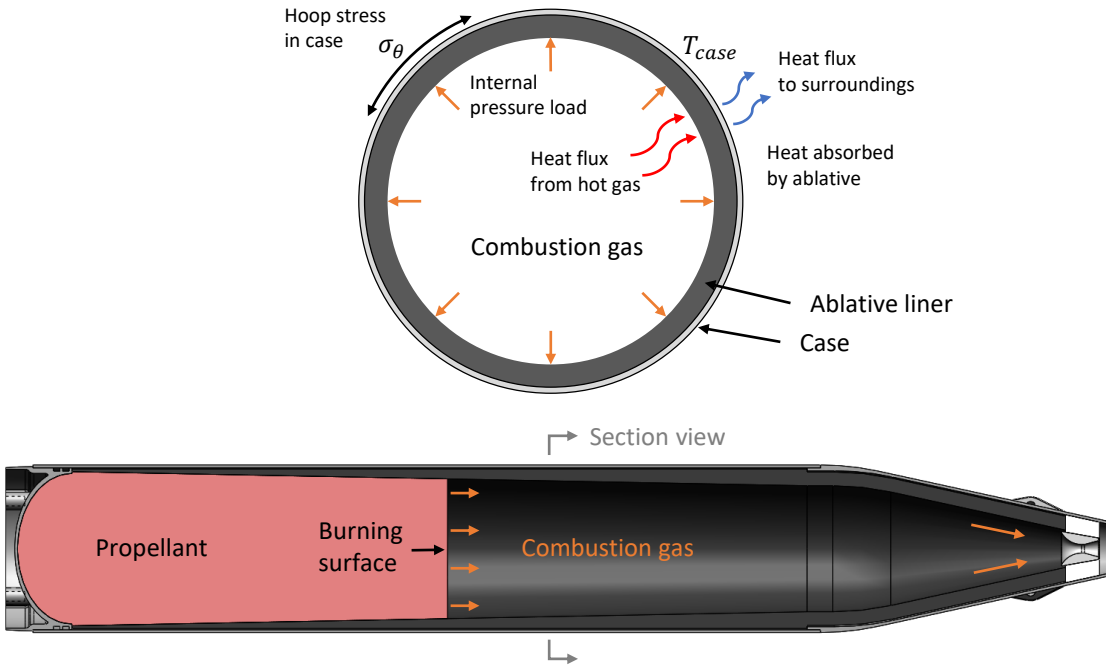

Figure 6-1: Internal pressure loads produce a hoop stress in the case which must not exceed the case's yield strength. The combustion gas transfers heat into the case. The case is protected from this heat by an ablative liner, but it will still become hot ($T_{case} \approx 500$–$700\,\mathrm{K}$).

The internal pressure load creates stresses in the motor case; the case must survive these stresses without yielding. The most efficient shape for internal pressure loads is a revolved shape with circular cross section. With a circular section, the principal stress is a tensile hoop stress σ_θ. Almost all motor cases have revolved geometry [77]. If a non-circular shape were used, there would be bending loads in the case, resulting in higher stress.

The combustion gas also transfers heat to the motor case. This is a particularly severe concern with an end-burn propellant grain, as a large area inside the case becomes exposed to combustion gases. The inside of the motor case is protected

by an ablative liner, which absorbs most of this heat; however some heat is still conducted through the liner into the case. The ablative liner is discussed further in chapter 8. The relevant factor here is that the motor case will operate at high temperatures. The hottest case temperatures, perhaps 500–700 K, occur at the aft end, which is exposed for the longest time. The motor case material must have sufficient tensile strength at the maximum case temperature.

The motor case also serves as the primary structure of the vehicle, and must provide mounting points for the wing, tails, and payload/control module. The baseline vehicle design is shown (again) in fig. 6-2 to illustrate how these components might mount onto the motor case.

The motor case design must be manufacturable at reasonable cost. It also must have a joint so that the propellant and liner can be loaded into the motor.

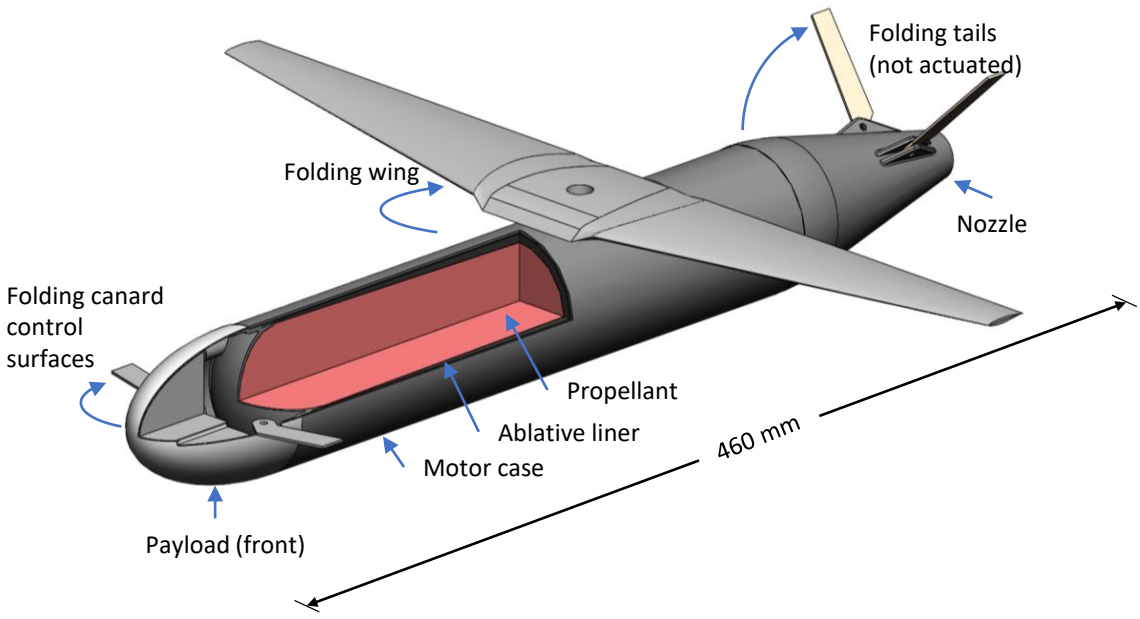

Figure 6-2: The motor case is the main structure of the fuselage. The wing, tails, and payload all mount to the motor case.

6.1.1 Baseline motor case design

The motor case shape is a compromise between propellant volume, drag, and manufacturing simplicity. The baseline motor case has a circular cross section. This is the lightest shape for a pressure vessel, and gives simpler manufacturing options. The motor case is mostly straight, with a conical 'boat-tail' at the aft end. The straight shape allows a large portion of the case to be made from off-the-shelf tube. Whether the motor case should have axial taper is an interesting design choice; this is discussed further in section 6.1.2.

The motor case has three major components: the forward closure, tube and aft section (fig. 6-3). A wing 'saddle' (which the wing and wing pivot mechanism mount to) is attached to the top of the motor case. The forward closure, tube and aft section are made from titanium alloy Ti-6Al-4V (material selection is discussed in section 6.2). The aft section and forward closure could be made by additive manufacturing; the tube would be made by standard tube production techniques (manufacturing is discussed further in section 6.1.3).

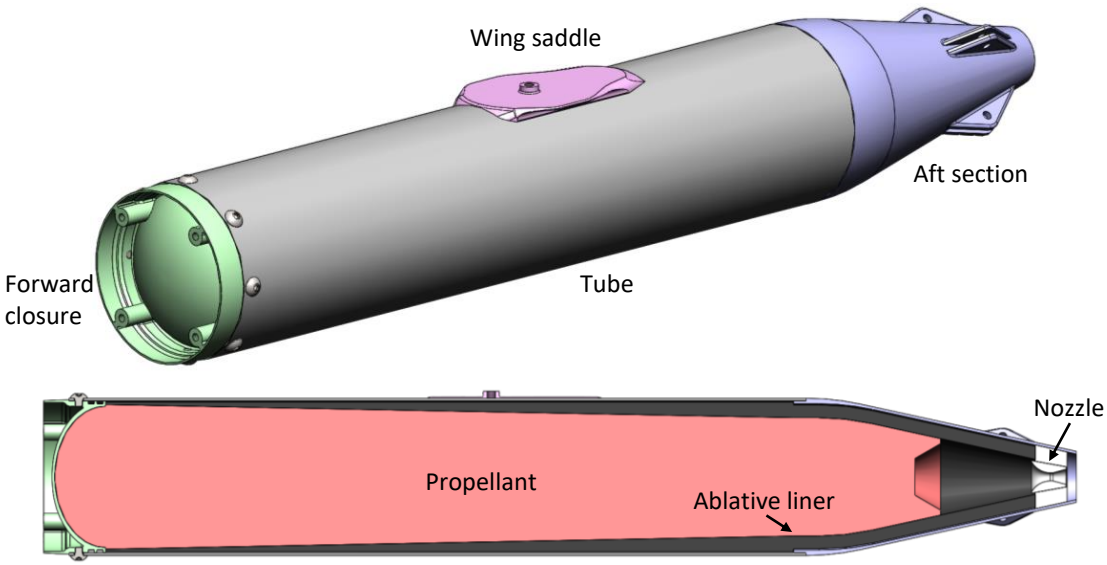

Figure 6-3: The motor case has three major components: the forward closure, tube and aft section. All are made from titanium alloy Ti-6Al-4V.

The aft section is welded to the tube, whereas the forward closure is removable.

A removable joint is necessary to load the motor (welding a joint with the motor loaded would be dangerous). The forward closure connects to the tube with radial bolts and seals with two redundant o-rings. This arrangement places the o-ring seal at the front of motor, where it is only exposed to hot gases for a short time.

The nozzle is bonded into the aft section of the motor case. The nozzle consists of a boron nitride nozzle insert surrounded by fused silica insulation. The insulation supports the insert and reduces heat transfer from the hot insert to the case aft section. The nozzle throat diameter is only 3–5 mm. The nozzle is described further in chapters 9 and 10.

A notional motor assembly sequence is shown in fig. 6-4. First, the nozzle assembly is bonded into the aft section with a flexible silicone adhesive. Then, the wing saddle and aft section are welded onto the tube. Finally, the propellant is loaded into the motor and the forward closure is installed. The wings tails, and payload can be mounted either before or after the motor is loaded.

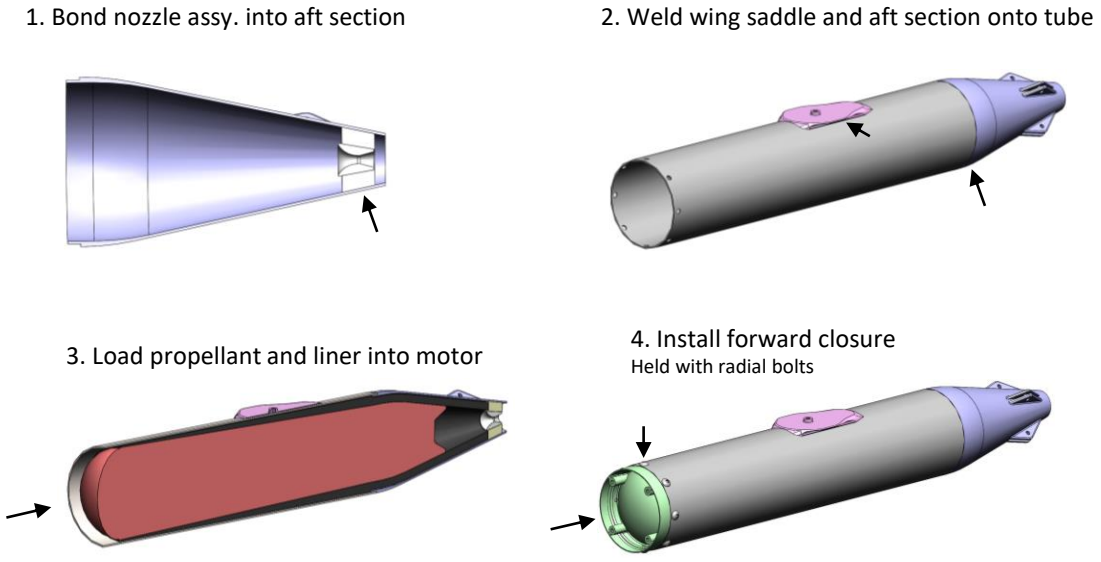

Figure 6-4: Notional motor assembly sequence.

The motor case wall thickness is set by minimum gauge constraints, thus the case walls are not highly stressed. The minimum feasible wall thickness is about 0.5 mm,

both for additive manufacturing[1] [67, 41] and for tube production [73, 72, 83]. At this thickness, the yield pressure of the case is over 8 MPa (assuming annealed Ti-6Al-4V at 600 K, with a yield tensile strength of 537 MPa [23]). This is many times the expected chamber pressure, about 0.3–1 MPa.

6.1.2 Motor axial taper

The axial taper of the motor affects the propellant volume, burn area profile, and drag. It also determines what joints are needed to load propellant into the motor, and how complex the motor components are to manufacture.

A straight case is the simplest geometry. It has the potential for low manufacturing costs, as a large section of the case can be made from off-the-shelf tube. A straight case gives the greatest propellant volume within a given bounding box. This is the most common design in small solid rocket motors.

Tapered cases can give lower drag. For transonic aircraft, the distribution of forward-facing cross-sectional area versus longitudinal distance is important. The transonic drag rise is smaller and begins at a higher Mach number for aircraft with a better (i.e. smooth) area distribution. This is known as the (Whitcomb) area rule [40]. A tapered case results in a lower-drag area distribution (fig. 6-5) [2].

If the case has a double taper (i.e. tapering forward and backward of a widest station), there must be a mid-case joint at the widest point in order to load the propellant and liner into the motor [3].

The tapered case has a more complex geometry that requires more expensive manufacturing techniques.

In a motor case with strong taper, the propellant burn area will vary significantly during the burn. This requires a multi-segment propellant grain to keep chamber

[1] specifically, powder bed fusion

[2] Due to area rule considerations, some transonic aircraft are 'wasp-waisted' – the fuselage becomes narrower near the wings. A wasp-waisted motor case is impractical, as the negative draft would prevent loading the propellant and liner into the motor.

[3] Alternatively, the propellant and liner could be cast directly into the case. However, this may make production and inspection more difficult.

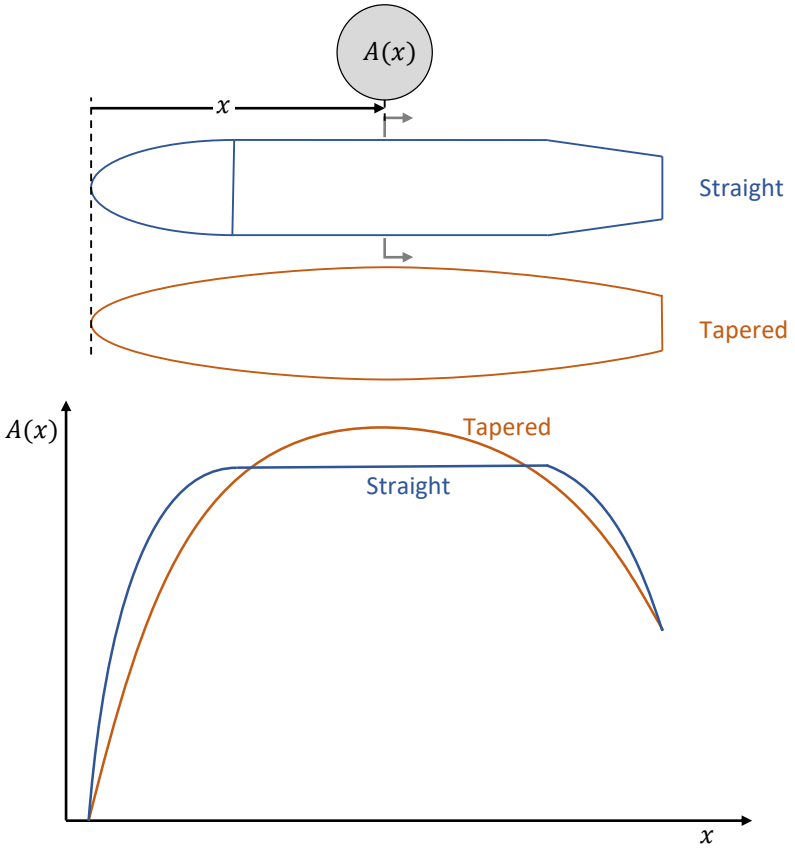

Figure 6-5: A tapered motor case has lower drag due to a better 'area rule' profile.

pressure and thrust within limits as A_b varies. A multi-segment propellant grain is more expensive to produce than a single-segment grain.

6.1.3 Manufacturing

The manufacturing options depend on the geometric complexity of the case. The baseline case design was kept simple, for easy manufacturing. For a non-tapered case, many off-the shelf tube options are available. Wing mounting hardware could be joined to the tube by welding, brazing, adhesive or fasteners. The forward and aft closures would be additively manufactured to near-net-shape, and then machined in certain areas. Or, the entire case could be additively manufactured with integral mounting features. The best option will depend on production volume and cost considerations, which are beyond the scope of this thesis.

For a tapered case, the complex geometry limits the manufacturing options. For prototyping, AM is certainly the best choice, and has been used on this project's motor case prototypes to date. For larger production volumes casting may be cheaper, but the geometry of the case (long, thin walls) would be quite difficult, perhaps impossible, to cast. Hydroforming is another method to consider for large-volume production of tapered cases.

With either choice, precision areas (e.g. mounting features) will need secondary machining after the near net shape has been produced.

6.2 Material selection

The material selection objective for the motor case is to give the lightest structure which can survive the temperatures and internal pressure loads. The material properties which minimize mass differ if the structure is loaded in bending or tension, and if the structure is strength-limited or stiffness-limited (see Ashby [4]). In each scenario, a different material property index ($S_{ty}/\rho, E/\rho, S_{ty}^{1/2}/\rho$ or $E^{1/3}/\rho$) is to be maximized. Ashby introduced a type of material selection chart, the Ashby Diagram, from which these indexes can be read [4].

Typical Ashby diagrams only show properties at room temperature. However, the maximum operating temperature of the case is expected to be 500–700 K, so material properties at elevated temperatures are important. As temperature increases, the material property indexes change, and the ranking of materials by index changes. Thus, special plots have been prepared for this section, which show the material property indexes as a function of temperature.

Only metals are considered here. Plastic-matrix composites are used for rocket motor cases, but were not considered here because of the high temperatures. Ceramic- or metal-matrix composites could be used, but it would be more difficult to include mounting features (for the wings, case joint(s), sensors, etc.). They were not considered in this work, but their application to motor cases may be an interesting area

for future research.

This section compares six alloys which are commonly used in aerospace applications:

AlSi10Mg An aluminum alloy,

AISI 316L An austenitic stainless steel,

Ti-6Al-4V A titanium alloy, also known as grade 5,

In718 A nickel-based alloy,

D6AC A high-strength low-alloy steel,

AISI 4130 A lower-cost low-alloy steel,

All of these alloys are currently available for additive manufacturing [4], except the low-alloy steels (D6AC and AISI 4130). Each alloy is also available in cast or wrought forms [5].

Figure 6-6 shows the material properties as a function of temperature. The properties of the conventional (wrought) forms are shown as curves, and the properties of the additively manufactured forms are shown as 'x's. For most of the materials, property data at elevated temperatures were only available for the conventional forms. These data, along with the densities, was used to produce fig. 6-7 and fig. 6-8.

[4] specifically powder bed fusion

[5] Aluminum alloy 360 is used for casting and is almost equivalent to AlSi10Mg.

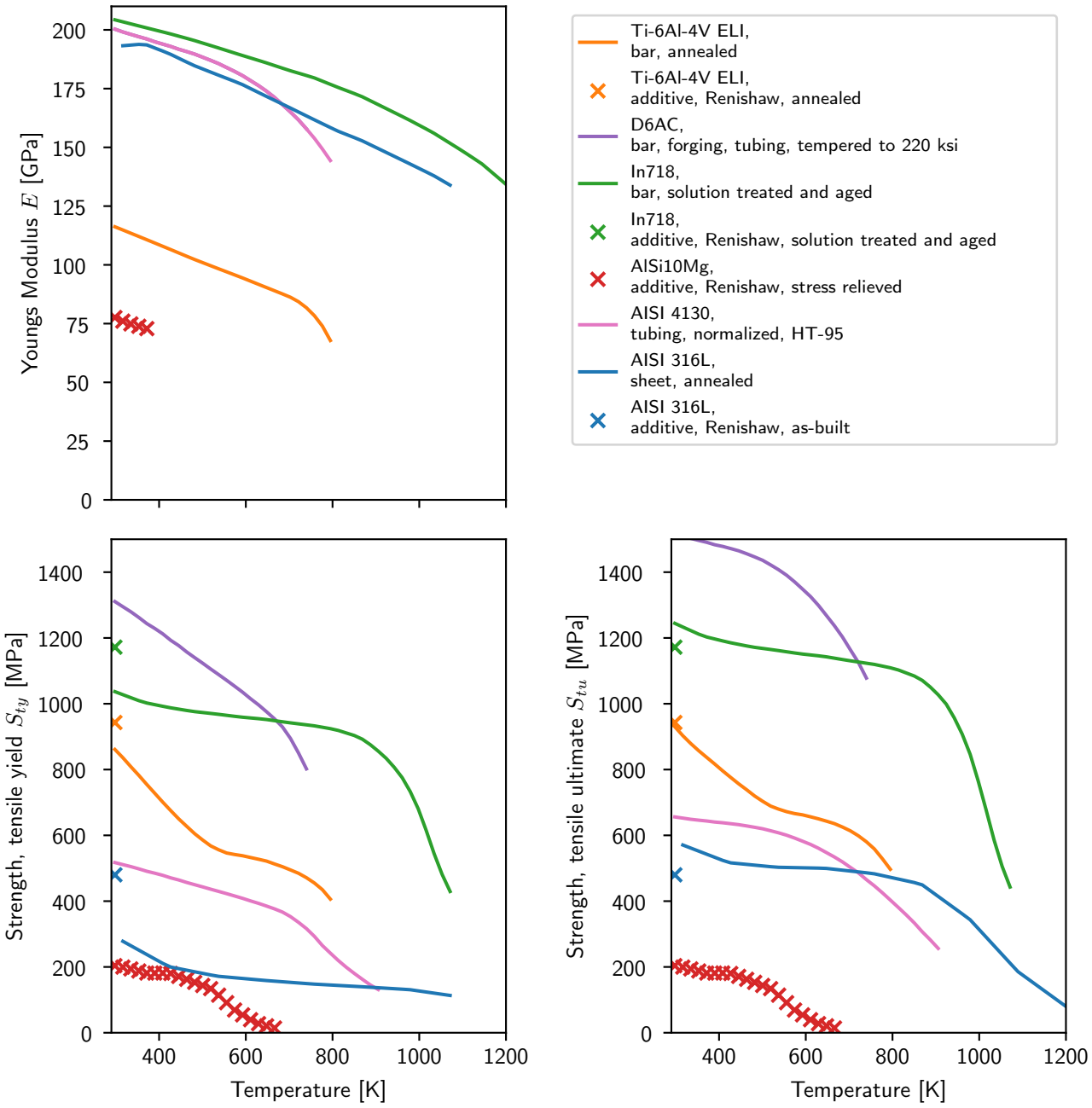

Figure 6-6: The strength and stiffness of metals are reduced at elevated temperature. Data for the wrought form of each alloy is shown as a smooth curve and is from MMPDS [23] or AISI [58]. Data for the additively manufactured form of each alloy are shown with 'x's and is from [69, 70, 68, 88].

6.2.1 Material selection for tension-loaded structures

This section discusses the mass-minimizing material choice for conventional, circular motor cases. These cases are loaded primarily in tension and are strength-limited, so S_y/ρ is the mass-minimizing material property index. S_y/ρ is plotted vs. temperature in fig. 6-7. The implications of S_y/ρ for each alloy's used in motor cases is discussed below.

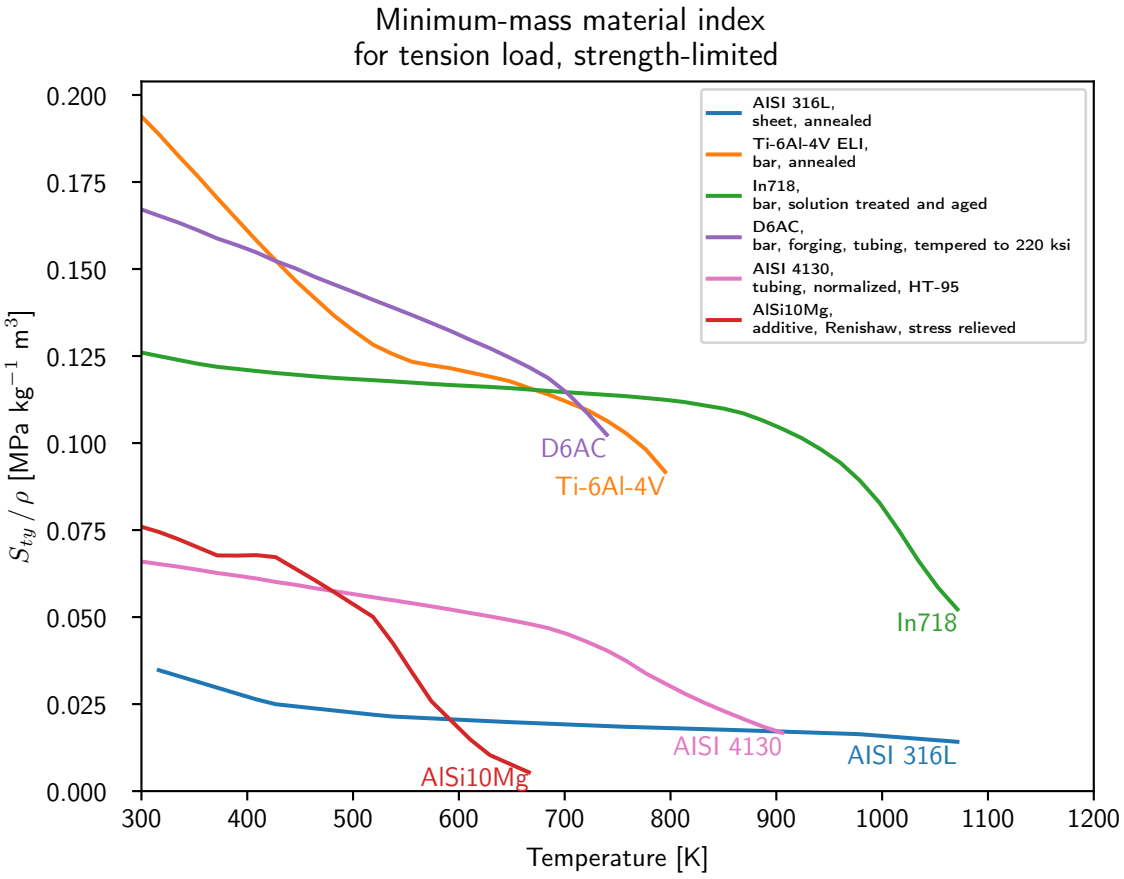

Figure 6-7: Materials with higher S_{ty}/ρ give lighter designs for tension-loaded, strength limited structures. Around the expected case temperature (500–700 K), Ti-6Al-4V, D6AC steel, or In718 are good choices.

AISI 4130 has a relatively low S_y/ρ; it is used in applications where low cost and ruggedness are more important than minimizing mass. For example, AISI 4130 is used in the motor cases of tactical missiles such as the Sidewinder [59]. Alu-

minum alloys (e.g. AlSi10Mg) also have low S_y/ρ but can be appealing for low cost applications. An aluminum alloy (6061-T6) is used in hobby rocket motor cases [13].

Ti-6Al-4V and D6AC steel have the highest S_y/ρ up to a temperature of about 700 K. They are used in space-launch and strategic missile applications where low inert mass is critical. For example, D6AC steel is used in the Shuttle SRBs [32] and Minuteman first stage [77], and Ti-6Al-4V in many of the STAR upper-stage motors [60].

At temperatures above 700 K, In718 has the highest S_y/ρ. However, it has not been widely used in solid rocket motor cases (to the author's knowledge). This is perhaps because existing motor cases seldom operate at such high temperatures.

AISI 316L has poor S_y/ρ and has not been widely used in solid rocket motor cases.

6.2.2 Material selection for bending-loaded structures

Figure 6-7 shows the material property indexes for a bending-loaded structure, with the strength-limited index in the top subplot and the stiffness-limited index in the bottom subplot. Bending loads are applicable to alternative motor case designs with non-circular cross sections. The bending load scenarios place a greater emphasis on low density. For the strength-limited bending scenario, Ti-6Al-4V is the mass-minimizing material up to the maximum temperature for which data are available, about 800 K. In718 is preferred above this temperature.

For the stiffness-limited scenario, AlSi10Mg is the the mass-minimizing material up to the maximum temperature for which data is available, about 400 K. Ti-6Al-4V is preferred up to 800 K; above that temperature In718 and AISI 316L are about equivalent.

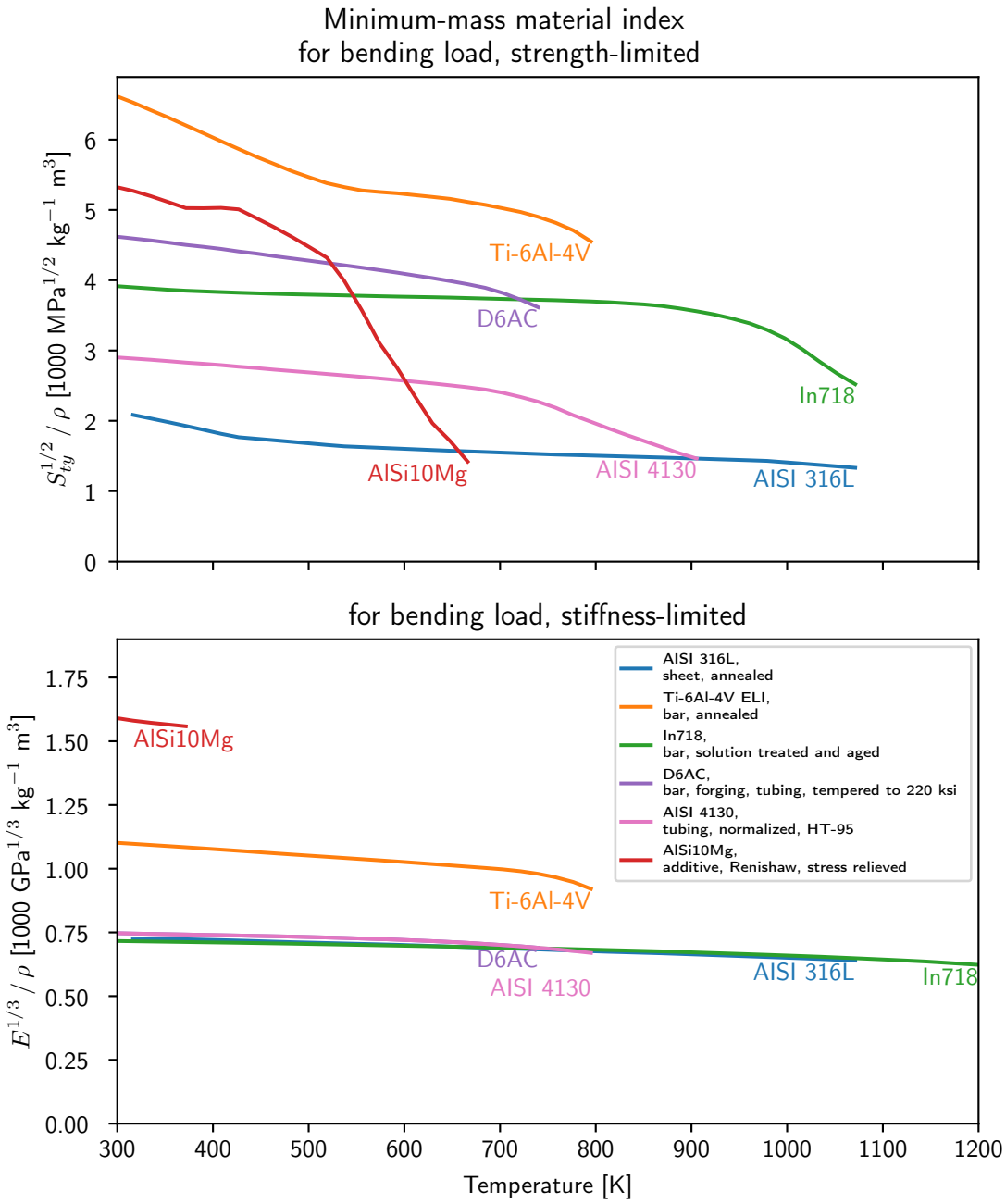

Figure 6-8: (top) Materials with higher $S_{ty}^{1/2}/\rho$ give lighter designs for bending-loaded, strength-limited structures. Around the expected case temperature (500–700 K), Ti-6Al-4V is the best material. (bottom) For stiffness-limited structures, Ti-6Al-4V is also preferred at these temperatures.

6.2.3 Other material selection considerations

Ductility is also a desirable property for a motor case material (to reduce shrapnel risk in the even of a failure). All the alloys considered have room temperature elongation at failure $\geq 5\%$.

Because the service life of the motor case is only a few minutes, creep and fatigue properties have not been considered.

Resistance to oxidation and corrosion may be important for storage. AISI 316, Ti-6Al-4V, In718 and AlSi10Mg and have good corrosion resistance at ambient conditions. The low-alloy steels (D6AC and AISI 4130) need to be protected, e.g. by paint.

6.2.4 Material recommendations

Based on these considerations, Ti-6Al-4V is the preferred motor case material for small, slow-burn rocket motors of either circular or non-circular section. This material has been used in this project's motor case development efforts to date.

If cost is a concern, low-alloy steels (e.g. D6AC or 4130) are a cheaper, but heavier, alternative. D6AC steel has roughly equivalent S_y/ρ to Ti-6Al-4V, and thus could be an alternative for circular cases. However, if the wall thickness is set by minimum-gauge constraints instead of strength (as is likely for a circular case), a D6AC steel case would be about twice as heavy as a Ti-6Al-4V case. AISI 4130 steel is less strong, but cheaper.

In718 is an interesting alternative for high-temperature circular section motors. Its higher temperature capability may allow for a reduction in the liner thickness within the motor [6]. This could allow for more propellant volume and increase the vehicle's range. This may be an interesting direction for future research.

[6] At high altitudes and temperatures, the case will be mostly cooled by radiation. As the radiated power scales with T^4, a slightly higher operating temperature could allow the case to tolerate a much higher internal heat flux.

Chapter 7

Research motor testing

Firings of a research motor were conducted to validate operation at low thrust, near the lower limit of the (thrust/burn area) ratio. The low thrust levels needed for the Firefly motor were successfully demonstrated. These tests also measured the nozzle and combustion efficiencies (ζ_{C_F} and ζ_{c^*}, see section 2.2.3). The research motor was also used to test the ablative liner (see chapter 8) and ceramic-insulated nozzle (chapter 9). A special thrust stand was built to accurately measure the low thrust levels in these firings.

7.1 Propellant mixing and casting

The propellant samples were mixed (under vacuum) and cast according to the procedures described in Mathesius [50]. The solids loading of the propellant affects how well it flows during mixing and casting; for these propellants it varies from 82.2% at 0% oxamide to 84.2% at 20% oxamide. All propellants flowed well enough to be mixed in a paddle mixer and poured into molds. The propellant was mixed in 500–1000 g batches and poured into a mold to cast a grain for the research motor (fig. 7-1, top). After the propellant was cast, the ablative liner was cast around it (fig. 7-1, bottom).

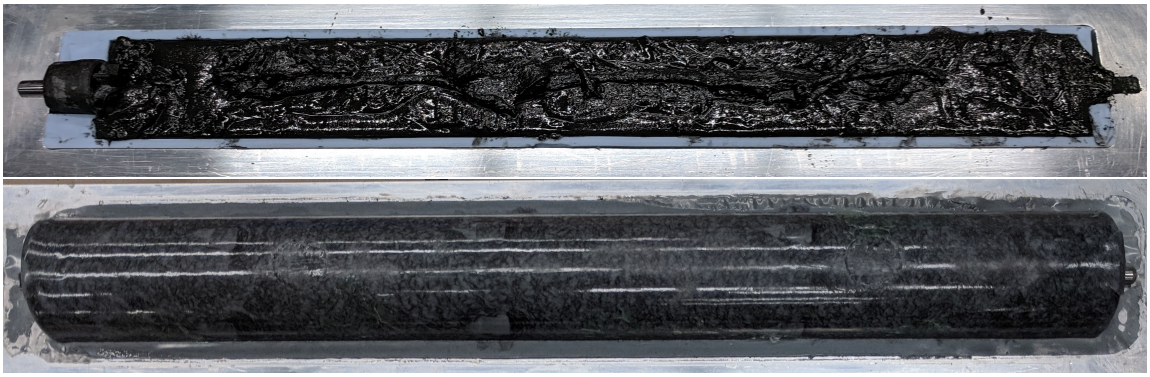

Figure 7-1: Top: Propellant slurry in half of the mold during the casting process. The pale blue mold insert occupies the space that will later be filled by ablative liner. Bottom: Ablative liner cast around a propellant grain.

7.2 Research motor

A research motor was designed and built to test the propellant, ablative liner, and nozzle. The research motor, informally called 'Titanium Candle', was fired in a blast chamber. During these static firings, the motor was mounted to a thrust stand which measured the thrust force. Cameras and other sensors also recorded data during the firings. These data capture information about the motor's performance and about heat transfer into the motor case.

The research motor has a simple cylindrical geometry, which allows for easier manufacturing and simpler analysis. The research motor was sized to test burn areas, thrust levels, and burn durations which are relevant for the Firefly aircraft concept. The motor design is discussed further in section 7.2.2.

The research motor and its instrumentation are shown in fig. 7-2. The motor was instrumented to measure chamber pressure, thrust, and the temperature of the motor case at several locations. Video of the motor firings was recorded with high-speed cameras (see fig. 7-3). The motor instrumentation is described in more detail in section 7.3. Measuring very low thrust levels required a specialized thrust stand, which is described in section 7.3.2.1.

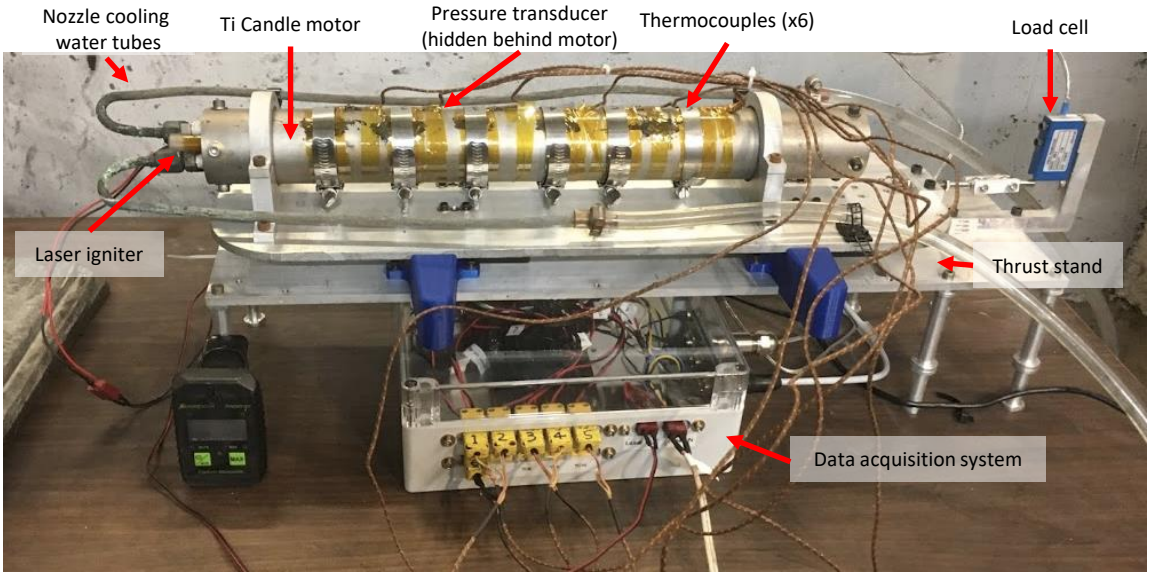

Figure 7-2: The 'Titanium Candle' research motor is instrumented to measure thrust, chamber pressure and case temperatures. It has a water-cooled nozzle and is ignited by a laser. Figure from Mathesius [50].

7.2.1 Test facility

The motor firings were conducted in a blast chamber, located in MIT's building 37. The blast chamber's thick reinforced concrete walls can contain explosive failures of the motor. The equipment setup in the blast chamber is shown in fig. 7-3.

For these tests, the blast chamber was fitted with a smoke suppression system [1]. An exhaust duct was connected to the room's ventilation system and the motor was positioned to fire into the exhaust duct. The exhaust duct was fitted with water sprayers, which sprayed a large amount of water mist into the duct. The water spray pulled soot and HCl out of the exhaust. This 1) reduced the corrosion damage to equipment in the blast chamber and 2) kept the air in the blast chamber clear. Without this system, the air would fill with smoke, obstructing the cameras' view of the motor.

[1]The smoke suppression system was built by Jakob Coray, and undergraduate researcher in our group.

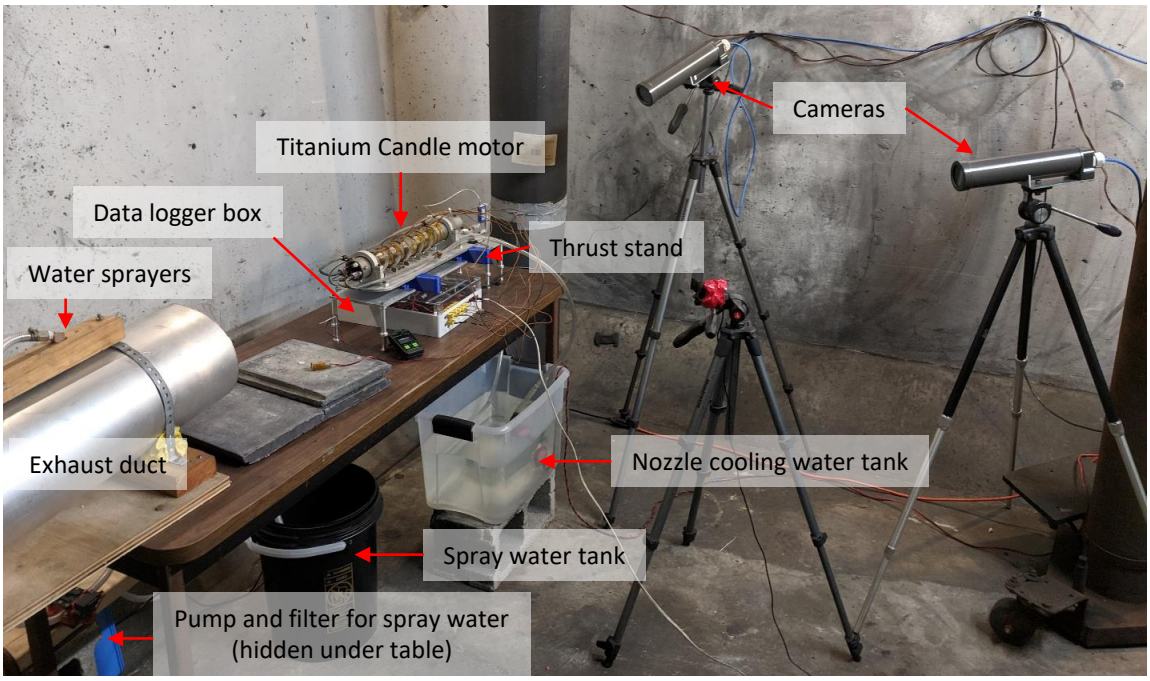

Figure 7-3: Equipment for a motor firing, set up in a blast chamber.

7.2.2 Research motor design

The research motor's components are shown in fig. 7-4. The motor case is a round tube made from grade 2 titanium. The case contains an ablative liner and the propellant grain. The end-burning propellant grain burns from right to left in fig. 7-4. The ablative liner protects the motor case from the hot combustion gases. The motor normally uses a water-cooled nozzle, but it can also be used to test prototypes of air-cooled nozzles (a nozzle for a flight motor needs to be air-cooled). The Ti Candle motor was originally designed by Jon Spirnak for his thesis research [76].

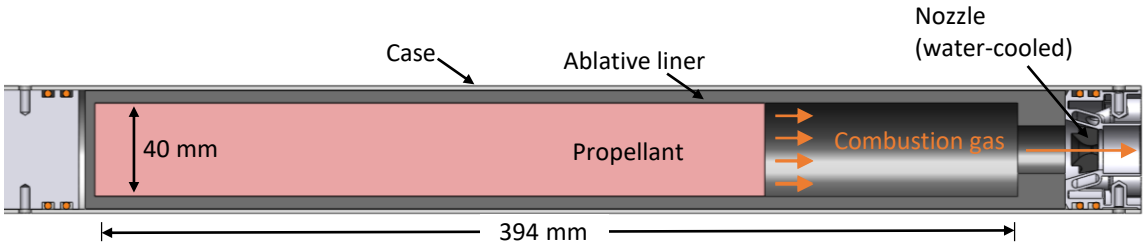

Figure 7-4: Cross section of the 'Ti Candle' research motor, showing the end-burn propellant grain, ablative liner, and water-cooled nozzle.

7.2.2.1 Propellant grain and ignition

The motor uses an end-burn propellant grain. The grain is 40 mm in diameter. A full-length propellant grain has a mass of about 700 g, although sometimes the motor has been tested with shorter-length propellant grains.

To facilitate ignition, a 'starter pocket' is cast into the aft face of the propellant grain. It was found that a flat face of slow-burn propellant could not be reliably ignited. Ignition was made more reliable by placing a small (2–4 g) piece of faster-burning propellant ('starter grain') into a 'starter pocket' in the aft end of the propellant grain (fig. 7-5). The starter grain was ignited by a laser shone through the nozzle. The burning starter grain then ignited the main propellant grain around it.

However, the starter pocket causes the burn area to vary with time as the burn progresses. The regression of the burning surface is depicted in fig. 7-6. The starter pocket is the initial burning surface (a). As the surface of the stater pocket regresses, the burn area initially increases (b), then decreases (c). The burn area levels off at $\pi(20\,\mathrm{mm})^2 = 1257\,\mathrm{mm}^2$ (d).

The non-constant burn area causes an initial peak in chamber pressure during motor firings (fig. 7-7).

Figure 7-5: Left: starter pocket cast into a propellant grain. Right: starter grain loaded into the starter pocket inside the motor. Figure from Mathesius [50].

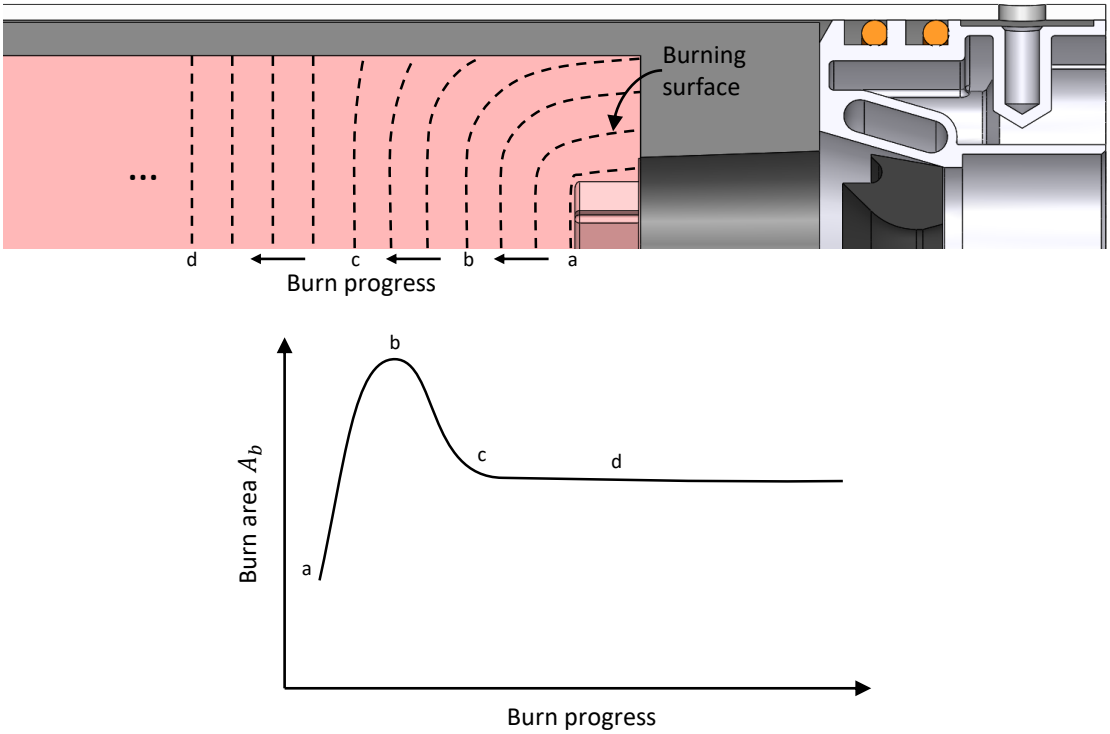

Figure 7-6: Just after ignition, there is an initial peak in the burn area of the propellant grain.

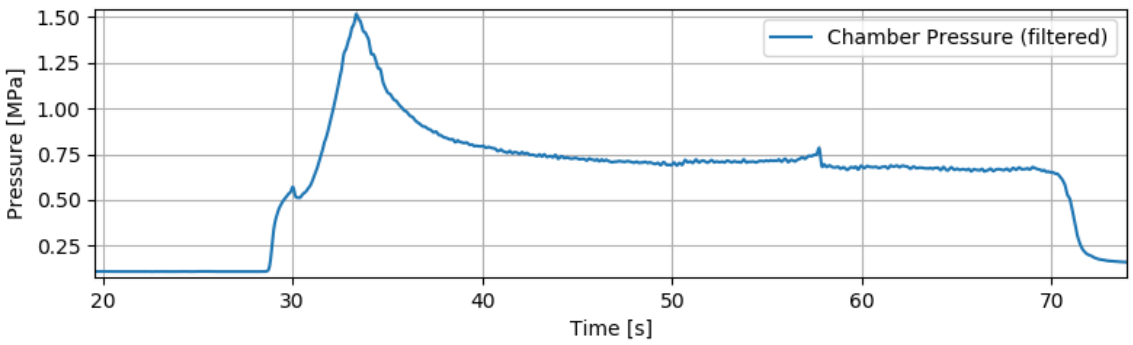

Figure 7-7: During a static firing, there is an initial peak in the chamber pressure due to the starter pocket. This pressure trace is from static fire SF9.

7.2.2.2 Water-cooled nozzle

For preliminary tests of the propellant and ablative liner, the motor used a water-cooled nozzle (fig. 7-8). This enabled experiments on the propellant and ablative to progress before the air-cooled nozzle and nozzle insulation materials had been developed. The water-cooled nozzle was designed by Jon Spirnak, and the details of the design are documented in his master's thesis [76].

The water cooled nozzle is only a research tool. The water cooling system is far too large to use on a flight vehicle.

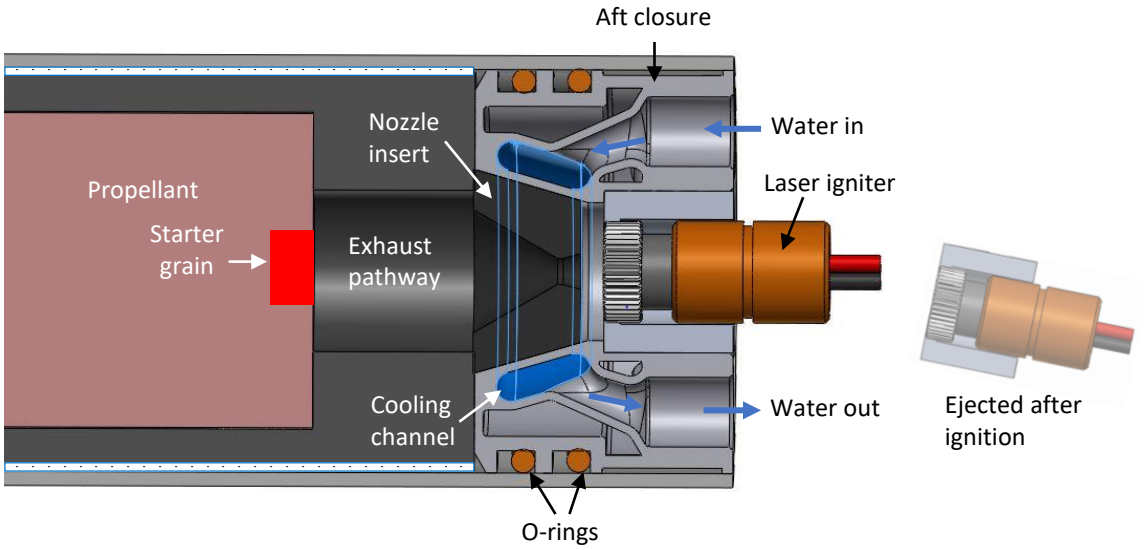

Figure 7-8: Cross-section of the water-cooled nozzle on Ti Candle.

7.2.2.3 Air-cooled nozzle

The Ti Candle motor can also be configured to test air-cooled nozzle prototypes. These nozzle prototypes are similar to what would be used on a flight vehicle; they use the ceramic insulation technology described in chapter 10. Testing on Ti Candle exposes the inside of the nozzle to realistic heating conditions. The in-flight external convection is simulated by air cooling jets which blow on the nozzle shell.

A motor firing with an air-cooled nozzle is shown in fig. 7-9. The nozzle is attached to the motor with an adapter, which takes the place of the usual water-cooled nozzle.

The adapter also provides a port for a chamber pressure transducer. The mechanical design of the adapter is shown in fig. 7-10. Returning to fig. 7-9, note the two air cooling jets mounted to the thrust stand's fixed platform on either side of the nozzle. The air cooling jets are supplied by a compressed gas cylinder (not pictured).

The amount of air cooling can be adjusted by a regulator in the gas supply system. The air cooling system was calibrated to determine a relationship between the regulator set pressure and the average convection coefficient on the nozzle shell [2].

In the calibration tests, it was also shown that the air jets did not create a measurable thrust force on the motor.

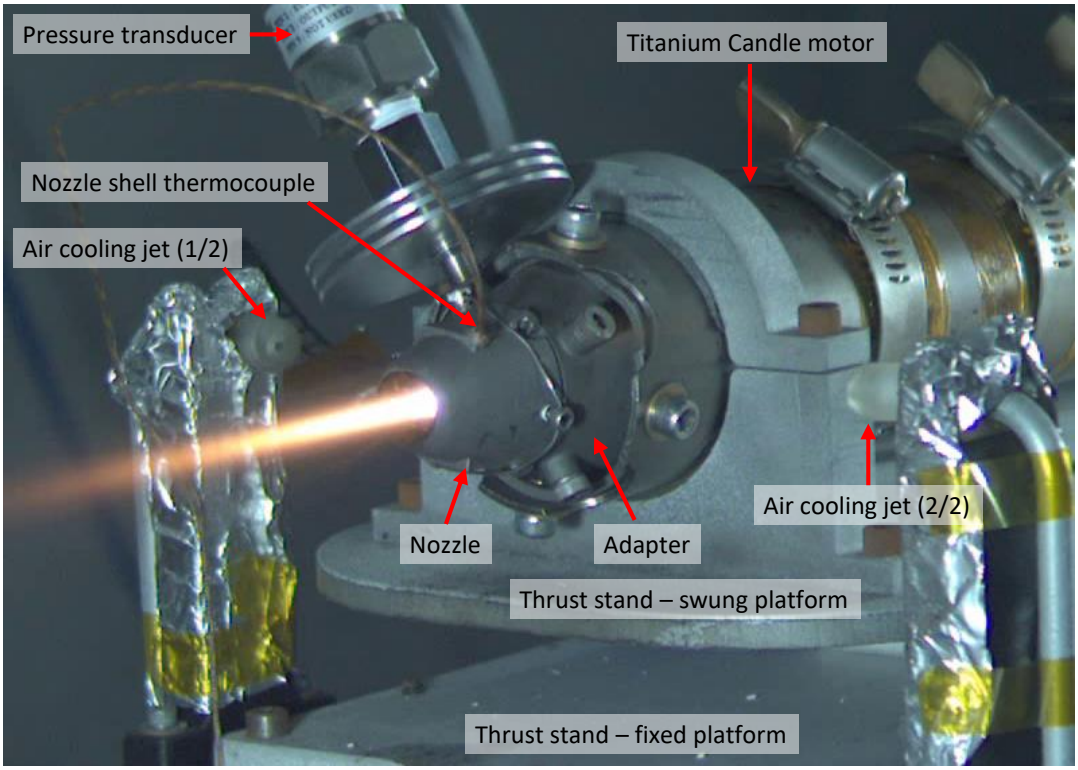

Figure 7-9: A prototype air-cooled nozzle is tested on the Ti Candle motor. Two air cooling jets blow onto the nozzle shell to simulate the in-flight external air flow.

[2]This work was performed by Jovan Zhang, an undergraduate researcher in our group.

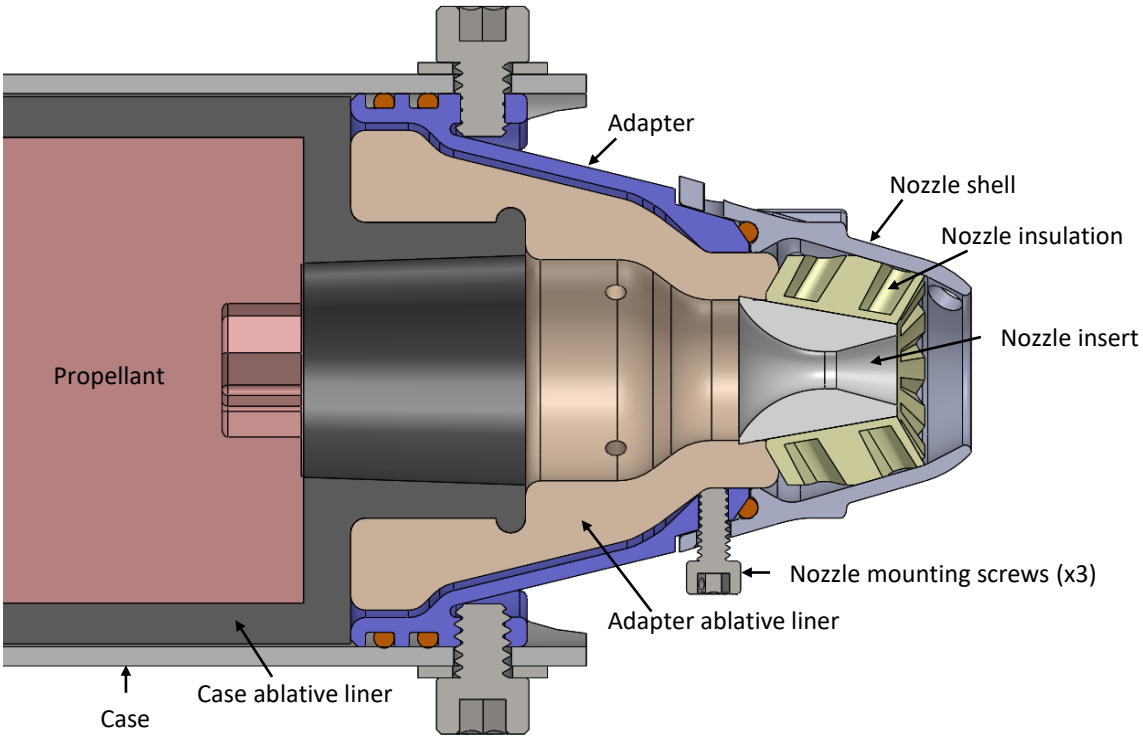

Figure 7-10: Cross-section of the air-cooled nozzle on Ti Candle.

7.3 Research motor instrumentation

7.3.1 Chamber pressure

The chamber pressure is measured by a pressure transducer, model PX119-600AI from Omega Engineering. The pressure transducer is connected to a port at the aft end of the motor. With the water-cooled nozzle, this port is in the aft closure, and the pressure transducer is connected to the port by a 15 cm length of 0.125 in OD steel tube. With the air-cooled nozzle, the pressure transducer is connected directly to a stem which screws into a port on the nozzle adapter (see fig. 7-9, upper left corner, and fig. 7-11).

The transducer element must be protected from the hot combustion gas. At first, in static fires SF4 and SF5, this was achieved by 1) connecting the transducer to the port with a long, narrow tube and 2) placing porous snubber in the plumbing. However, the narrow tube and snubber became clogged with soot, which interfered

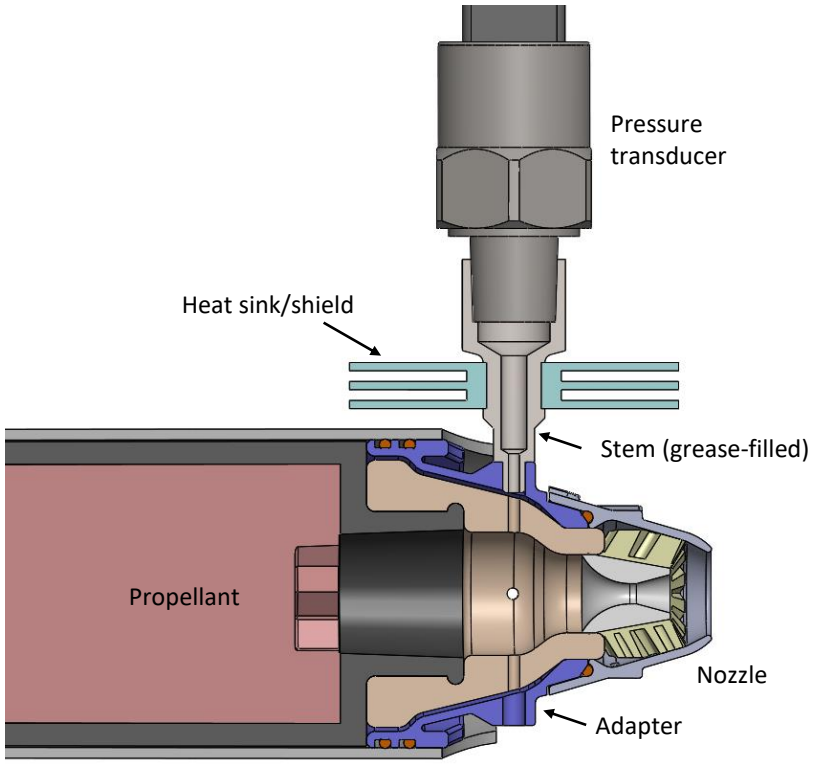

Figure 7-11: With the air-cooled nozzle, the pressure transducer connects to a port on the nozzle adapter.

with the pressure measurements.

In later static fires, a different approach was used to protect the transducer element. The pressure transducer and connected plumbing are filled with silicone grease to avoid exposing the sensor element to the combustion gas. Filling the plumbing with grease also prevents it from becoming clogged by soot.

The grease pack introduces some damping into the sensor dynamics. To quantify this, the sensor's response to a 2 MPa step change in pressure was measured with the sensor alone, and with the grease-filled sensor and plumbing. The settling time of the sensor alone was 25 ms, with the grease fill it increased to 220 ms. However, this is still much better than the first approach: with a clogged snubber the settling time is tens of seconds.

7.3.2 Thrust

Thrust is measured by a load cell, model LCEB-5 or LCEB-10 (depending on the anticipated thrust) from Omega Engineering. The motor is mounted to a swung platform on the thrust stand, which is free to move in the thrust direction. The swung platform is connected to the load cell (fig. 7-2), which measures the thrust force applied to the swung platform by the motor.

7.3.2.1 Thrust stand

The thrust stand supports the motor during firing, and enables thrust measurements. Kinematically exact design and frictionless flexures are used to enable accurate low-thrust measurements.

The design of the thrust stand is illustrated in fig. 7-12. The design employs the kinematically exact design principles described in Hale [29]. The motor is mounted to a swung platform, which has 1 degree of freedom: translation in the thrust direction. The swung platform is connected to the load cell by a double-ball-joint linkage, which *only* constrains the thrust direction. Thus, the swung platform is exactly constrained, and the thrust force is applied to the load cell.

The swung platform is supported by two flexures. Flexures are a type of structure which allow motion along a direction of low stiffness, but are stiff in the other directions. The use of flexures in precision mechanisms is reviewed in Hale [29]. A flexure is shown in fig. 7-13. It consists of two blocks connected by thin arms. One block is bolted to the fixed platform, and the other to the swung platform. The arms are 25.4 mm thick in the direction which supports the motor's weight, but only 0.635 mm thick in the thrust direction. Thus, they are stiff enough to support the motor's weight in one direction, but are 1600 times less stiff in the 'free' direction. In the free direction, the flexures are 100 to 1000 times less stiff than the load cell, so they do not interfere with the thrust measurement.

The flexures are frictionless, an important advantage for low-thrust measurement. The frictionless-ness is easily demonstrated: if the load cell is removed and the

swung platform is given a light push, the platform will oscillate on the flexures for several minutes (until the energy is dissipated by air resistance). Linear bearings, by contrast, have some sticking and friction. A previous thrust stand version, which used high-quality linear bearings, had about 2 N of static friction, quite large compared to the 5–20 N thrust levels the stand is meant to measure.

Unlike bearings, the flexures do not rely on precise, hard surfaces. This is useful for the blast chamber environment, where HCl exposure would ruin the surface of hardened steel bearings.

On the thrust stand, the flexures are enclosed in plastic covers to protect the thin arms from accidental damage. The plastic covers were made via additive manufacturing. The blue plastic covers are visible in fig. 7-2.

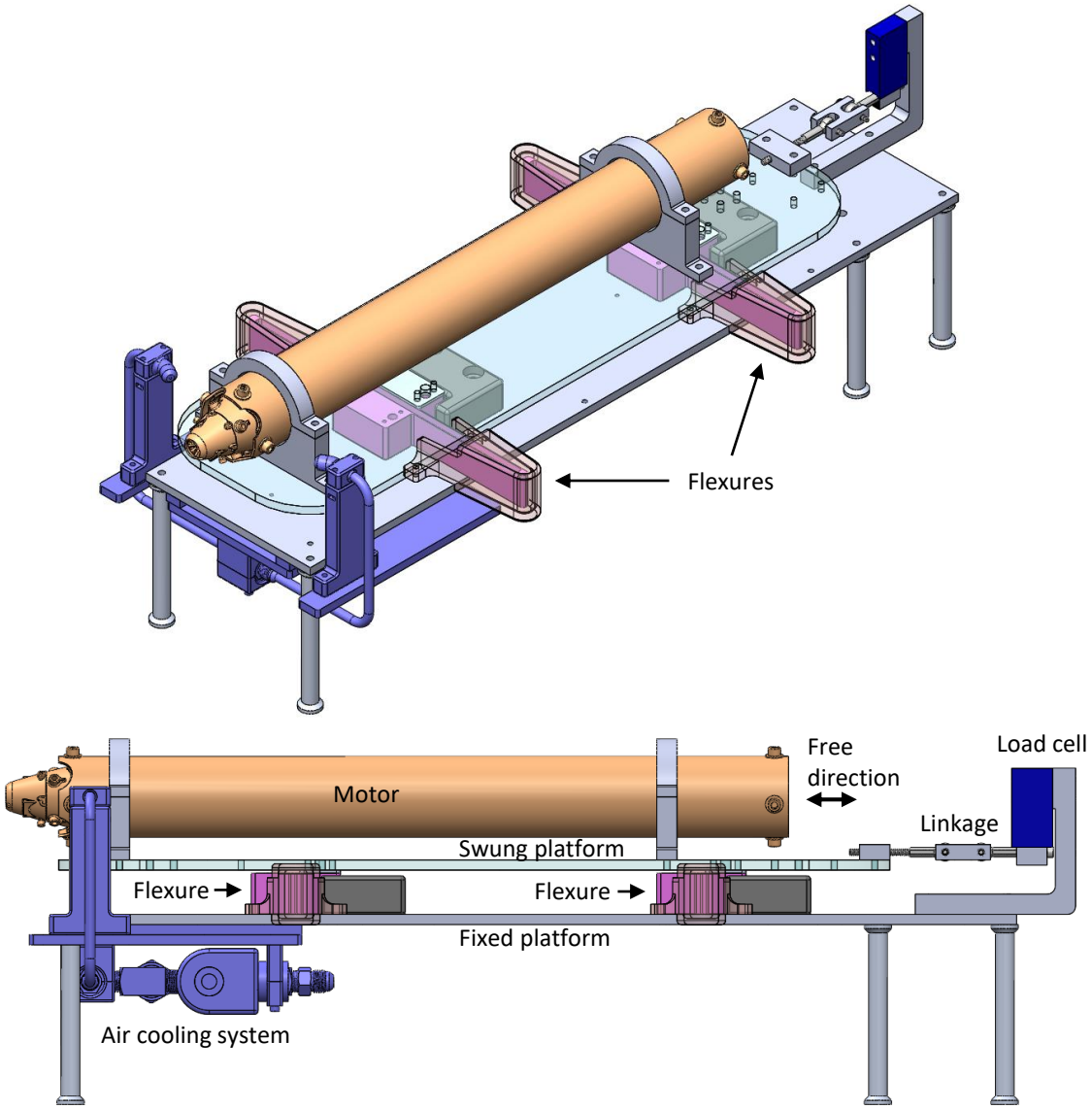

Figure 7-12: The thrust stand supports the motor on a 1 degree-of-freedom swung platform. A load cell measures the force in the free direction. Flexures provide frictionless support.

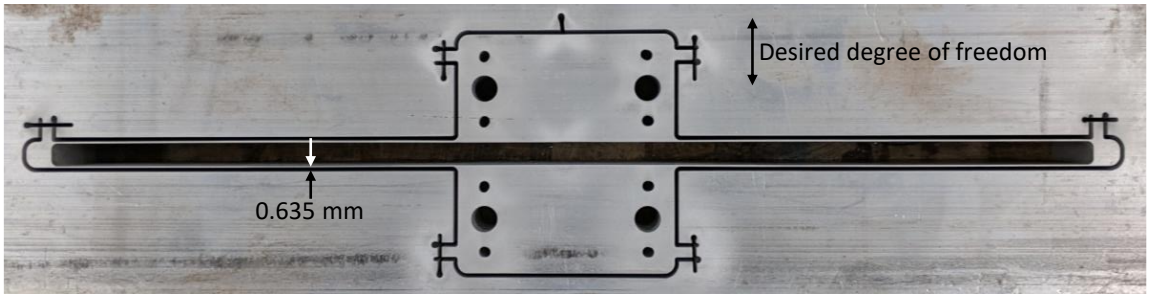

Figure 7-13: The thrust stand's flexures allow motion in one direction by bending thin arms. The flexure arms are only 0.635 mm (0.025 in) wide. They were waterjet-cut from 25.4 mm (1 in) aluminum stock.

7.3.2.2 Resonance in the thrust measurement system

Because the load cell acts like a spring, the load cell and swung platform form a mass-spring system with little damping. This system has a resonant frequency at 26 Hz. Due to this resonance, there is a noticeable amount of noise in the thrust signal near 26 Hz (fig. 7-14).

Resonances are a common issue in low-thrust measurements (e.g. [48]). There is not a clear way to resolve this issue. The resonant frequency could be increased by making the load cell stiffer, but then there would not be enough strain in the load cell to measure low thrust levels. The quality of the resonance could be reduced by adding damping, but this would interfere with the thrust measurement.

The important features of the thrust curve are comparatively slow (< 5 Hz), so the 26 Hz noise does not impair the thrust measurements.

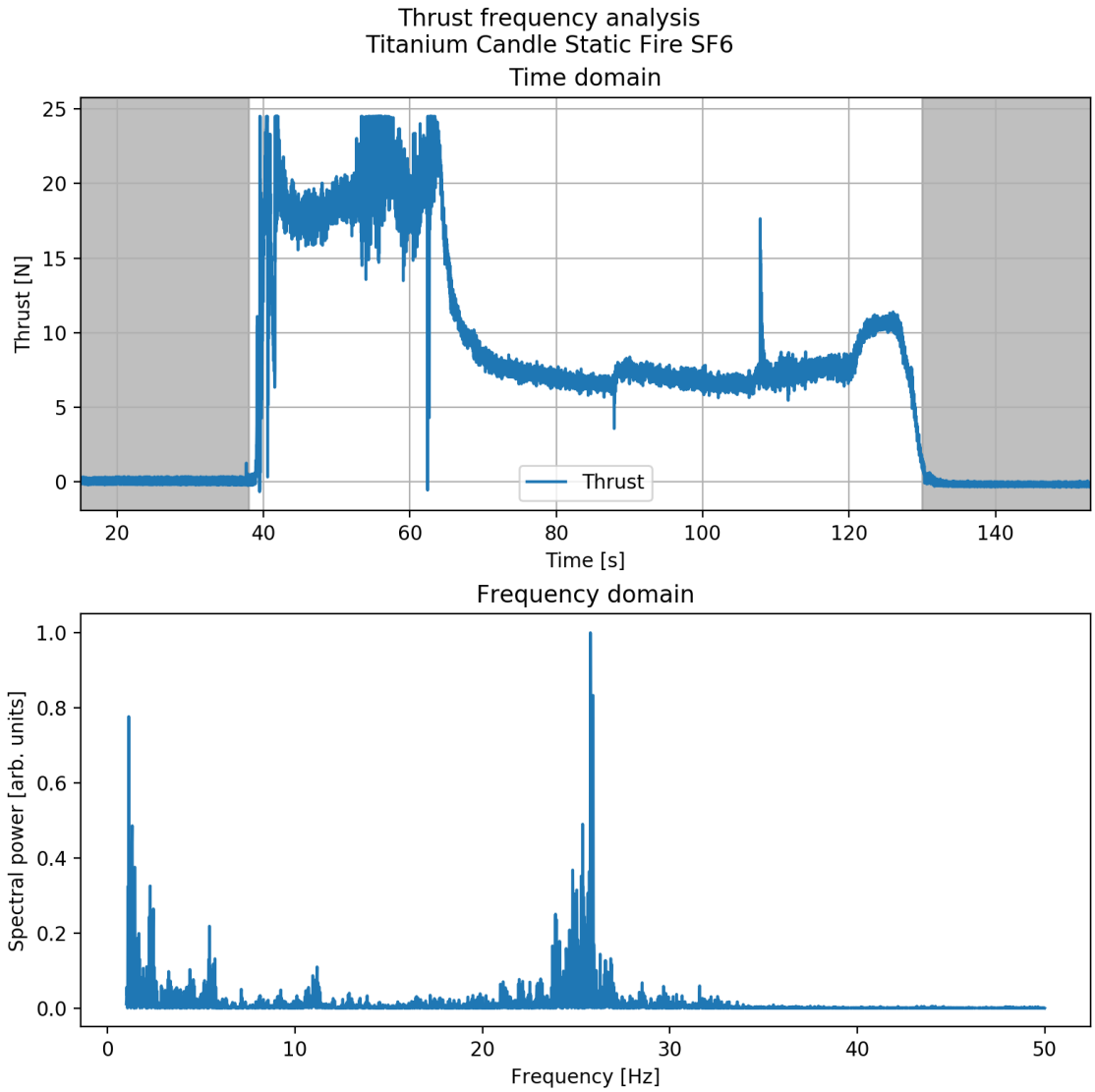

Figure 7-14: There is a large amount of noise in the thrust signal at 26 Hz, due to a resonance of the load cell and thrust stand.

7.3.3 Case temperature

The case temperature is measured by six Type K thermocouples, which are affixed to the case by stainless steel hose clamps. The locations of the thermocouples are shown in fig. 7-15.

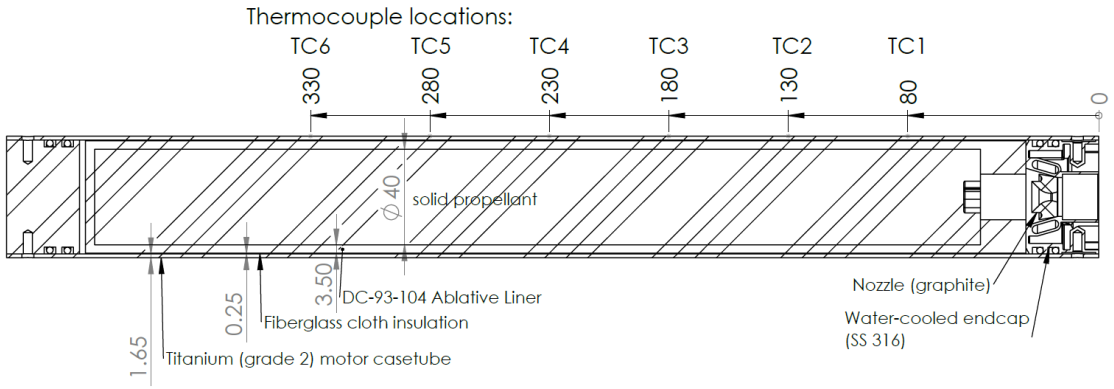

Figure 7-15: Six Type K thermocouples were mounted to the outside of the motor case. Dimensions in millimeters.

7.3.4 Cameras

The motor firings are recorded with two cameras: a FLIR Blackfly recording at 82 fps and a Balser Ace recording at 250 fps. Both cameras stream to a computer over gigabit Ethernet.

7.3.5 Data logger

The analog sensors (pressure, thrust, case temperature, and laser current) are recorded by a LabJack U3 analog-to-digital converter (ADC). LabJack LJTick InAmp instrumentation amplifiers are used to amplify the thermocouple signals. For all sensors, the ADC's flicker-free resolution was better than 0.2% of the sensor's full-scale range. The signals were sampled and recorded at 100 Hz. The electronics are mounted in an enclosure under the thrust stand (fig. 7-2).

7.4 Motor testing results

Four static firings of the research motor are analyzed here; the conditions of these firing are listed in table 7.1. These firings were used to measure the motor's thrust coefficient and characteristic velocity, and to verify operation at low F/A_b.

Nine static firings of the motor have been conducted, but only static fires SF4, SF5, SF6, and SF9 are referenced in this work. Static fires SF1-3 were conducted early in the propellant development process and used different propellant formulations. Static fires SF7 and 8 were early attempts to test the air-cooled nozzle; in these tests the mechanical interface between the air-cooled nozzle and the motor failed. The interface was changed for SF9; this test succeeded.

	Propellant			Nozzle	
Static fire number	Oxamide [% by mass]	AP blend	Burn length [mm]	Cooling	Throat diam. [mm]
SF4	13%	400/200 µm	175	Water	2.99
SF5	13%	400/200 µm	175	Water	3.02
SF6 seg. 1	0%	400/200 µm	182	Water	3.02
SF6 seg. 2	10%	400/200 µm	182		
SF9	10%	400 µm	86	Air	2.82-2.95[3]

Table 7.1: Firings of the research motor referenced in this section. SF6 used a multi-segment propellant grain with two different propellants; the multi-segment grain is described further in Mathesius [50].

7.4.1 Thrust and chamber pressure measurements

Thrust and chamber pressure measurements were recorded for all static fires (fig. 7-16). The thrust and pressure curves for SF4, 5 and 9 all have a similar shape: a peak followed by a plateau. The peak is due to increased burn area just after ignition; the thrust and pressure plateau once a flat end-burn surface is achieved (see section 7.2.2.1). SF6 used a multi-segment propellant grain. The aft (first to

[3]Throat diameters before-after firing; the nozzle eroded during the firing.

burn) segment contained 0% oxamide, burned faster, and produced higher chamber pressure and thrust. The front (last to burn) segment contained 10% oxamide, burned slower, and produced lower chamber pressure and thrust.

SF4 and 5 had the highest oxamide content (13%). These firings achieved a very low chamber pressure, only 0.5 MPa, in the steady portion of the burn.

In static fires SF4 and SF5 there is a large amount of noise in the thrust data. A cooling pump was mounted near the thrust stand; vibrations from the cooling pump caused the noise. The cooling pump was mounted elsewhere for SF6, and was not used in SF9.

In SF4 and 5, the measured chamber pressure decays very slowly after burnout. This is not realistic; the true chamber pressure decays to atmospheric pressure within a few seconds. In these firings, the path to the pressure transducer became clogged with soot, so it took a long time for the volume within the pressure transducer to de-pressurize. In SF5, the pressure transducer pluming contained a porous-disk type snubber; this became clogged and caused a particularly long pressure decay. The pressure transducer plumbing was modified for subsequent static fires to remedy this issue.

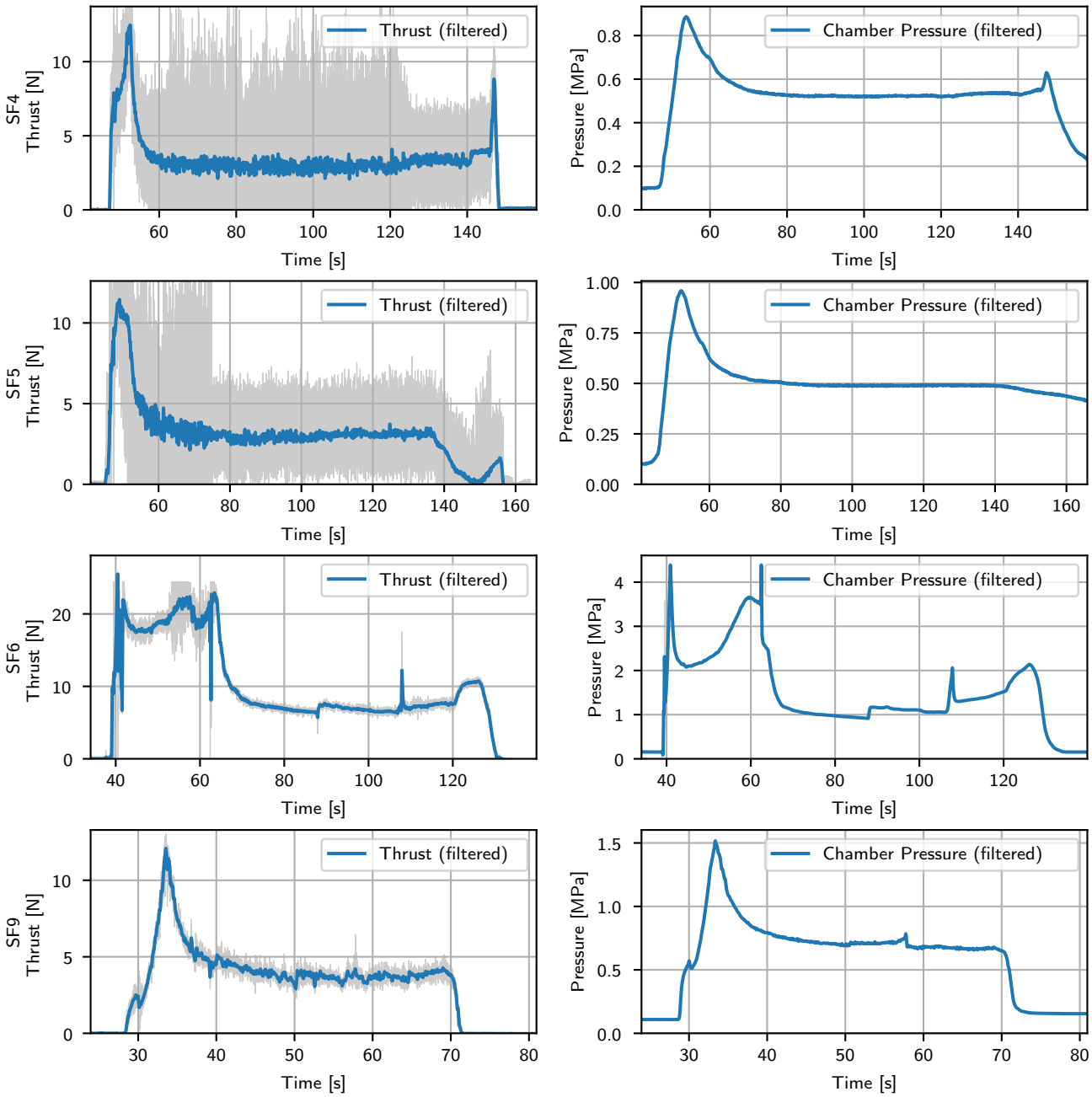

Figure 7-16: Thrust (left column) and chamber pressure (right) measurements for each static fire. Raw measurements are shown in gray, the filtered signals (5 Hz low-pass) are shown in blue.

7.4.2 Research motor burn rate measurements

In addition to the strand burner burn rate measurements described in section 5.4, the burn rate was also estimated from the research motor firings. Estimating burn rate from the motor firings is somewhat involved. Two techniques were used: a 'average burn rate method' and a 'c^*-based method'; these methods are described in appendix A.

The research motor burn rate data are shown in figs. 7-17 to 7-19 with black 'x' and '+' marks. Each plot shows data for a different propellant. For comparison, the strand burner data for that propellant (from fig. 5-8) are also shown on each plot.

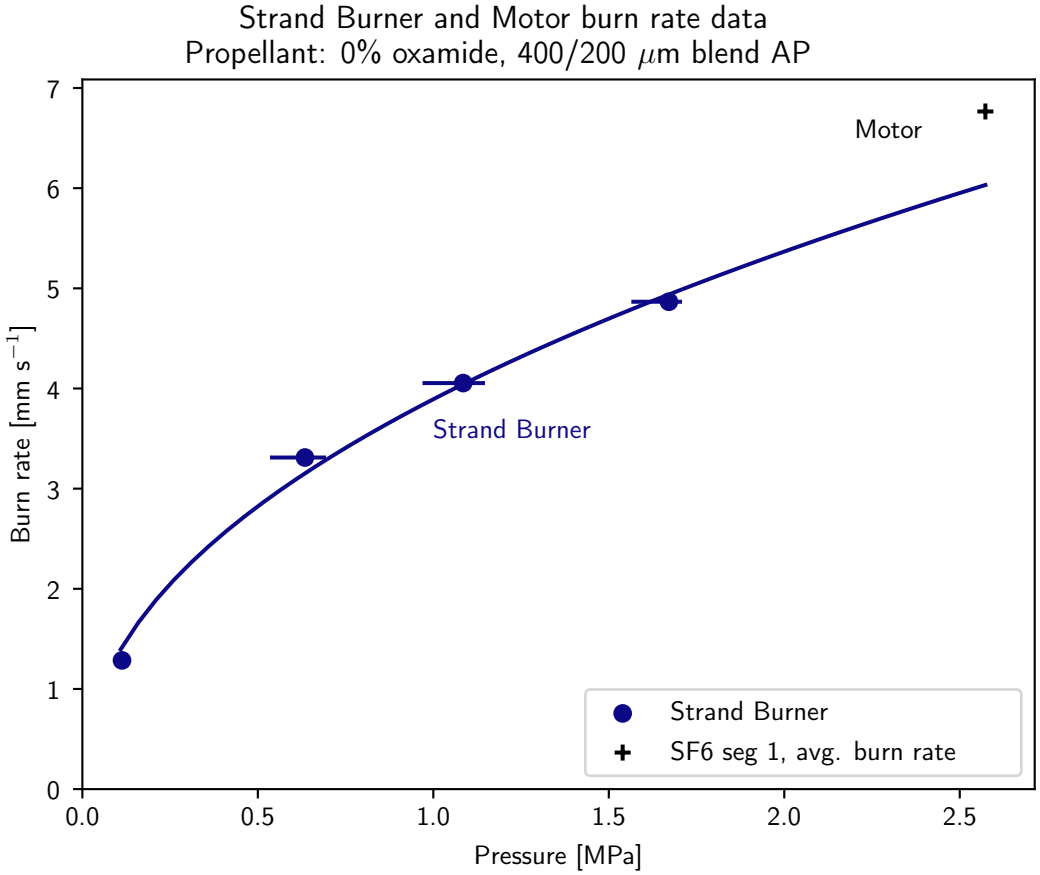

Figure 7-17: Burn rate data from the research motor (black '+' mark) and strand burner (blue curve and points) for the 0% oxamide propellant. The propellant burns faster in the motor than in the strand burner.

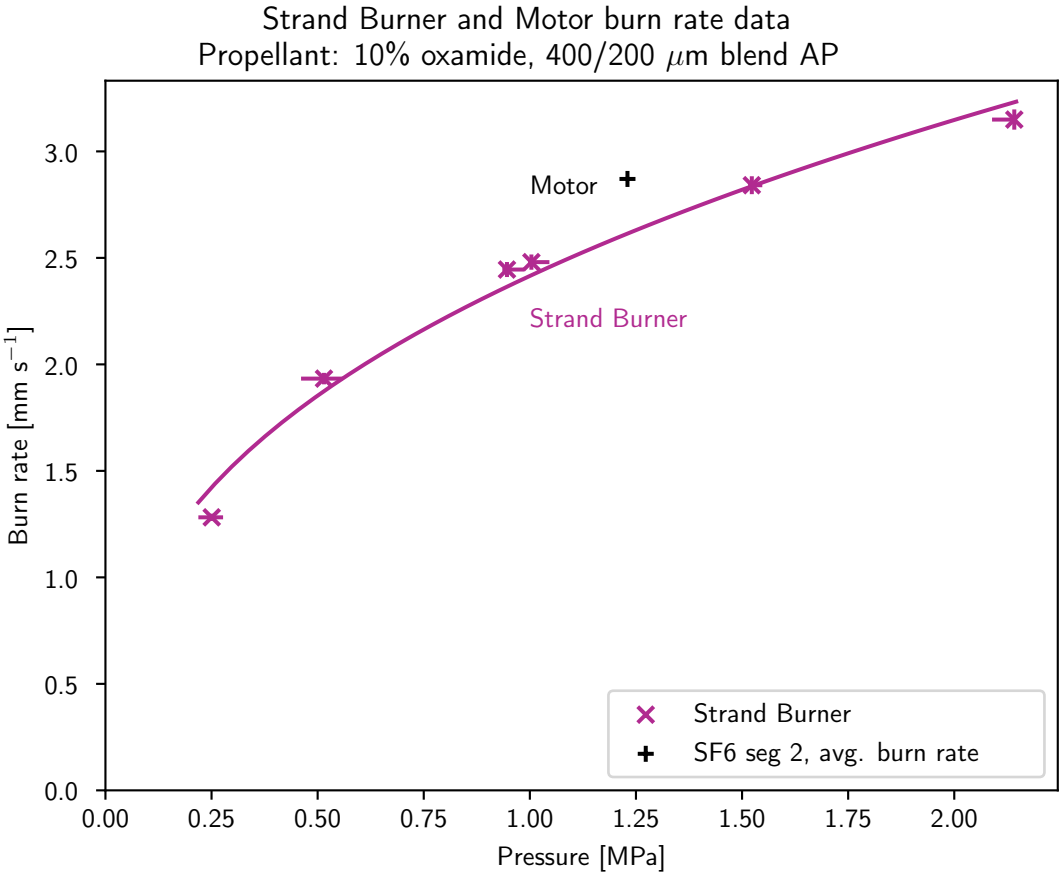

Figure 7-18: Burn rate data from the research motor (black '+' mark) and strand burner (pink curve and points) for the 10% oxamide propellant. The propellant burns faster in the motor than in the strand burner.

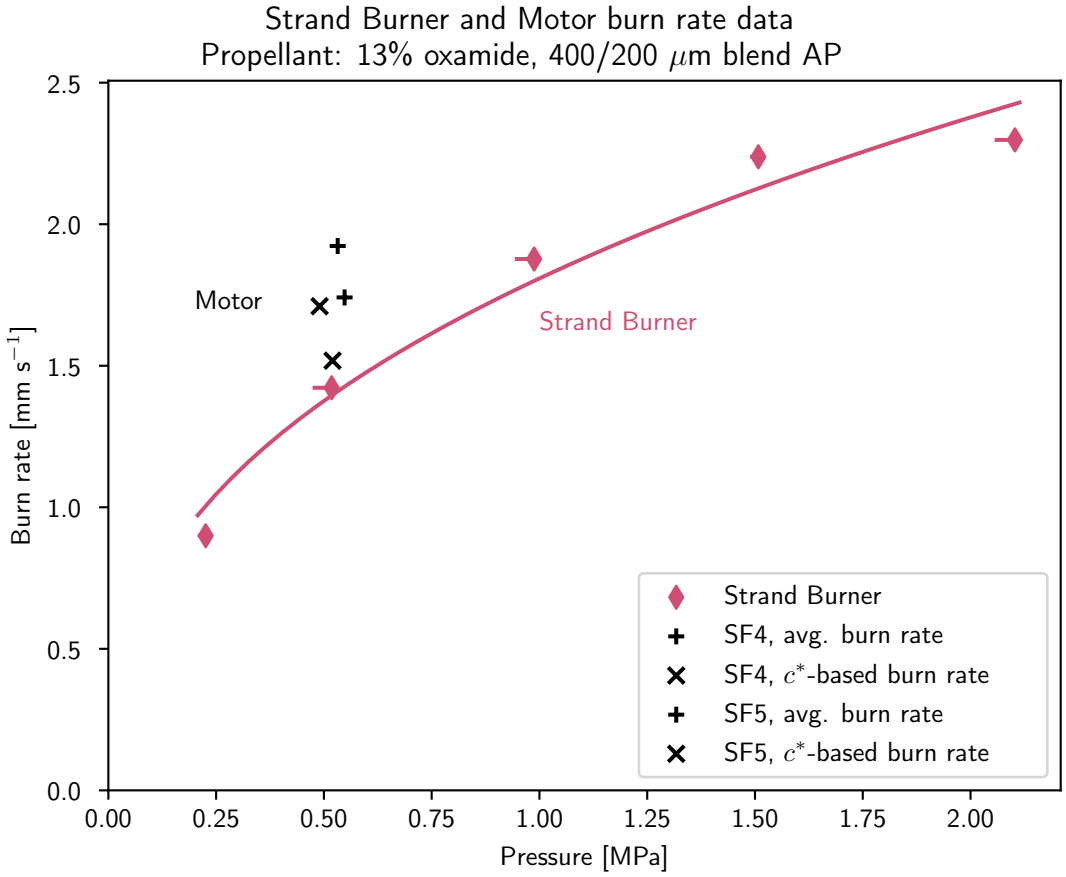

Figure 7-19: Burn rate data from the research motor (black '+' and 'x' marks) and strand burner (orange curve and points) for the 13% oxamide propellant. The propellant burns faster in the motor than in the strand burner.

The burn rates measured in the motor are consistently higher than those measured in the strand burner (fig. 7-20). On average, the motor burn rates were 19% higher than the stand burner fits would predict.

This is a common feature of strand burner tests [77]. In a small strand, a noticeable fraction of the flame's heat is lost (to radiation and convection to the walls of the sample tube). This reduces the amount of heat transfered into the propellant surface and thus reduces the burn rate. The propellant burns faster in the hot environment of the motor [77]. A study of the influence of strand diameter on burn rates indicated that 10 mm diameter strands burn at 11% less than the motor rate [6] (the strand used in this work were 9.7 mm diameter).

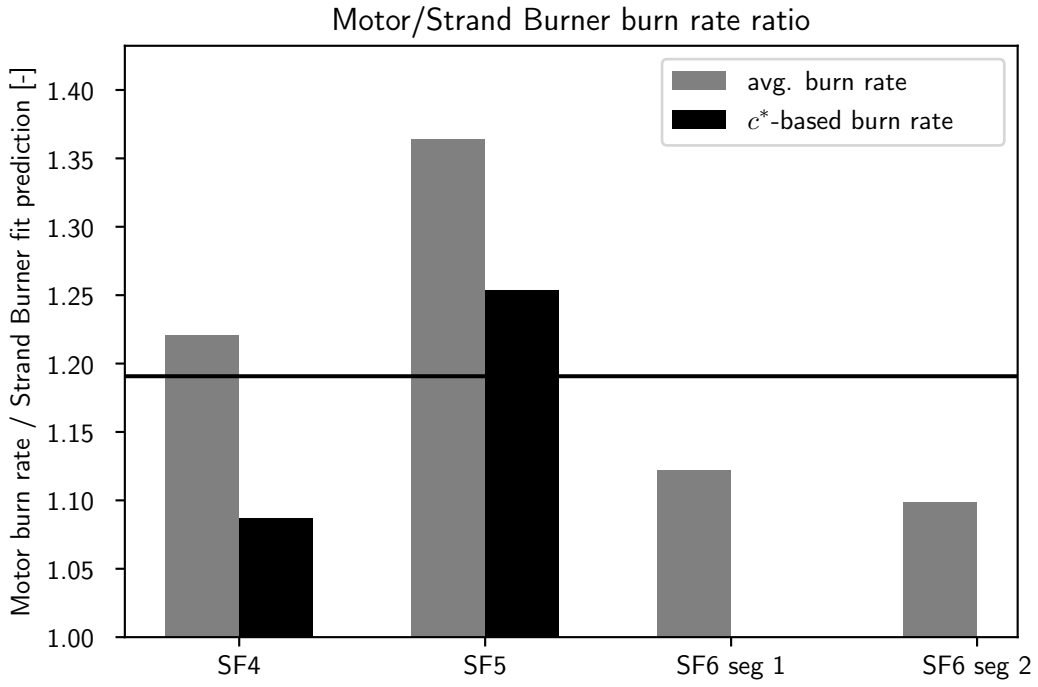

Figure 7-20: Burn rates in the motor are 1.08 to 1.36 times higher than burn rate in the strand burner. The propellant burns faster in the motor because the flame loses less heat.

The propellant burn rate coefficient vs. oxamide content is shown in fig. 7-21. The motor firing burn rate measurements are shown as black marks. The oxamide

model (black curve) fits the motor firing data well. The fit curve for the motor firings is 19% higher than that for the strand burner. The oxamide model fit for the strand burner is shown in gray; it is the same fit as in the top plot of fig. 5-9. This figure is only for propellants with the '400/200 micron blend' AP particle size. Propellants with the '400 micron blend' AP particle size burn more slowly.

The oxamide model as fit to the motor firings in fig. 7-21 is used as the model for propellant burn rate in all other analyses in this work (e.g. chapters 3 and 6).

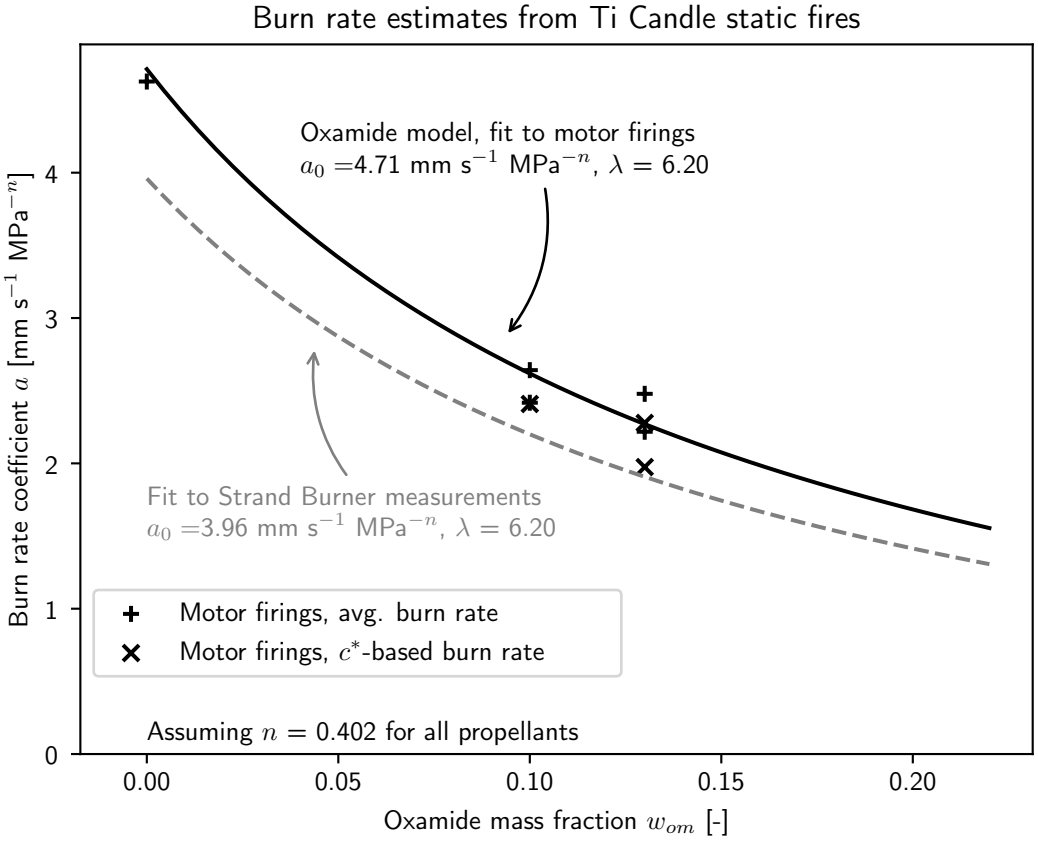

Figure 7-21: The oxamide model is also a good fit for burn rate vs. oxamide measurements from motor firings. The baseline burn rate coefficient a_0 for the motor is 1.19 times that for the Strand Burner.

7.4.3 Operation at low thrust/burn area ratio

A very low thrust / burn area ratio of $F/A_b = 2.4\,\text{kPa}$ was achieved in static fires SF4 and SF5. Both firings used a 13% oxamide propellant, and operated at a very low chamber pressure. The 'steady' chamber pressure (after the starter pocket transient, see section 7.2.2.1) was 0.52 MPa in SF4 and 0.49 MPa in SF5.

These tests were very close to the lower limit on F/A_b. Using the methods from section 3.2, the lowest possible F/A_b for this propellant was predicted to be 2.7 kPa. However, this analysis assumed ideal nozzle flow. Taking into account the measured nozzle losses ($\zeta_{C_F} = 0.851$), the predicted lower limit is $F/A_b = 2.3\,\text{kPa}$. Thus, SF4 and SF5 operated very close to the lowest possible F/A_b for their propellant.

Demonstrating operation at low chamber pressure, close to the F/A_b limit, is an important technology risk reduction for low-thrust motors. Other propellants and motors exhibit low-frequency combustion instability (chuffing) when operated at low chamber pressure [77]. Chuffing causes problematic variation in the motor's thrust, and can extinguish the propellant. Chuffing was *not* observed in SF4 or SF5. These tests show that this slow-burn propellant can operate at very low p_c without chuffing, which is necessary for low-thrust motors.

It is possible to reduce the F/A_b further by increasing the AP particle size. The SF4 and SF5 propellant used '400/200 micron blend' AP. With '400 micron blend' AP, the propellant burn rate would be even slower and a slightly lower F/A_b could be achieved.

7.4.4 Characteristic velocity measurements

Characteristic velocity c^* measures the energetic-ness of propellant combustion. Characteristic velocity was defined and described in section 2.2.3.3. Theoretically, c^* is proportional to the square root of the nozzle inlet stagnation temperature. In this work, the time-averaged c^* was measured from the pressure recording $p_c(t)$, the nozzle

throat area A_t, and the propellant grain mass m_p:

$$\langle c^* \rangle = \frac{A_t}{m_p} \int_{t_{start}}^{t_{end}} p_c(t) dt \tag{7.1}$$

Characteristic velocity measurements for static fires SF4, SF5, and SF9 are presented in fig. 7-22 (top subplot). For comparison, the ideal c^* computed from combustion simulations (see section 5.2) is plotted as a black curve. As expected, the measured c^* values are less than the ideal values. The c^* efficiencies (ζ_{c^*}) are plotted in the bottom subplot.

These values for ζ_{c^*} are unusually low. In larger motors, ζ_{c^*} is typically > 0.95 [77]. The low values of ζ_{c^*} are probably due to heat loss from the combustion gas to walls of the motor (see sections 8.3.3 and 8.5.2). Heat loss cools the gas before it reaches the nozzle; c^* is proportional to the square root of temperature at the nozzle inlet.

The c^* measurements in SF6 were not reliable because of throat clogging (clogging is discussed further in section 7.4.6). Using the nominal throat area gives unrealistically high c^* values for SF6, and the exact area of the clogged throat is not known. Thus, no datum for SF6 is included in fig. 7-22.

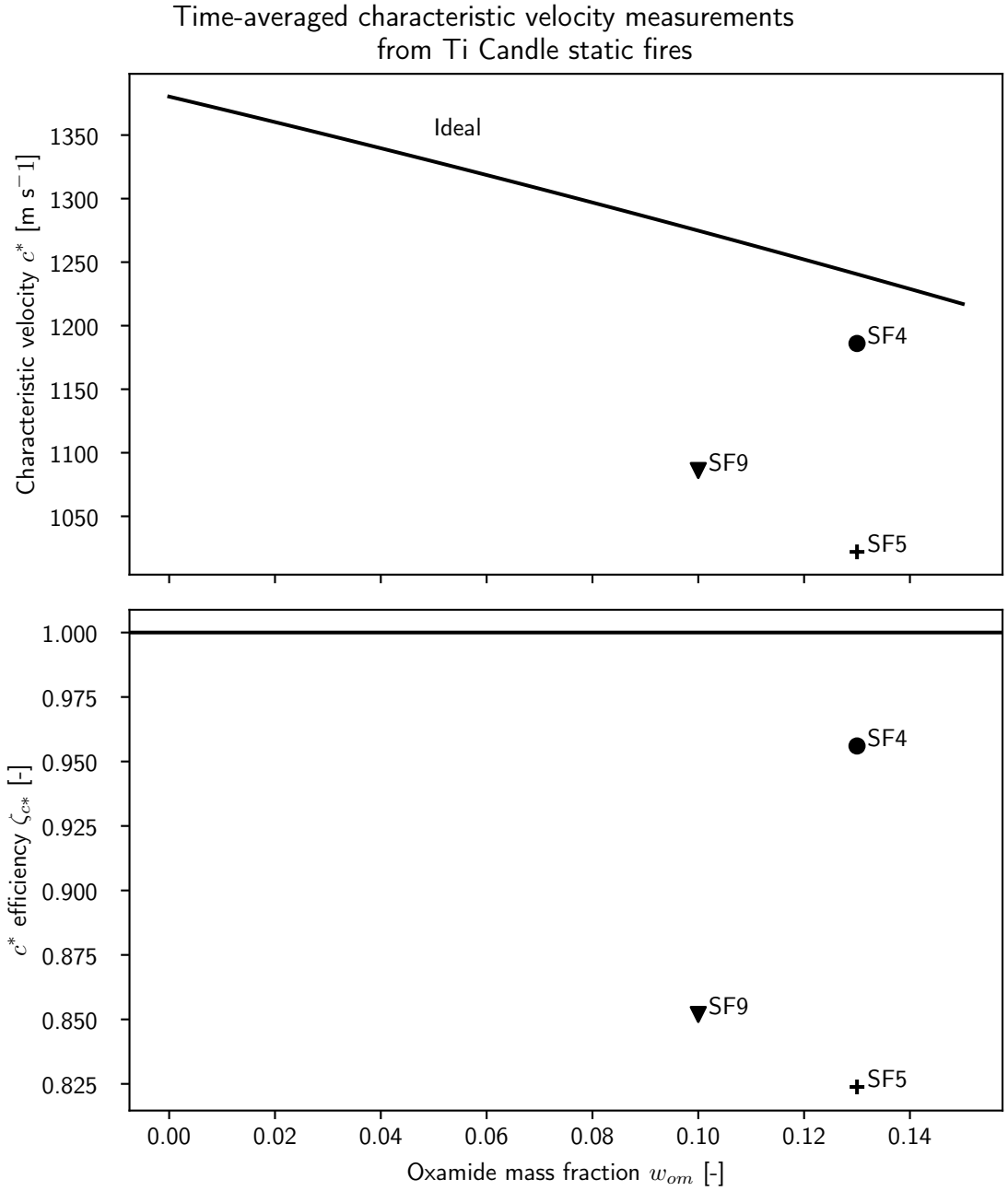

Figure 7-22: Characteristic velocity measurements for static fires SF4, SF5, and SF9. These values for c^* efficiency are unusually low, probably due to energy loss from the combustion gas to the walls of the motor.

7.4.5 Thrust coefficient measurements

The thrust coefficient C_F measures the effectiveness of the nozzle expansion process. The thrust coefficient was defined and described in section 2.2.3.2. C_F is computed from the thrust recording $F(t)$, chamber pressure recording $p_c(t)$, and nozzle throat area A_t:

$$C_F = \frac{F}{A_t p_c} \tag{7.2}$$

The ideal value of C_F can be calculated from first principles. The thrust coefficient efficiency is the ratio of the measured and ideal values: $\zeta_{C_F} = C_F^{meas}/C_F^{ideal}$.

In all tests, the ideal C_F was rather low due to low chamber pressure. The measured C_F values were even lower. For example, in SF5, the average ζ_{C_F} was 0.851. Figure 7-23 shows the ideal and measured C_F vs. time during this firing.

This is a fairly low value of ζ_{C_F} – in large, well-designed nozzles, ζ_{C_F} is usually > 0.95. However, the nozzles in this work are expected to have larger viscous losses due to their small size. These losses are an unavoidable feature of small nozzles.

Other firings had even lower thrust coefficients due to nozzle clogging or nozzle damage. In SF9, the C_F was reduced by damage to the inner surface of the nozzle. This test is discussed in the nozzle design chapter, section 9.4.2. In SF6, the nozzle was clogged by a solid deposit; this is discussed below.

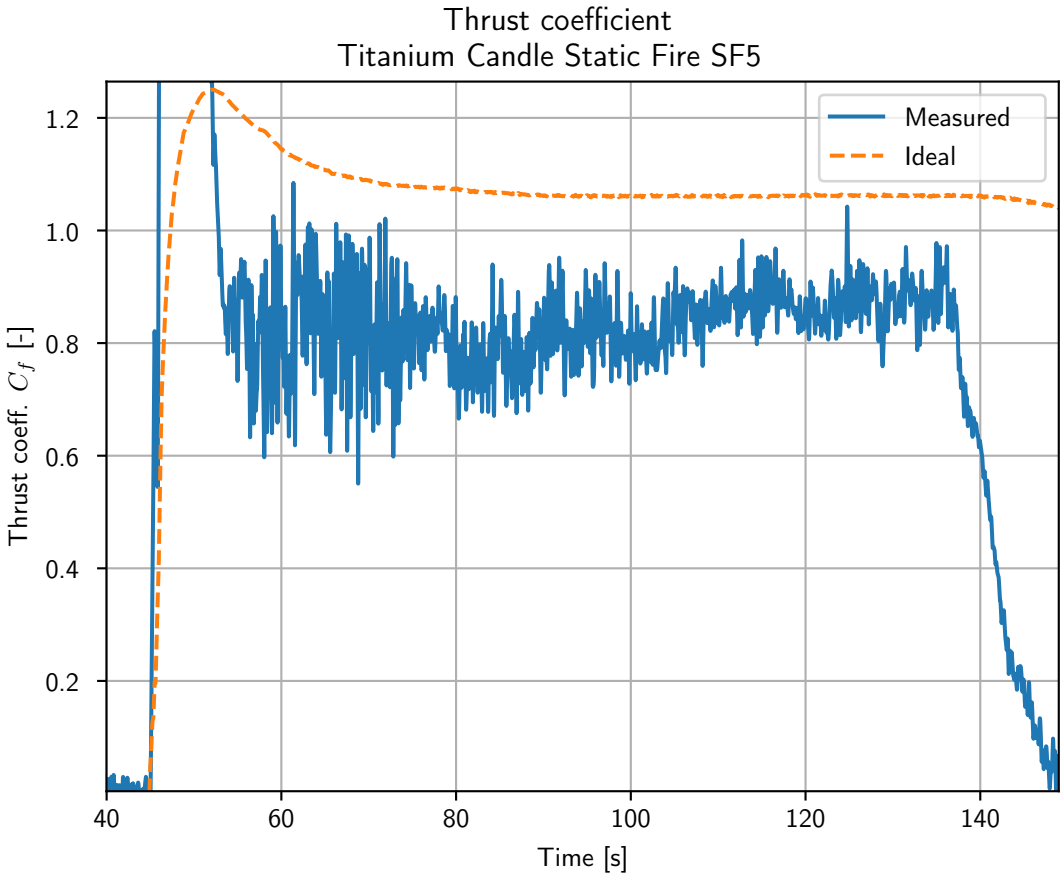

Figure 7-23: In static fire SF5, the thrust coefficient was low, but did not change much during the burn. The initial peak is due to the starter pocket (see section 7.2.2.1).

7.4.6 Nozzle clogging

In some motor firings with the water cooled nozzle, the nozzle became clogged with solid, porous material (comprised of carbon, silicon and oxygen). This significantly disrupted the gas flow through the nozzle and reduced the motor's specific impulse. If this were to occur in flight, the vehicle's range would be compromised. Severe nozzle clogging could cause an increase in chamber pressure which might overload the nozzle or case. Clogging was not observed with the air cooled nozzle, but only one firing has been performed with that nozzle. It is currently not known what factors cause clogging, or if clogging could occur in the air cooled nozzle. This issue is a significant technical risk and should be addressed in future research.

In SF6, the nozzle became clogged with solid material (see fig. 7-24). This reduced the C_F, as the exhaust gas experienced large viscous losses flowing through the porous clog. The C_F decreased with time as the clog grew (see fig. 7-25).

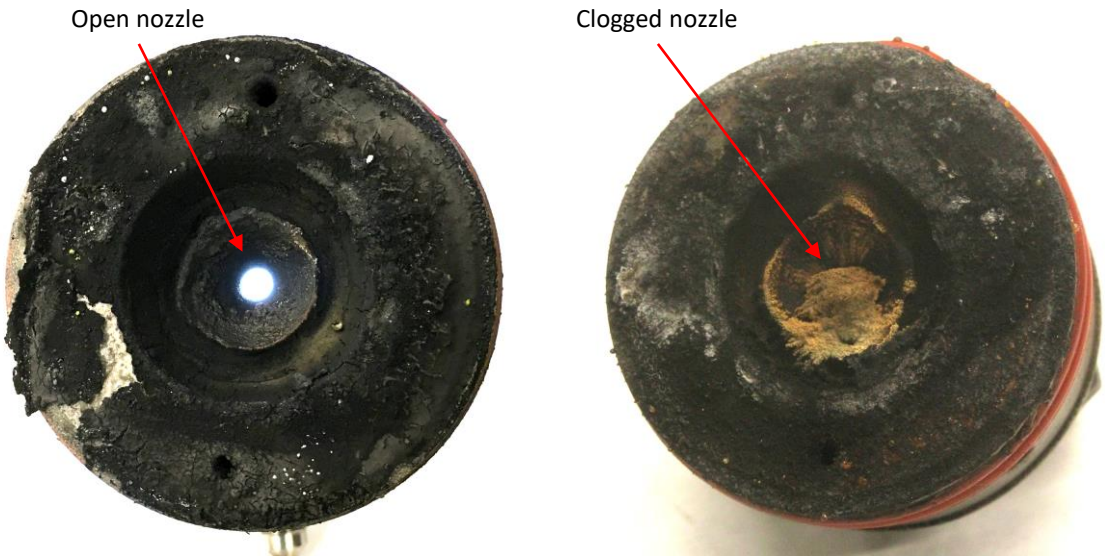

Figure 7-24: Left: after static fire SF4, the nozzle remained unobstructed (at it is supposed to be). Right: after SF6, the nozzle inlet was clogged with solid material.

At one point some solid debris was ejected from the nozzle, as shown by infrared imagery in fig. 7-26(a). The time of this image corresponds to 63 s in fig. 7-25; the C_F briefly recovered after the debris was ejected. Then, more solid material continued to build up in the nozzle, and remained until the end of the firing.

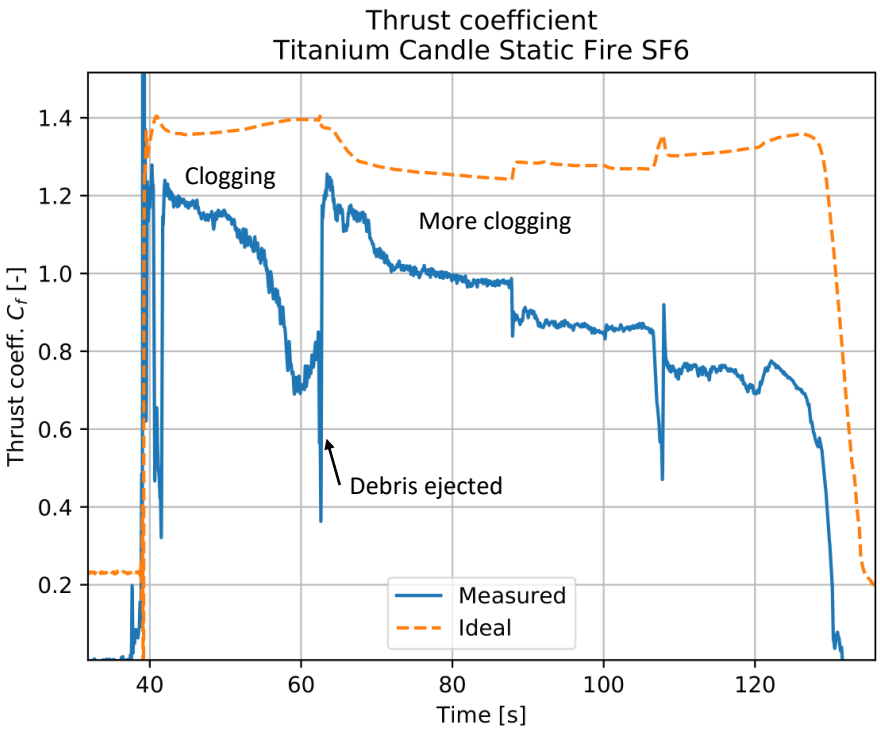

Figure 7-25: In SF6, the measured C_F falls further below the ideal C_F as the firing goes on. This is due to a buildup of solid material clogging the small nozzle.

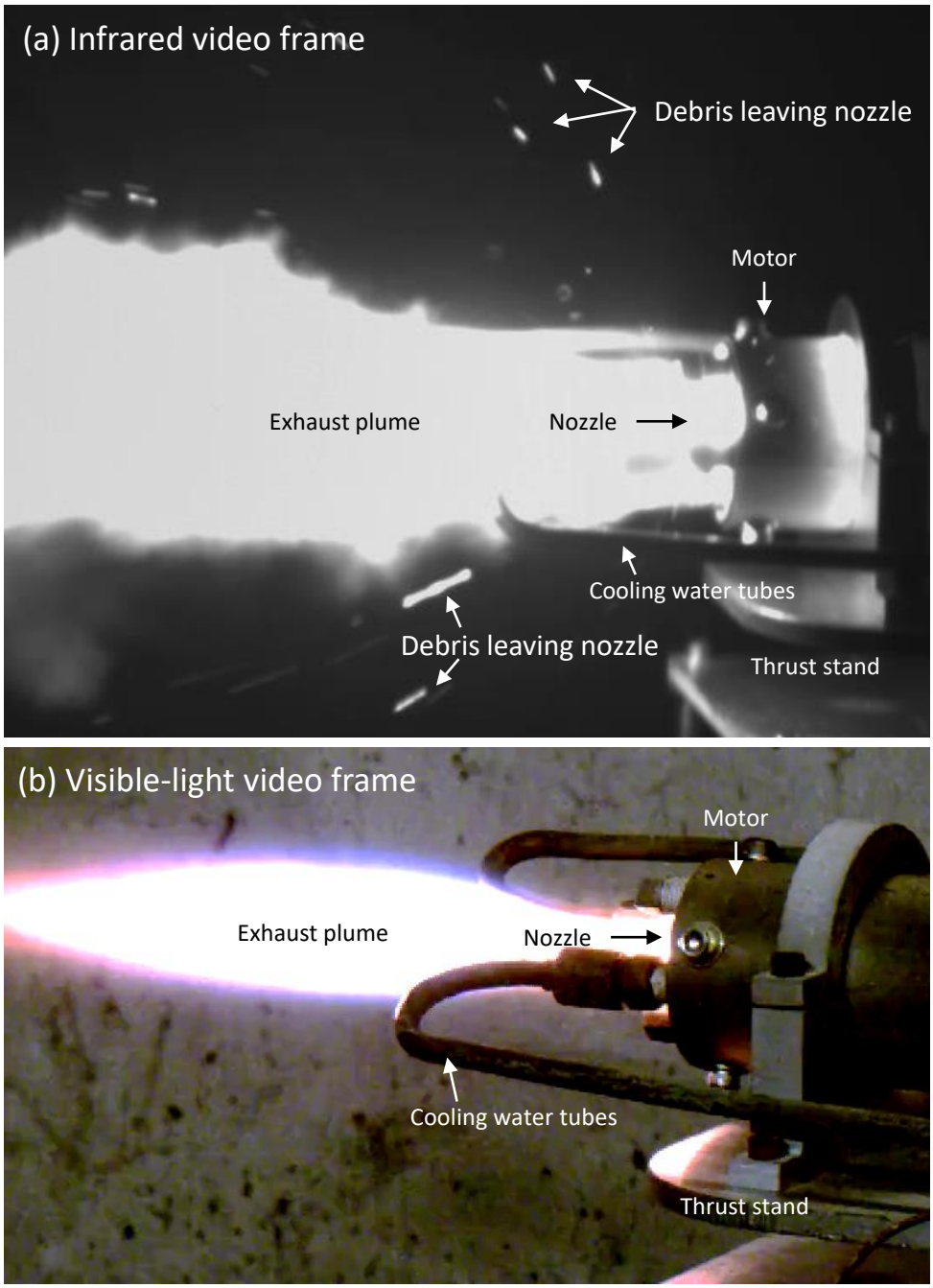

Figure 7-26: An infrared image (top) shows streaks from solid debris leaving the nozzle during SF6. A visible-light image (b) is provided for context; the visible-light camera was slightly to the right of the infrared camera.

The nozzle clogging deposit from SF6 is shown in more detail in fig. 7-27. There are two kinds of material in the deposit: an orange, 'fluffy' material on the outside and a black, sticky material underneath. Scanning electron microscope images and energy dispersive x-ray spectroscopy (EDS) maps of the material are shown in appendix B.

EDS indicates that the orange material is mostly silicon and oxygen, and the black material is mostly carbon. The silicon and oxygen probably come from silicone and glass in the ablative liner; the carbon probably comes from soot released by propellant combustion.

It was suspected that the deposit's orange color may be due to iron compounds released by the corrosion of the stainless steel aft closure. However, EDS did not detect iron in the deposit, which rules out this hypothesis.

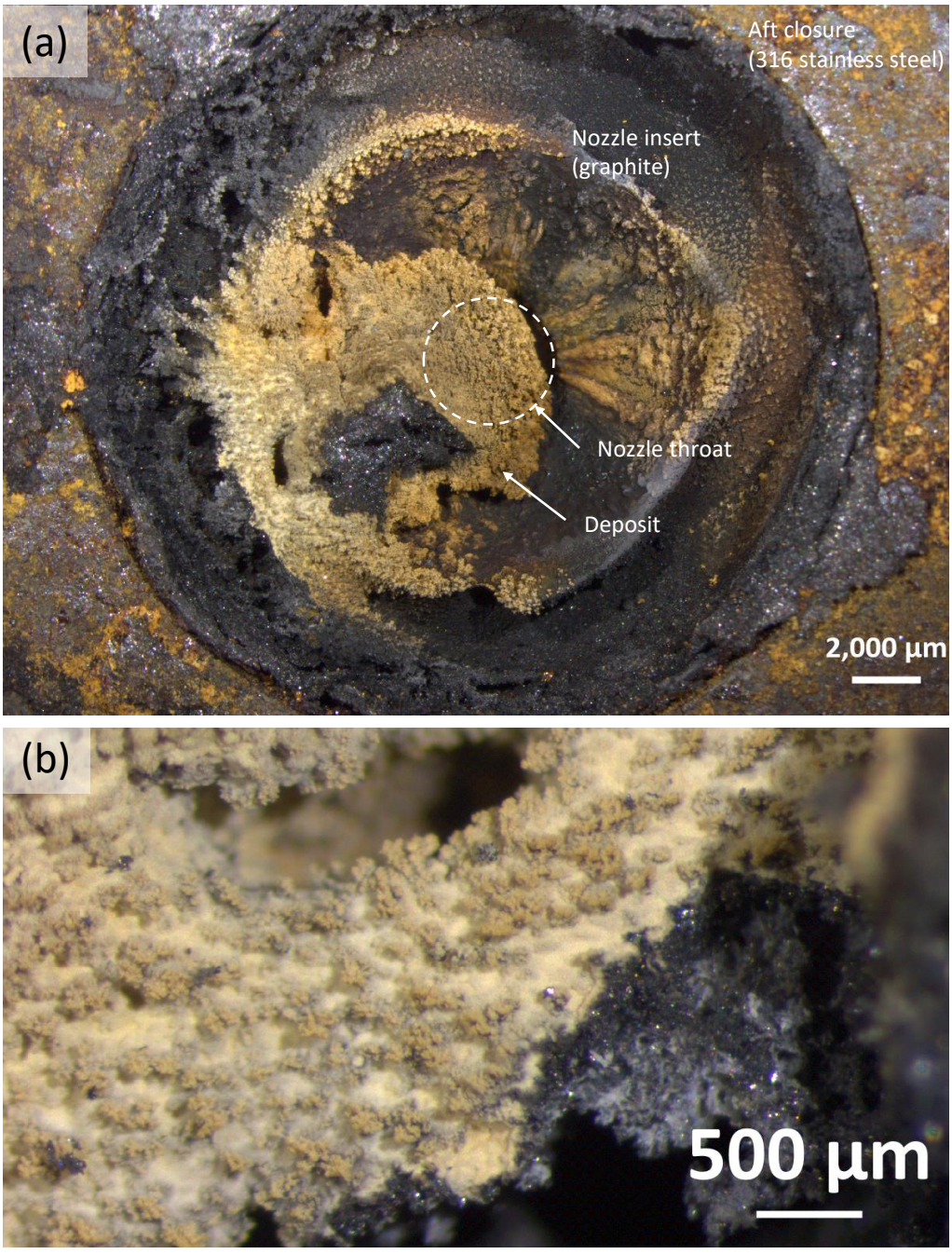

Figure 7-27: (a) After SF6, the nozzle throat was almost completely blocked by a deposit of orange material. (b) Detail of the deposit.

There is a vague correlation between vibration and nozzle clogging. The vibration levels in several motor firings are shown in fig. 7-28. An earlier static fire, SF3, is included in addition to the static fires conducted for this work (SF4, 5, 6, and 9). SF3 also had nozzle clogging. For tests with the water-cooled nozzle, firings with more vibration (SF4 and SF5) did not clog, whereas firings with less vibration (SF3 and SF6) did have nozzle clogging. There was more vibration in SF4 and SF5 because a water pump (for the smoke suppression system) was mounted near the thrust stand. In SF3 the pump was not present; in SF6 and SF9 it was located further from the thrust stand. It is plausible that vibration could shake solid material loose from the nozzle, preventing the buildup of a large deposit.

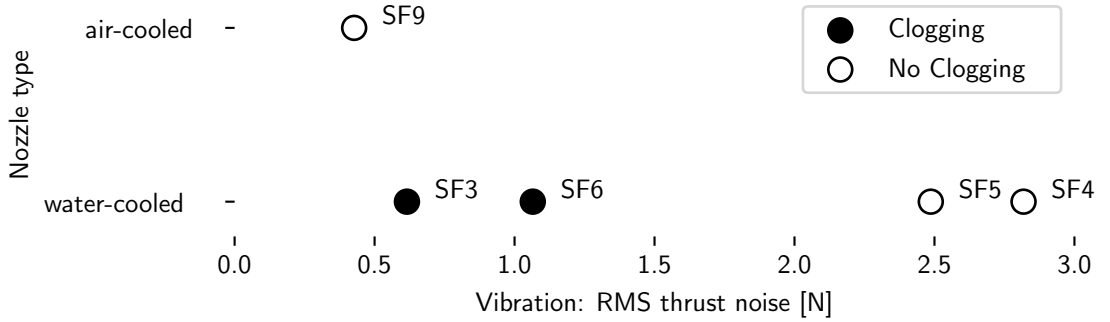

Figure 7-28: For the water-cooled nozzle, firings with more vibration were less likely to have nozzle clogging. Vibration is measured by the root-mean-square of the noise on the thrust signal during the firing.

SF9, which used an air-cooled nozzle, had low vibration and no nozzle clogging. The air-cooled nozzle has a smoother nozzle inlet than the water cooled nozzle (fig. 7-29). The inlet shape may affect the deposition of solid material. The temperature and material of the nozzle inserts are also different – these factors could affect clogging as well.

Until the causes of the issue are identified and resolved, nozzle clogging remains a major technical risk for small, low-thrust motors.

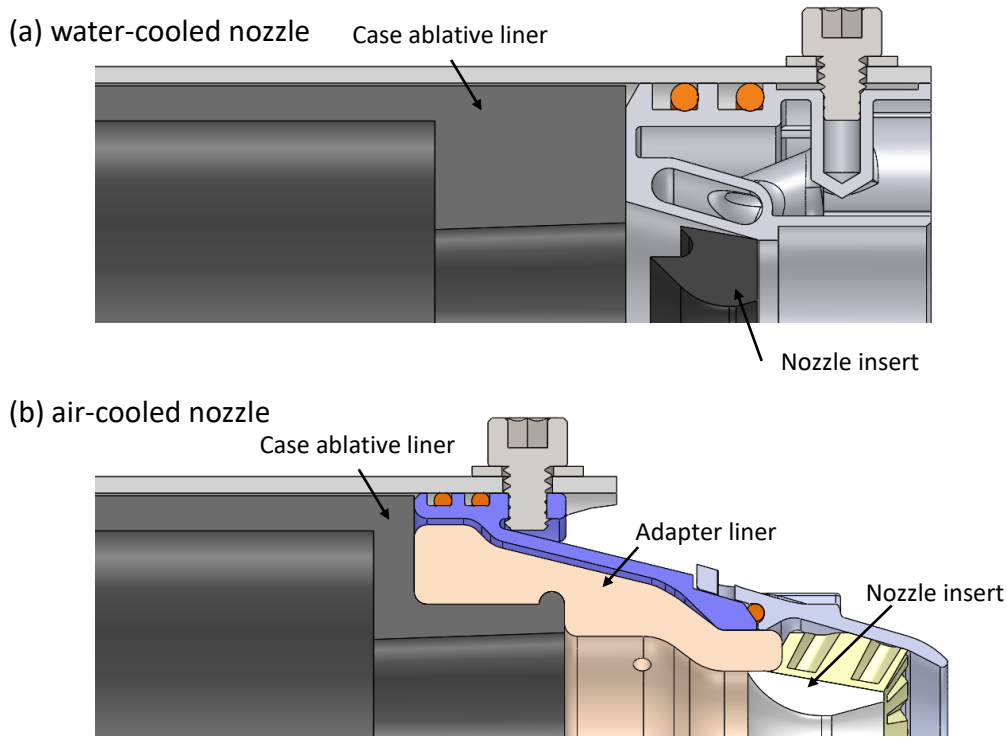

Figure 7-29: The water-cooled and air-cooled nozzles have different-shaped passages upstream of the nozzle.

7.4.7 Pressure spikes

Several temporary 'spikes' in chamber pressure were observed in the motor firings; it is believed that these are due to pieces of solid debris passing through the small nozzle throat. Figure 7-30(a) shows one of the larger-amplitude spikes, with an amplitude of 1 MPa above the earlier chamber pressure. Figure 7-30(b) shows a smaller spike of 0.09 MPa. The rise time of both spikes is about 1 s.

These pressure spikes coincide with debris being ejected from the nozzle. Figure 7-31, from SF9, shows an image of debris leaving the nozzle at the time of the pressure spike in fig. 7-30(b).

A possible explanation of these events is that a piece of solid debris, likely char from the ablative liner, temporarily blocks the nozzle. This reduces the amount of gas which can flow out through the nozzle, causing the chamber pressure to rise. The piece of debris is then ejected, suddenly re-opening the nozzle throat and returning

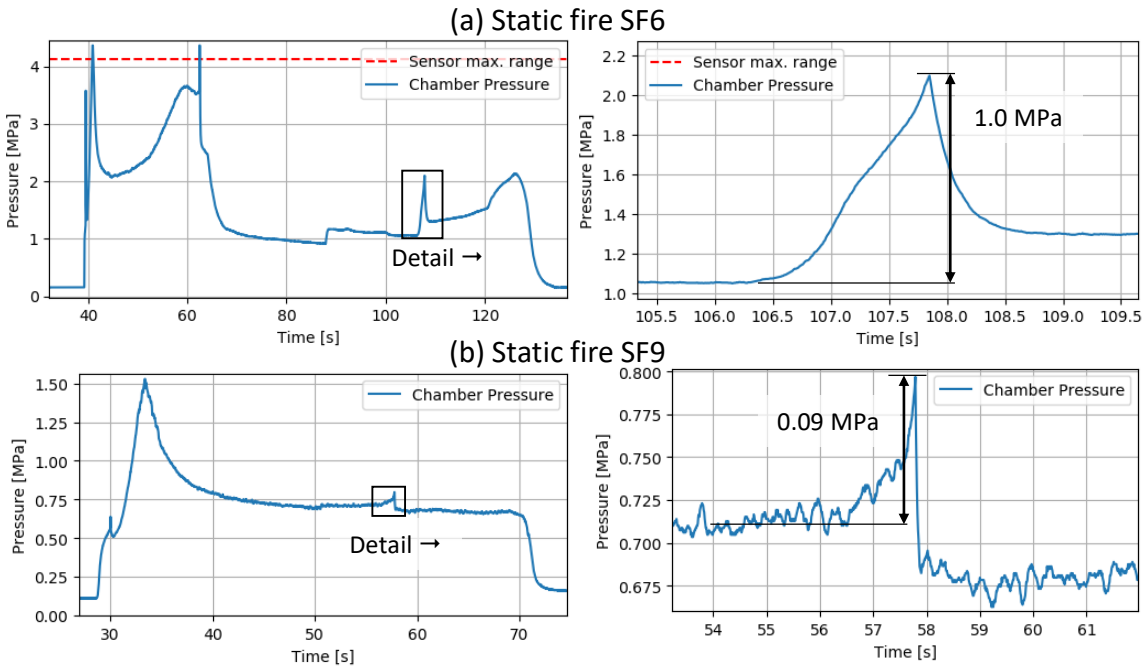

Figure 7-30: Temporary 'spikes' in the chamber pressure were observed in several static firings.

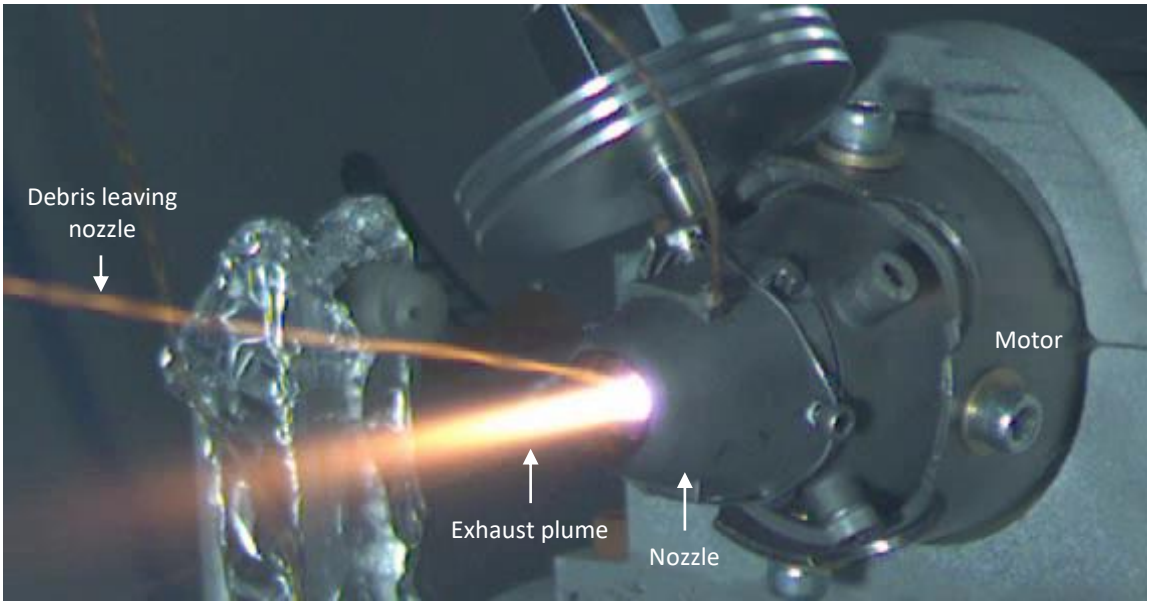

Figure 7-31: The orange streak in this image shows a piece of debris leaving the nozzle during static fire SF9. The time of this image corresponds to the time of the pressure spike in fig. 7-30(b) (about 58 s).

the chamber pressure to its normal level. The nozzle throat diameters were only ∼3 mm, so even small pieces can block most of the throat area.

An alternative explanation is that the pressure spikes are caused by flaws in the propellant grain which temporarily increase the burn area [50].

To survive these pressure spikes, the motor case must be designed to withstand higher pressures. A somewhat arbitrary suggestion is that the motor case's 'design pressure' should be 2.0 MPa above the maximum expected chamber pressure – 2.0 MPa is 2× the amplitude of the largest observed pressure spike.

As discussed in chapter 6, the baseline motor case exceeds this design pressure, even at the minimum manufacturable wall thickness.

Chapter 8

Motor case thermal protection

The motor case and other vehicle systems must be protected from the heat of propellant combustion. The end-burning grain configuration and long burn time make the thermal protection problem more difficult for small, slow-burning solid rockets than for typical small solid rockets. The end-burning grain leaves the interior of the case more exposed to combustion gases (see fig. 8-1). In an internal burning grain, the remaining propellant sits between the flame front and the motor case. The propellant insulates the majority of the case, and only small regions near the nozzle (and possibly the front) are exposed to combustion gases. In an end-burning grain, by contrast, the propellant exposes a large interior surface as it burns away.

As described in the next section, the hot combustion gas transfers a substantial heat flux (several hundred $\mathrm{kW\,m^{-2}}$) to the inner wall of the motor. The equilibrium temperature of a bare motor case would be about 1700 K, too hot for titanium or steel alloys. To reduce the heat flux into the motor case, a thermal protection layer is applied to its inner surface. The thermal protection layer is an ablative material which absorbs heat by decomposing endothermically; this is the standard design for solid rocket motors. This chapter discusses an ablative thermal protection liner for small, low-thrust rocket motors.

This ablative liner has been under development for several years. The ablative liner design was initially proposed in Vernacchia [89]. A more thorough design and

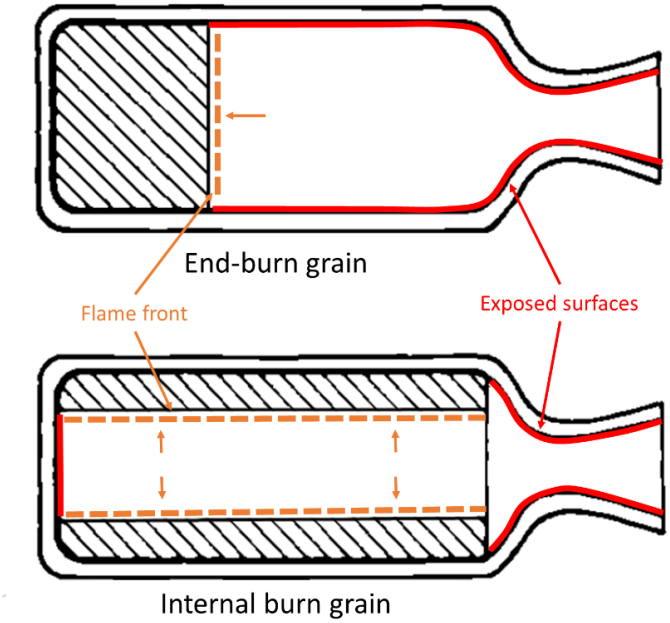

Figure 8-1: In an end burning motor, more of the motor interior is exposed to combustion gases. The exposed surfaces are highlighted in red; the flame front is shown by orange dashed lines. Adapted from [77].

simulation, along with initial motor firing tests, was presented in Spirnak [76]. Manufacturing techniques were discussed in Mathesius [50]. The additional contributions of this work are:

1. Identifying radiation, not convection, as the primary mode of heat transfer from the hot gas to the ablative liner.

2. Conducting additional experimental measurements of liner charring and heat flux to the motor case.

3. Considering the loss of energy from the combustion gas to the walls, and the resulting decrease in characteristic velocity (a measure of motor performance). The large loss of energy is a unique feature of small, low-thrust motors.

8.1 Ablative materials for thermal protection

Ablative liners are the preferred thermal protection strategy for solid rockets [77, 56]. Regenerative liquid cooling is not an option for solid rockets. Non-ablative insulators or refractory structures typically weigh and cost more than ablative solutions [56].

Ablative materials are sacrificial: they are destroyed in the process of providing thermal protection. Because they are sacrificial, ablative materials are most often applied on single-use systems; most solid rockets are single-use, as are the expected use-cases of small, transonic, deployable UAVs.

Ablative materials are typically composites, consisting of a polymer binder and a matrix (usually fibers) of glass, ceramic or carbon. As heat is applied to an ablative material, a decomposition front advances through it. The decomposition process (pyrolysis) absorbs energy and blocks heat transfer, providing thermal protection to structures behind the ablative. The decomposition process is illustrated in fig. 8-2. The ablation rate (the speed at which the decomposition front progresses) determines the endurance of an ablative liner, and depends on the fluid- and thermo-dynamics of the heat transfer process. Generally, the ablation rate is higher if the heating flow is hotter, denser, and faster [64].

Two important processes occur when an ablative material decomposes under high heat flux: gasification and charring. These processes reduce the rate of heat transfer into the ablative material, allowing it to have a usefully slow ablation rate. At some depth beneath the surface of the material, there is the pyrolysis zone, where the virgin material has reached a high enough temperature to undergo chemical and physical reactions at a significant rate (fig. 8-2). Here, the more volatile components of the material (e.g. the polymeric binder) gasify and the more refractory components (e.g. the fibers and binder residue) form a solid char. In most ablatives, the net decomposition reaction is endothermic; much of the incoming heat flux is carried away in the chemical potential of the gaseous and char products [56]. The char layer insulates the virgin material behind it from direct exposure to the heating flow. The

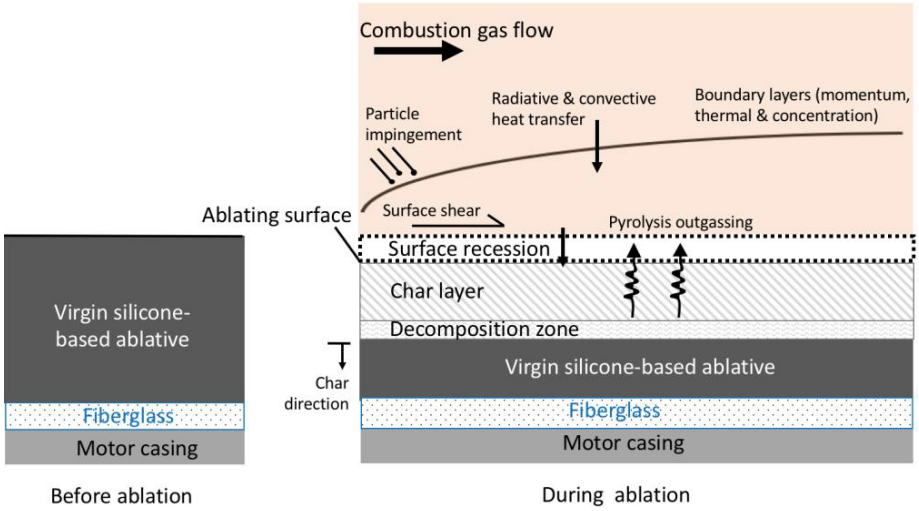

Figure 8-2: As an ablative composite is exposed to high heat flux, its surface gasifies and chars, processes which block heat flow deeper into the material. This protects the remaining virgin ablative and the structure behind it. Reprinted from Spirnak [76].

gaseous products diffuse out through the porous char to the surface, where they mix with the heating flow. This injection effect thickens the thermal boundary layer of the heating flow and reduces heat transfer to the surface [64] [1]. Additionally, a layer of molten glass can form at the surface if the requisite species (e.g. Si and O) are present in the char.

8.2 Thermal protection used in this work

The Ti Candle research motor was used to test an ablative liner under typical conditions for small, long-burn motors. The thermal protection in Ti Candle consists of an ablative liner and fiberglass insulation which surround the propellant grain. The design is illustrated in fig. 8-3. The ablative liner is made from Dowsil 93-104, a silicone-matrix ablative material. The case is made from grade 2 titanium. The purpose of the ablative liner is to absorb heat through its decomposition. The purpose

[1] Because the primary mode of heat transfer to the inside of our motor case is radiation, not convection, the injection effect is less important. As discussed in section 8.3.1.2, the boundary layer of cool gas is thin enough to be mostly transparent to infrared radiation.

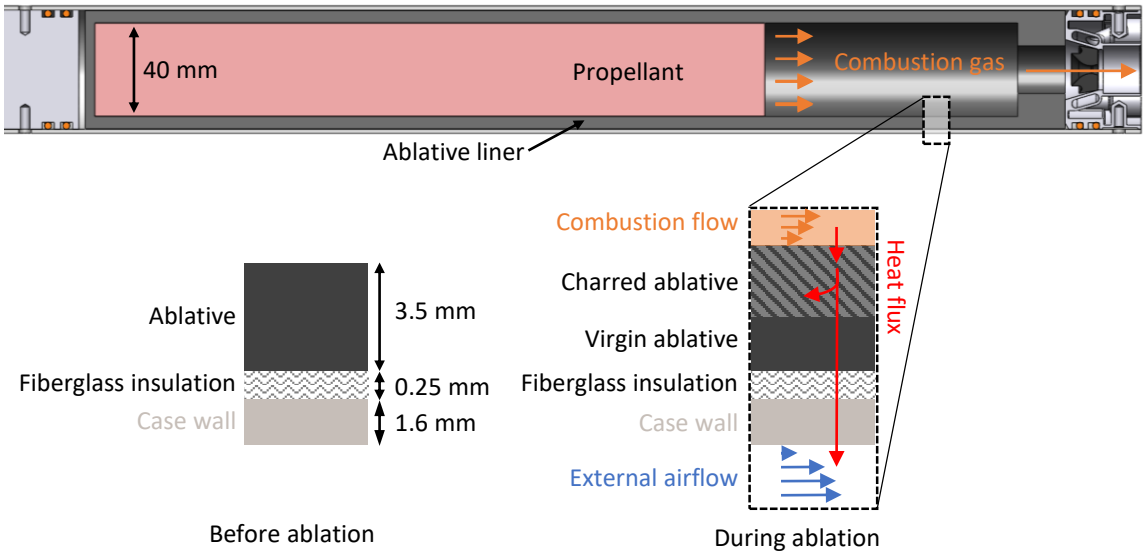

Figure 8-3: The thermal protection system tested in Ti Candle consists of an ablative liner backed by fiberglass insulation. The ablative undergoes pyrolysis reactions, which absorb heat and form a protective char.

of the fiberglass insulation is the reduce the heat flux through the ablative into the case; the fiberglass has 0.14 times the thermal conductivity of the (virgin) ablative material. The properties of the materials are listed in table 8.1. The Ti Candle motor was designed by Jon Spirnak; further details are available in his master's thesis [76]. The procedures for producing the propellant and ablative liner are discussed in Mathesius [50].

The ablative material Dowsil 93-104 (formerly Dow-Corning 93-104) consists of glass, ceramic and carbon fibers in a silicone rubber matrix. It has been used extensively in solid-propellant rocket-ramjet combustion chambers [12] and in a few liquid-propellant rockets [56]. The rationale for selecting this material is described in [76]. The ablation of this material has been extensively characterized; Resch [71] provides more details on the ablation reactions and properties of the virgin material and its char.

Material	k [$\mathrm{W\,m^{-1}\,K^{-1}}$]	ρ [$\mathrm{kg\,m^{-3}}$]	c [$\mathrm{J\,kg^{-1}\,K^{-1}}$]
Ablative (charred)	1.1	1153	1510
Ablative (virgin)	0.35	1470	1260
Fiberglass insulation	0.05	—	—
Case (Ti grade 2)	16.4	4510	523

Table 8.1: Properties of the thermal protection materials used in this work. Ablative material data are from [71, 20]. Thermal properties of the ablative vary with temperature; typical values are used here. Resch [71] gives values at various temperatures. Fiberglass insulation thermal conductivity is from Vernacchia [89]. Titanium data are from [82].

8.3 Models of heat transfer to the motor case

There are three important heat transfer phenomena in the motor case: 1) heat transfer from the hot gas to the inner wall of the ablative liner, which is discussed and modeled in section 8.3.1, 2) heat transfer through the ablative and fiberglass insulation into the motor case (section 8.3.2), and 3) the hot gas cooling due to heat loss to the inner wall (section 8.3.3). These phenomena are discussed and modeled below.

8.3.1 Heat flux to the inner wall

Heat is transfered from the hot gas to the inner wall (ablative liner) by both convection and radiation.

8.3.1.1 Convective heat flux to the inner wall

In most rocket motors, convection is the largest mode of heat transfer from the hot gas to the walls [77, 31]. Convective heat transfer is modeled by the convection coefficient, h:

$$q_{conv} = h(T_{aw} - T_w) \tag{8.1}$$

where q_{conv} is the convective heat flux to the wall, T_{aw} is the adiabatic wall temperature, and T_w is the actual wall temperature. For the low-speed flows considered here, T_{aw} equals the bulk temperature of the hot gas.

h can be estimated with empirical correlations for flow in tubes. Different correlations are used for laminar or turbulent flows, so it must be determined whether the flow in the combustion chamber will be turbulent. The Reynolds number for typical conditions in Ti Candle (with $\dot{m} = 4.8\,\mathrm{g\,s^{-1}}$) is:

$$\begin{aligned} Re_D &= \frac{\bar{v}\rho D}{\mu} \\ &= \frac{(2.9\,\mathrm{m\,s^{-1}})(1.3\,\mathrm{kg\,m^{-3}})(40\,\mathrm{mm})}{(6.67\times10^{-5}\,\mathrm{kg\,m^{-1}\,s^{-1}})} \\ &= 2260 \end{aligned} \tag{8.2}$$

Flow in a smooth tube transitions from laminar to turbulent at Re_D of 2300 to 2900. However, the charred liner walls are quite rough (millimeter-scale roughness, see fig. 8-12) so the flow will be become turbulent at lower Re_D than in a smooth tube. Thus, the flow in the combustion chamber will be assumed to be turbulent.

The Colburn correlation for convection in turbulent pipe flow is [31]:

$$\frac{h}{\rho c_p \bar{v}} = St = 0.023 Re_D^{-0.2} Pr^{-0.67} \tag{8.3}$$

where St is the Stanton number and Pr is the Prandtl number. For typical conditions in Ti Candle, $h \approx 49\,\mathrm{W\,m^{-2}\,K^{-1}}$.

Note that the convection coefficient increases with the mass flux though the chamber:

$$h \sim (\rho\bar{v})^{0.8} \tag{8.4}$$

This is the main dependence of h on operating conditions. The other parameters in eq. (8.3) (Pr, μ, c_p) do not vary much with chamber pressure or oxamide content of the propellant.

8.3.1.2 Radiative heat flux to the inner wall

The combustion gas may transfer a substantial amount of heat to the wall via radiation. Given that the hot gas temperature is about 2000 K, the radiation will mostly come from 1) soot and 2) gas molecules with emission bands at relevant energies (i.e. H_2O, CO_2, HCl, and CO). Soot is expected to be the dominant source [33, 10].

Radiative heat transfer with participating media (e.g. a gas which absorbs and emits radiation) is a complex subject. An overview of the topic, with a focus on engineering applications, is presented in Howell [33] (chapters 1, 2, 5 and 9.4 are particularly helpful).

This analysis neglects scattering, as scattering is negligible for soot particles [33, 10].

Rudimentary model of heat transfer between a gas and an enclosure Consider a volume of isothermal gas and the boundary surface enclosing that volume. The average heat flux from the gas incident on the bounding surface is approximately [equation 5-58 in [33]]:

$$q_i = \int_0^\infty [1 - \exp(-a_\lambda L_e)]\, e_b(\lambda, T_g)\, d\lambda \tag{8.5}$$

where:

- λ is wavelength
- a_λ is the spectral absorption coefficient of the gas at wavelength λ, which depends on the gas pressure, temperature, and composition (and to some extent on path length through the gas). a_λ is higher at higher densities of gas molecules or soot particles.
- L_e is the mean beam length through the gas, which depends on the size and shape of the volume. The mean beam length approximation is discussed in chapter 5.5 of Howell [33]. For a long cylinder, L_e is 0.95 times the diameter.

- $e_b(\lambda, T_g)$ is the blackbody spectral emissive power at wavelength λ and gas temperature T_g. It is given by Plank's law.

Equation (8.5) can be re-written as:

$$q_i = \epsilon_g \sigma T_g^4 \tag{8.6}$$

where σ is the Stefan-Boltzmann constant and ϵ_g is the gas total emittance. ϵ_g is defined as:

$$\epsilon_g \equiv \frac{\int_0^\infty \left[1 - \exp(-a_\lambda L_e)\right] e_b(\lambda, T_g)\, d\lambda}{\sigma T_g^4} \in [0, 1] \tag{8.7}$$

For some gas species (e.g. H_2O or CO_2), ϵ_g has been tabulated, usually as a function of (partial pressure times L_e) and temperature (see section 5.6.1 of Howell [33]). ϵ_g can also be computed for soot clouds, in which case it depends on volumetric concentration of soot (see section 9.4.3 of Howell [33]). The estimation of ϵ_g for gas mixtures is more complicated due to spectral overlap between the absorption bands of gases in the mixture. Some mixtures of H_2O and CO_2 have been tabulated. A technique for computing ϵ_g for arbitrary mixtures of soot, H_2O and CO_2 is presented in Cassol et al. [10].

If an isothermal gas volume is surrounded by a black wall at temperature T_w, the net average heat flux to the wall is (equation 5-63 in [33]):

$$q_w = \sigma \left[\epsilon_g T_g^4 - \alpha_g(T_w) T_w^4\right] \tag{8.8}$$

where $\alpha_g(T_w)$ is the absorptance of the gas for radiation emitted from the wall [2]. This equation will be used to estimate the radiative heat transfer to the inner walls of the motor case.

The combustion gas in the rocket motor contains a substantial amount of soot

[2] According to Kirchoff's law, the directional spectral absorptance and emittance of a gas volume are equal, $\alpha'_\lambda = \epsilon'_\lambda$. However, it is not guaranteed that the *total* absorptance and emittance (α_g and ϵ_g) will be equal.

(about 2% by mass). In sooty combustion gases, the soot's emission and absorption is much more significant than that of the gas molecules [33]. Thus, this analysis only considers the radiation due to soot; it ignores the (complicated) emission and absorption of gas molecules.

Estimating the emittance of a soot cloud This section describes equations for estimating the emittance of a cloud of radiating (black) soot particles suspended in a non-radiating gas. It is assumed that all the soot particles are at the same temperature as the gas, T_g. To make the math tractable, it is assumed that the temperature is uniform throughout the entire soot cloud. The emittance of the soot cloud depends mainly on the soot concentration and the optical path length through the cloud.

The spectral absorption of soot can be modeled as (equation 5 from [10], equation 9-18 from [33]):

$$a_{\lambda,soot} = C_{soot} k_1 \lambda^{-1} \tag{8.9}$$

where C_{soot} is the volumetric concentration of soot[3] and k_1 is a dimensionless constant, which is between 4 and 8 depending on the kind of soot (assume $k_1 = 6$). For example, at $\lambda = 1.45\,\mu\text{m}$ (peak emission wavelength for 2000 K blackbody) and $C_{soot} = 10^{-5}$ (see note [4]), $a_{\lambda,soot} = 41.4\,\text{m}^{-1}$.

Optical thickness, the product of a_λ and path length S, determines how opaque the gas is to radiation. For the length scale of the entire combustion gas, e.g. a cylinder with 65 mm diameter, the sooty gas will be optically thick:

$$a_{\lambda,soot} S \approx (41.4\,\text{m}^{-1})(65\,\text{mm}) = 2.69 \tag{8.10}$$

[3] C_{soot} is the volume occupied by soot particles within a unit volume of the soot and gas cloud. It is dimensionless.

[4] This is a crude estimate, assuming a gas density of $1\,\text{kg}\,\text{m}^{-3}$, as soot particle density of about $1770\,\text{kg}\,\text{m}^{-3}$, and that the combustion gas is 2% soot by mass. For comparison, Cassol et al. [10] suggest $C_{soot} = 10^{-7} - 10^{-5}$ as a typical range of soot concentration for methane flames. The propellant flame contains more soot than a clean-burning methane flame.

(the gas is considered optically thin if $a_\lambda S \ll 1$). For the boundary layer of cooler gas, with a thickness of $S \approx 2$–$4\,\mathrm{mm}$, the optical thickness of the sooty gas would be about 0.083 to 0.17. The transmittance through the boundary layer ($\exp(-a_\lambda S)$) would be 0.92 to 0.84; thus the cool boundary layer will not significantly block radiation from the hot core of the gas from reaching the walls. Of course, these numbers will be different if the assumed value of C_{soot} is wrong.

The ϵ_g of an isothermal soot cloud can be evaluated by integrating eq. (8.7) with eq. (8.9) substituted for a_λ:

$$\epsilon_g = \frac{\int_0^\infty \left[1 - \exp(-k_1 C_{soot} L_e \lambda^{-1})\right] e_b(\lambda, T_g)\, d\lambda}{\sigma T_g^4} \tag{8.11}$$

The results of a similar integration are shown in figure 9-10 of [33] and fig. 8-4. For $T_g = 2000\,\mathrm{K}, C_{soot} = 10^{-5}, L_e = 0.95 \cdot 65\,\mathrm{mm}$, the emittance is 0.792.

The radiation heat flux predicted by eq. (8.8) and eq. (8.11) is shown in fig. 8-5. The equations are evaluated for several soot concentrations (broken orange curves), as the exact C_{soot} is not known. The maximum possible radiative heat flux (at $\epsilon_g \to 1$) is shown as a solid orange curve. For comparison, the convective heat flux from section 8.3.1.1 is shown in blue. Both heat fluxes depend on the wall temperature; it is assumed that the temperature of the charred ablative surface might be about 1200 K.[5] The radiative heat flux to a 1200 K wall is expected to be 500–800 $\mathrm{kW\,m^{-2}}$, whereas the convective heat flux is only 20–40 $\mathrm{kW\,m^{-2}}$. Thus, radiative transfer will be the primary mode of heat transfer to the inner walls of the motor case.

[5]The exact value of the wall temperature will depend on the history of heat flux to the wall and the details of the ablation process.

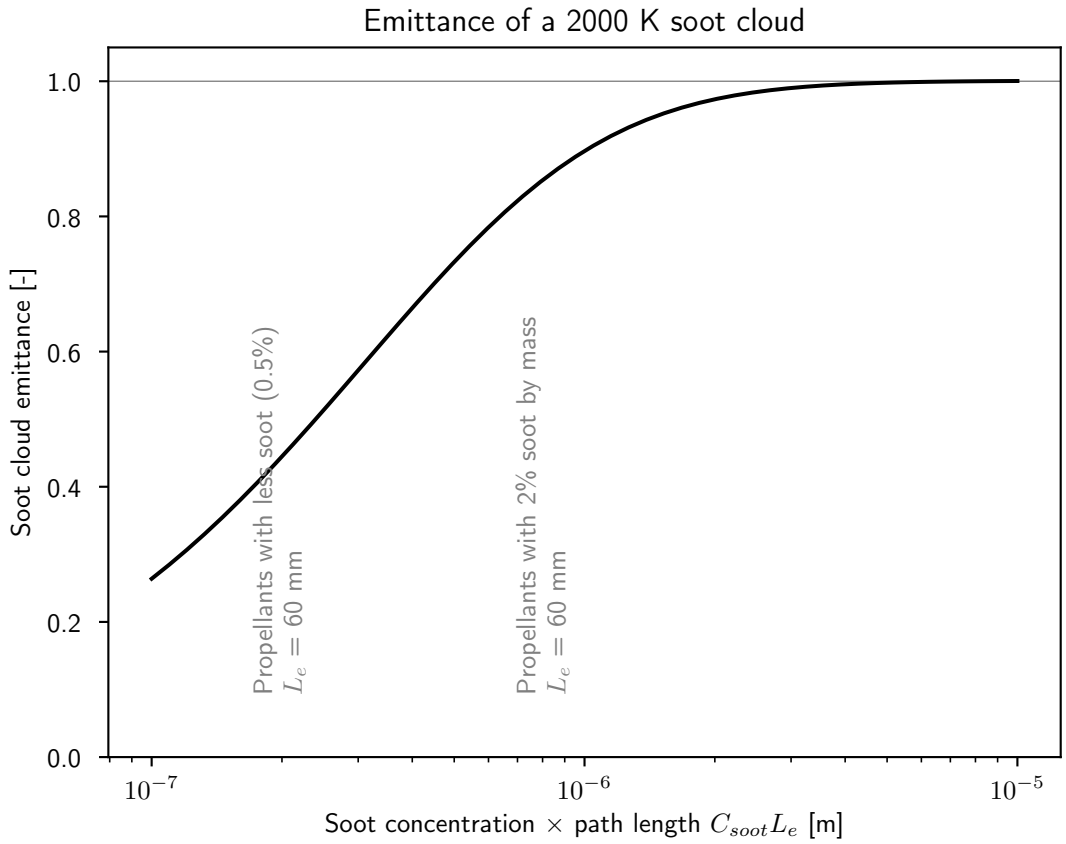

Figure 8-4: The emittance of a soot cloud increases to 1 as the soot concentration and path length increase. The propellants used in this work produced exhaust with 2% soot by mass. A less sooty propellant would reduce the emittance and transfer less heat to the walls.

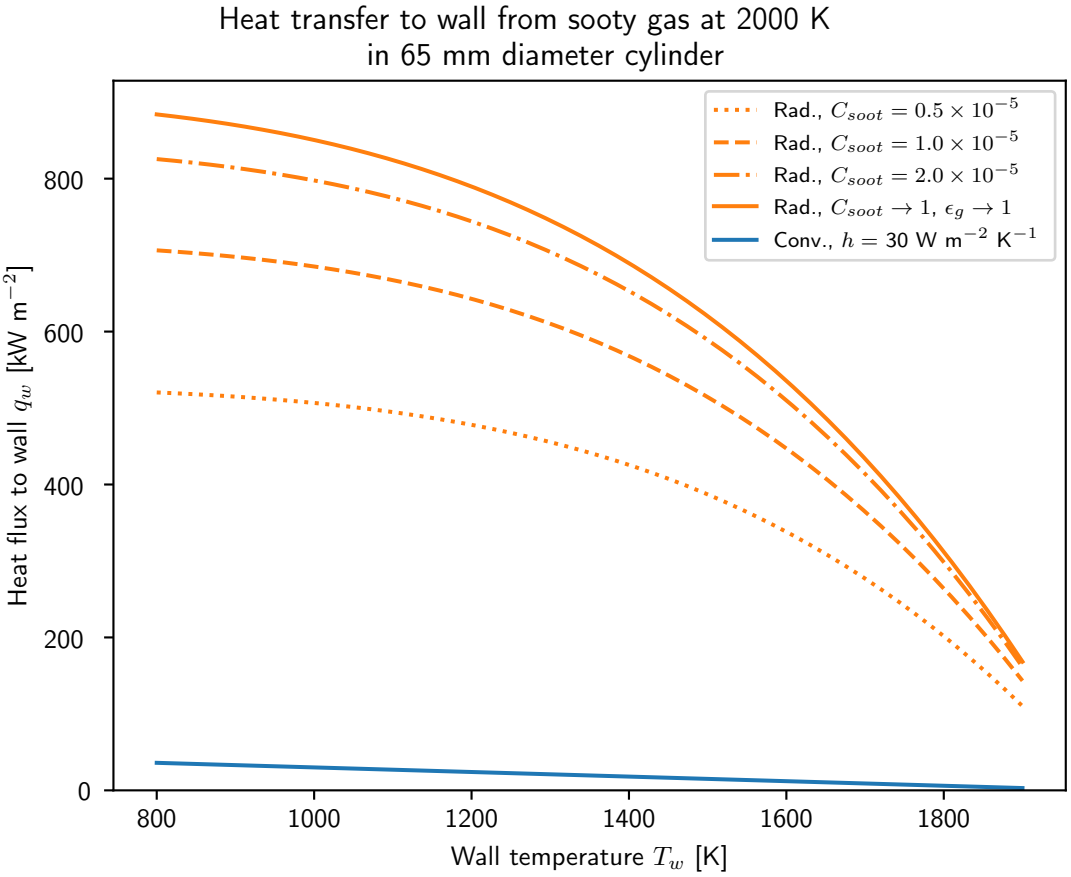

Figure 8-5: Across a range of wall temperatures and soot concentrations, radiation (orange curves) will transfer much more heat to the walls than convection (blue curve). There is more radiation heat transfer if the soot concentration C_{soot} is higher.

8.3.1.3 Effect of gas conditions on heat flux

The radiation and convection heat transfer modes have different dependencies on the gas conditions.

Effect of soot mass fraction Radiative heat transfer depends strongly on the volumetric soot concentration C_{soot}, whereas the convective heat transfer does not. C_{soot} depends on the gas conditions and on the soot mass fraction w_{soot}:

$$C_{soot} = w_{soot}\frac{\rho_{mix}}{\rho_{soot}} \tag{8.12}$$

where ρ_{mix} is the density of the soot-gas mixture and $\rho_{soot} \approx 1770\,\mathrm{kg\,m^{-3}}$ is the density of the soot particles [63]. The mixture density is:

$$\rho_{mix} = \left(w_{soot}\rho_{soot}^{-1} + (1 - w_{soot})\rho_{gas}^{-1}\right)^{-1} \tag{8.13}$$

For $w_{soot} \ll 1$ and $\rho_{gas} \ll \rho_{soot}$, combining these equations gives:

$$C_{soot} \approx \frac{w_{soot}}{1 - w_{soot}}\frac{\rho_{gas}}{\rho_{soot}} \approx w_{soot}\frac{\rho_{gas}}{\rho_{soot}} \tag{8.14}$$

Note that the volumetric soot concentration increases with pressure (if the soot mass fraction is constant):

$$C_{soot} \sim \rho_{gas} \sim p \tag{8.15}$$

As shown in eq. (8.11), the soot cloud emittance increases with the product of soot concentration and path length, $C_{soot}L_e$. At high values of $C_{soot}L_e$, the emittance asymptotes to 1. This effect is illustrated in fig. 8-4. In these motors, the combustion chamber $C_{soot}L_e$ is expected to be on the order of $1 \times 10^{-6}\,\mathrm{m}$. For $C_{soot}L_e > 1.5 \times 10^{-6}\,\mathrm{m}$, ϵ_g is > 0.95 and further increases in $C_{soot}L_e$ have little effect on radiative heat transfer.

The propellants used in this work contained 2% carbon powder by mass as an

opacifier. Measurements indicate that the soot mass fraction of the combustion gas w_{soot} is also about 2% (see section 5.6). With $\rho_{gas} = 1\,\mathrm{kg\,m^{-3}}$ and $L_e = 60\,\mathrm{mm}$, the soot cloud emittance is expected to be about 0.8. It is probably possible to reduce the soot concentration by roughly 1/4 by using less opacifier. This would halve the emittance to about 0.4.

Effect of tube diameter Radiation is the dominant heat transfer mode in the combustion chamber, whereas convection is dominant at the nozzle throat. This occurs because radiation and convection have opposite dependencies on the diameter of the gas flow passage.

To illustrate these effects, fig. 8-6 plots heat flux versus diameter for a circular flow passage with the diameter D decreasing along its length, e.g. the chamber and converging section of the nozzle. The mass flow is constant through the passage.

For turbulent flow, the convection coefficient scales like $h \sim D^{-1.8}$ [31]. As D narrows, the flow accelerates, increasing the convective heat transfer to the wall.

For radiative heat transfer, the flow velocity is not important, but the diameter determines the mean beam length through the gas ($L_e = 0.95D$ for a cylinder). The emittance increases with path length (but asymptotes to 1) as shown in fig. 8-4. At small D, the typical optical path through the gas is short, the gas is more transparent, and the emittance is low [6]. At larger D, the radiative heat transfer is higher, although this effect saturates as the emittance approaches 1.

Thus, convection is more significant at smaller diameters (i.e. the nozzle) and radiation is more significant at larger diameters (i.e. the combustion chamber).

[6] Another effect is that the gas density drops as the flow accelerates. Lowering the gas density lowers the soot volume fraction C_{soot}, which reduces the emittance.

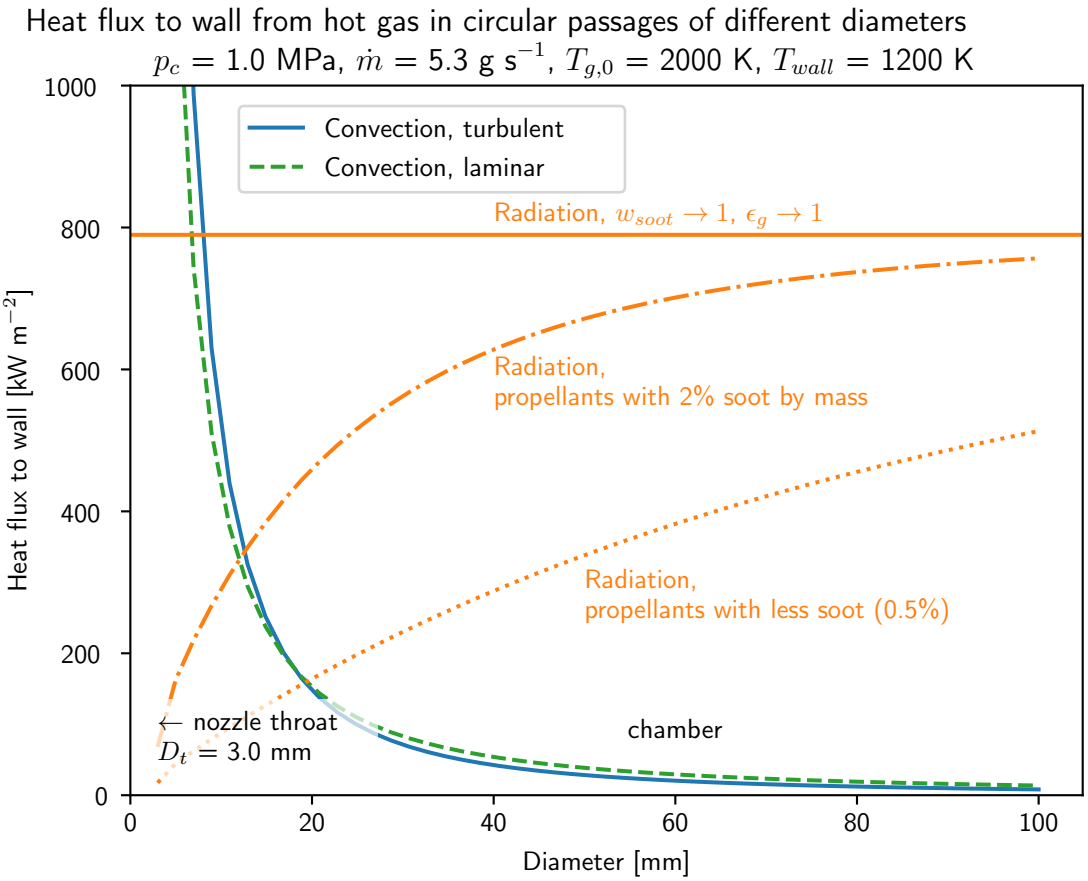

Figure 8-6: At smaller diameters (e.g. nozzle throat), convection is the dominant heat transfer mode. At larger diameters (e.g. combustion chamber) radiation is the dominant heat transfer mode. There is more radiation heat transfer if the propellant is sootier.

Effect of chamber pressure and mass flux Radiation and convection also have different dependencies on chamber pressure, as shown in fig. 8-7. Consider a motor with a fixed chamber diameter and throat diameter operating at different chamber pressures. Convective heat transfer increases with chamber pressure, as the hot gas mass flux is higher. For turbulent flow, the scaling is $h \sim p_c^{0.8}$ [31].

For radiative heat transfer, higher p_c results in higher heat flux (as the gas is more emissive), but the effect of p_c on heat flux saturates once the emittance approaches 1. Higher p_c makes the gas denser, which increases the soot volume fraction at a given soot mass fraction (see section 8.3.1.3). The emittance will saturate to 1 at a lower

pressure if w_{soot} or D are larger. The foregoing discussion (and fig. 8-7) assume w_{soot} is independent of p_c; however, pressure probably affects the soot formation during combustion.

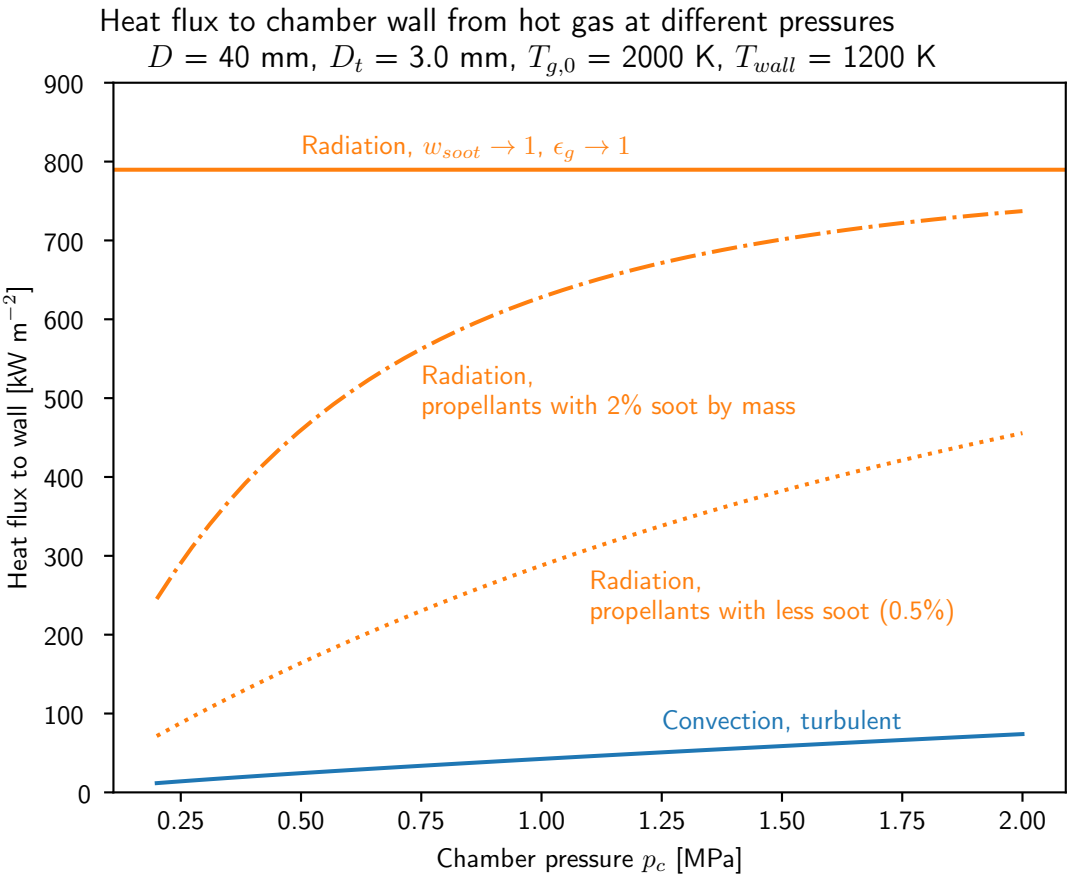

Figure 8-7: In the combustion chamber (diameter = 40 mm), the dominant heat transfer mode is radiation. Both radiative and convective heat transfer increase with pressure, but for different reasons.

8.3.2 Heat flux through the thermal protection layers

This section will attempt to model the flow of heat through the ablative, insulation and motor case. This problem is very complex, so only some approximate arguments will be provided.

The governing equations for heat flow in a solid material are the conservation of

energy (per unit volume):

$$\frac{\partial(\rho h)}{\partial t} = -\nabla \vec{q} \tag{8.16}$$

and the law of heat conduction:

$$\vec{q} = -k\nabla T \tag{8.17}$$

where ρ is density, h is specific enthalpy, $\vec{q}$ is heat flux, k is thermal conductivity and T is temperature.

In simple problems, these equations can be combined to give the well-known heat equation:

$$\rho c_p \frac{\partial T}{\partial t} = \nabla \cdot (k\nabla T) \tag{8.18}$$

An ablating material is more complicated because:

1. The enthalpy h includes chemical reactions, not just sensible heat.

2. The density ρ changes due to chemical reactions.

3. Pyrolysis gas convects heat through the char.

The governing equation for an ablating material is [7]:

$$\underbrace{\rho c_p \frac{\partial T}{\partial t}}_{\text{sensible heat}} = \underbrace{\nabla \cdot (k\nabla T)}_{\text{conduction}} \quad \underbrace{-(h_g - \bar{h})\frac{\partial \rho}{\partial t}}_{\text{pyrolysis energy consumption}} \quad \underbrace{+(\rho_g \vec{v_g}) \cdot \nabla h_g}_{\text{pyrolysis gas convection}} \tag{8.19}$$

where ρ is the solid density; $\bar{h}$ is the partial heat of charring (defined in [15], Equation 4); $h_g, \rho_g, \vec{v_g}$ are the pyrolysis gas enthalpy, density and velocity within the porous char.

[7] This equation is derived in one dimension in Moyer and Rindal [52], and the 2 or 3d equation is given in Chen and Milos [14]. Both these sources include extra terms to account for a moving coordinate system, which is used for numerical reasons. These terms have been omitted here.

The pyrolysis rate ($\frac{\partial \rho}{\partial t}$) is modeled by a few Arrhenius-type reaction rate models [52, 15]. The reaction rate depends on the remaining concentration of resin/filler and on the temperature. The pyrolysis only occurs within a narrow zone [see fig. 8-2]. Inwards of this zone the material is fully charred, so the reaction rates are negligible due to a low concentration of reactants. Outwards of this zone, in the virgin material, the pyrolysis rates are negligible because the temperature is too low. Pyrolysis begins once the virgin material is heated to a sufficient temperature; for Dowsil 93-104 this is about $T_{pyrol} = 720\,\mathrm{K}$ [71].

Outwards of the pyrolysis zone (in the virgin material, insulation, and case) eq. (8.19) simplifies to the ordinary heat equation (eq. (8.18)).

This ablation model is usually solved numerically, due to its complexity. Two notable simulation programs are Aerotherm Corporation's *CMA* [52] and NASA Ames' *FIAT* [15]. Given appropriate boundary conditions and material properties, these programs can solve for the temperature profile and char depth vs. time.

In the following discussion, the problem is simplified to one dimension, radially through the wall. Also, curvature effects in cylindrical coordinates are ignored, which is valid if the wall is thin compared to its radius.

Without resorting to black-box solvers, we can make a few approximate arguments:

1. The heat flux out of the pyrolysis zone (into the virgin material) must be less than the heat flux into the pyrolysis zone. This provides energy for the endothermic pyrolysis reactions.

2. The outside of the pyrolysis zone will always be at about the same temperature, T_{pyrol}.

3. If the pyrolysis zone were stationary and the case temperature were constant, then the steady state solution to the 1d heat equation could be applied to the virgin ablative, insulation and case. In the steady-state solution, heat flux is constant with location.

4. While the pyrolysis zone is moving and the case temperature is increasing, the virgin material will be warming at all locations. The energy to warm the material must come from a heat flux imbalance. Thus the heat flux must decrease through the the virgin material, and the heat flux into the case will be less than the steady-state solution.

Figure 8-8 illustrates the actual temperature and heat flux profiles (solid red curves) and the limiting steady-state introduced in item 3 (dashed red curves). The steady-state heat flux is:

$$q_{into\,case,ss} = \left(\frac{l_{virg}}{k_{virg}} + \frac{l_{insul}}{k_{insul}} \right)^{-1} (T_{pyrol} - T_{case}) \tag{8.20}$$

where l_{virg} is the remaining thickness of virgin material (which decreases with time).

From these arguments, we can make a few conclusions relevant to thermal protection system design. So long as the ablative does not char through:

1. The case temperature will not exceed T_{pyrol} during the burn. At T_{pyrol} for Dowsil 93-104 (720 K), the case material (Ti-6Al-4V) is still useful.

2. $q_{into\,case,ss}$ is an upper limit on the heat flux into the case during the burn.

3. The temperature T_{case} at which $q_{into\,case,ss}(T_{case}) = q_{rad\,out}(T_{case}) + q_{conv\,out}(T_{case})$ is an upper limit on the actual case temperature during the burn.

4. The fiberglass insulation significantly reduces $q_{into\,case,ss}$, despite being very thin. With $l_{virg} = 1.5\,\text{mm}$ and $l_{insul} = 0.25\,\text{mm}$, the insulation provides more thermal resistance than the remaining virgin ablative.

The actual temperature and heat flux is only expected to approach steady state after a long exposure time, if at all. The time to reach steady state will be on the order of the thermal diffusion timescale:

$$t_{diffuse} \approx \frac{l_{liner,init}^2}{\alpha_{virg}} \tag{8.21}$$

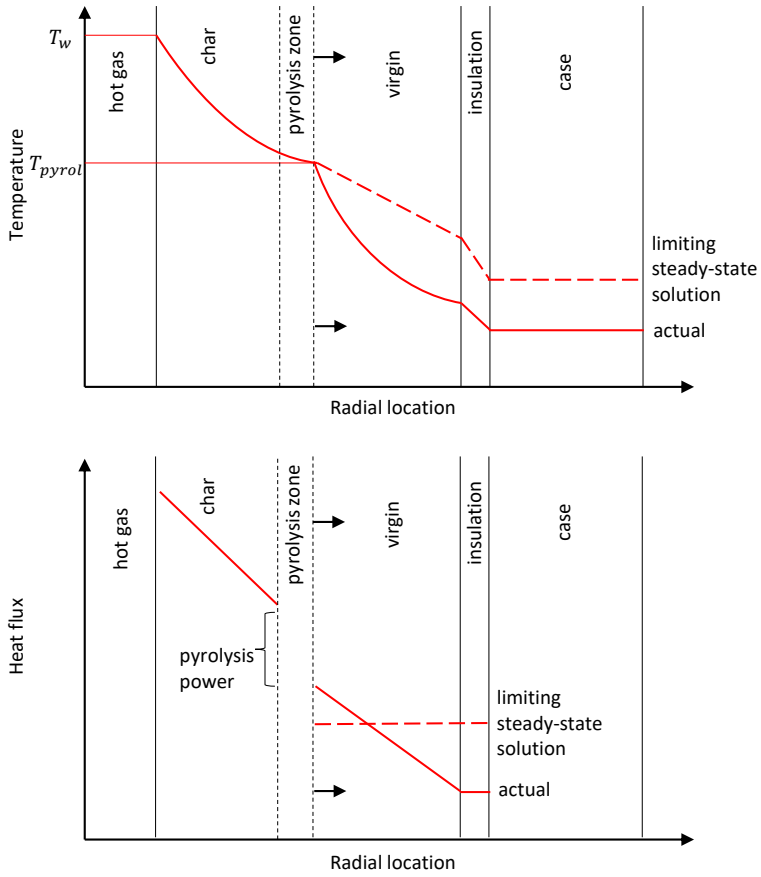

Figure 8-8: A notional cartoon of the temperature and heat flux profiles through the thermal protection layers. The pyrolysis zone advances through the liner, and has an almost constant temperature (T_{pyrol}).

For the 3.5 mm liner thickness used in Ti Candle, this is:

$$t_{diffuse} \approx \frac{(3.5\,\mathrm{mm})^2}{(1.88 \times 10^{-7}\,\mathrm{m^2\,s^{-1}})} = 65\,\mathrm{s} \tag{8.22}$$

This time scale is almost as long as the burn duration for SF6, 90.3 s. Thus, it is expected that only the aft end of the case (where the liner was heated for the longest time) would approach the steady state.

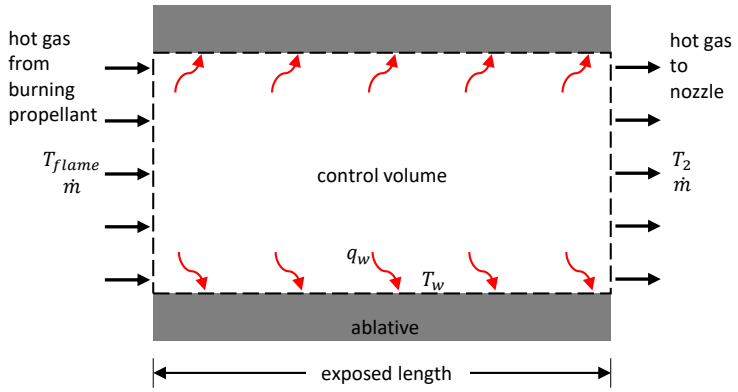

Figure 8-9: Control volume for a simple model of energy loss from the hot gas.

8.3.3 Hot gas energy loss

The combustion gas loses a substantial amount of heat to the case walls via radiation. Heat loss to the walls cools the combustion gas before it reaches the nozzle. This decreases the motor's c^* and I_{sp}, as both are proportional to the square root of temperature at the nozzle inlet.

Also, cooling of the hot gas reduces the radiative heat flux to the walls, which scales with the gas temperature to the fourth power. With the gas at 2000 K, the heat flux would be 500 kW m^{-2}; when cooling is taken into account, the expected average heat flux is closer to 250 kW m^{-2}.

This section presents a simple model for the cooling of the hot gas by radiation to the walls of the chamber. Consider as a control volume the cylindrical space within the motor between the burning surface of the propellant and the nozzle inlet (fig. 8-9). Combustion gas enters this volume at the propellant flame temperature T_{flame}, with a mass flow rate $\dot{m}$. It exits this volume (into the nozzle) at a lower temperature T_2. The char surface surrounding this volume is assumed to be at a uniform temperature T_w, and receives a heat flux q_w.

The conservation of energy equation for this control volume is:

$$\dot{m} c_p (T_{flame} - T_2) = q_w A_w \tag{8.23}$$

where c_p is the heat capacity of the gas and A_w is the wall area.

The heat flux q_w is crudely estimated by treating the gas as an isothermal radiator at a average temperature between T_{flame} and T_2:

$$T_{avg} = \frac{T_{flame} - T_2}{2} \tag{8.24}$$

The heat flux from an isothermal gas to the surrounding walls is given by eq. (8.8):

$$q_w = \sigma \left[\epsilon_g(T_{avg}) T_{avg}^4 - \alpha_g(T_w) T_w^4 \right] \tag{8.25}$$

Example results of this model are presented in fig. 8-10. As the exposed wall area A_w increases, more heat is lost and the gas T_2 becomes cooler. This lowers the average temperature of the gas, so q_w decreases with increasing A_w (although the thermal power $q_w A_w$ increases). The model assumes that q_w is uniform over the entire wall. In reality, q_w would be higher near the flame where the gas is hotter, and less near the nozzle, where the gas has cooled. The model assumed a uniform (in space) and constant (w.r.t. time or exposed area) wall temperature. T_w is shown as a black dashed line in fig. 8-10. In reality, the char surface would likely be cooler where and when there is less heat flux into the surface.

The cooling of the hot gas is significant. Just before burnout, the combustion gas cools by 650 K before reaching the nozzle inlet. This reduces the instantaneous c^* efficiency to 0.81. This severe heat loss is an unusual feature of small, long-burn motors. Because the motor has an end-burning propellant grain, heat radiated from the hot gas is mostly lost to the walls. With a typical core-burning grain, thermal radiation from the hot gas mostly warms the propellant surface; most of the heat is returned to the gas when the propellant burns. Because the motor is long, small diameter, and operates at low thrust, the ratio $A_w/\dot{m}$ is large. Equation (8.23) shows that $A_w/\dot{m}$ is proportional to the drop in hot gas temperature.

Hot gas cooling also affects the nozzle thermal design. The reduction of the hot gas temperature at the nozzle inlet reduces the heat flux to the nozzle's inner surface.

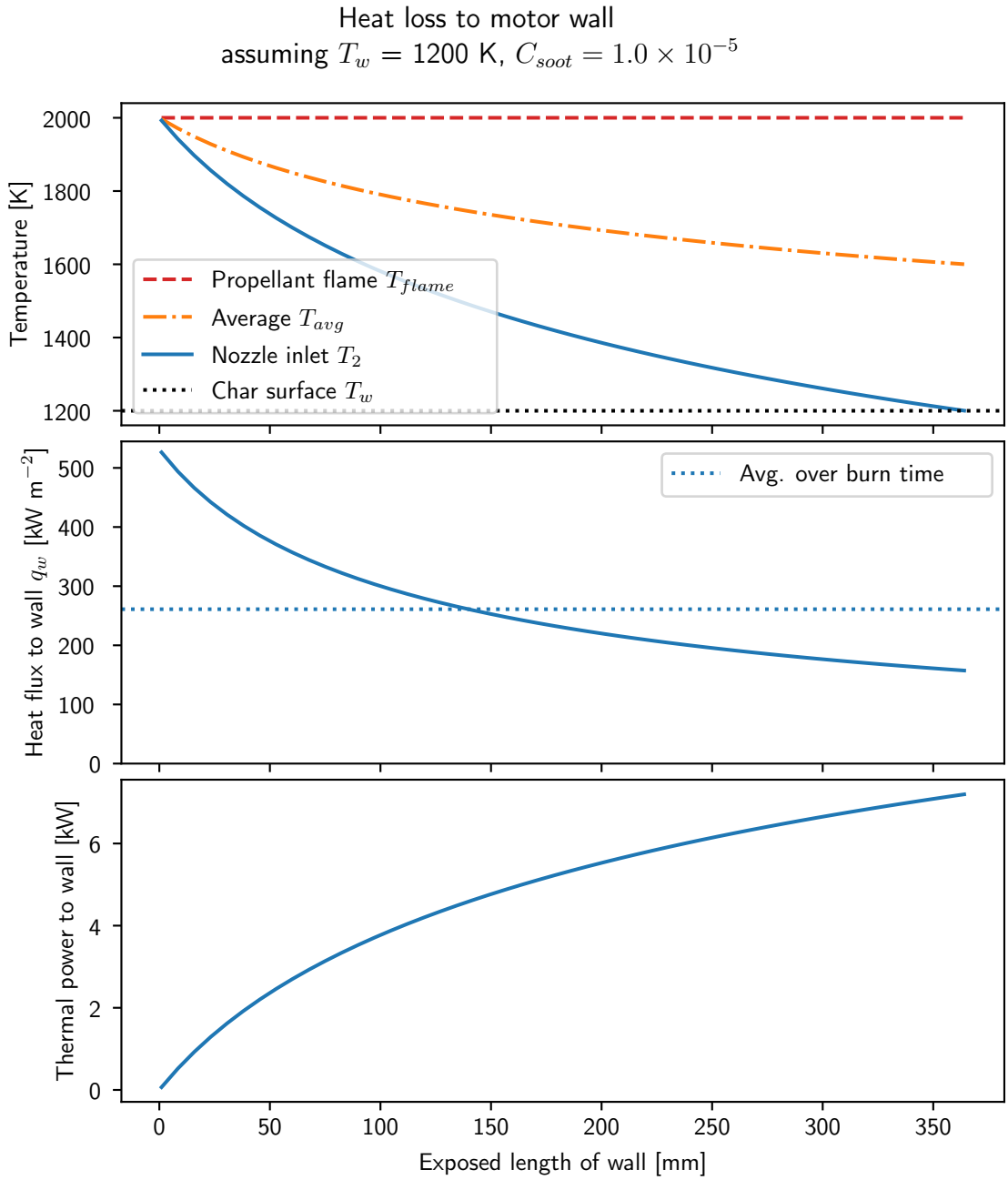

Figure 8-10: A model of heat loss from the combustion gas to the walls suggests that the combustion gas will be cooled significantly.

This model neglects the mixing of gaseous pyrolysis products with the combustion gas. In SF6, about 22 g of pyrolysis gas was released [8], 3% of the propellant

[8] This value was estimated from the volume of charred ablative, assuming that the pyrolysis products are 21% gas by mass, as indicated by the densities reported in Resch [71].

mass. Mixing in this small amount of gas has a much smaller impact on the hot gas temperature than the radiation losses described above.

8.4 Ablation and char depth in the research motor

The char penetration depth determines the required initial thickness of the ablative liner. The char penetration depth was characterized experimentally in a research motor [9]. An empirical approach is chosen as the char depth is difficult to predict from first principles.

8.4.1 Char depth measurements

After static firings of the motor, the char depth was measured by cutting the liner in half and photographing the section. The liner charring is shown in fig. 8-11. Figure 8-11(a) shows the original shape of the ablative liner (gray) in the Ti Candle test motor. The propellant grain burns from aft (right) to front (left). As the combustion gas flows from the burning surface (left) to the nozzle inlet (right) it transfers some of its heat to the inner surface of the liner. Figure 8-11(b) is a photograph of a fired liner, which was cut in half to reveal the char layer. One section through the liner wall is boxed in red. The boxed region of the image is shown in fig. 8-11(c), stretched in the vertical direction to make the features easier to see. There are two distinct regions of char: a black layer on top and a white layer beneath it. The remaining virgin (un-charred) liner material is gray.

The end-burning propellant grain burned from right to left in these figures, so the right side was exposed to hot gas for longer. At the right side of fig. 8-11(c), the char has penetrated deeper into the liner, and less virgin material remains. The char penetration depth increases with increasing exposure time. The char layer extends beyond the original surface of the liner (marked by a red dashed horizontal line in

[9] Our group's test motor and char depth measurement techniques were developed by Jon Spirnak for his Master's thesis research [76]

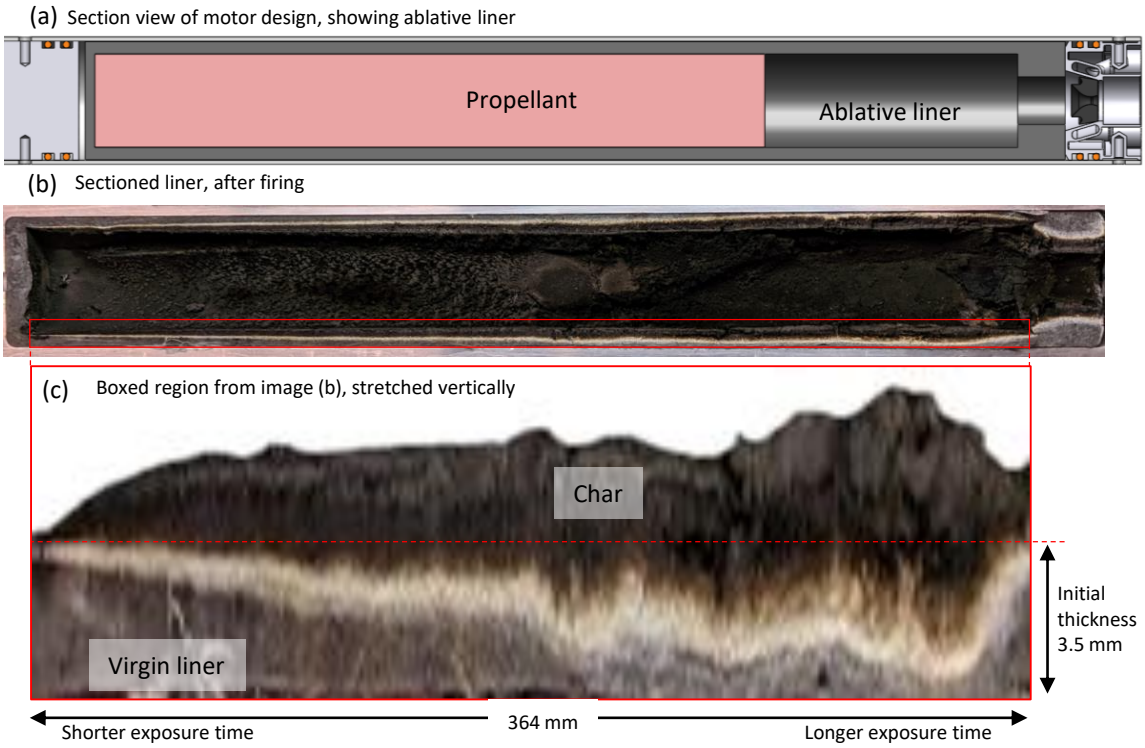

Figure 8-11: The ablative liner is charred by exposure to hot gas. The char has penetrated deeper where the exposure time is longer. Char also builds up beyond the initial thickness of the liner.

fig. 8-11(c)). This is partially due to the liner material swelling as it chars, and partially due to soot deposited on the liner from the combustion gas. In typical ablative applications the hot gas is flowing quickly and shears away char from the surface. However, in the slow-burn rocket motor, the hot gas speed is only about $3\,\mathrm{m\,s^{-1}}$, so the shear forces on the char are minor, and a thick layer can form.

The char is shown in more detail in fig. 8-12. The char consists of three distinct layers. On top is a layer of fluffy black char. The author supposes that this comes from soot deposited onto the liner from the combustion gas. Below is a layer of dense black char. This material probably originated in the liner, and is the solid product of the pyrolysis reaction. The dense black char extends beyond the original surface of the liner because the material expands slightly when it chars. Below the black layer is a layer of white char, separated form the black char by a yellowish transition

layer. The two different colors of char probably correspond to two different reactions which occur at different temperatures - the lower-temperature reaction first turning the material white, and the higher-temperature reaction then turning it black. Below the white char layer is the gray virgin ablative material. In the remainder of this work, the 'char penetration depth' or 'char depth' will refer to the distance from the original surface of the liner to the interface of the white and virgin layers, as illustrated on the left side of fig. 8-12.

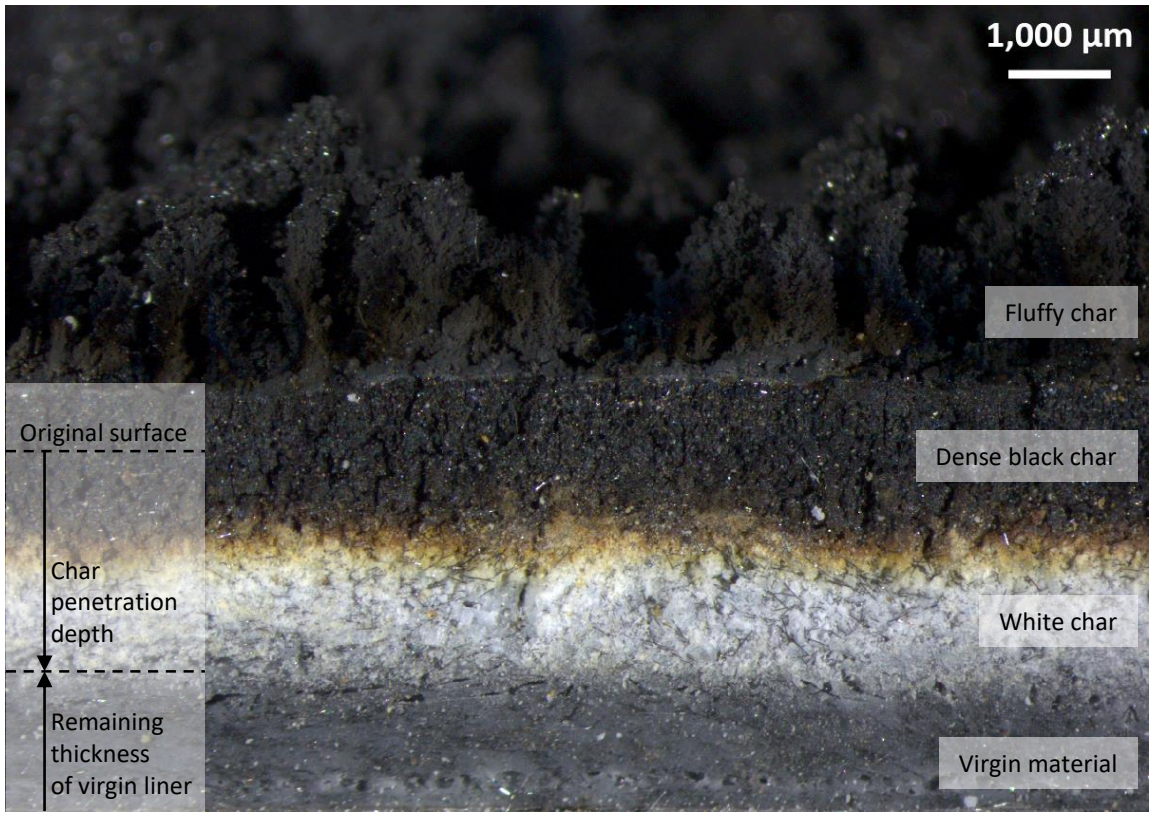

Figure 8-12: A microscope image of the charred liner shows three distinct layers of char: fluffy black char, dense black char, and white char.

Char depth measurements for four static firings are shown in fig. 8-13. These firings used propellant with 10% or 13% oxamide, and had chamber pressures of 0.5–1.0 MPa. [10] For two of the firings (SF4 and SF9), two sets of depth measurements

[10]For SF6, which used a multi-segment propellant grain, only data from the forward segment are included in figs. 8-13 to 8-15. The aft portion of the liner was exposed to combustion gases from both grain segments, so its char depth is more difficult to interpret.

were taken, one from each side of the cut through the liner. The data show that the char depth increases *sub-linearly* with exposure time. Once the surface has charred somewhat, the char provides insulation between the ablation reaction zone and the hot gas. This reduces the heat flux to the reaction zone and slows the reaction. Thus, the char penetration rate slows as the char layer becomes thicker.

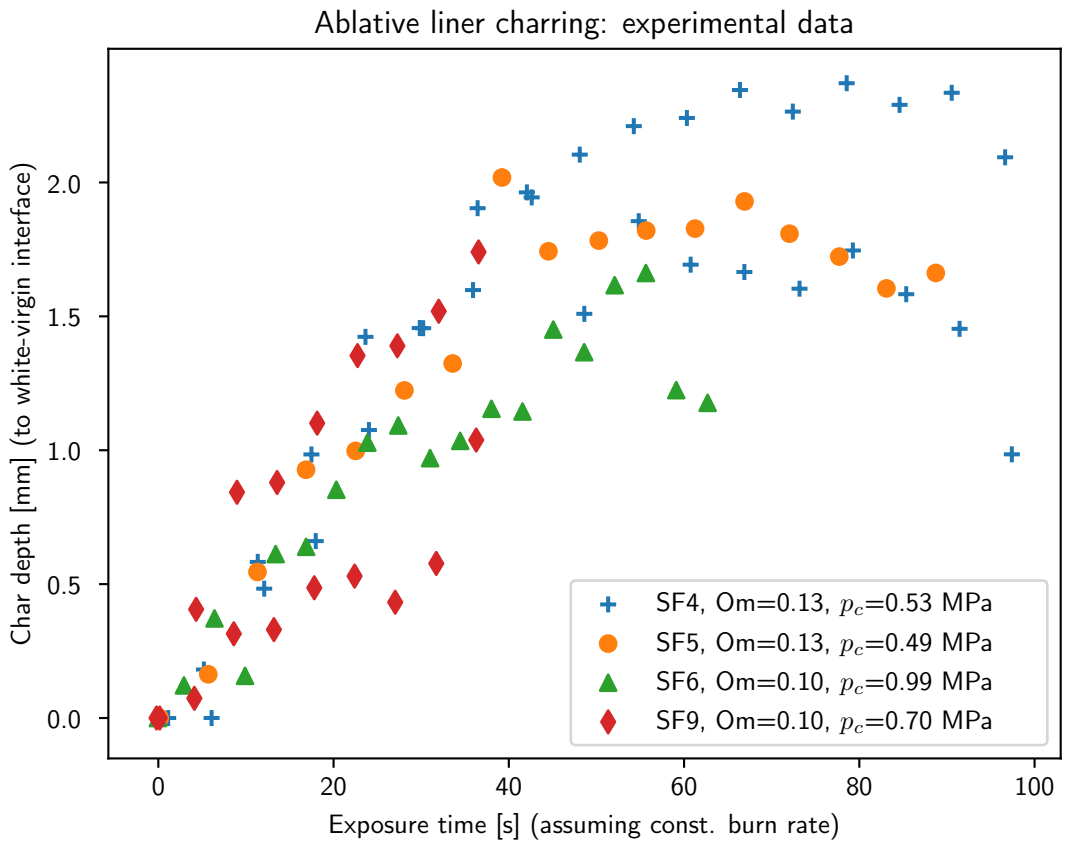

Figure 8-13: Char depth measurements from four static firings show that char depth generally increases with exposure time, but there is much scatter in the trend. SF6 used a two-segment propellant grain; only char data from the forward segment (seg. 2) are included.

8.4.2 Char depth fits

Theoretically, the char penetration depth should be proportional to $t^{1/2}$ [44], if the hot gas temperature is constant. A power-law fit[11] to the char data is shown in fig. 8-14; the time exponent of the fit is 0.533. As will be discussed later, the hot gas temperature probably varies significantly. It is interesting that the time exponent is nonetheless near 1/2.

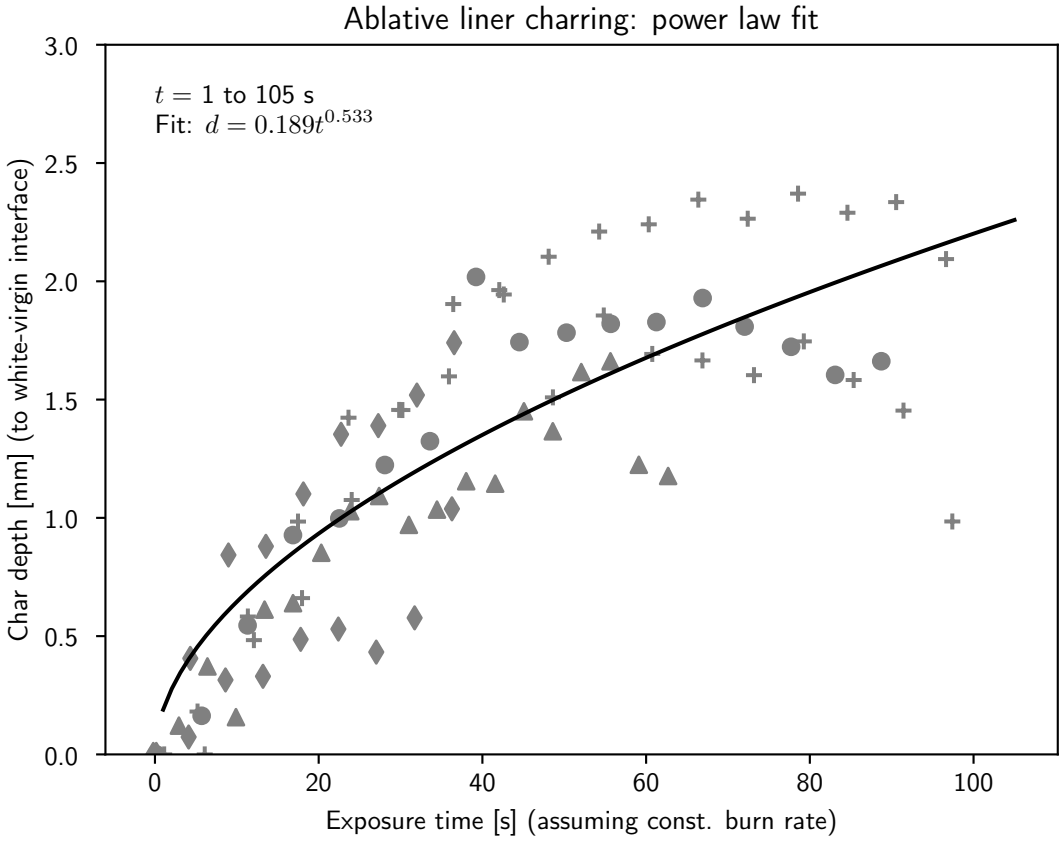

Figure 8-14: A power law fit to the char depth data agrees with a simple physics model which suggests that $d \sim t^{1/2}$.

A piecewise linear upper bound on the char depth is shown in fig. 8-15. This may be useful for designing a tapered liner for future motors which are similar to Ti Candle and use propellants with $\geq 10\%$ oxamide. It is recommended to add an

[11] by the least-squares method, using the python package `lmfit`

extra 1 mm to these depths for margin against burn through. This information is not useful for motors which are significantly different from these Ti Candle firings in chamber pressure, diameter, and mass flow rate, or which use different propellants. For example, the aft segment of SF6 used a hotter-burning propellant grain with no oxamide and operated at a higher p_c (2.1 MPa); it had greater char penetration depths than those shown here (3.1 mm after 80 s).

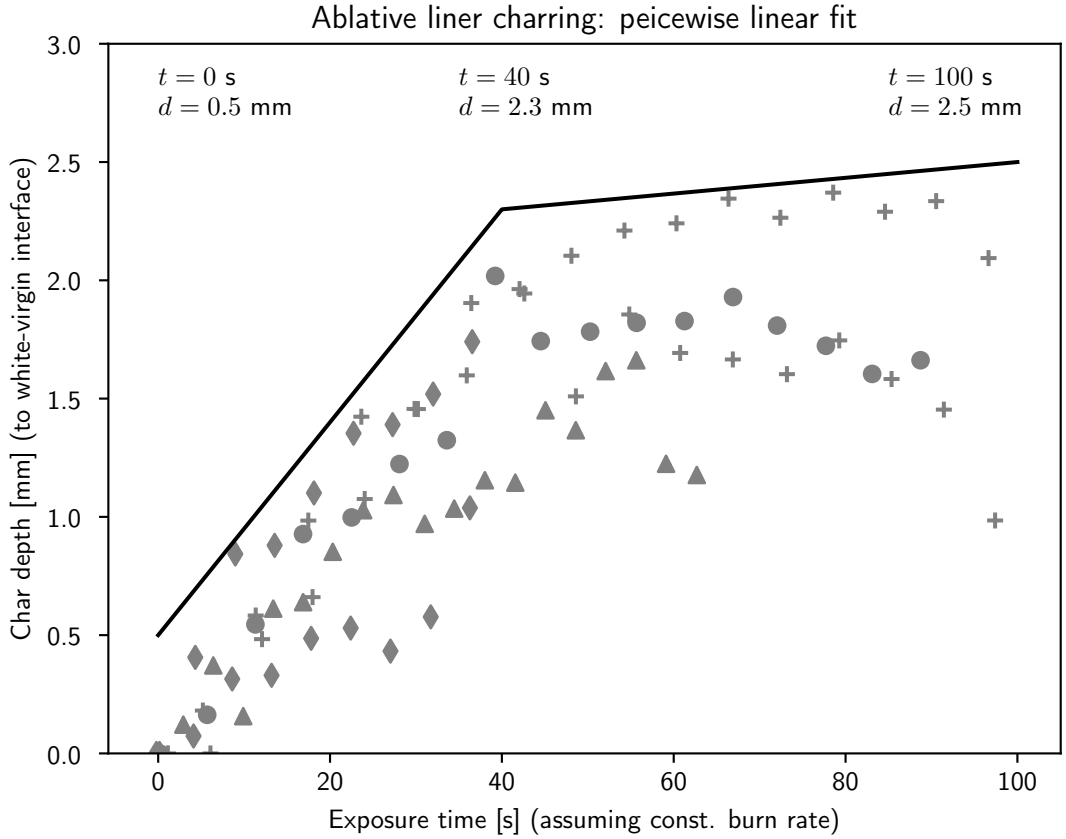

Figure 8-15: A piecewise linear upper bound on the char depth may be useful for designing the thickness of future ablative liners.

No clear trend of char depth vs. pressure is discernible in the data in fig. 8-13. This is consistent with fig. 8-7, which shows that radiative heat transfer to the wall has a weak dependence on pressure for a fairly sooty gas. The range of chamber pressures in this data set is fairly small (only 0.5–1.0 MPa) and there is a large

amount of variance in the char depth data.

8.4.3 Alterations in char structure due to inhibitor layer

In static fires SF4, SF5 and SF6 the liner was bonded directly to the propellant [12]. In SF9, an inhibitor layer was added between the propellant and the liner. The inhibitor consists of HTPB, oxamide and carbon powder. Its purpose is to prevent the outer surface of the propellant from burning, even if the ablative liner peels off of that surface [13].

It appears that adding the inhibitor changed the structure of the char. In SF4, SF5 and SF6 the 'fluffy' char layer was attached to the layer of dense char beneath it. In SF9 the fluffy char was separated from the dense char by a small gap (see fig. 8-16).

It is supposed that in SF9, a charred remnant of the inhibitor layer remained on top of the ablative liner. This layer separated from the ablative liner beneath it (perhaps due to their different coefficients of thermal expansion). Soot from the combustion gas deposited onto this separated layer, forming the fluffy char.

The separated char layer may be more fragile and susceptible to breaking away from the wall.

[12]The propellant-liner bonding technique used in these experiments is described in Mathesius [50].

[13]The HTPB-based inhibitor forms a stronger bond with the propellant than the silicone-based ablative material.

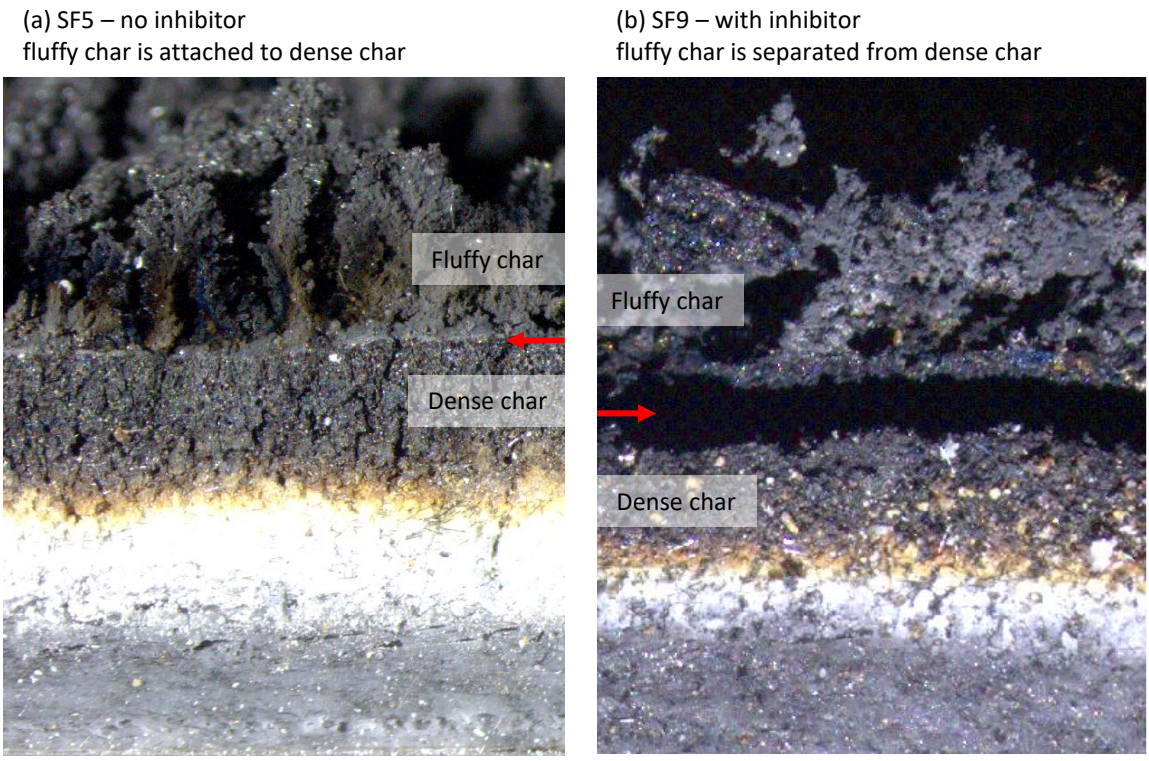

Figure 8-16: (a) Without an inhibitor layer, the fluffy char was attached to the dense char. (b) With an an inhibitor layer, a gap (red arrow) formed between the fluffy and dense char.

8.4.4 Effects of acceleration and vibration on char

If the motor is accelerating or vibrating in flight, there may be greater loads on the char than in the static tests described above. This could cause some char (particularly the fluffy char) to fall off of the wall. This would increase the heat flux to the ablative material beneath, increasing the rate of char penetration. Thus, a liner thickness which does not burn through in static tests may burn through in flight. Also, this the char that falls of the wall may pass through the nozzle, causing pressure spikes (see section 7.4.7). The author believes that this possibility can only be assessed by flight tests of the motor.

8.4.5 Liner buckling

In static fires SF6 and SF9, a region of the liner buckled inwards [see fig. 8-17]. The buckled region from SF6 is shown from the inside of the liner in fig. 8-17(a) and from the outside in (b). Notice that the virgin material tore open at the buckling site. The buckled region from SF9 is shown from the inside in (c) and from the outside in (d). The virgin material did not tear at the buckling site. In SF6, buckling occurred at the aft end, where the most charring had occurred. In SF9, buckling occurred at the front end, where the least charring had occurred. The liners in SF4 and SF5 did not buckle. The cause of buckling is not known.

Liner buckling could be avoided by bonding the liner to the inside of the motor case. However, this would require removing the fiberglass insulation which sits between the liner and the case. Operating without the fiberglass insulation would increase the heat flux to the motor case. However, the case temperature should still remain below T_{pyrol} so long as the liner does not burn through (see section 8.3.2). This may be acceptable for this ablative liner and the baseline motor case: for this ablative, $T_{pyrol} \approx 720\,\mathrm{K}$, which is within the acceptable temperature range for the baseline motor case's titanium alloy.

Bonding the liner to the case would also apply stresses to the liner during storage due to the different thermal expansion coefficients of the liner and the case. Considerations for case bonded liners are discussed further in Sutton and Biblarz [77], chapter 12.

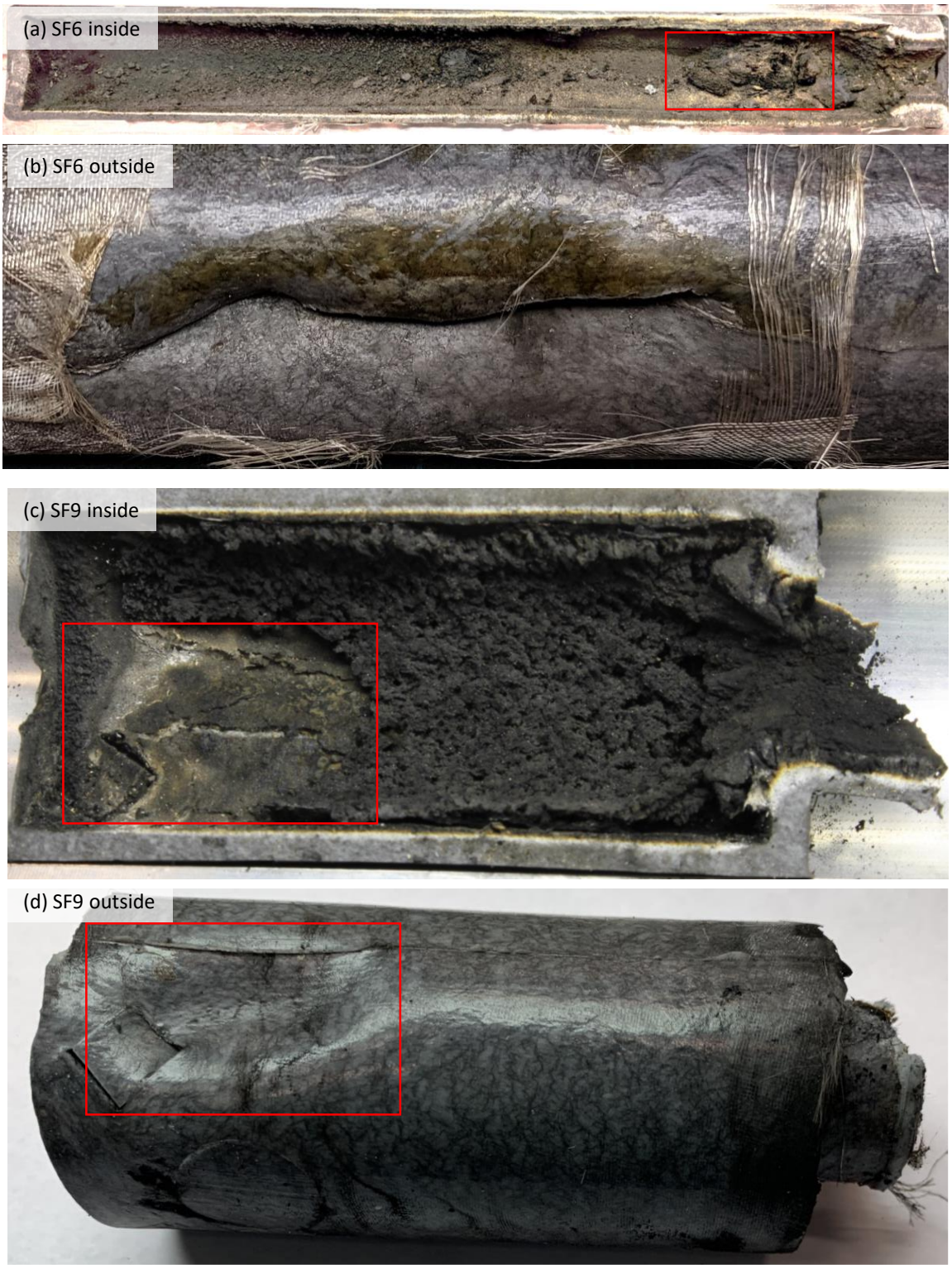

Figure 8-17: In static fires SF6 and SF9, part of the liner buckled inwards. The cause of the buckling is not known.

8.5 Heat transfer and liner effectiveness measurements in the research motor

8.5.1 Case temperature and heat flux measurements

The primary purpose of the thermal protection is to reduce the heat flux into the case and keep the case temperature low to avoid weakening the case material. This section discusses the case temperature and heat fluxes, using data measured in SF6 of Ti Candle.

Six thermocouples (type K) were mounted on the outside of the motor case; their locations are shown in fig. 8-18. The temperatures recorded during the firing are shown in fig. 8-19.

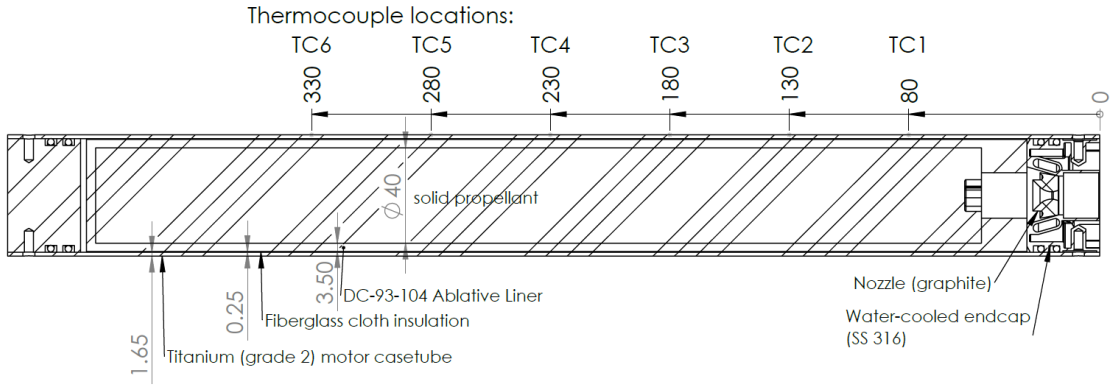

Figure 8-18: Thermocouple locations on the Ti Candle motor. Dimensions in millimeters.

The flame front passed under TC1 (the aft-most thermocouple) first; its temperature is the first to rise. There is almost no thermal conduction along the case; the thermocouples remain at the initial temperature until after the flame front passes them. Despite the long test duration (90.3 s), the case did not reach thermal steady state; its temperature was still rising at burnout. After burnout, the case temperature continued to increase as heat from the hot char soaked out to the case.

Heat fluxes can be estimated from the time derivative of the case temperature.

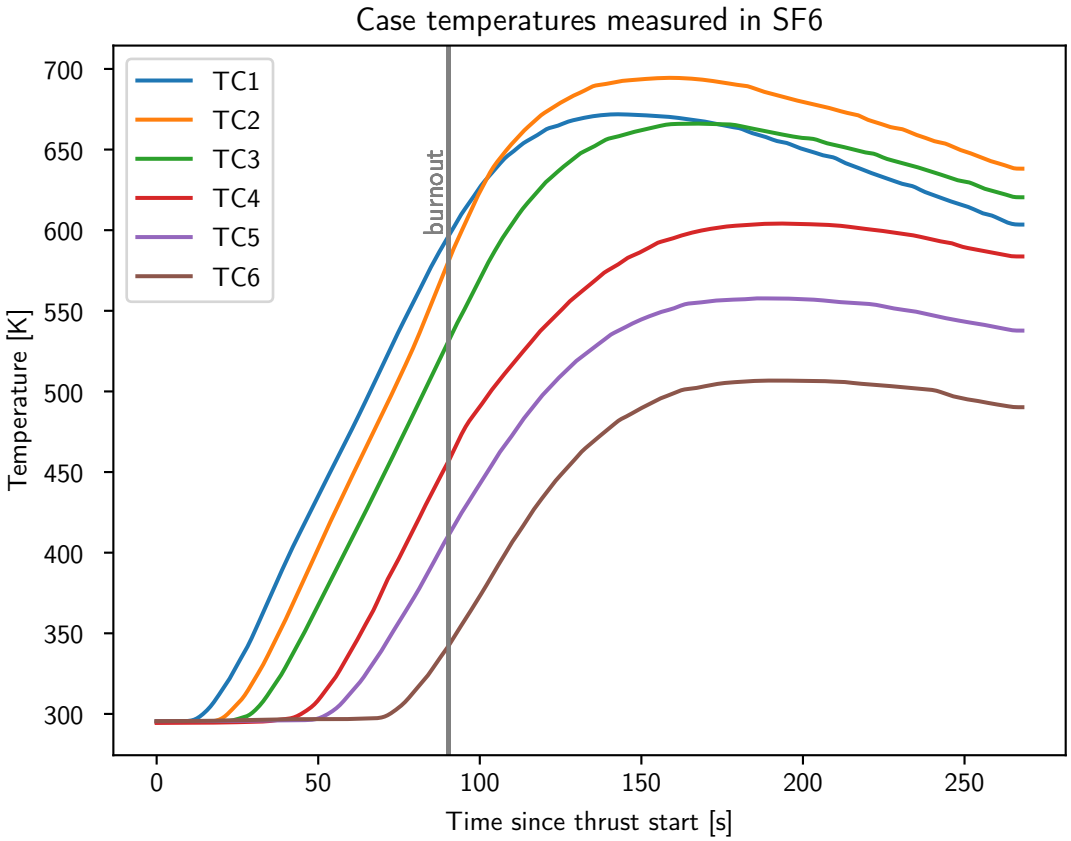

Figure 8-19: Case temperatures from static fire SF6. The temperature of each thermocouple (TC1-6) begins to rise after the flame front passes it.

The net heat flux is approximately:

$$q_{net} = \rho_{case} c_{case} l_{case} \frac{\mathrm{d}T_{case}}{\mathrm{d}t} \tag{8.26}$$

where ρ_{case} is the case density, c_{case} is the heat capacity, and l_{case} is the case radial thickness [14].

The radiative and convective heat fluxes from the case outer surface are estimated

[14]The case is assumed to have uniform temperature through its radial thickness, as its thermal conductivity is $> 40\times$ that of the ablative or fiberglass. This assumption is supported by a detailed model presented in Vernacchia [89], Fig 63.

from the case temperature:

$$q_{rad,out} = \epsilon_{case}(T_{case}^4 - T_{ambient}^4) \tag{8.27}$$

$$q_{conv,out} = h_{out}(T_{case} - T_{air}) \tag{8.28}$$

The emissivity of the case outer surface is assumed to be $\epsilon_{case} = 0.3$ [82]. The convection coefficient on the outer surface was measured to be $h_{out} = 2.8\,\mathrm{W\,m^{-2}\,K^{-1}}$ in a separate experiment [93].

The heat flux into the case from the hot side (inside) is [15]:

$$q_{into\,case} = q_{net} + q_{rad,out} + q_{conv,out} \tag{8.29}$$

This heat flux analysis is shown for TC3 in fig. 8-20. The thermocouple data were filtered (0.2 Hz low pass) before performing numerical differentiation. The heat flux first quickly increases to $15\,\mathrm{kW\,m^{-2}}$ and then gradually rises to $18\,\mathrm{kW\,m^{-2}}$. The oscillations in the heat flux trace are not physical, they are an artifact of numerical differentiation on noisy data. These heat fluxes are much less than the heat flux to the inner surface of the liner (100–$800\,\mathrm{kW\,m^{-2}}$) or the heat flux to an unprotected 500 K case ($> 1000\,\mathrm{kW\,m^{-2}}$). After burnout, the hot side heat flux decays as the hot liner and char cools.

[15] This ignores the slight (6.7%) difference in area between the inside and outside of the case.

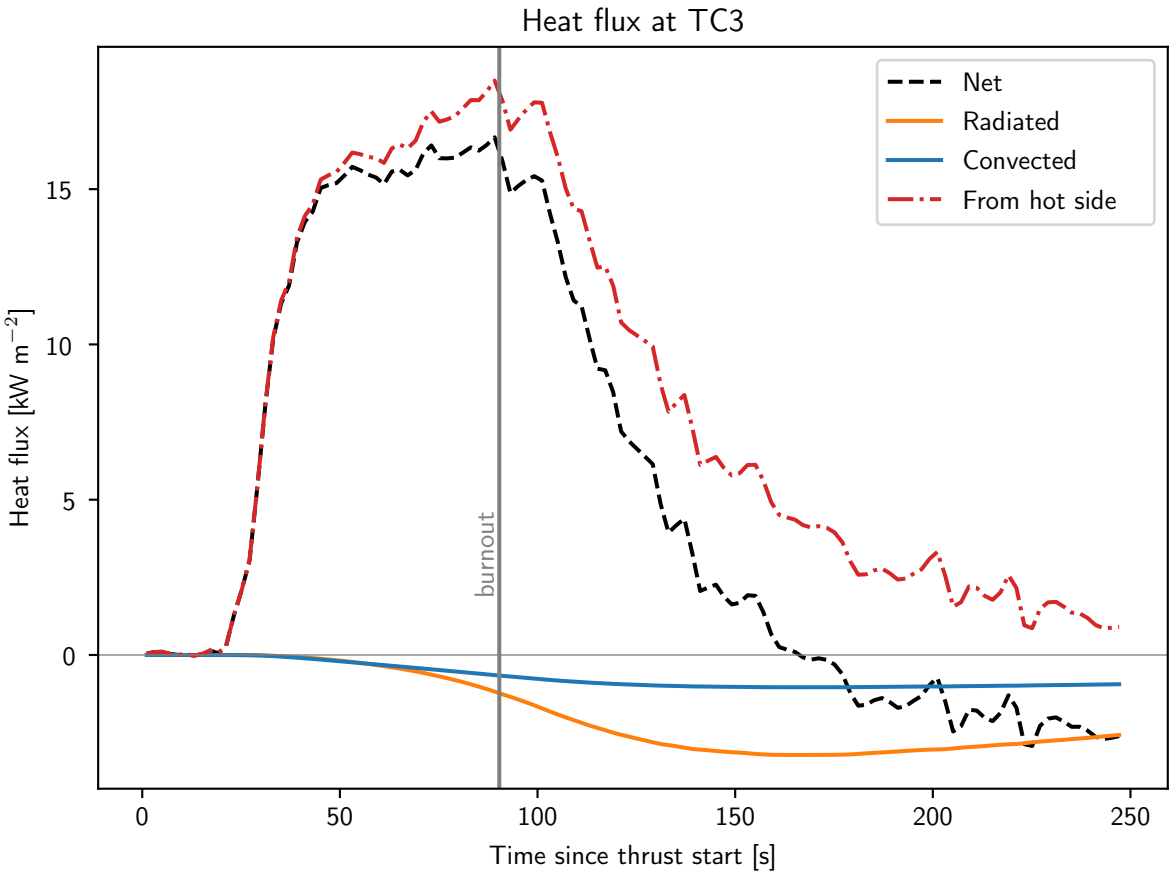

Figure 8-20: Heat flux analysis for the case at thermocouple TC3.

Next, we compare the heat flux data from SF6 to the steady-state limit. Given the arguments in section 8.3.2, we expect the measured heat flux to be less than $q_{into\,case,ss}$, and to only approach it near the end of the burn.

Figure 8-21 shows $q_{into\,case}$ vs. T_{case} measurements from SF6. The colored dots show the value of eq. (8.20) evaluated with the virgin thickness and T_{case} measured at burnout at each thermocouple. For thermocouples TC1-3, at the aft end of the motor (long exposure time), the predictions from eq. (8.20) are close to the measured heat flux. There was a tear in the liner near TC2, which may account for the higher heat flux measured at TC2 [see fig. 8-17].

For thermocouples TC4-6, at the forward end of the motor (short exposure time), the predictions from eq. (8.20) are higher than the measured heat flux at burnout.

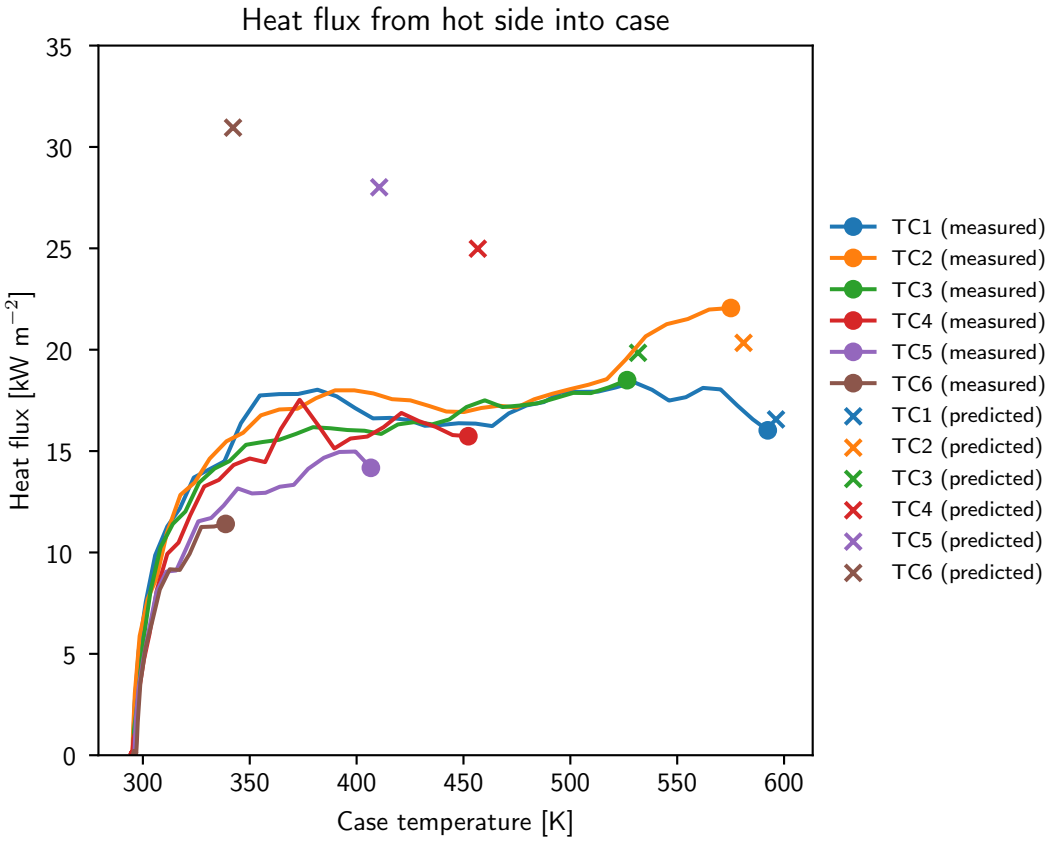

Figure 8-21: For locations with longer exposure times (TC1, 2, 3), the measured heat flux at burnout (right end of curves, marked with dots) was close to the heat flux predicted by eq. (8.20) ('x' marks).

These locations have not yet approached steady state. The heat flux is lower than the steady state model predicts because the heat 'wave' has not yet soaked though the liner and insulation to the case.

These temperature and heat flux measurements support the arguments made in section 8.3.2, and show that the thermal protection system adequately protects the motor case.

8.5.2 Hot gas energy loss measurements

A substantial amount of energy is required to ablate the liner and heat the char, liner and case. This energy of course comes from the hot combustion gas.

The heat loss is substantial – in SF6, about 24% of the energy released by combustion was lost to the walls. Figure 8-22 compares the combustion energy release to various energy sinks. This amount of heat loss reduces the c^* efficiency to $(1-0.24)^{1/2} = 0.87$. This is consistent with the low (0.85-0.9) c^* efficiency measured in motor firings (see section 7.4.4).

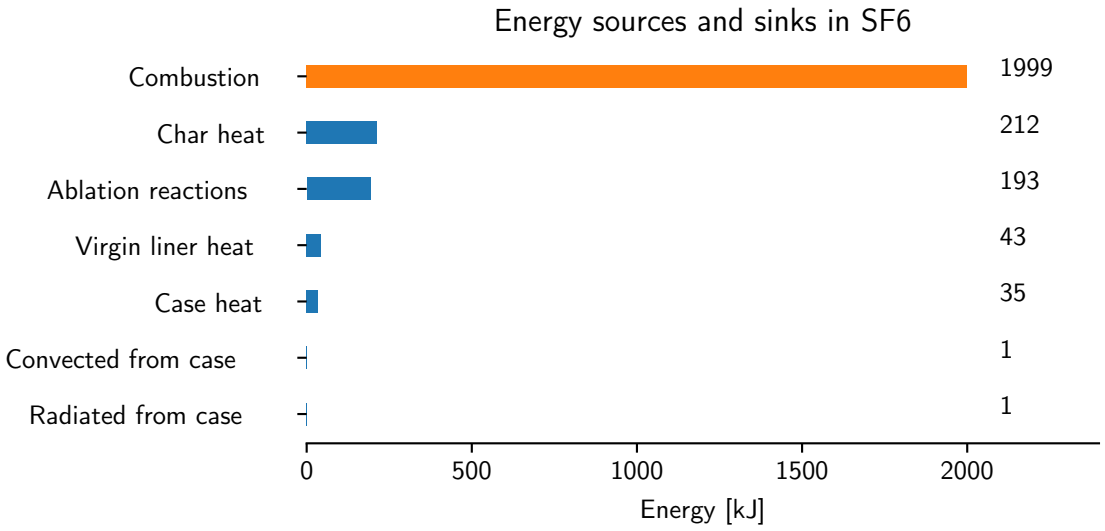

Figure 8-22: Estimated energies released (by combustion) and absorbed (other items) at burnout of static fire SF6. The energy lost to the walls, 485 kJ, was 24% of the heat released from combustion.

The heat losses were estimated by various means. The char heat was calculated assuming the average temperature of the char was $(T_w - T_{pyrol})/2$, where T_w is the surface temperature of the char. T_w depends on the char thickness, heat flux into the surface, and exposure time. T_w was not measured, but assuming a value of 1200 K

gives consistent results with the hot gas energy loss model [16].

The heat consumed by pyrolysis reactions was determined from the volume of charred material and the heat of reaction. The volume of charred material was calculated from the post-burn char depth measurements described in section 8.4.1. The Δh of the reaction was calculated to be $1.87\,\mathrm{MJ\,kg^{-1}}$ using the heats of formation given in Resch [71].

The hot gas cooling model from section 8.3.3 was also evaluated for the conditions in the SF6 static fire; the results are shown in fig. 8-23. The average q_w from this model is $246\,\mathrm{kW\,m^{-2}}$. The total heat transfered to the wall in this model is 441 kJ. This agrees with the observed heat delivered to wall components, 485 kJ.

To further validate the hot gas energy loss model, it would be useful to measure:

1. the surface temperature of the char, and

2. the temperature of the combustion gas at the nozzle inlet vs. time.

If the above model is correct, the char surface temperature should be about 1200 K. The combustion gas temperature should start near the adiabatic flame temperature, and decrease by 600–800 K during the burn. An attempt was made to measure these temperatures during a recent static fire (SF10); however the motor exploded before any useful data could be collected.

[16] Both analyses (the accounting of energy sinks, and the hot gas energy loss model) give estimates of the heat transfer to the wall, and both depend on an assumed wall temperature. If T_w =1200 K is assumed in both analyses, then both analyses give similar values of the total heat transfered to the wall in SF6. The two analyses would disagree if a different value were assumed for T_w. I.e., if a higher value were assumed for T_w, 1) the estimated heat in the wall components at burnout would be larger (heating the char to a higher temperature), but 2) q_w in the gas energy loss model would be lower. Future work should measure T_w to check this assumption.

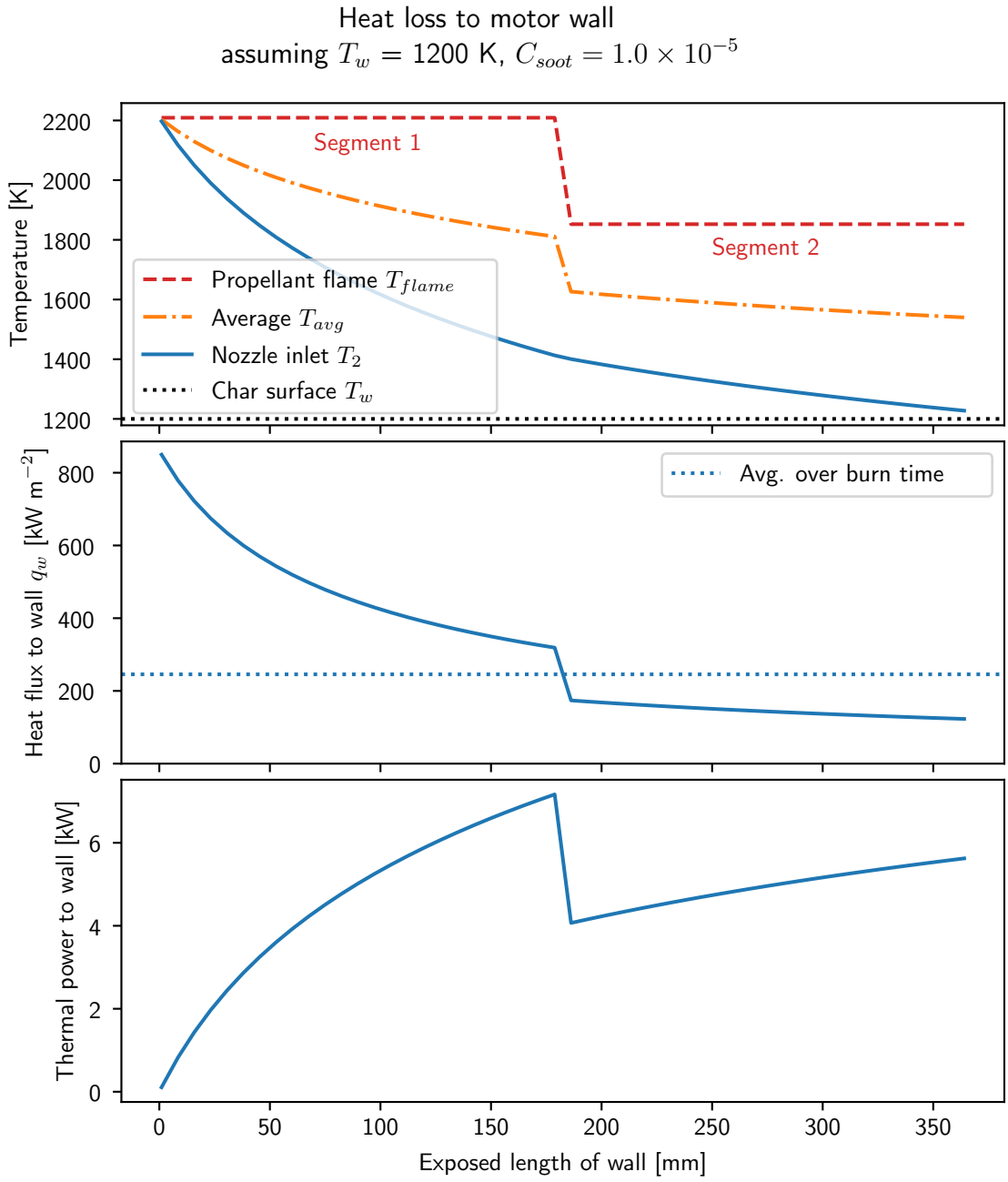

Figure 8-23: A model of heat loss from the hot gas to the wall, run for the conditions in SF6. This model predicts 441 kJ of heat was lost to the wall. This agrees with the observed heat delivered to wall components in SF6.

8.6 Recommendations for further thermal protection development

This work, along with the work presented by Spirnak [76], has demonstrated a feasible thermal protection solution for the motor cases of small, long-burn solid rocket motors. However, further work can be done to improve the design, and to better understand the ablative liner and its impacts on motor performance.

8.6.1 Design recommendations

In future designs, it may be desirable to alter the design to reduce the case temperature. To reduce the maximum case temperature, the easiest options are:

1. Paint case outside black to increase heat rejection by radiation.

2. Increase thickness of fiberglass insulation.

Increasing the fiberglass insulation thickness should be an effective means to reduce the heat flux into the case. Increasing the ablative thickness is less effective, as the ablative is much more thermally conductive. The ablative liner should be only thick enough to not char through.

8.6.2 Experiment recommendations

The ablation process is complicated to model, and experiments will continue to be necessary to benchmark models and qualify new designs.

As discussed above, it is important to instrument the case with thermocouples at many axial locations and calibrate the convective and radiative heat rejection from the case before firing. This allows the heat flux into the case to be determined.

In future experiments, the char surface temperature and combustion gas temperature at the nozzle inlet should be measured. These measurements will help understand the loss of energy from the hot gas to the walls. This energy loss appears

to cause a moderate reduction (5-20%) in the motor's delivered impulse. Better understanding would enable more accurate models of motor performance.

The loss of energy from the hot gas also reduces the heating of the nozzle. For now, a conservative approach has been taken to the nozzle design, which does not take the energy loss into account and assumes the hot gas temperature is 2000 K. Experimentally measuring the hot gas temperature at the nozzle inlet would allow for a better understanding of heat transfer within the nozzle.

8.6.3 Modeling recommendations

Higher fidelity modeling of the ablation process will be difficult, due to the interaction of the hot gas flow, soot, and ablation.

Numerical models such as FIAT [15] or CMA [52] have been used to accurately model 1-d ablation problems with known boundary conditions. However, our motor is more complex than typical ablation problems, as the gas and solid phases are tightly coupled. The temperature distribution in the gas depends on the heat flux to the wall, which depends on the wall temperature. The wall temperature in turn depends on the history of heat flux to the wall. Thus, the gas phase and solid phase (ablation) models must be coupled.

Solving the radiative heat transport through the non-isothermal gas would be difficult and computationally expensive, although doing so is possible (e.g. [7]). Perhaps some initial progress could be made (at the cost of accuracy) by assuming an isothermal gas at some average temperature, as was done above, but coupling this model to FIAT instead of assuming a fixed wall temperature.

Also, there is a significant amount of soot/char deposition on the surface of the ablative in our motors – about half of the char thickness is due to soot deposition. FIAT and CMA do not include provisions for modeling soot deposition.

In summary, a substantial software development effort would be needed to accurately model the ablation process in a small, long burn rocket motor. Such an effort would be interesting, and might lead to modest performance improvements, but is

not necessary to the development or deployment of small, fast aircraft.

Chapter 9

Nozzle mechanical and thermal design

Small, low-thrust motors need unusually small nozzles which can operate for burn times of a few minutes. Conventional nozzle designs are not suitable. To address this need, a novel design was devised using ceramic insulation.

The development of the ceramic insulation is described in chapter 10. This chapter descries the challenge of small, long-burn-time nozzles, assesses the thermal boundary conditions on the nozzle, and presents a thermal simulation of the nozzle under flight conditions.

This new nozzle design was successfully tested in a motor firing, which is reported at the end of this chapter. The demonstration of this nozzle is a major technology risk reduction for small, low-thrust motors.

9.1 Design challenges for small, long-burn-time nozzles

The nozzle for a small, fast aircraft will have an unusual combination of small size and long burn time: because of the low thrust levels, the nozzle throat diameter will be

only a few mm; the burn time is 1-4 minutes. These factors make the thermal design of the nozzle unusually challenging, and rule out conventional nozzle designs using ablative materials. To address these challenges, special ceramic insulation was developed, and a new nozzle was designed using this insulation. This section compares the size and duration requirements to the capabilities of existing nozzles (below), reviews conventional nozzle designs which are not suitable for this application (section 9.1.1), and presents the new design (section 9.1.2).

The size vs. duration design space for solid rocket motor nozzles is shown in fig. 9-1. There is a vague trend of longer burn times with larger-nozzle motors. The Firefly nozzle (blue star) is almost alone in the bottom-right corner. Some other motors have similarly small nozzles (e.g. the STAR 4G) but much shorter burn times. Other motors have long burn times (e.g. over 100 s for the Shuttle RSRM, Orbus-21, and Condor), but have throat diameters orders of magnitude larger. The bottom-right corner (small, long-burn) of the design space is associated with difficult thermal issues because of the physics of heat transfer within the nozzle.

Generally, the length scales for heat penetration phenomena (e.g. thermal diffusion, char depth, erosion) scale with exposure time like $t^{1/2}$ to t^1. For a typical motor, these length scales may be small compared to the nozzle size (stated another way, the heating time scales are long compared to the burn time). This allows some transient techniques to be used in the thermal design. We will see that these are not feasible for a small, long-burn nozzle. Particularly:

- A heat-sink nozzle would reach thermal steady state, as the thermal diffusion length scale is larger that the available wall thickness.

- The nozzle cannot use an ablative surface, as the ablative erosion/regression length would be larger than the throat diameter, causing an unacceptable increase in throat area.

- The nozzle cannot use an ablative insulator, as the char depth would be much larger than the available wall thickness.

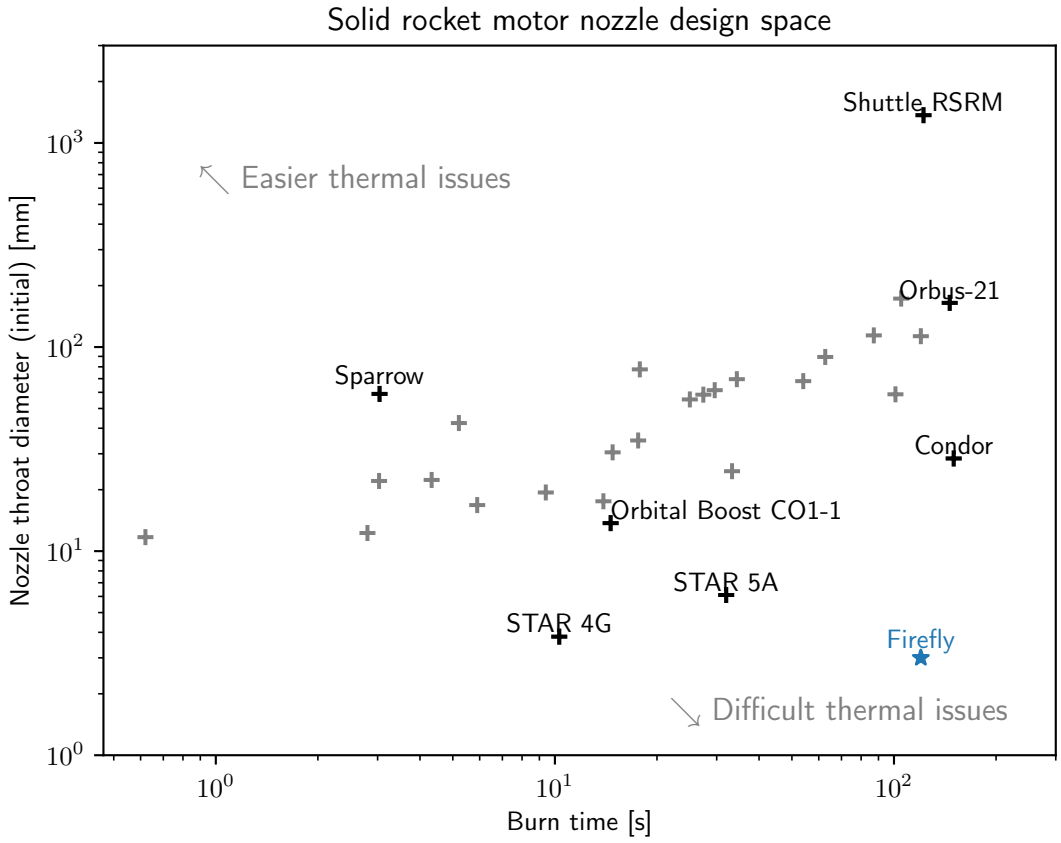

Figure 9-1: Design space of nozzle throat diameter vs burn time. Small, long-burn-time nozzles are unusual (bottom-right corner of the plot). This corner has more difficult thermal issues because the thermal diffusion and ablation length scales are large compared to the nozzle. Data from [60, 21, 77].

The following subsections will discuss these existing design techniques for solid rocket nozzles and explain why they are not applicable to small, long-endurance nozzles.

9.1.1 Conventional nozzle thermal design techniques

This subsection reviews the conventional designs used in solid rocket motors from a perspective of thermal protection. A large number of solid rocket motor nozzles have been developed over the past 80 years and the design techniques are now quite mature. An overview of modern designs is given in Chapter 15.2 of Sutton and

Biblarz [77], and Ellis and Keller [21] provide detailed diagrams of several circa-1970 nozzles. Almost all designs rely on transient phenomena and would fail at their thermal steady state [77].

Most solid rocket nozzles feature an outer structural shell, with ablative or refractory components between the shell and the hot gas. The structural shell carries the loads applied to the nozzle (e.g. from internal pressure, thrust vector control actuators, etc.). Shells are made from steel, aluminum, or titanium alloys, or plastic-fiber composites. To maintain its strength, the shell must be kept at a temperature much lower than that of the hot gas [1].

In many nozzles, the hot-gas-facing components are composite ablative liners bonded to the shell [2]. The ablative is typically carbon or silica fibers in a phenolic matrix. Heat flux from the hot gas causes the liner to ablate – this cools the nozzle wall, but also causes the surface of the wall to regress. Longer exposure times and faster regression rates require a thicker liner, and cause more change in the nozzle's internal contour. In some nozzles, this contour change is tolerable, and ablative liners are used on the entire nozzle (e.g. the Shuttle RSRM, fig. 9-3). In other nozzles, an insert is used at the nozzle throat, where an ablative liner would regress too much.

Inserts are made from a refractory material that can withstand exposure to high-velocity hot gas with minimal erosion. Polycrystalline graphite is the cheapest material option but is not particularly erosion-resistant; pyrolitic graphite or carbon-carbon composites erode less but are more expensive. Tungsten inserts were used in the past, but have been superseded by carbon-carbon [77]. Most insert materials have a relatively high thermal conductivity, so insulation is often layered between the insert and the shell. The insulation may be the same piece as the ablative liner (e.g. Orbital Boost Motor, fig. 9-4), or may be a separate part (e.g. Orbus-21 motor,

[1] Some nozzle structures, particularly those used in upper stage nozzle extensions, are made from materials which can tolerate direct exposure to the hot gas (e.g. carbon-carbon, refractory metal alloys). However, these materials generally have high thermal conductivity. In the context of a small, long-burn nozzle, they would conduct excessive heat into the mounting hardware on the motor case.

[2] In some cases, a single composite part functions as both an ablative liner and the structural shell.

fig. 9-5). In other designs, no insulation is used and the insert is in direct contact with the shell (e.g. Sparrow motor, fig. 9-2).

Nozzles for in-space propulsion may also have a nozzle extension to give a high expansion ratio; nozzle extension materials and designs are discussed in Sutton and Biblarz [77], but are not relevant to the present discussion.

The following subsections will discuss three particular nozzle designs (based on the above design elements). In each case, the heat transfer physics leads to a relation between the burn time and the required thickness of the thermal protection elements of the nozzle wall. Then, this relation will be used to assess the design's applicability to small, long-duration nozzles. A nozzle thermal protection design for the motors in this work must support a burn time of a few minutes with a wall thickness of less than 10 mm.

9.1.1.1 Heat sink nozzle

A heat sink nozzle uses only an insert and a shell. As an example, consider the nozzle of the Sparrow rocket motor, shown in fig. 9-2. Sparrow is a short-duration motor with a burn time of only 3 s. This design is appealing for its simplicity and low cost. It illustrates that thermal issues are easily resolved in the large-size, short-time region of the design space in fig. 9-1, which Sparrow occupies.

This nozzle design relies on the timescale of thermal diffusion through the insert being less than the burn time of the motor. As a quick model of the physics, we will use the equation for thermal diffusion into a semi-infinite solid from a convective boundary (see Equation 11.42 in [31]). This 1-D model neglects the geometric complexity of the nozzle and misrepresents the outer boundary condition, but gives results that are mathematically tractable and capture the essential relationships.

The model predicts that the depth of an isothermal contour is approximately proportional to the square root of time (for times after an initial surface-warming

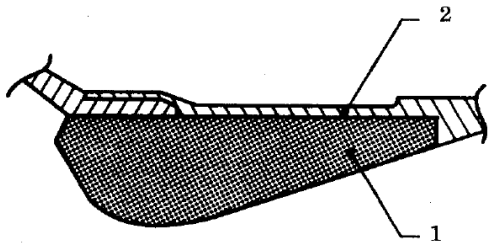

Item	Material	Function
1	Polycrystalline graphite	Entrance, throat, and exit thermal liner and insulation
2	Steel	Entrance, throat, and exit structure

Figure 9-2: The heat-sink nozzle of the Sparrow missile. Reprinted from [21].

period):

$$x_T \sim \sqrt{\alpha_D t} \tag{9.1}$$

where x_T is the isotherm depth, α_D is the thermal diffusivity of the nozzle insert material, and t is time.

Isotherms were calculated using the convection coefficient in the Firefly nozzle (see section 9.2.1) and material properties for polycrystalline graphite [21] [3]. The time to reach 1000 K at a depth of 10 mm is only 10 s.[4]

Thus, the heat-sink design is not suitable for small, long-endurance nozzles. In agreement with this simple analysis, Sutton and Biblarz [77] advise that this design is generally not usable for burn times longer than 10 s.

[3] Hill and Peterson [31] mention an 'amorphous graphite' material with exceptionally low thermal diffusivity, which could allow a heat-sink nozzle to operate for several minutes. However, no mention of this material's low thermal diffusivity could be found in other sources, and it is not mentioned in [77] or [21].

[4] A Ti-6Al-4V shell could operate at up to 800 K, a steel or In718 carrier up to 1100 K.

9.1.1.2 Ablatively cooled nozzle

Some nozzles use ablative liners on their entire surface, with no insert. An example is the Shuttle RSRM, which uses a carbon fiber and phenolic composite ablative (fig. 9-3).

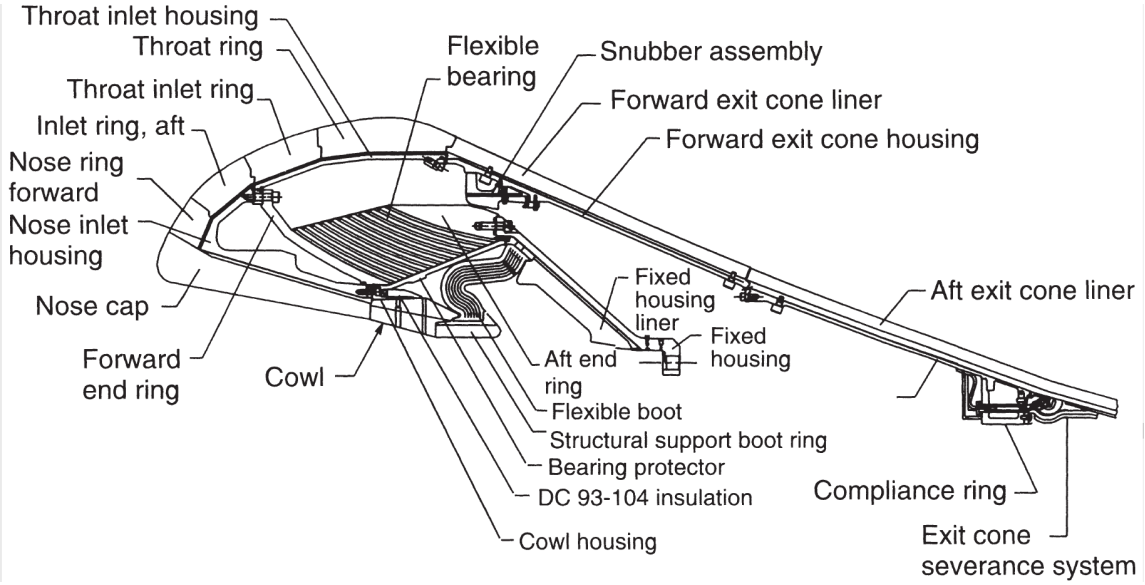

Figure 9-3: Ablatively cooled nozzle of the Shuttle RSRM. Reprinted from [77].

The endurance-limiting physics of this design is the erosion of ablative material at the nozzle throat. Excessive throat erosion (>25% increase in A_t [21]) reduces the expansion ratio of the nozzle and decreases performance. It can also reduce the chamber pressure and thrust [5].

The erosion depth is the product of the average erosion rate and the burn time: $x = rt$. The erosion rate is difficult to predict from first principles, but correlations can be used to 'correct' measured erosion rates to nozzles with different chamber pressure and throat diameter. The correlation recommended by Ellis and Keller [21] is:

$$r_2 \approx r_1 \left(\frac{p_{c2}}{p_{c1}}\right)^{0.8} \left(\frac{D_{t1}}{D_{t2}}\right)^{0.2} \tag{9.2}$$

[5] unless the propellant grain is designed to compensate for the throat erosion

As a point of comparison, the RSRM has 27.2 mm of throat erosion during a burn time of 120 s [77]. Corrected to the chamber pressure and throat diameter of Firefly, this gives an erosion rate of

$$r = \left(\frac{27.2\,\text{mm}}{120\,\text{s}}\right)\left(\frac{1.0\,\text{MPa}}{6.9\,\text{MPa}}\right)^{0.8}\left(\frac{1368\,\text{mm}}{3\,\text{mm}}\right)^{0.2} = \frac{19.7\,\text{mm}}{120\,\text{s}} \tag{9.3}$$

This rough calculation probably overestimates the erosion in a Firefly nozzle, as the RSRM used a hot-burning, aluminized propellant. However, this result is $\sim 100\times$ the acceptable erosion for Firefly's nozzle (0.15 mm throat radius increase for a 25% increase in A_t).

As the erosion depth is almost independent of nozzle size, erosion leads to a smaller relative change in throat area for larger nozzles. Thus, the all-ablative design is only applicable to very large nozzles, where the nozzle diameter is much larger than the throat erosion. [6]

Comparing the nozzles in fig. 9-1, note that the RSRM is very large. The Orbus-21 and Condor, which have a similar burn times but smaller throat diameters, use throat inserts to reduce erosion.

9.1.1.3 Nozzle insert with reinforced plastic insulator

This nozzle design uses an insulator, usually a silica fiber and phenolic composite, around a refractory insert. Examples of this design are the Orbital Boost CO1-1 (fig. 9-4), Condor, and Orbus-21 (fig. 9-5) motors.

[6] Another consideration is that it is difficult to build carbon-carbon inserts for very large nozzles [77].

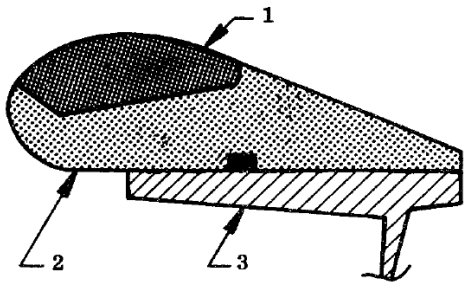

Item	Material	Function
1	Polycrystalline graphite	Throat insert
2	Carbon/phenolic tape	Entrance and exit thermal liner and insulation
3	Steel	Structure

Figure 9-4: The nozzle of the Orbital Boost CO1-1 motor used a graphite insert set into carbon-phenolic insulation. The same carbon-phenolic part also serves as an ablative liner on the inlet and diverging sections. Reprinted from [21].

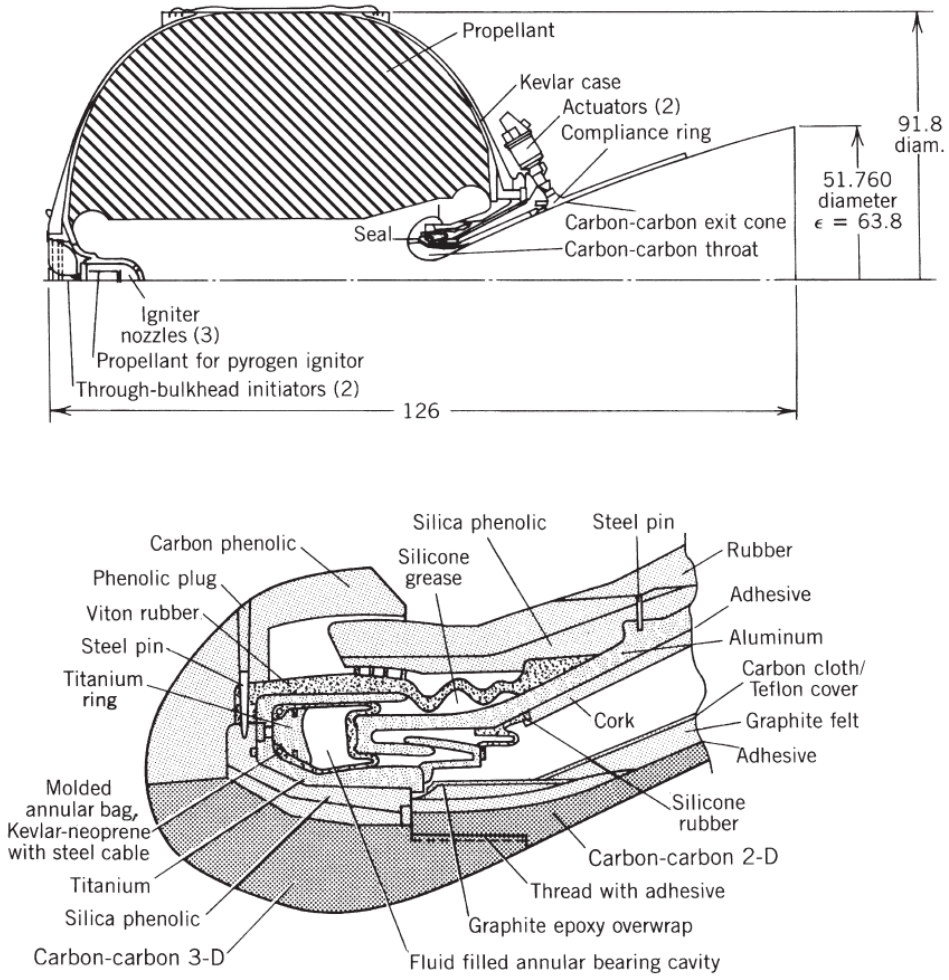

Figure 9-5: The nozzle of the Orbus-21 motor used a carbon-carbon 'integrated throat entrance' insert backed by silica-phenolic insulation. Drawing dimensions are in inches. The throat diameter is 6.48 in (164.6 mm). This nozzle is more complex than the Orbital Boost CO1-1, in part because this nozzle is mounted on a flexible bearing for thrust-vector control. Reprinted from [77].

The endurance-limiting phenomenon here is charring of the insulation at high temperatures. The char depth increases sub-linearly with exposure time. A 1-D analytical model of the charring process by Kuby and Richardson [44] suggests that $x_{char} \sim t^{1/2}$. Ellis and Keller [21] give an empirical relation for silica-phenolic insulation:

$$x_{char} \approx A t^{0.68} \exp(-B/q) \tag{9.4}$$

where q is the heat flux into the wall and $A = 0.787\,\mathrm{mm\,s^{-1}}$ and $B = 1.027 \times 10^6\,\mathrm{W\,m^{-2}}$ are fit parameters.

This gives an estimated char depth of 16.6 mm for the Firefly nozzle, assuming $q = 5 \times 10^6\,\mathrm{W\,m^{-2}}$ [see section 9.2.1]. However, the available insulator thickness is only 5–10 mm. Thus, we should expect that a phenolic composite insulator for Firefly would char through entirely. Indeed, a prototype nozzle we tested with a phenolic composite insulator did char entirely (see fig. 9-6) [7]. The material's strength, gas-tightness, and insulating properties are compromised after it chars. Insulation and liners are typically designed to be thicker than the expected char depth [21].

Inserts backed with reinforced phenolic insulation have been used on > 100 s burn time motors, such as Condor and Orbus-21. However, these nozzles were larger and could fit thicker insulation; it appears the required insulation thickness for a 120 s burn is 2-3 times thicker than can be fit in the Firefly nozzle. Thus, an insert backed by a reinforced plastic insulator is not suitable for small, long-endurance designs.

[7] This prototype was subjected to a torch test in which the nozzle insert was heated with an oxy-acetylene torch. The heat power and duration were set to match a motor firing.

Figure 9-6: A Firefly nozzle prototype with graphite insert, phenolic and ceramic foam composite insulation, and steel shell. The left image shows the nozzle before testing. The right image shows a section cut after testing; the insulation has entirely charred.

9.1.2 Small, long-burn time nozzles with steady-state ceramic insulation

None of the 'transient' thermal protection techniques discussed in the previous section can work for the 1-4 minute burn duration needed for the small, low-thrust motors of this work. Each has a characteristic length scale (isotherm depth, throat erosion, char depth), which scales with time as $t^{1/2}$ to t^1. With a long burn time, the throat erosion or insulation thickness is too large for a very small nozzle.

Instead, we will consider steady-state insulation solutions, which do not rely on transient phenomenon. In this case, the insulation material must have a very low thermal conductivity ($< 5\,\mathrm{W\,m^{-1}\,K^{-1}}$) and survive temperatures of 1500–2000 K. A novel design using ceramic insulation was developed to meet these challenging requirements.

A representative nozzle design is shown in fig. 9-7. The nozzle consists of an insert through which the hot gas flows and insulator which contains the heat convected into

the insert. The nozzle's structural shell is an extension of the aft section of the motor case. The insert material is boron nitride ceramic, the insulator is fused silica, and the shell is titanium alloy Ti-6Al-4V. This is the same baseline design as chapter 6, fig. 6-3.

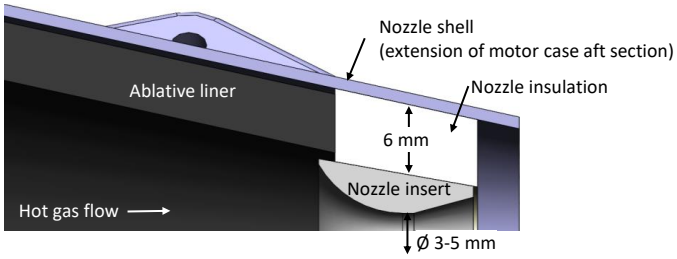

Figure 9-7: Section view of the nozzle from the baseline motor design.

In the baseline design the nozzle shell is a continuation of the aft end of the motor case. Alternatively, the nozzle shell could be a separate component which screws into the motor case (fig. 9-8). In terms of the nozzle thermal performance, these design are equivalent. The separate-shell design allows the shell to be made from a different material than the rest of the motor case; however it is also more mechanically complex.

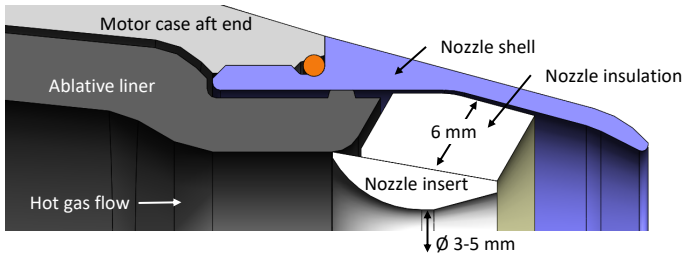

Figure 9-8: Section view of the nozzle, with the nozzle shell as a separate part. The nozzle assembly consists of a shell, insulator and insert. The nozzle shell connects to the aft end of the motor case with screw threads.

In either case, the outer surface of the nozzle's shell forms part of the fuselage's aerodynamic outer surface. Thus, the outer dimensions of the nozzle are constrained to a tapered shape which reduces drag. This constrains the insulator to be fairly thin - only 6 mm in these designs. The insulation could be made thicker, but the base diameter of the fuselage would need to be enlarged, which would increase drag and

slightly decrease the range of the vehicle. The choice of the fuselage base diameter is discussed further in section 9.5.2.

The operating temperature of the insert is up to 2000 K whereas the operating temperature of the shell is only 800 K. Thus, the (relatively thin) insulator must provide a very large thermal resistance, and withstand the thermal stresses induced by an extreme thermal gradient. The nozzle must survive these temperatures for the entire burn time of a few minutes. The shell is only cooled by airflow and radiation; if the vehicle operates at high altitudes (low air density) to maximize range, the available air cooling is very low.

The extreme requirements on the nozzle insulation motivated the development of a new cellular ceramic insulation material. The ceramic insulation is described in chapter 10.

9.2 Nozzle heat transfer boundary conditions

This section discusses models for the thermal boundary conditions on the nozzle. The nozzle has two important thermal boundary conditions: the internal boundary, where the nozzle insert is heated by the hot exhaust gas (section 9.2.1), and the external boundary, where the nozzle shell rejects heat to the surroundings (section 9.2.2). These boundary conditions are used in a thermal model of the nozzle, which is presented in section 9.3.

9.2.1 Internal hot gas thermal boundary

It is important to know how much heat will be transfered into the nozzle's inner wall at a given wall temperature. This, along with the thermal conductivity of the insulator, determines how much heat must be rejected at the outside of the shell. If much heat needs to be rejected, either the vehicle will not be able to operate at low air density (insufficient convection cooling) or will need to operate the shell at higher temperature to reject sufficient heat by radiation (this requires making the shell out

of high-temp material and might cause too much heating of the aft end of the motor case).

The hot gas will primarily transfer heat to the nozzle via convection, as shown in section 8.3.1.3. Radiative heat flux to the nozzle wall will be 1-2 orders of magnitude less than the convective heat flux and is neglected in this analysis.

Convective heat transfer into a wall is usually modeled by two parameters: the convection coefficient h and the adiabatic wall temperature T_{aw} [35, 31]. In this model, the heat flux into the wall is (equation 4-10 in [35], equation 11.27 in [31]):

$$q = h(T_{aw} - T_w) \tag{9.5}$$

All of these variables vary with axial location along the wall, x.

The convection coefficient h represents how well heat is transfered though the boundary layer at the wall. It is generally higher for faster moving fluid and denser fluids. h is difficult to predict from first principles. Correlations have been developed for various flow conditions which can predict h with moderate accuracy.

The adiabatic wall temperature T_{aw} is the wall temperature at which no heat would flow into the wall. For a slow-moving fluid, it is equal to the temperature of the fluid. For fast-moving fluids, T_{aw} is usually between the stagnation and static temperatures of the fluid. T_{aw} can be predicted by assuming a 'recovery factor' (see equation 11.28 in [31] or equation 4-10-a in [35])

Ablation of liner upstream of the nozzle may provide a film of cool gas which would reduce the heat transfer into the nozzle. The magnitude of this effect depends on whether the cool film persists through the nozzle, or if it is mixed out into the flow. The differences here are significant: in the extreme of full mixing the adiabatic wall temperature will be only a few hundred kelvin below the flame temperature of the propellant, perhaps 1800–2000 K; in the extreme of no mixing the adiabatic wall temperature will be the temperature of the ablated gas, perhaps 900–1100 K. Clearly, the heat transfered into the wall could be *much* less if the cool film remains.

The film cooling effect is typically quantified by the film cooling effectiveness parameter (equation 10 in [49], equation 8.26 in [31]):

$$\eta_f = \frac{T^0_{aw} - T^f_{aw}}{T^0_{aw} - T_f} \quad \in [0, 1] \tag{9.6}$$

where:

- T^0_{aw} is the adiabatic wall temperature without film cooling,
- T^f_{aw} is the adiabatic wall temperature with film cooling,
- T_f is the starting temperature of the film.

η_f, T^0_{aw} and T^f_{aw} vary with location along the wall. The film cooling is maximally effective (up to $\eta_f = 1$, $T^f_{aw} = T_f$) where the cool gas is injected, and the effectiveness declines ($\eta \to 0$) downstream as the cool film mixes with the hot core flow.

The goal of this section is to estimate h, T^0_{aw} and η_f versus x along the nozzle wall. With these parameters, eq. (9.5) and eq. (9.6) can be used to calculate the heat transfered into the nozzle wall for a given nozzle insert temperature. That relation will be used in a thermal model of the nozzle to determine the nozzle shell operating temperature and cooling requirements.

The following sections discuss methods for estimating h, T^0_{aw} and η_f 1) using empirical correlation formulas (sections 9.2.1.1 and 9.2.1.2) and 2) using computation fluid dynamics (section 9.2.1.3).

These analyses all assume a chamber pressure of 0.7 MPa. At lower chamber pressures, the convection coefficient h will be lower.

9.2.1.1 Correlations for the convection coefficient

The standard convection estimation technique for rocket nozzles is the Bartz correlation (equations 4-13 and 4-14 in [35]). The Bartz equation assumes that the flow through the nozzle is turbulent. However, the nozzle flow can re-transition and become laminar for nozzles with low p_cF. Because of its small size, the Reynolds

number Re_D in the Firefly nozzle is exceptionally low, only 25×10^3 at the throat [fig. 9-9]. Laminar flow is found for throat $Re_D < 2 \times 10^5$ [55] [fig. 9-10].

For laminar flow, NASA [55] recommends the correlation:

$$St = 0.318 Re^{-0.5} Pr^{-0.6} \tag{9.7}$$

where $St = h/(\rho v_{core} c_p)$ is the Stanton number and Pr is the Prandtl number.

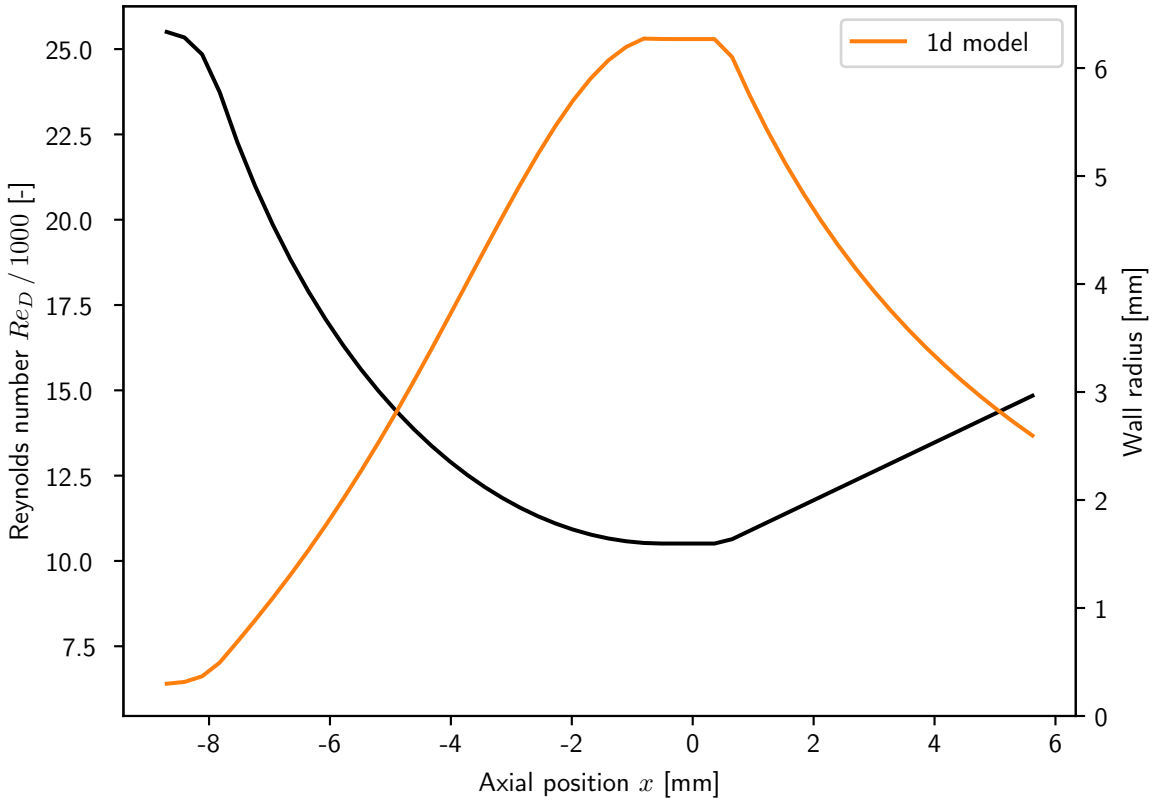

Figure 9-9: Reynolds number in the Firefly v2.1 nozzle (orange curve) and wall profile (black curve). The length scale is the diameter at each station. These Re_D values are unusually low for rocket nozzles (by at least an order of magnitude).

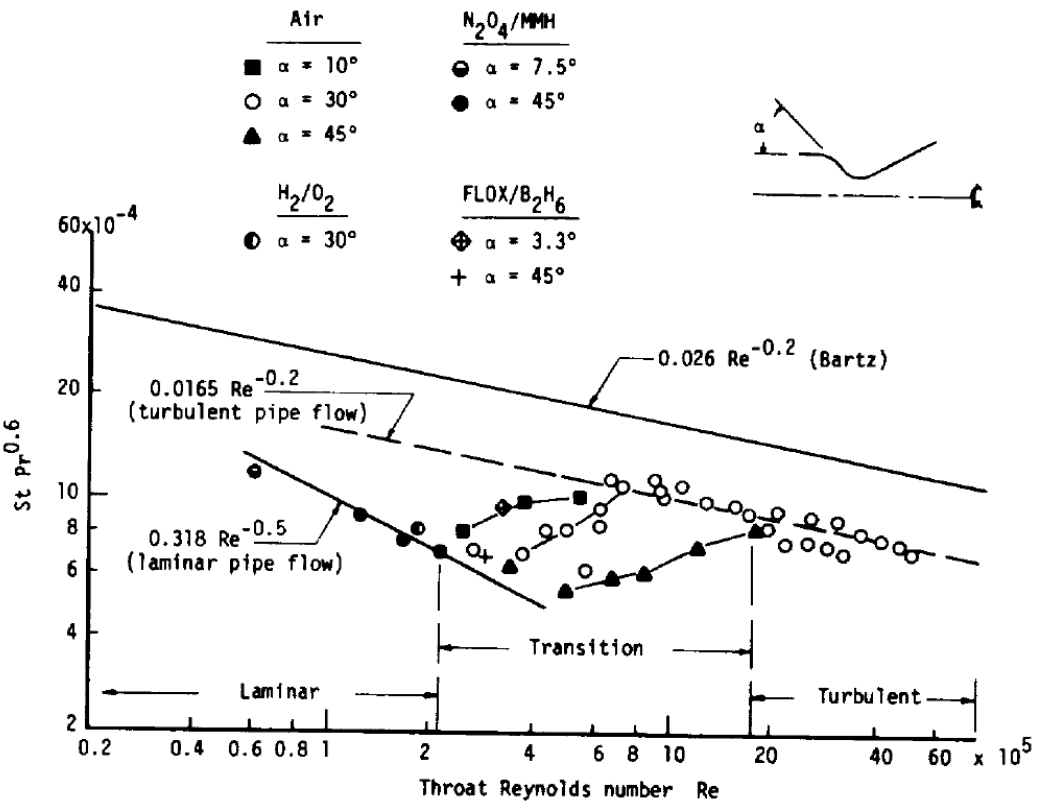

Figure 9-10: "Graph of heat transfer data illustrating regions of reverse transition and laminarization." Reprinted from [55].

9.2.1.2 Correlations for film cooling

Various correlations exist for η_f vs. a non-dimensionalized distance from the injection point. Reviews of these models are presented in Section III.2 of Terry and Caras [79] and Section 2.5.2 of NASA [55]. Some correlations are based on unaccelerated flow over a flat plate; these do not extend well to nozzle flows [55]. All these correlations are for liquid propellant engines, where the film is injected at a single location, such as a line of holes or an annular slot (see e.g. Figure 3 in [47]). Their formula depend on the slot height and film velocity. These are not applicable to the present ablative film cooling situation, in which the film gas is injected from a distributed surface of ablating material. Even for liquid propellant rockets, these correlations do not yield accurate predictions, and require empirical correction factors of $1 \sim 4\times$ [55]. Thus, these models will not be used in the present study.

We can, however, gain some useful insight from the excellent work in Carlson and Talmor [9]. Carlson gives useful insight that the η_f decays more quickly at higher turbulence intensity (fig. 9-11). At higher turbulence intensities, there is more mixing between the cool film gas and the hot core gas, and the film cooling effect decays more quickly with downstream distance.

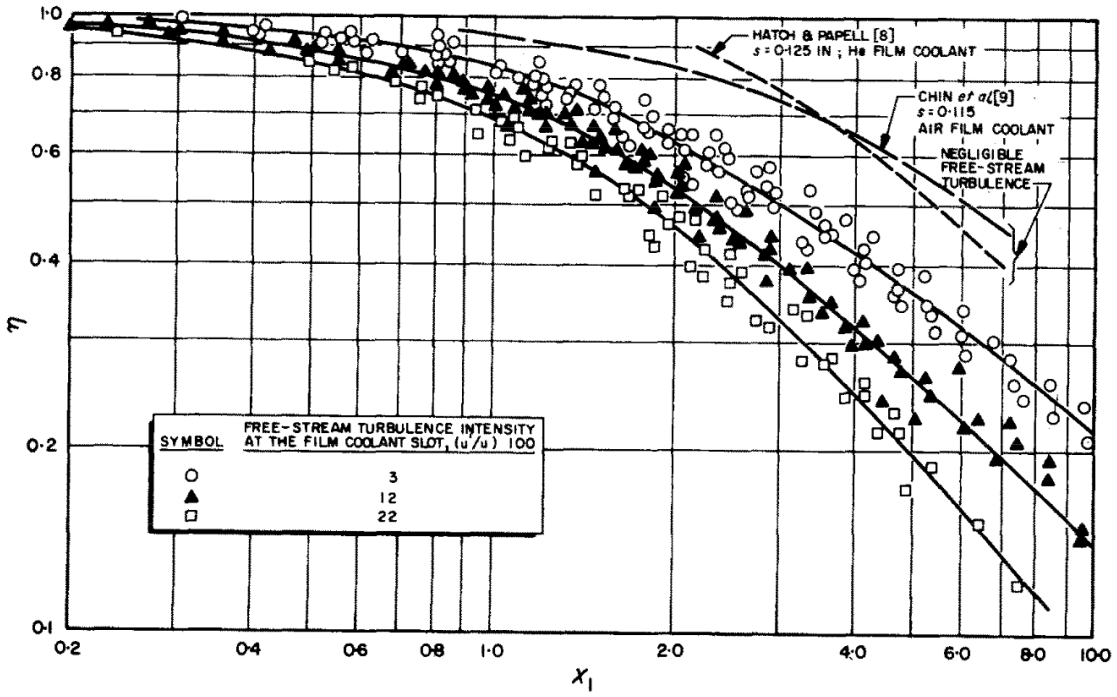

Figure 9-11: Film effectiveness η_f vs. non-dimensionalized distance from the film injection slot, for three different values of the free-stream turbulence intensity. The film effectiveness decays more quickly at higher turbulence intensities. Reprinted from [9].

9.2.1.3 Computational fluid dynamics simulation of heat transfer from the hot gas

Computational fluid dynamics (CFD) simulations were used to estimate the heat transfer to the nozzle's inner wall, and to examine the effect of upstream ablation on heat transfer in the nozzle. The CFD model was used to simulate two cases:

1. with ablating upstream walls, giving a mass flux of $1.78 \times 10^{-2}\,\mathrm{kg\,m^{-2}\,s^{-1}}$ of gas at 1000 K.

2. no ablation – adiabatic upstream walls.

Method for computing h, T_{aw}^0 and η_f from CFD results In each case, the CFD model was run twice. One run used an adiabatic boundary condition on the nozzle wall to find the adiabatic wall temperature along the nozzle $T_{aw}(x)$. The second run used an isothermal condition on the nozzle wall at temperature T_w^*. The heat flux along the wall $q^*(x)$ was taken from the isothermal case. Then, the convection coefficient was calculated as:

$$h(x) = \frac{q^*(x)}{T_{aw}(x) - T_w^*} \tag{9.8}$$

Different T_w^* were used in the ablation vs. no ablation cases; in each case T_w^* was set to about 250 K below T_{aw} at the throat.

The film efficiency was calculated using eq. (9.6) with the adiabatic wall temperature profiles from the ablation and no ablation cases.

Domain The nozzle design from Firefly version 2.1 was used as an example geometry for this analysis. The nozzle geometry and model domain are shown in fig. 9-12.

Solver The CFD analysis was performed in ANSYS FLUENT 19.2 [8]. A 2D axisymmetric domain was used (see fig. 9-12). The domain included 30 mm of ablative wall upstream of the nozzle inlet. The nozzle exit opened into a 30 mm radius by 30 mm long ambient region, bordered with pressure outlets at 30 kPa. The mesh was unstructured but quadrilateral dominant. The boundary layer on the ablative and nozzle walls was meshed down to $y^+ = 1$. The compressible Reynolds Averaged Navier-Stokes (RANS) equations were used with the SST $k - \omega$ turbulence closure. The gas properties were taken from the combustion products of the 10% oxamide propellant calculated by RPA [65]. The ideal gas law was used as the equation of state, with constant c_p. Thermal conductivity and viscosity were assumed to

[8] The author thanks Peter Sharpe for performing the CFD analysis and helping to interpret the results.

vary linearly with temperature, based on two values taken from RPA. The chemical composition of the flow was frozen (no reactions). The solver was initialized with compressible potential flow, and iterated until the residuals [9] dropped by 10^{-6}.

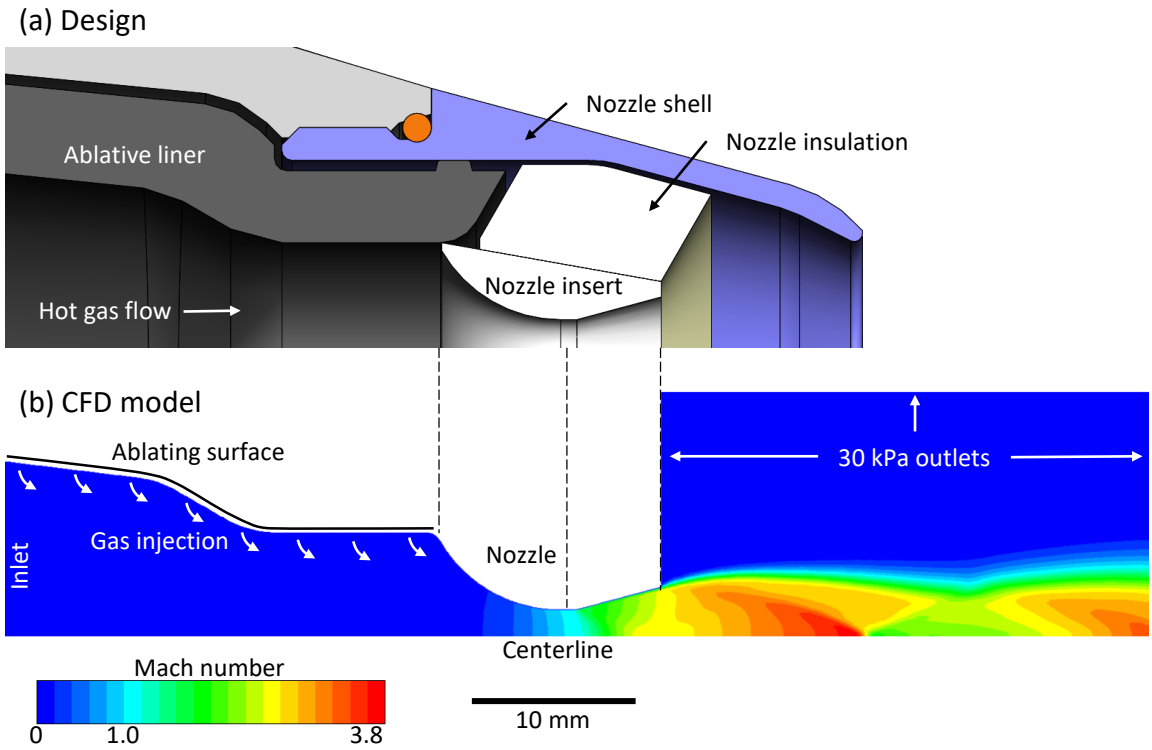

Figure 9-12: (a) In this motor design, the walls upstream of the nozzle are made of an ablative material. (b) A CFD model of the flow through the nozzle. 'Cool' gas injected from the ablating surface reduces heat transfer into the walls of the nozzle.

Turbulence conditions Turbulence is also important for the CFD model. The turbulence intensity of the core gas can be set as a boundary condition in the CFD model. It is important to choose a reasonable value, as η_f has been shown to depend on the turbulent intensity (see section 9.2.1.2 and Carlson and Talmor [9]).

However, turbulence intensity data are not available for combustion gas flows in small, end-burning rocket motors [10], and equipment to measure it in this motor was not available. Some reference values for turbulence intensity:

[9] continuity, x momentum, y momentum, energy, k and ω

[10] Very high turbulence intensities have been predicted for some core-burning solid rocket motors [2], but these have a very different flow.

- 10-40% in some fuel-air combustors [27]
- 5% in a H_2 / O_2 rocket, far from the injector [9]
- 15% in a N_2O_4 / hydrazine rocket, far from the injector [9]
- 6% based on fully developed pipe flow correlation: $I = 0.16 Re_D^{-1/8}, Re_D = 2300$

The combustors intentionally create turbulence to mix the fuel and air, and thus have a higher turbulence intensity than the other examples. Due to the uncertainty in the turbulence intensity, the CFD model was run at turbulence intensities of both 5% and 100%; the results are compared in section 9.2.1.4.

Validation As a crude validation of the CFD model, the centerline Mach number from CFD is compared to the Mach number computed from 1d area ratios (fig. 9-13). The centerline Mach number profiles agree reasonably well.

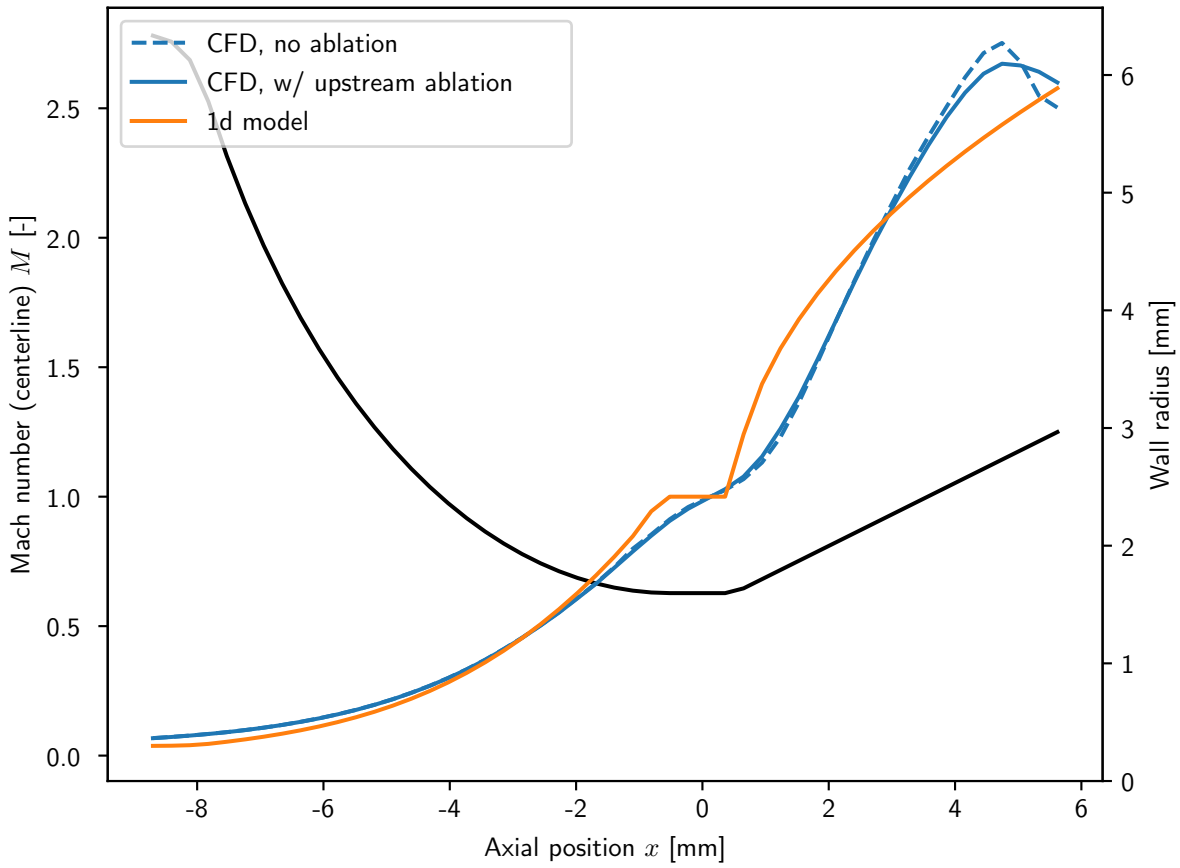

Figure 9-13: As a crude validation, the centerline Mach numbers from the CFD analysis (blue) are compared to a 1d analytic solution (orange). The nozzle contour is shown in black.

9.2.1.4 Results and Discussion

Convection coefficient The predicted convection coefficients are shown in fig. 9-14 for the CFD model (ablation and no ablation) and for the Bartz and laminar correlations. NASA SP-8124 [55] states that the Bartz correlation under-predicts h "in the first part of the converging section, where the boundary layer is still in its initial stages of development, but over-predicts in the throat region where the pressure gradient is large." Comparing the Bartz model (orange curves) to the CFD model (blue curves) in fig. 9-14, we see exactly these trends. Thus, the disagreement between the CFD model and the Bartz model should not cause us to lose faith in

the CFD model.

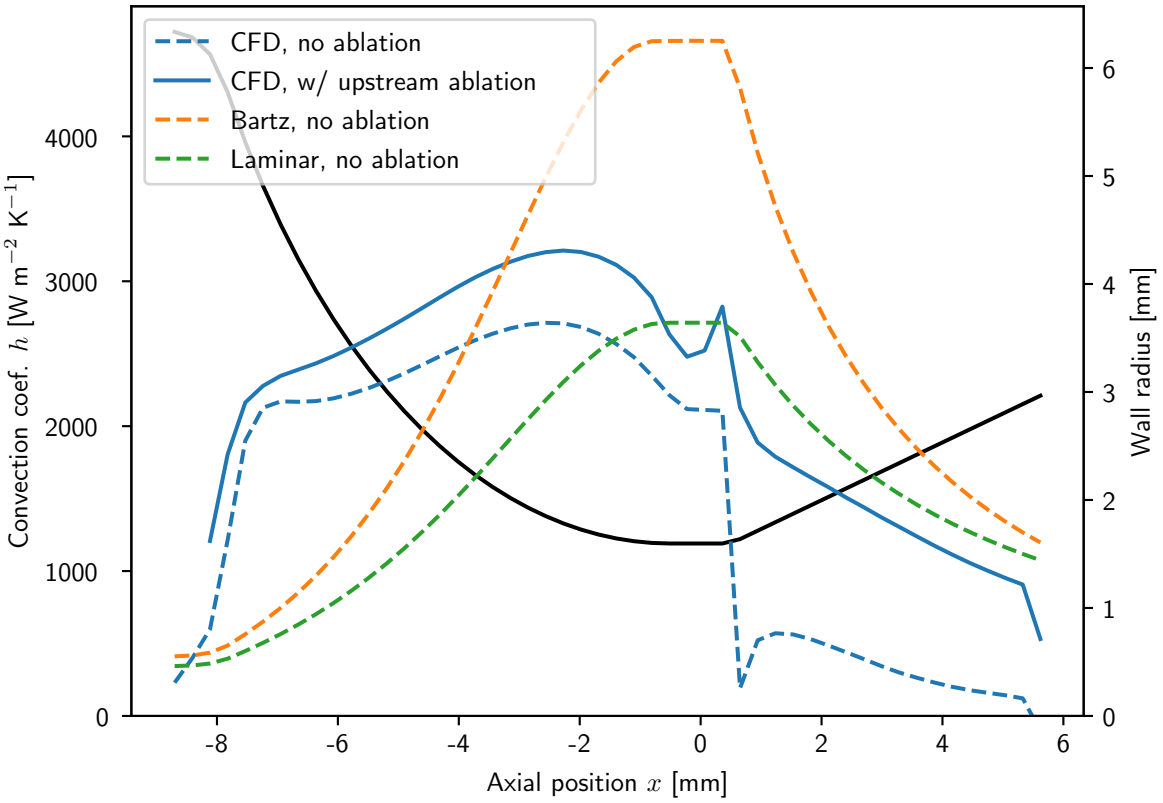

Figure 9-14: The turbulent Bartz model (orange) over-predicts the convection coefficient at the throat, compared to the CFD model (blue).

The laminar model (green curves) better matches the CFD model (as the flow is almost certainly laminar at the throat). However, it predicts a lower convection coefficient in the converging section than the CFD model.

In the converging and throat sections, the CFD ablation and no ablation cases have similar h. This is expected – Huzel et al. [35] state "it has been found that there is practically no difference in the gas-side heat transfer coefficient with and without film cooling". In the CFD model no ablation case (blue, dashed curve) there is a sudden drop in the convection coefficient just after the throat; the cause of this phenomenon was not known at the time of this writing.

Adiabatic wall temperature and film effectiveness Without ablation, there is reasonable agreements between the CFD T_{aw} (blue dashed line) and the Bartz model (recovery factor) T_{aw} (fig. 9-15). The CFD model predicts much lower T_{aw} with ablation (blue solid line). The CFD-predicted film effectiveness η_f is quite high, over 0.5 for most of the nozzle (fig. 9-16). As expected, η_f declines with distance along the nozzle, as the cool film mixes with the hot core flow.

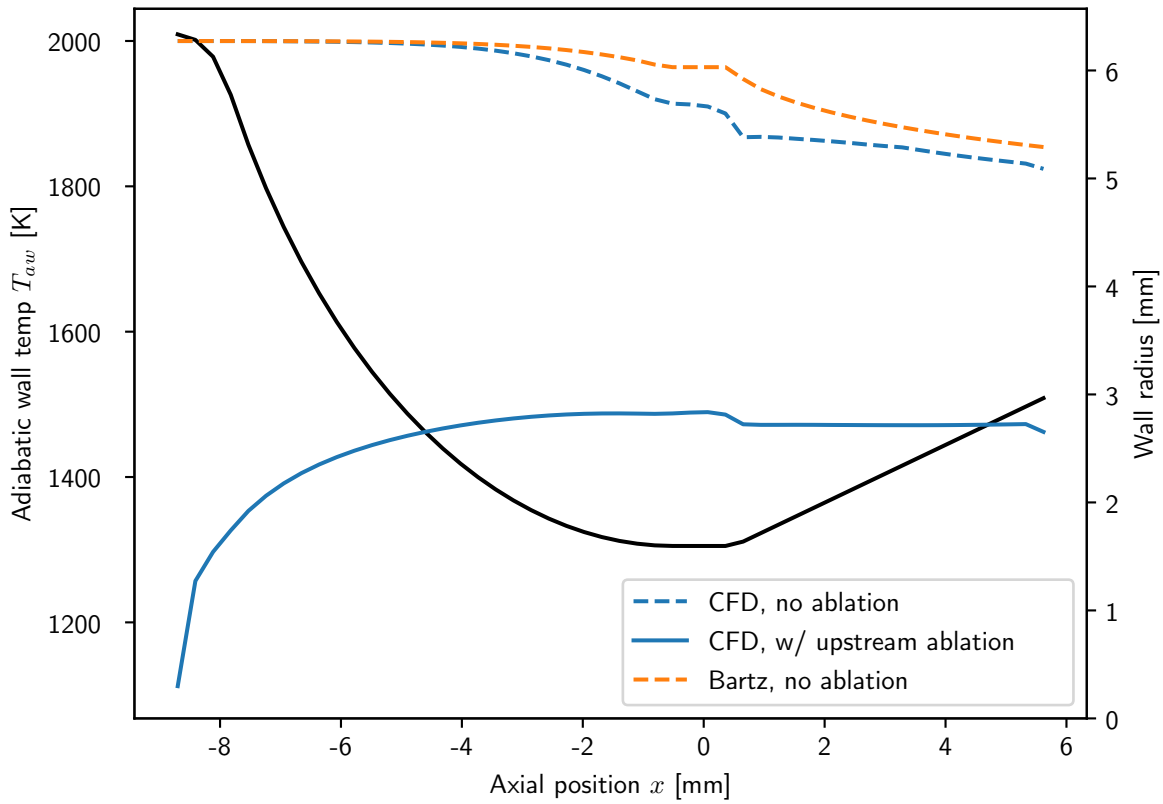

Figure 9-15: Upstream ablation creates a cool film of gas in the nozzle, which reduces the adiabatic wall temperature of the flow (solid blue curve). Without upstream ablation, the adiabatic wall temperature is higher (dashed curves).

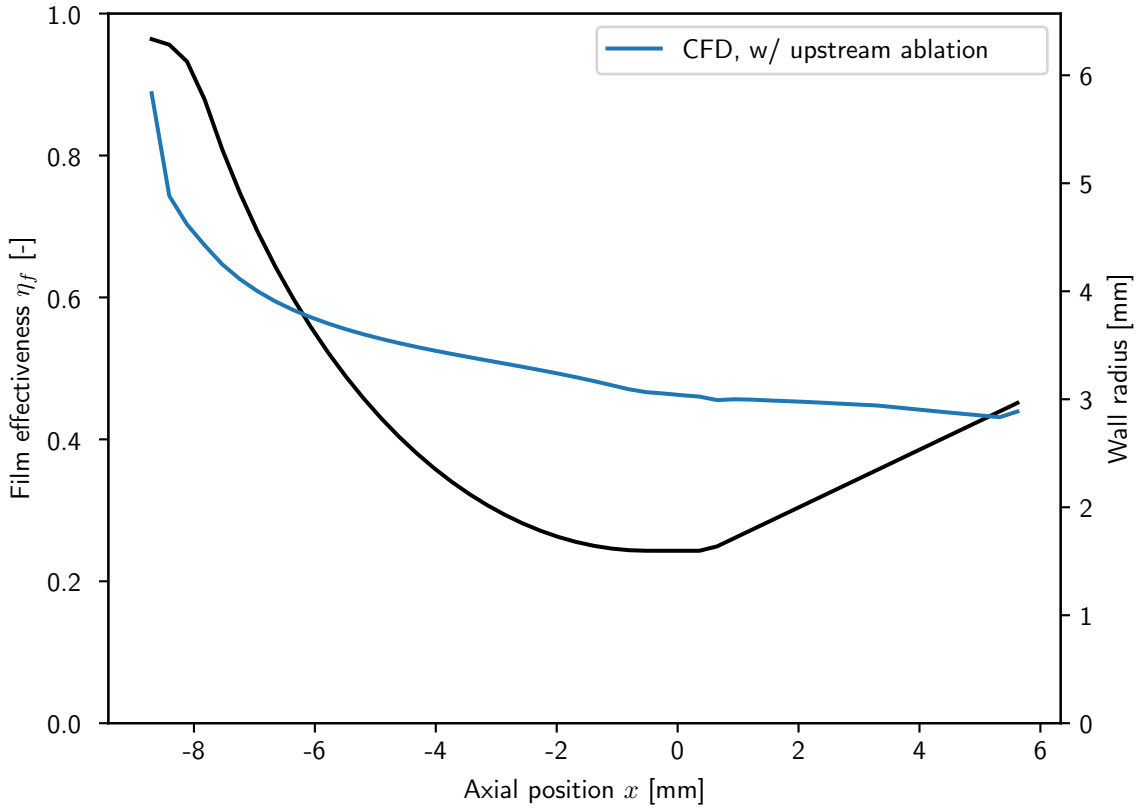

Figure 9-16: The film effectiveness of the cool gas from upstream ablation decreases farther form the gas source.

Effect of Turbulence Intensity The above CFD results were calculated assuming a turbulence intensity of 5%. However, the turbulence intensity can alter the film cooling effectiveness (see section 9.2.1.2, fig. 9-11). To examine the sensitivity to turbulence intensity, the ablating CFD model was re-run with the turbulence intensity set to 100% (on the hot gas and ablating inlets). A turbulence intensity of 100% is higher than expected based on a comparison to other combustion devices (see 'Turbulence conditions' paragraph at end of section 9.2.1.3). The actual turbulence intensity almost certainly lies between 5% and 100%. In all cases the turbulence length scale was the same (set based on the hydraulic diameter of the inlet). The results are compared in fig. 9-17, fig. 9-18, and fig. 9-19.

The convection coefficient is almost unchanged (fig. 9-17). It is suspected that because the boundary layer in the nozzle re-transitions to laminar flow (see section 9.2.1.1), the upstream turbulence intensity does not have much effect on h in the nozzle.

At higher turbulence intensity, the adiabatic wall temperature is somewhat higher (by about 30 K) (fig. 9-18) and thus η_f is lower (by about 0.05) (fig. 9-19). This is qualitatively consistent with the experimental results from Carlson and Talmor [9] presented in fig. 9-11.

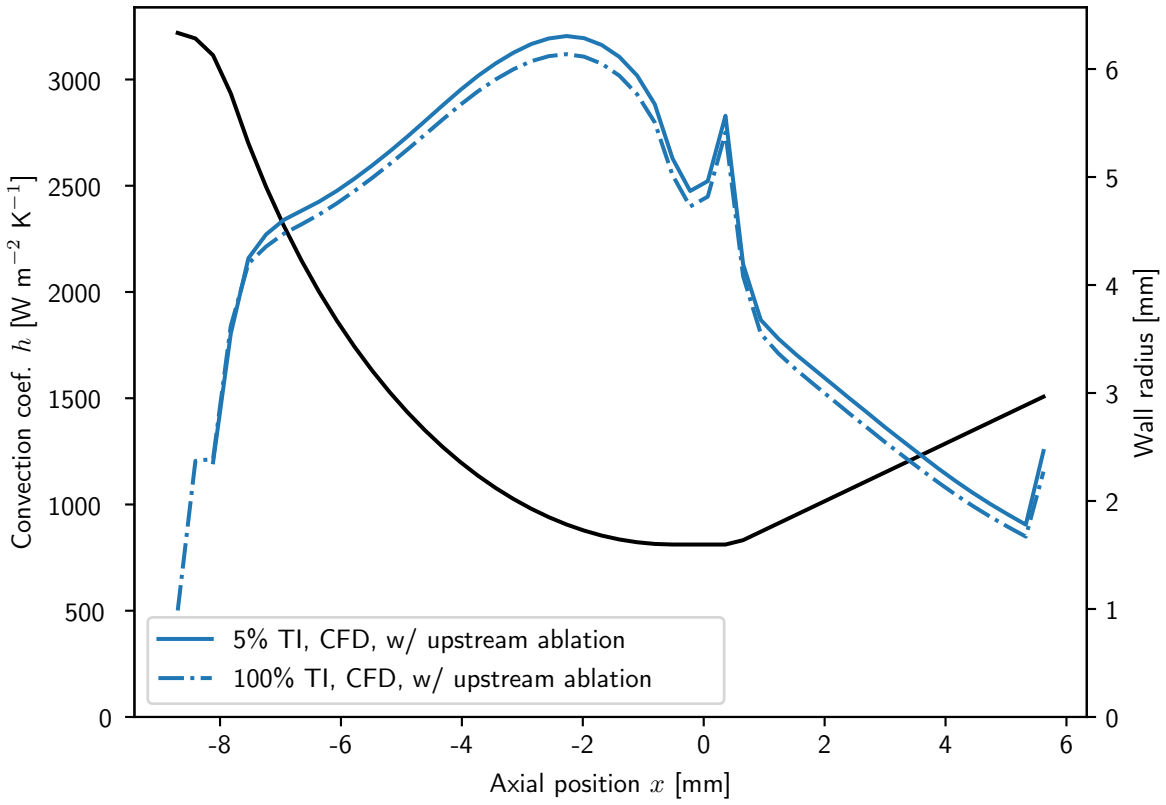

Figure 9-17: Comparison of (upstream ablation case) CFD results for 5% and 100% turbulence intensity. The effect on h is negligible.

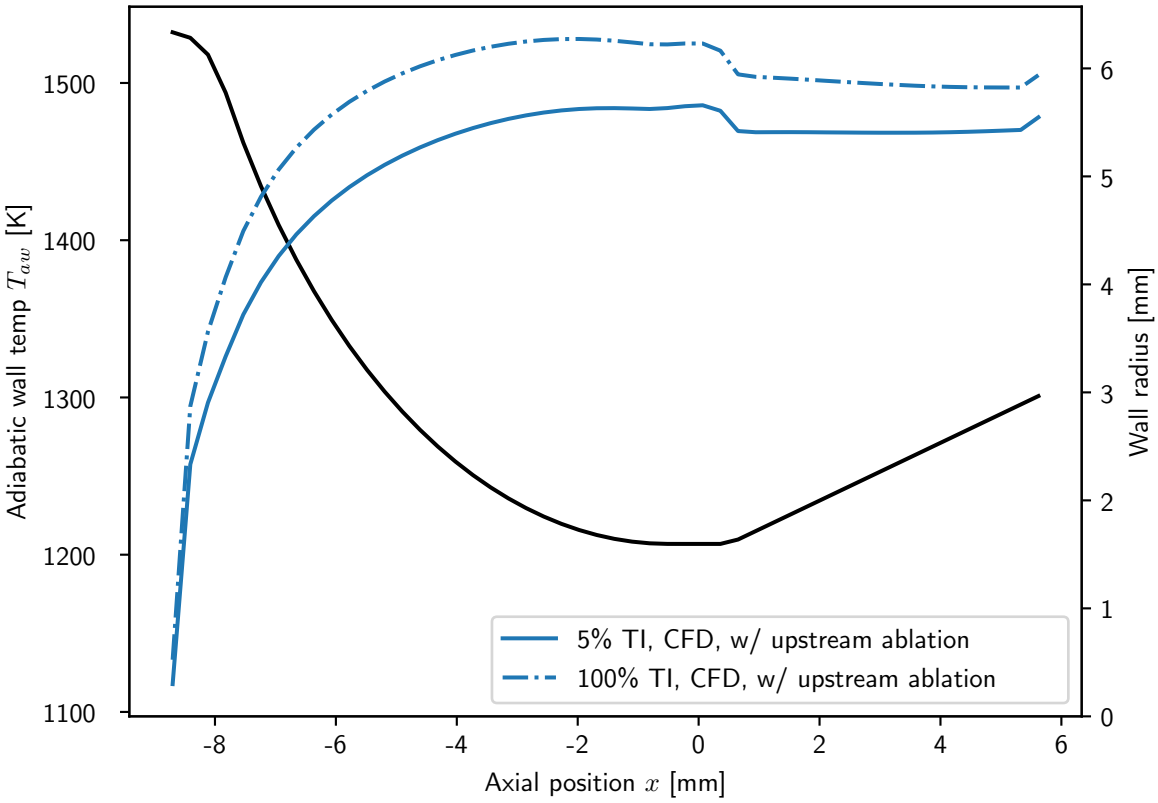

Figure 9-18: Comparison of (upstream ablation case) CFD results for 5% and 100% turbulence intensity. T_{aw} is higher with higher turbulent intensity, as more hot gas is mixed with the cool film.

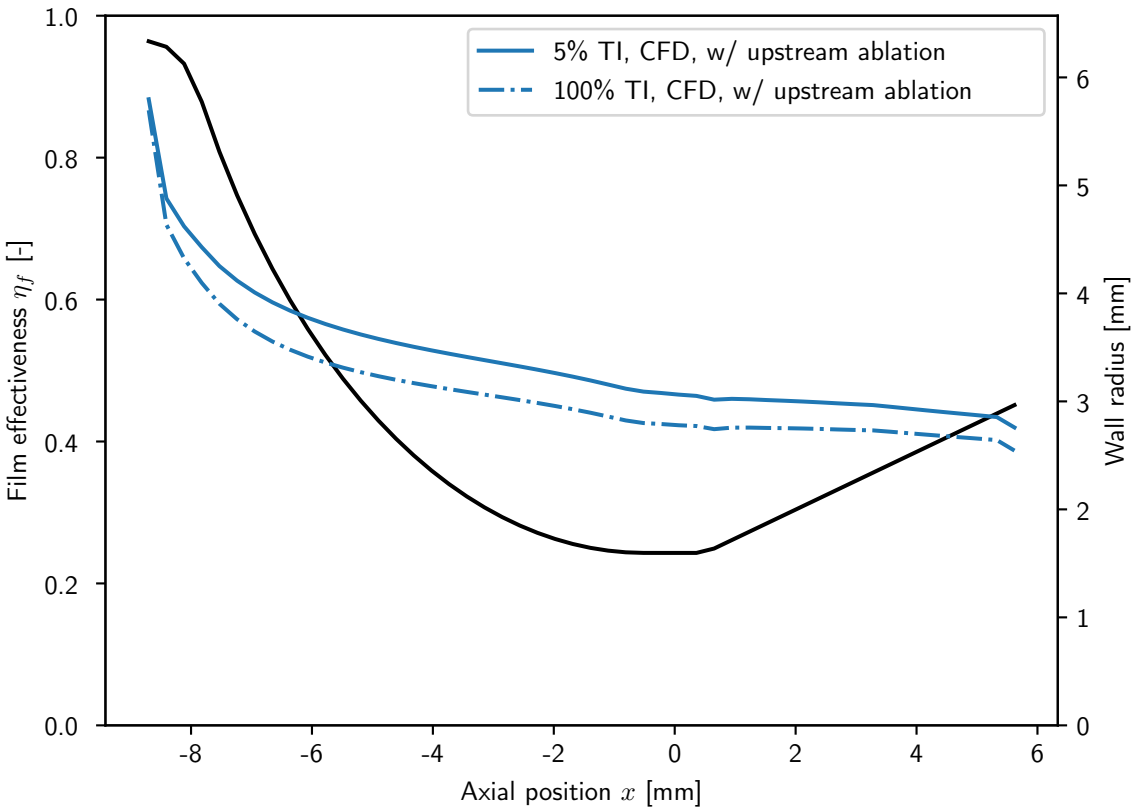

Figure 9-19: Comparison of (upstream ablation case) CFD results for 5% and 100% turbulence intensity. The film cooling effectiveness is lower with higher turbulent intensity, as more hot gas is mixed with the cool film.

9.2.2 External thermal boundary

The external thermal boundary conditions on the nozzle shell depend on the flight conditions, fuselage design, and surface color.

The convective heat transfer (parameterized by the convection coefficient h) will be greater if the airflow is faster and denser. h will be less if the aircraft flies slower or if the flow separates before reaching the nozzle (this depends on the fuselage design). h will also be less at higher altitudes because of the lower air density. h might be between 10 and $80\,\mathrm{W\,m^{-2}\,K^{-1}}$, depending on these factors.

The radiative cooling depends on the surface emissivity ϵ. It might be 0.4 with bare metal, or 0.9 if the shell is painted black to increase emissivity.

Figure 9-20 compares the available cooling from convection and radiation.

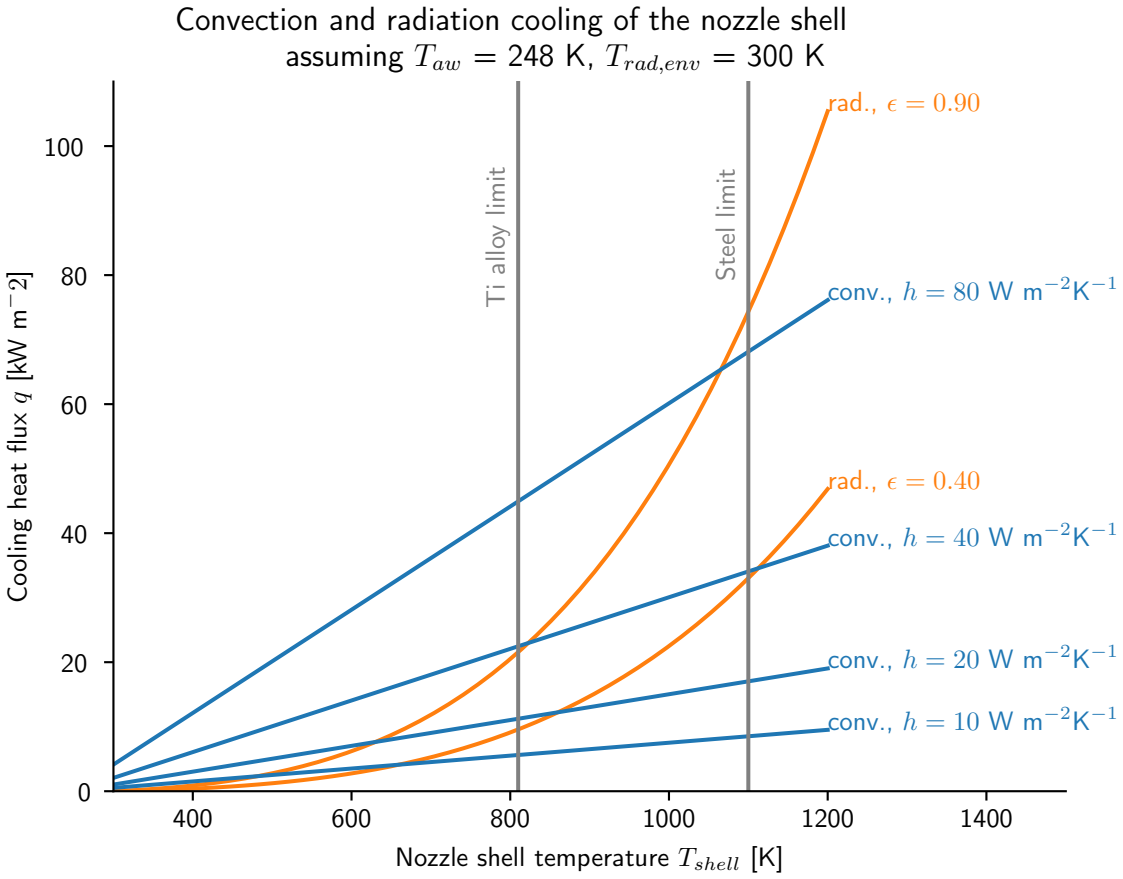

Figure 9-20: Both convection and radiation provide cooling heat flux on the nozzle shell.

9.3 Nozzle thermal simulation

The boundary conditions described above were used in a thermal simulation of the nozzle design from section 9.1.2. The key value to predict with the thermal simulation is the nozzle shell temperature. The nozzle shell temperature must remain within the acceptable temperature limits for the alloy it is made from.

Preferably, the shell temperature would be acceptable for titanium alloy Ti-6Al-4V, the material selected for the motor case. Then, the nozzle shell and motor case can be made as a single part, which would reduce mechanical complexity and mass.

For the example nozzle design analyzed below, the thermal simulation predicts that the shell temperature will be compatible with Ti-6Al-4V if the external convec-

tion coefficient is $\geq 20\,\mathrm{W\,m^{-2}\,K^{-1}}$.

9.3.1 Model description

The thermal simulations were performed on a finite element model of the nozzle insert, insulator and shell. Figure 9-21 shows the model domain for an example nozzle – the example nozzle is from Firefly version 2.1, the same as used in the CFD model in section 9.2.1.3. A 2d axi-symmetric model was used. The insulator was approximated as a solid, with varying thermal conductivity with temperature. The effective thermal conductivity of the ceramic honeycomb was taken from section 10.3.3. The boundary conditions were taken from section 9.2 and are listed in table 9.1.

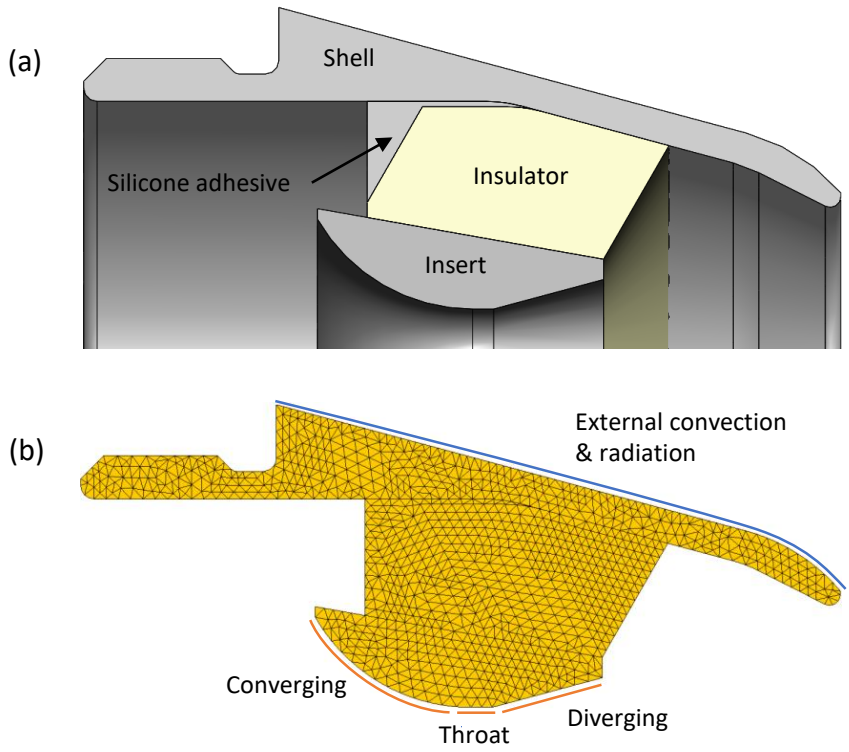

Figure 9-21: (a) The model domain is an axi-symmetric slice through the shell (Ti-6Al-4V), insulator (silica), and insert (boron nitride). The silicone adhesive between the insulator and shell is also modeled. (b) The mesh and boundary conditions.

Region	h [$\mathrm{W\,m^{-2}\,K^{-1}}$]	T_{aw} [K]
Converging	2275	1441
Throat	2416	1519
Diverging	1195	1499

Table 9.1: Internal boundary conditions for the nozzle thermal simulation. Values for h are from the CFD case with upstream ablation and 100% turbulence intensity. Each value is the area-weighted average over that region of the nozzle. T_{aw} is also taken from the CFD data, assuming a combustion gas temperature of 2000 K.

9.3.2 Prediction of nozzle shell temperatures in flight conditions

The thermal model was used to predict the shell temperatures of an example nozzle (the Firefly v2.1 design) under flight conditions.

For this analysis, the internal boundary conditions are those from table 9.1, which assumes a 2000 K combustion gas and 0.7 MPa chamber pressure.

The external boundary conditions are:

- Convection, with several convection coefficients and airflow T_{aw} of 248 K. Several convection coefficients were examined because the convection coefficient depends on the aerodynamic design and flight conditions.

- Radiation, with emissivity of 0.9 to a 300 K environment. This high emissivity would be realized by painting the nozzle shell black.

The simulation results are shown in fig. 9-22. If the external air convection coefficient is above $20\,\mathrm{W\,m^{-2}\,K^{-1}}$, the model predicts that the nozzle shell equilibrium temperature will be within the operating limit of Ti-6Al-4V. With only radiation cooling (i.e., $h = 0$), the predicted nozzle shell equilibrium temperature is 869 K; above the operating limit for Ti-6Al-4V.

However, this model may overestimate the nozzle shell temperatures. The combustion gas could be cooler than assumed in this model, because this model does not

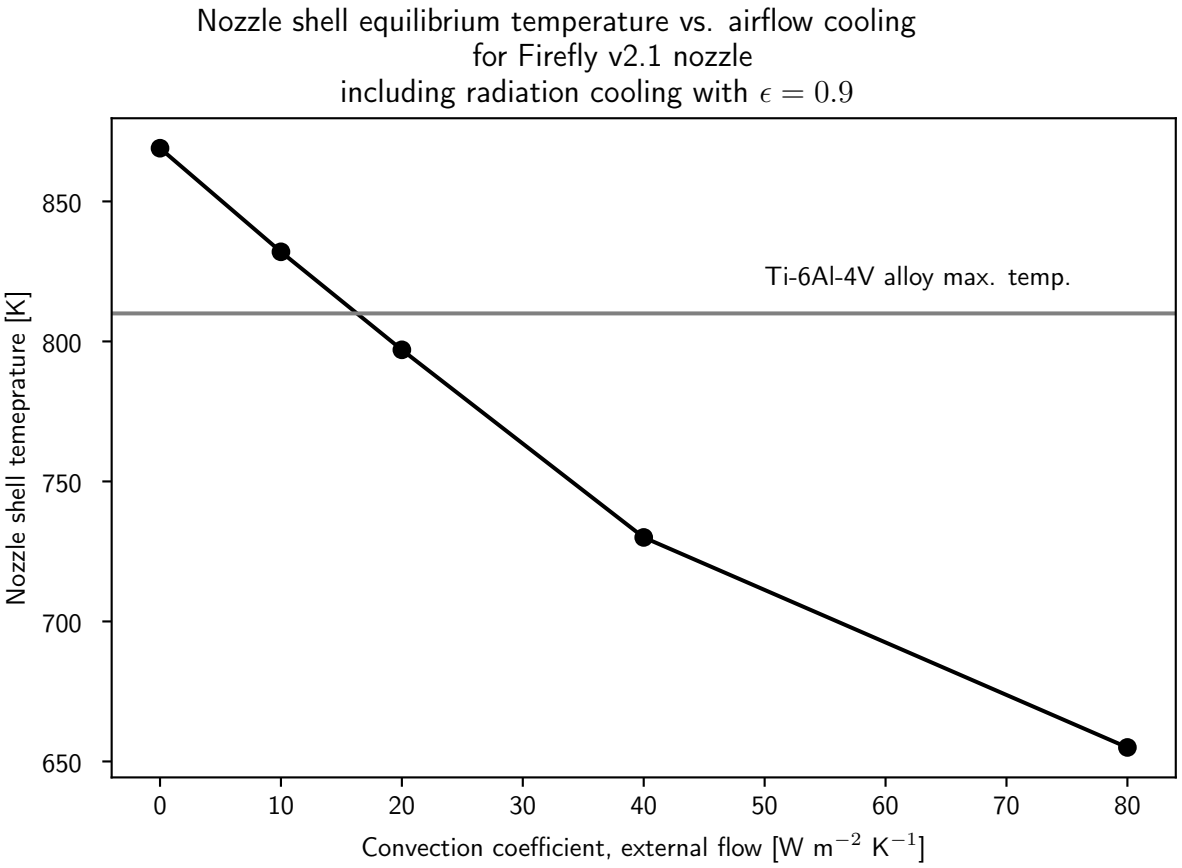

Figure 9-22: Thermal simulations predict an external convection coefficient $\geq 20\,\mathrm{W\,m^{-2}\,K^{-1}}$ is needed to keep the shell temperature within the 'handbook limits' [23] for Ti-6Al-4V. These are the maximum simulated temperatures anywhere in the shell.

take into account the heat loss from the combustion gas to the walls of the motor. As discussed in section 8.3.3, the combustion gas could cool by several hundred kelvin before reaching the nozzle inlet. This would reduce the heat transfer into the nozzle, and possibly lower the shell equilibrium temperature so that a Ti-6Al-4V shell can be used with radiation cooling alone.

Also, different motor designs may used different propellants and different chamber pressures, which would alter the heat transfer into the nozzle. Additionally, the nozzle shell temperatures could be reduced by increasing the radial thickness of the

insulator[11]. Thus, although this example requires some convective cooling, other designs may be able to rely on radiation cooling alone (or may need even more convective cooling).

In some designs, nozzle cooling may limit the altitude and speed the aircraft can fly at. If the nozzle relies on convective cooling, the aircraft must fly low and fast enough to provide sufficient convective cooling. If the nozzle shell can be cooled by radiation alone, then the aircraft can fly at any altitude. For a given design, it is important to determine how much (if any) external convection is needed to keep the nozzle shell temperature within acceptable limits. This can be done using the analysis techniques from this chapter.

If the nozzle shell needs to operate a higher temperature, it could be made from a different alloy, such as stainless steel 316 or In 718 (both usable to about 1100 K). The nozzle shell can be made from a different alloy if it is a separate component from the motor case (as in the Firefly v2.1 example used here). However, if the shell can be the same material as the motor case (Ti-6Al-4V), they could be made as a single part, which would reduce mass and complexity (as in the baseline motor case design from chapter 6). Thus, it is beneficial to keep the nozzle shell temperature within the limits of Ti-6Al-4V.

9.4 Nozzle testing

A ceramic insulated nozzle was tested on the 'Ti Candle' research motor in static fire SF9. The test hardware is described in section 7.2.2.3 and shown in fig. 9-23. The nozzle was instrumented with a single thermocouple (type K) to measure the shell temperature.

[11] although this would increase the base drag of the fuselage

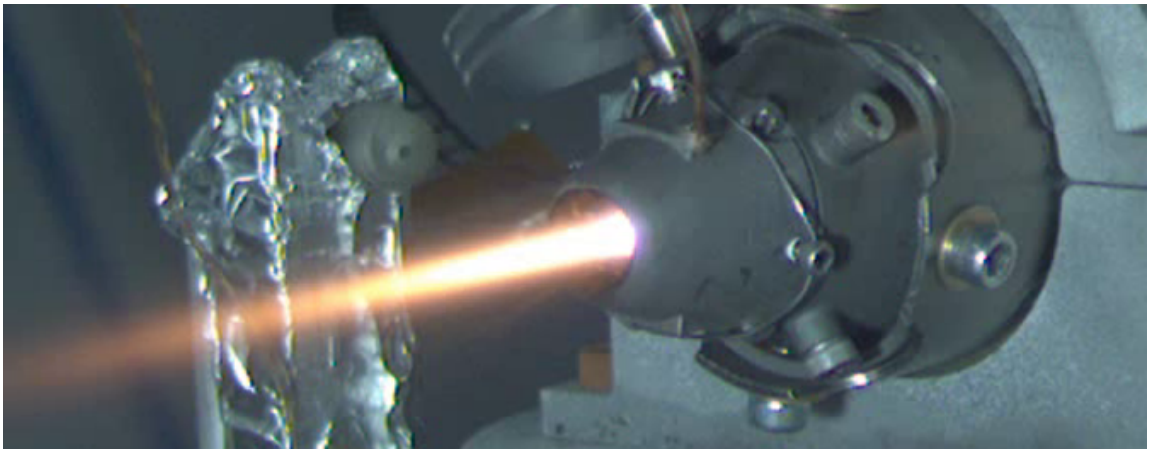

Figure 9-23: A ceramic-insulated nozzle was successfully fired for 39 s in static fire SF9. The nozzle used a silica honeycomb insulator.

9.4.1 Comparison of shell temperature measurements to thermal model

To benchmark the nozzle thermal model, the simulation was run with the nozzle geometry and boundary conditions from SF9. There is moderately good agreement between the simulated and measured shell temperatures [12].

The internal boundary conditions are listed in table 9.2. They are taken from the CFD model in section 9.2.1, but with the combustion gas inlet temperature changed to 1853 K, the flame temperature of the 10% oxamide propellant used in SF9.

The external boundary conditions were:

- Convection, with $h = 630\,\mathrm{W\,m^{-2}\,K^{-1}}$, $T_{air} = 295\,\mathrm{K}$.
- Convection, with emissivity of 0.4, to a 295 K environment.

The nozzle shell material in SF9 was stainless steel 316.

The simulation results are shown in fig. 9-24. The predicted and simulated nozzle shell temperatures match until 11 s. After that, the simulation predicts slightly hotter nozzle shell temperatures than the measurements. This could be due to:

[12] The Biot number of the shell is $\ll 1$ under these conditions, so it is appropriate to speak of a single shell temperature.

Region	h $[\mathrm{W\,m^{-2}\,K^{-1}}]$	T_{aw} [K]
Converging	2275	1376
Throat	2416	1438
Diverging	1195	1419

Table 9.2: Internal boundary conditions for the nozzle thermal simulation of SF9. Values for h are from the CFD case with upstream ablation and 100% turbulence intensity. Each value is the area-weighted average over that region of the nozzle. T_{aw} has been corrected for the lower flame temperature of the 10% oxamide propellant used in SF9.

- Overestimating the thermal conductivity of the insulator at higher temperatures.

- Not accounting for cooling of the combustion gas due to heat loss to the chamber walls. The simulation boundary conditions assume the combustion gas at the nozzle inlet is always at 1853 K. In reality, the combustion gas will become cooler later in the burn, as more chamber wall is exposed.

Both of these factors would lead to an error which increases with time, as observed in fig. 9-24.

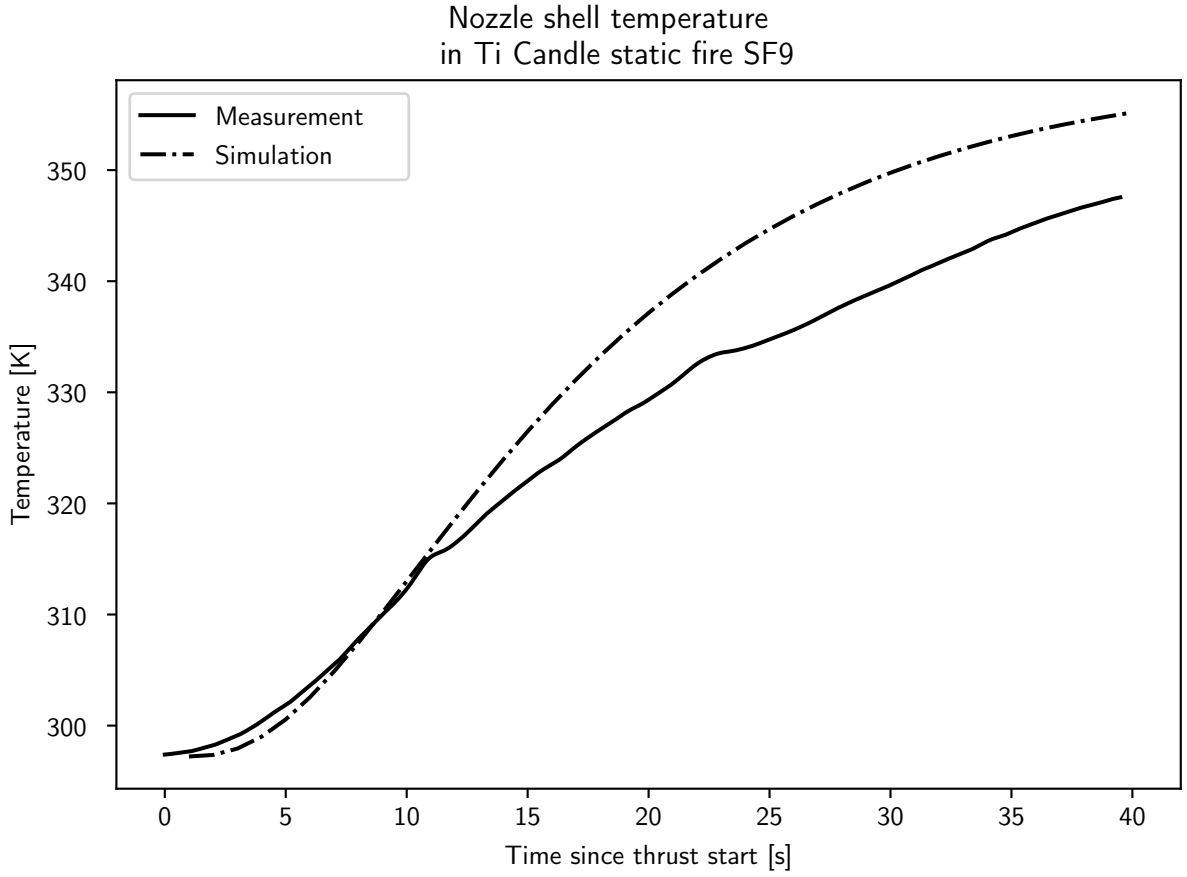

Figure 9-24: The simulation predicts slightly higher nozzle shell temperatures than were measured in SF9.

9.4.2 Damage to boron nitride nozzle insert

The nozzle insert suffered some damage during static fire SF9. The throat eroded, increasing the throat diameter from 2.82 mm to 2.95 mm. This is more erosion than was observed on the graphite nozzle inserts with the water-cooled nozzle. Also, the diverging section of the nozzle insert surface became pitted (see fig. 9-25).

The thrust coefficient efficiency ζ_{C_F} was lower than typical in this firing, probably due to the damaged nozzle surface distorting the flow in the diverging section. The measured thrust coefficient was about 0.789 times the ideal value, i.e. $\zeta_{C_F} = 0.789$ (see fig. 9-26). For comparison, in another test without nozzle damage (SF5) the thrust coefficient efficiency was higher: $\zeta_{C_F} = 0.851$. The low ζ_{C_F} in SF9 is likely

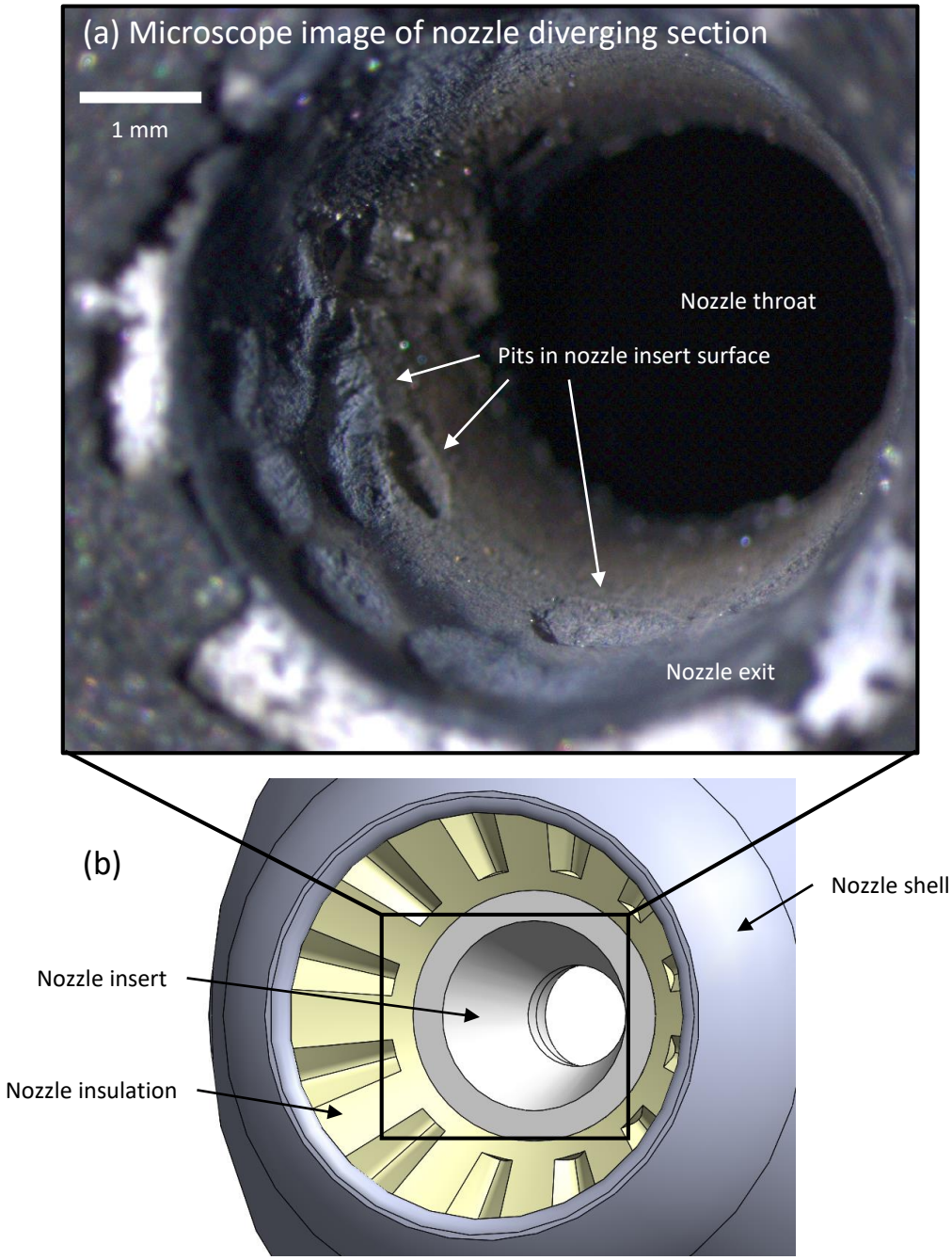

Figure 9-25: The nozzle's diverging surface became pitted during SF9. A CAD model of the nozzle from the same view (b) is provided for context.

due to the pitting.

The pitting and erosion occurred because this nozzle prototype used a lower-grade boron nitride material. The SF9 nozzle insert was made from impure boron

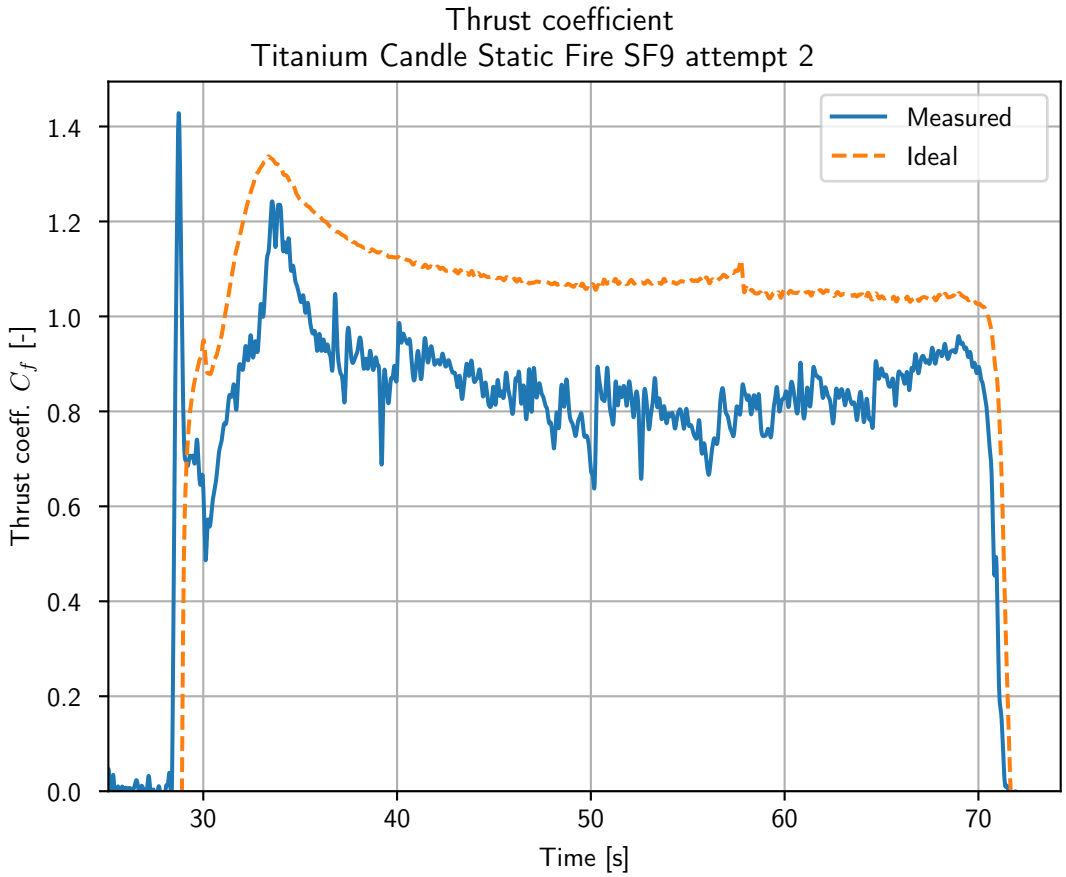

Figure 9-26: In SF9, the measured C_F is (on average) 0.789 times the ideal C_F.

nitride, which contained 5% B_2O_3 as a binder [13]. B_2O_3 has a much lower temperature tolerance than pure BN; the maximum rated temperature of the BN-B_2O_3 ceramic was only 822 K. Clearly, the material was exposed to much higher temperatures during the motor firing. This could account for the pitting.

It is expected that using better BN will resolve the pitting issue. Since this test, new nozzle inserts have been machined from a 99% pure BN material with a maximum rated temperature of 3300 K (see section 10.5). The improved inserts have not yet been tested in a motor firing.

[13]The material used was Momentive HBN 2109106, purchased from McMaster Carr as stock number 84995K24.

9.5 Recommendations for further nozzle development

In this work, a new nozzle has been design and demonstrated. This nozzle uses ceramic insulation, so that it can survive long burn times despite its small size. The demonstration of this nozzle is a major technology risk reduction for small, low-thrust motors.

9.5.1 Nozzle testing and modeling recommendations

Further work to refine this design should begin with a full duration test of this nozzle on the research motor. The nozzle insert should be made from high quality boron nitride - this should resolve the surface pitting issue observed in the initial test. The nozzle should be instrumented to measure:

- combustion gas temperatures at the nozzle inlet
- nozzle insert temperature
- nozzle shell temperature

These data will help to further validate the nozzle thermal simulations described in this chapter.

Also, the external convection coefficient on the nozzle shell in flight should be better estimated. This is coupled to the design of the aircraft and trajectory.

9.5.2 Nozzle design recommendations: base diameter trade-offs

Increasing the fuselage base diameter is an option to make the nozzle thermal design somewhat easier. The base diameter is the diameter of the circular aft end of the fuselage (fig. 9-27). Selecting the fuselage base diameter involves trade-offs between drag, propellant volume, and nozzle design. Increasing the base diameter increases drag. However, it also increases the fuselage volume, allowing for more propellant.

Extra drag would decrease the vehicle's range, whereas extra propellant would increase range. Estimating the net effect (extra drag and extra propellant) of increasing base diameter on range is thus a complicated question. It can be addressed by a multi-disciplinary design optimization framework which models propulsion, aerodynamics and trajectory [14]. This modeling effort was still in progress at the time of this writing.

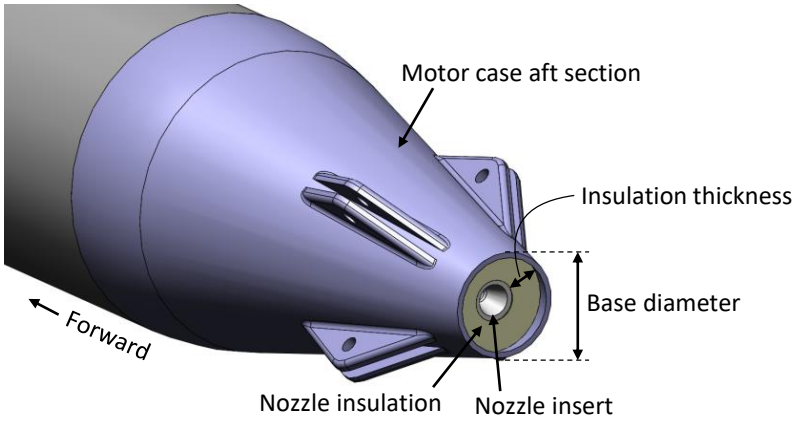

Figure 9-27: The fuselage base diameter determines how thick the nozzle insulation can be.

For the baseline Firefly design, preliminary results indicate that a 2 mm increase in base diameter (a 1 mm increase in nozzle insulation thickness) would only decrease range by 0.1%. Thus, increasing the insulation thickness by a mm or two is probably a viable option [15].

Putting more insulation between the hot gas boundary and the nozzle shell reduces the nozzle shell temperature. As was shown in fig. 9-22, the predicted shell temperatures with 6 mm thick insulation are marginal. Under some cooling conditions, the shell temperature would exceed its allowable temperature. Slightly thicker ceramic insulation would 1) keep the predicted shell temperature within limits under all cooling conditions and 2) make the nozzle thermal design more robust to modeling

[14] This optimization framework is developed by Peter Sharpe, a graduate student in the Firefly group.

[15] However, it does not seem possible to make the nozzle insulation thick enough for any of the conventional designs listed in section 9.1.1 to work. The ceramic insulation is necessary.

errors. These improvements seem to be worth a possible 0.1% decrease in range.

Chapter 10

Ceramic nozzle insulation

Chapter 9 introduced a small nozzle capable of operating in thermal steady state for long burn durations; this nozzle design relies on ceramic insulation. This chapter discusses the use of ceramics for nozzle insulation. Small, long-burn-time nozzles require an insulation material which can withstand exposure to high ($> 1500\,\mathrm{K}$) temperatures for several minutes without ablating or otherwise degrading. Ceramics can meet these requirements, but are susceptible to thermal stress failures. Thermal stresses must be taken into account in the selection of the ceramic material and in the design of the insulation. With the right material and design, ceramic insulation can be made to withstand the extreme thermal gradients in small rocket nozzles. Ceramic nozzle insulation was successfully demonstrated in a motor firing in this work.

Section 10.1 of this chapter reviews how thermal stresses due to temperature gradients can cause fracturing in poorly designed ceramic insulators. However, thermal stresses can be reduced by appropriate material selection. A material property index for resiliency to thermal stress is introduced in section 10.1.2 and used to compare common engineering ceramics in section 10.1.3. This comparison identifies fused silica as a promising material.

A novel insulator – a ceramic material with a cellular (honeycomb) structure – is presented in section 10.2, and its thermal stresses and thermal conductivity are ana-

lyzed in section 10.3. The production of cellular ceramic via additive manufacturing is described in section 10.4.

The nozzle design from chapter 9 uses a nozzle insert, which forms the converging-diverging gas flow path and is bonded into the nozzle insulation. The nozzle insert material must be compatible with the nozzle insulation material. The selection of boron nitride as a nozzle insert material is described in section 10.5.

Finally, testing of the ceramic insulation and ceramic insulated nozzles is reported in section 10.6. This ceramic insulation was subjected to thermal stress tests, and successfully used in a motor firing.

10.1 Thermal stress issues in ceramic insulators

Ceramics seem like a natural choice for high-temperature insulation; however, a monolithic ceramic insulator would be prone to cracking due to thermal stresses. [1]

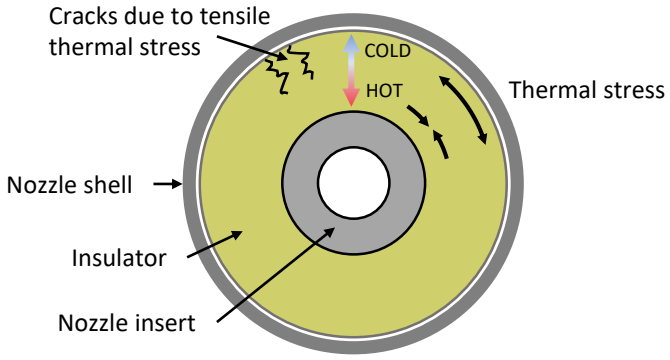

Figure 10-1: The inside of the nozzle insulation is much hotter than the outside. This creates tensile thermal stress at the outside of the insulation, which can cause the brittle ceramic to crack.

In the nozzle insulation, thermal stresses are caused by the large temperature difference between the inside and outside of the insulation (fig. 10-1). The inside of the insulation can be over 1000 K hotter than the outside. The thermal expansion of

[1] Monolithic ceramic (clay) nozzles are used on some small black-powder motors for model rockets [22]. However, the black powder propellant only burns at ~1300 K [8], so the thermal shock is less, and these motors only operate for a few seconds.

the hot inner material is constrained by the cool outer material. This creates thermal stresses, in compression at the inside and in tension at the outside. Ceramics are weak in tension, so cracks can occur due to the tensile thermal stresses at the outside of the insulation. These cracks can cause the insulation, and the nozzle, to fail.

10.1.1 Example of failure due to thermal stress

As an example of ceramics failing due to thermal stresses, this section describes the failure of a ceramic nozzle in an early prototype of the Firefly rocket motor. Firefly version 1 used a solid zirconia[2] nozzle. This nozzle was a single piece of cast zirconia bonded into the aft end of the motor case (fig. 10-2). The nozzle design is described in more detail in the author's MS thesis [89].

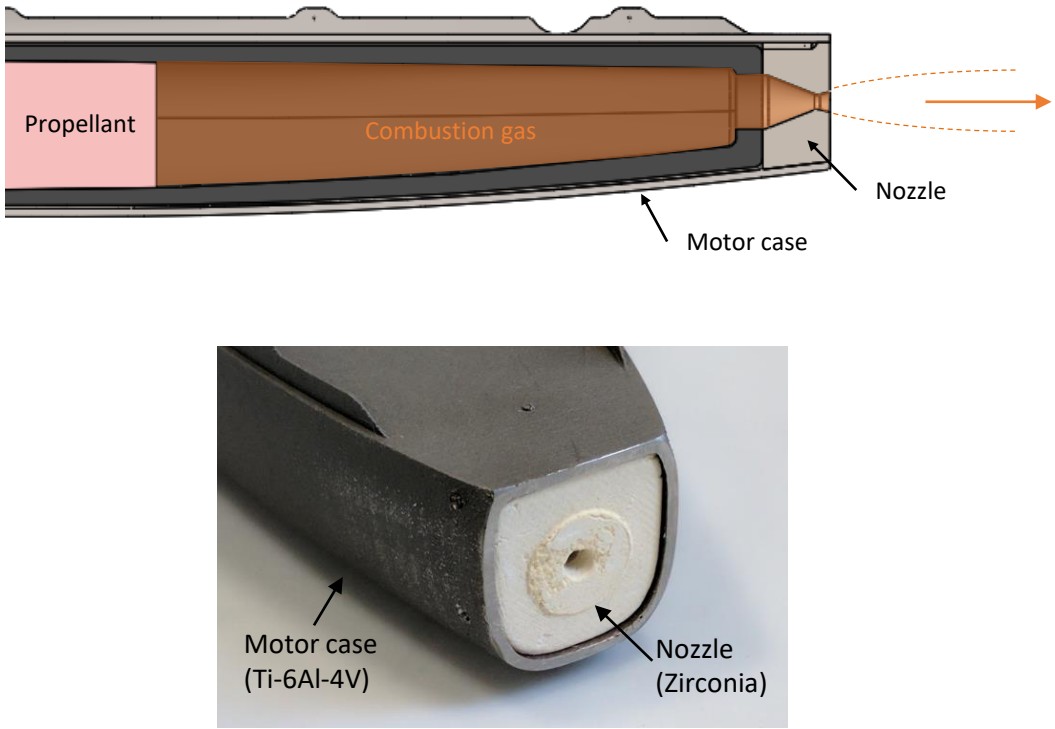

Figure 10-2: A solid zirconia nozzle was used on Firefly v1. Top: section view of the nozzle design. Bottom: the nozzle, just before being bonded into the motor case.

These nozzles cracked due to thermal stresses during both static firings of the v1

[2]Rescor 760 form Cotronics Corp.

motor. During one static firing, a crack at the outside of the nozzle allowed a large hot gas leak to flow around the nozzle – this leak is visible as a second bright plume in fig. 10-3(a). The heat from the hot, flowing gas softened and deformed the case material around the leak path (fig. 10-3(b)). After the firing, numerous other cracks were also observed in the zirconia nozzle (fig. 10-3(c)).

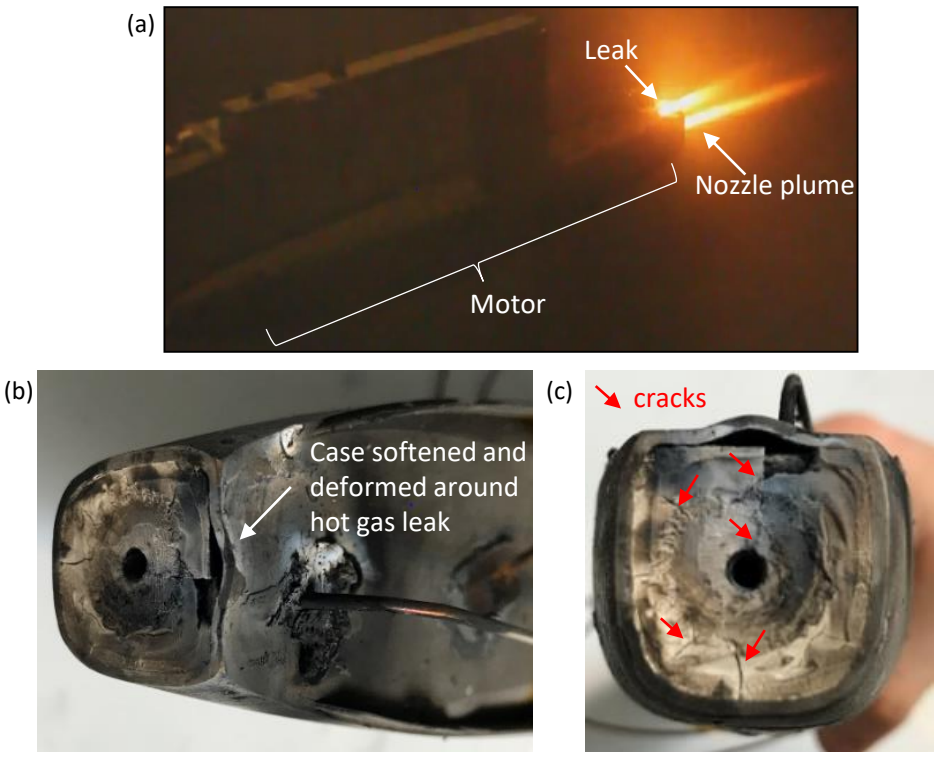

Figure 10-3: During firing, the zirconia nozzle cracked in several places (bottom images). One crack was large enough to cause a large leak of hot gas during the firing (top image).

The next two subsections will examine the mechanics of thermal expansion to assess why that nozzle failed, and to determine if any other solid ceramic materials are suitable as nozzle insulation. It will be shown that another ceramic material, fused silica, is much more resilient to thermal stresses than the zirconia used in the Firefly v1 nozzle.

10.1.2 The thermal shock resistance parameter for comparing materials

The 'thermal shock resistance parameter' is a material property which compares different material's ability to withstand thermal stresses.

Thermal stresses arise from the large thermal gradient across the insulator. If the insulator is performing adequately, its inner surface will be $> 1000\,\mathrm{K}$ hotter than its outer surface. The inside of the insulator will expand more than the outside, inducing a tensile thermal stress which is maximum at the outer surface. This subsection quantifies this thermal stress and determines its dependence on the material properties of the ceramic.

Barron and Barron [5] provide an analytic solution to the thermal stresses in a thick-walled cylinder heated from the inside. This is only an approximation of the insulator geometry, but captures the essential physics. The circumferential tensile stress on the outer surface is proportional to:

$$\sigma_\theta \sim \frac{\alpha_{LE} E}{1-\nu} \Delta T \tag{10.1}$$

where α_{LE} is the linear coefficient of thermal expansion, E is Young's modulus, ν is Poisson's ratio, and ΔT is the temperature difference between the inner and outer surface. The proportionality factor depends on the temperature distribution and the ratio of inner to outer radii, but is generally of order unity (it can be found by solving the integrals presented in Barron and Barron [5]).

The thermal stresses depend on the mechanical properties, and will be different for different materials. We wish to define a material property index which compares a material's strength to the magnitude of the thermal stress. Following Kübler and Gauckler [42], we define the thermal shock resistance parameter R_s:

$$R_s \equiv \frac{S_{flex}(1-\nu)}{E\alpha_{LE}} \sim \frac{S_{flex}\Delta T}{\sigma_\theta} \tag{10.2}$$

where S_{flex} is the flexural strength. Materials with higher R_s are more resilient to differences in thermal expansion [3]. R_s has units of kelvin, and $R_s/\Delta T$ is proportional to (strength) / (thermal stress at temperature difference ΔT). Because the proportionality factor in eq. (10.1) is roughly 1, R_s is roughly the inside-to-outside temperature difference a ceramic insulator can withstand without cracking[4]. We would like a material with $R_s \gg 1000\,\mathrm{K}$, to reliably withstand a 1000 K temperature difference in steady state, and higher temperature differences during the warm-up transient.

10.1.3 Thermal shock resistance of common engineering ceramics

Several common engineering ceramics are compared in table 10.1, on the key parameters of maximum service temperature T_{max}, thermal conductivity k, and thermal shock resistance parameter R_s. The desired properties are $T_{max} > 1800\,\mathrm{K}$, $k < 5\,\mathrm{W\,m^{-1}\,K^{-1}}$, and $R_s > 1000\,\mathrm{K}$. None of the ceramics meets the desired values for all three parameters, although Formlabs silica comes close. More detailed analysis is required to determine if Formlabs silica, with its marginal R_s, could function as an insulator for the Firefly nozzle. This is examined in the next section. That section will consider both a solid insulator and one with a cellular structure.

[3] Kübler and Gauckler [42] define R_s as the resistance to an instantaneous surface temperature change. Equation (10.1) shows that this is also the relevant parameter for an internally heated cylinder in steady state.

[4] Intuition for R_s: imagine subjecting a sample of the ceramic to thermal shock by heating it to a uniform temperature and then dunking it in water. If the temperature difference is much above R_s, the ceramic will crack (This is a standard test for thermal shock resistance – e.g. JIS R 1648). For example, the silicon nitride ceramic in table 10.1 can be quenched from a temperature difference of up to 800 K without cracking [45]; this is almost equal to its R_s value of 742 K.

Material	Grade	T_{max} [K]	k [$\mathrm{W\,m^{-1}\,K^{-1}}$]	R_s [K]	α_{LE} [$10^{-6}\ \mathrm{K^{-1}}$]	E [GPa]	ν [-]	S_{flex} [MPa]
Zirconia	Rescor 760	2478	0.94	2.8	10.1	200*	0.31*	8.27
	Aremco 502-1900 YTZP	2070	2.2	67.9	10.5	200*	0.31*	206.8
Silica	Rescor 750	1755	0.58	226	0.54	70*	0.17*	10.3
	Formlabs ceramic	1850*	1 *	960	0.6*	50	0.14	33.5
Magnesium oxide	Aremco 502-676	2070	2.2	37.0	13.9	300	0.36	241
Boron nitride	Aremco 502-1600	3270	22	965	0.3	50	0.25	19.3
Aluminum oxide	Aremco 502-1400	1922	31.7	126	6.3	300	0.25	317
Silicon nitride	Kyocera SN240	2100*	27	742	3.3	300	0.28	1020

Table 10.1: Comparison of candidate ceramic materials for nozzle insulation. The first three properties are the most important: the maximum service temperature T_{max}, thermal conductivity k, and thermal shock resistance parameter R_s. A material with $T_{max} > 1800\,\mathrm{K}$, $k < 5\,\mathrm{W\,m^{-1}\,K^{-1}}$, and $R_s > 1000\,\mathrm{K}$ is desired. The four rightmost columns document the properties used to calculate R_s. Properties marked with $*$ were not listed for the particular grade, and are instead general estimates for that class of ceramic. Data from [3, 24, 45, 18].

10.2 Cellular ceramic insulation

Ceramic materials with a porous structure are widely used as insulation materials: examples include firebrick, ceramic foam kiln insulation, and silica-fiber Reusable Surface Insulation tiles used on the Space Shuttle Orbiter [54]. A porous structure reduces the stiffness of the material, which reduces the intensity of thermal stresses in the material. Thus, porous ceramics can have excellent thermal shock resistance (high R_s). For example, Reusable Surface Insulation tiles can withstand a thermal shock of 1200 K (by plunging into water while hot) without damage [54].

Because the insulator should be gas-tight, we will consider ceramic materials with a closed cellular structure. There are many ways to produce closed cellular structures. We chose to produce the structures via additive manufacturing, as this gives design freedom for choosing the shape, size and orientation of the cells [5].

The geometry for the cellular insulator is a honeycomb wrapped onto the revolved shape of the insulation (fig. 10-4). This orientation of the honeycomb gives low stiffness in the circumferential direction at the outer face. The walls in the $r\theta$ plane are corrugated so they can flex to comply with thermal expansion. There are multiple solid walls in the axial direction. This gives redundancy against leaks; the insulator will remain gas tight even if a few cell walls crack. The thickness of the cell walls is just over 1 mm; this is about the thinnest wall that can reliably be produced.

Further, this shape is compatible with the vat photo-polymerization[6] printing process (on the Formlabs Form 2 printer).

[5]The author credits Kelly Mathesius for originating the idea of a cellular ceramic insulator produced by additive manufacutring.

[6]also known as stereo-lithography (SLA)

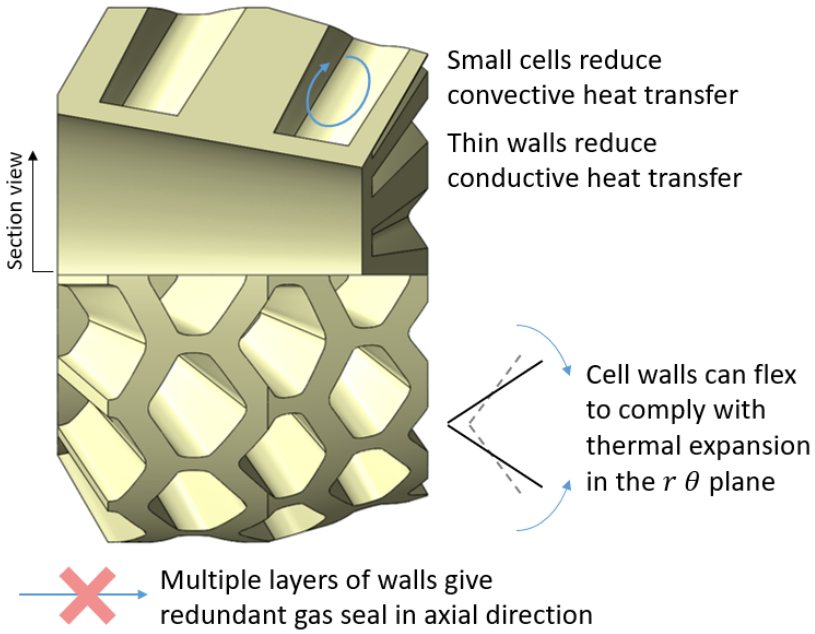

Figure 10-4: Geometry of the honeycomb cellular ceramic insulation invented for this work.

10.3 Modeling thermal stresses and heat transfer in cellular ceramic insulation

The thermal stresses were assessed via both honeycomb mechanics theory (section 10.3.1) and a finite element model (section 10.3.2). Both models predict that the peak stress is higher in the honeycomb insulation than in solid insulation, but the stressed volume is smaller. Both the stress level and the stressed volume are important to the failure probability of ceramics.

10.3.1 Honeycomb mechanics theory

This section will attempt to estimate the thermal shock resistance parameter R_s of the honeycomb structure. To calculate R_s, it is necessary to determine the effective strength, stiffness and Poisson's ratio of the honeycomb structure. A simplified model is used here: imagine unrolling the honeycomb into a planar form (see fig. 10-5). The strength, stiffness and Poisson's ratio will be computed for the planar honeycomb,

using the honeycomb mechanics theory presented in Gibson and Ashby [26]. Gibson's theory suggests that, if one zooms out enough, the honeycomb can be treated as a continuum material, with mechanical properties which depend on the cell geometry and the mechanical properties of the solid material. As the honeycomb insulator is only a few cells tall, the application of the continuum model is dubious.

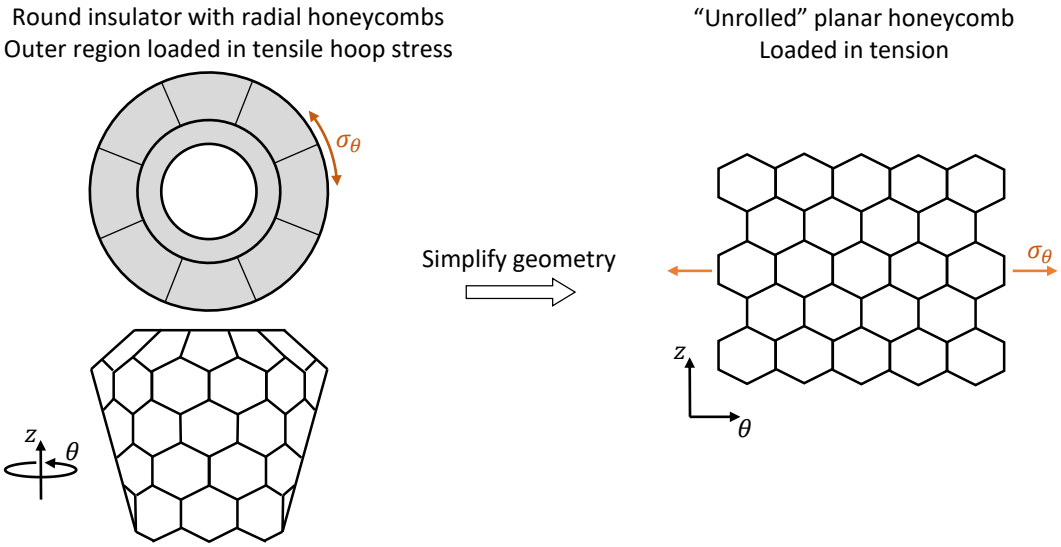

Figure 10-5: The effective strength and stiffness of the honeycomb insulator are estimated using a simpler model of an 'unrolled' planar honeycomb.

Following Gibson's notation, we use superscript $*$ to denote the effective mechanical properties of the honeycomb, and superscript s to denote the properties of the solid material from which it is made. To compute R_s^*, the thermal shock resistance of the honeycomb, we need:

- E_θ^* the stiffness of the honeycomb in the θ direction.
- $S_{f\theta}^*$ the fracture strength of the honeycomb in the θ direction.
- $\nu_{\theta r}^*$ the Poisson's ratio of the honeycomb (ratio of strain in the radial direction to strain in the circumferential direction)

Cell geometry The cell geometry used in the honeycomb insulator is (see fig. 10-6):

- $\theta = 33^\circ$
- $l = 3.2\,\mathrm{mm}$
- $h = 1.8\,\mathrm{mm}$
- $t = 1.1\,\mathrm{mm}$

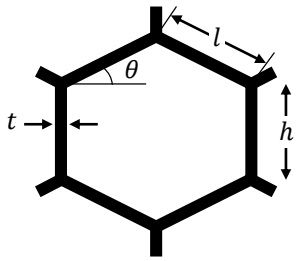

Figure 10-6: The cell geometry parameters.

Stiffness The stiffness of the honeycomb is given by equation 4.7 from [26]:

$$\frac{E^*_\theta}{E^s} = \left(\frac{t}{l}\right)^3 \frac{\cos\theta}{(h/l + \sin\theta)\sin^2\theta} \approx 2.553 \left(\frac{t}{l}\right)^3 \tag{10.3}$$

For our cell geometry, the coefficient is 2.553 and the stiffness ratio is 0.104. The coefficient is 2.3 for a regular hexagonal honeycomb.

Strength The fracture strength of a brittle honeycomb in tension is [7]:

$$\frac{S^*_{f\theta}}{S^s_f} = \left(\frac{t}{l}\right)^2 \frac{1}{6(h/l\sin\theta)^{1/2}\sin\theta} \approx 0.291 \left(\frac{t}{l}\right)^2 \tag{10.4}$$

For our cell geometry, the coefficient is 0.291 and the fracture strength ratio is 0.034. The coefficient is $4/9 \approx 0.444$ for a regular hexagonal honeycomb.

There is a further complication. The effective strength of a (brittle) ceramic depends on the volume, and the stressed volumes are different in the honeycomb vs.

[7] This is for a single wall failing in bending, due to either either tension or compression. Gibson gives a different equation specifically for tension in brittle foams based on fracture mechanics, but its only valid for large defects of >7 broken walls.

the solid. Failure occurs due to stress concentration at defects; a larger volume is more likely to contain a defect large enough to cause failure at a given stress level. Thus, the honeycomb, which has less (highly stressed) volume, will have higher strength than the solid.

Solid mechanics theory treats the failure of brittle parts as a random process, modeled by a Weibull distribution [26, 42]. This theory predicts the probability of failure to be:

$$P_f = 1 - \exp\left(-\int_{V_0}\left(\frac{\sigma}{\sigma_0}\right)^m \frac{dV}{V_0}\right) \tag{10.5}$$

where σ is the stress magnitude in each dV element, σ_0 is the characteristic stress of the Weibull distribution, and m is the Weibull modulus [8]. The parameters σ_0 and m are properties of the material which depend on the distribution of flaws in the material; they are determined experimentally by (many) tension or bending tests [26, 42]. For a given test specimen size, materials with small m (< 10) have a large spread in the stress at failure. Materials with high m have a less variance in the failure stress, and in the limit $m \to \infty$ failure always occurs at a stress level of σ_0.

The effective strength (which here means the stress level that gives a certain probability of failue P_f) depends on volume. For two regions (1, 2) each with uniform stress, the ratio of effective strengths is [26]:

$$\frac{\sigma_1}{\sigma_2} = \left(\frac{V_2}{V_1}\right)^{\frac{1}{m}} \tag{10.6}$$

Smaller regions are stronger, and the volume effect is more significant in materials with lower m.

The honeycomb and the solid have different loading configurations (large region in tension vs. small regions in bending); a precise comparison would be mathematically difficult. As a sloppy approximation, use eq. (10.6), with the right hand side as the fraction of the plane which is at 'high' stress in the 2D honeycomb. There are two

[8] The stress term is sometimes written as $(\sigma - \sigma_u)/\sigma_0$, but σ_u is usually 0 for ceramics [26]

regions of high stress (due to bending) per cell, each is roughly $(\frac{1}{2}t) \times (\frac{1}{4}l)$ [see fig. 10-7]. The area of a whole cell is $2l^2 \cos\theta(h/l \sin\theta)$. Thus the volume fraction of the honeycomb which is highly stressed is roughly:

$$\frac{2\frac{1}{8}tl}{2l^2 \cos\theta(h/l \sin\theta)} \approx \frac{1}{10}\frac{t}{l} \tag{10.7}$$

Thus, to account for volume effects, we could include a 'bonus' factor of $(\frac{1}{10}\frac{t}{l})^{-1/m}$ in the strength ratio:

$$\frac{S^*_{f\theta}}{S^s_f} \approx \left(\frac{t}{l}\right)^2 \frac{1}{6(h/l \sin\theta)^{1/2} \sin\theta} \left(\frac{1}{10}\frac{t}{l}\right)^{-\frac{1}{m}} \sim \left(\frac{t}{l}\right)^{2-\frac{1}{m}} \tag{10.8}$$

For $t/l = 1.1/3.2$, the magnitude of the volume-based strength increase $(\frac{1}{10}\frac{t}{l})^{-1/m}$ is 5.4 at $m = 2$ and 1.4 at $m = 10$.

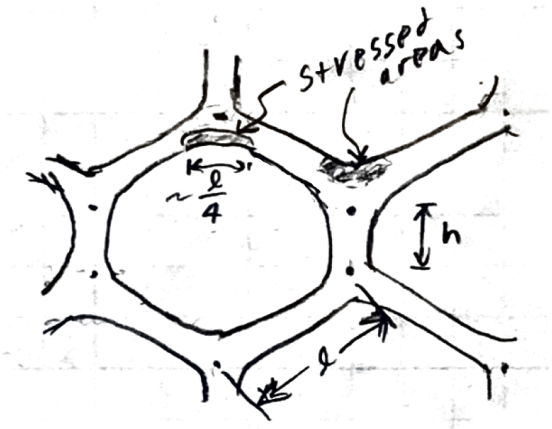

Figure 10-7: The highly stressed areas associated with one cell of a 2D honeycomb, loaded in tension left-right across the page.

Poisson's ratio The Poisson's ratio $\nu^*_{\theta r}$ (out-of-plane strain due to in-plane strain) is zero [26].

Combining the above equations,

$$\frac{R^*_s}{R_s} = \frac{S^*_{f\theta}}{S^s_f} \frac{\left(\frac{\alpha_{LE} E^s}{(1-\nu^s)}\right)}{\left(\frac{\alpha_{LE} E^*_\theta}{(1-\nu^*_{\theta r})}\right)} \tag{10.9}$$

$$\frac{R_s^*}{R_s} = \frac{S_{f\theta}^*}{S_f^s}\frac{E^s}{E_\theta^*}\frac{1}{(1-\nu^s)} \tag{10.10}$$

For regular hexagonal cells,

$$\frac{R_s^*}{R_s} \approx 0.19\left(\frac{t}{l}\right)^{-1}\left(\frac{1}{10}\frac{t}{l}\right)^{-\frac{1}{m}}\frac{1}{1-\nu_s} \tag{10.11}$$

For our cell geometry,

$$\frac{R_s^*}{R_s} \approx 0.11\left(\frac{t}{l}\right)^{-1}\left(\frac{1}{10}\frac{t}{l}\right)^{-\frac{1}{m}}\frac{1}{1-\nu_s} \tag{10.12}$$

Ignoring Weibull volume effects ($m \to \infty$), R_s^*/R_s for our honeycomb is 0.39. Thus, the honeycomb is predicted to have *lower* thermal stress resistance than the solid material. To make the honeycomb more shock resistant than the solid ($\frac{R_s^*}{R_s} > 1$), we would need thinner walls, $t/l < 0.22$ (for regular hexagons) or $t/l < 0.13$ for the current cell geometry. The current wall thickness ratio is $t/l = 0.34$. However, the walls cannot be made much thinner due to manufacturing considerations.

The honeycomb may have more thermal stress resistance than the solid if Weibull volume effects are taken into account. For our honeycomb, the above model predicts the honeycomb is better if $m < 3.6$. The Weibull modulus m of Formlabs silica is not known to the author. According to Kübler and Gauckler [42], m is usually between 1 and 10 for ceramics which are not specially toughened – this plausible range contains the 'critical' value of 3.6. With the current state of knowledge, the author cannot determine if the honeycomb geometry improves the thermal shock resistance of the silica insulator.

10.3.2 Finite element model of thermal stresses

Finite element analysis was used to gain more insight into the thermal stresses present in honeycomb and solid insulators. The analysis was performed in two steps: First, a transient thermal simulation was performed to find the most extreme tempera-

ture profile in each insulator during the warm-up transient. Second, a mechanical simulation calculated the stresses due to that temperature profile.

10.3.2.1 Model setup

The simulations were performed in SolidWorks Simulation 2019. Each model consists of an insulator bonded to an insert. The simulation domain is a 30° slice – this is the smallest repeating unit for the honeycomb insulator. The domain and mesh are shown in fig. 10-8. The structural shell is not included because the insulator is bonded to the shell with a compliant adhesive, thus insulator is free to expand or contract within the shell.

Pressure loads on the nozzle are not included in this analysis.

For the thermal model, the boundary conditions (for all time steps) are:

- convection with $T = 2000\,\mathrm{K}, h = 5000\,\mathrm{W\,m^{-2}\,K^{-1}}$ on the internal faces of the insert.
- adiabatic on all other faces.

These boundary conditions are chosen (conservatively) to give more extreme thermal gradients. The convection coefficient is on the high end of the estimated range (see section 9.2.1). Also, in reality the convection coefficient rises gradually as the motor pressurizes. Radiative heat transfer was neglected.

The meshes were generated with the 'curvature-based mesh' setting, a maximum element size of 0.5 mm and a minimum element size of 0.1 mm

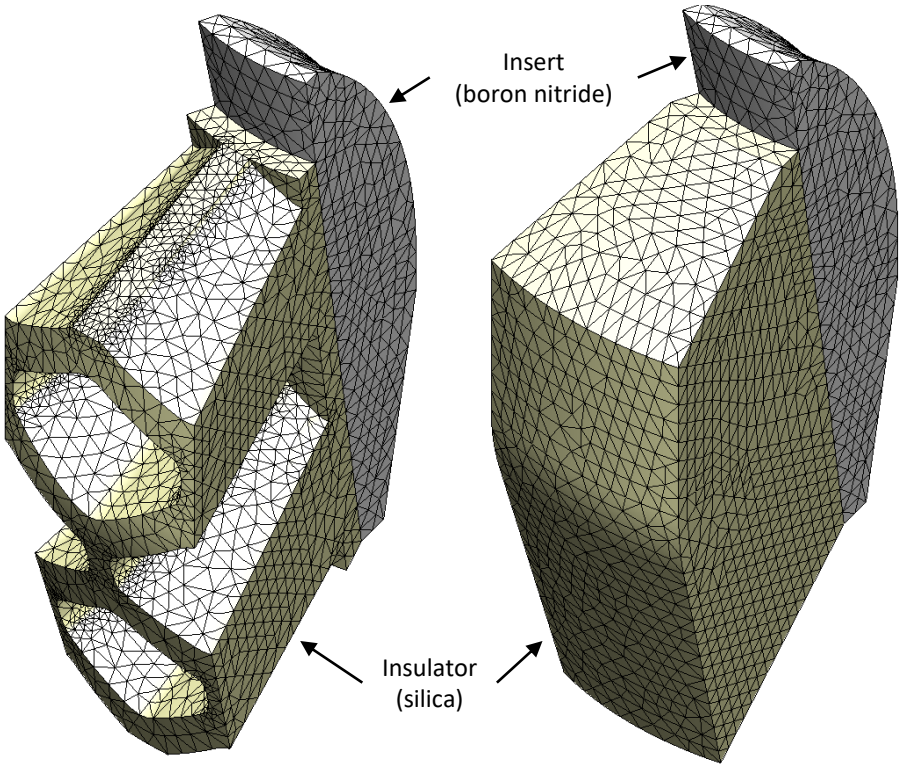

Figure 10-8: Meshes used for FEA of the honeycomb and solid insulators. The insulator (silica) is tinted yellow, the insert (boron nitride) is grey. Each domain is a 30° slice of the nozzle, with symmetry boundary conditions.

10.3.2.2 Thermal simulation results

The goal of the thermal simulation is to find the temperature field during the warm-up transient which will cause the greatest thermal stresses. It is assumed that the greatest thermal stresses will occur when the difference between the maximum and minimum temperature (ΔT) in the insulator is greatest. For both insulators, the maximum ΔT occurs at 8 s (fig. 10-9). The temperatures from these time steps are used in the mechanical analysis.

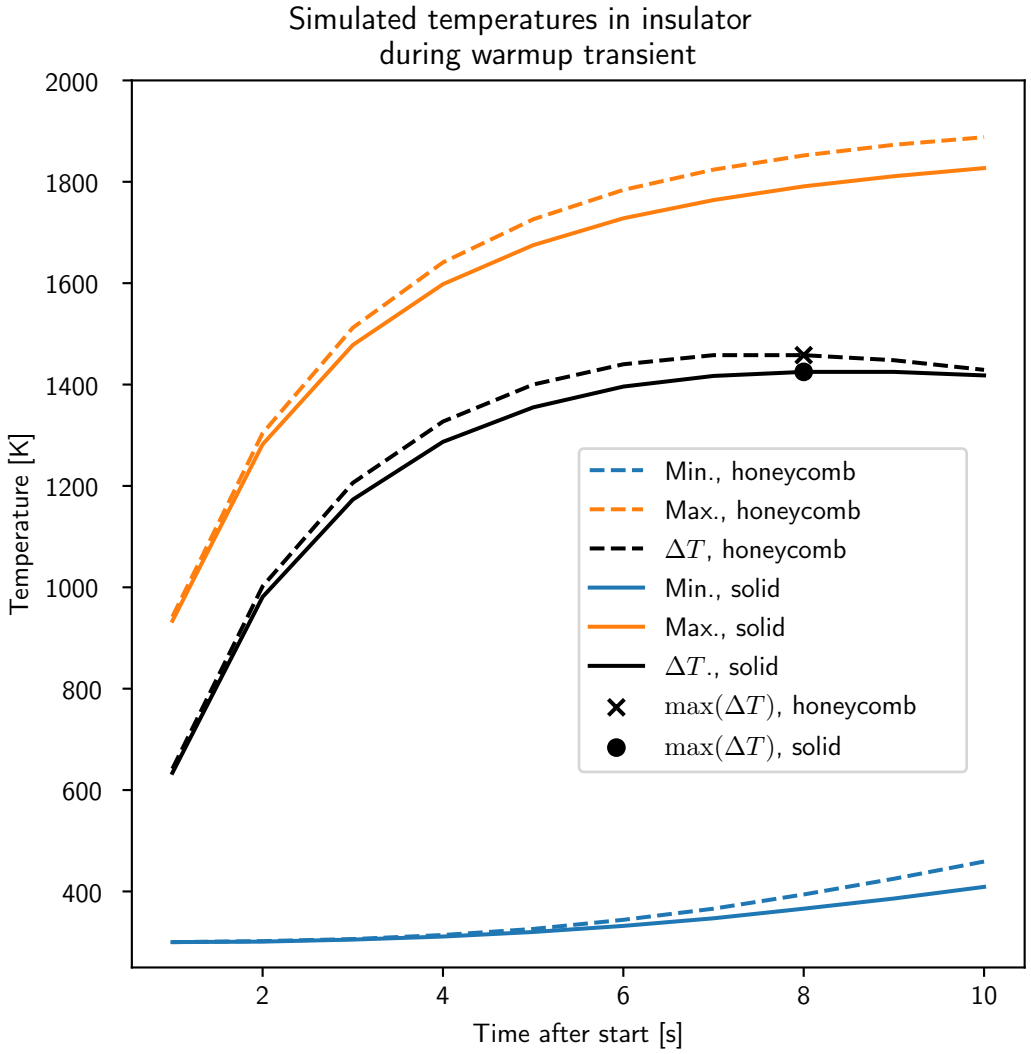

Figure 10-9: For both insulators, the highest temperature difference across the insulator occurs 8 s after heating starts.

10.3.2.3 Mechanical simulation results

The predicted thermal stresses are shown in fig. 10-10 and fig. 10-11. The locations of high stress in the honeycomb (fig. 10-11) are consistent with the predictions of the 2D model (fig. 10-7). The maximum (tensile, θ direction) stress in the honeycomb is 65.2 MPa, whereas it is only 17.9 MPa in the solid insulator. The flexural stress at break of the silica material is 33.5 MPa [24] [9]. These three stress values should not be compared directly, as the stressed volume is different in each case.

If the parameters of the Weibull distribution for this ceramic were known, the integral in eq. (10.5) could be computed for each stress state to determine which design has a lower probability of failure. In the absence of knowledge, we are left to guesswork. The author guesses that the solid insulator has a lower probability of cracking, due to the much lower maximum stress. However, with the honeycomb geometry it may be less likely for a crack to spread far enough to compromise the function of the part.

[9] In a ASTM C1161 flexural strength test.

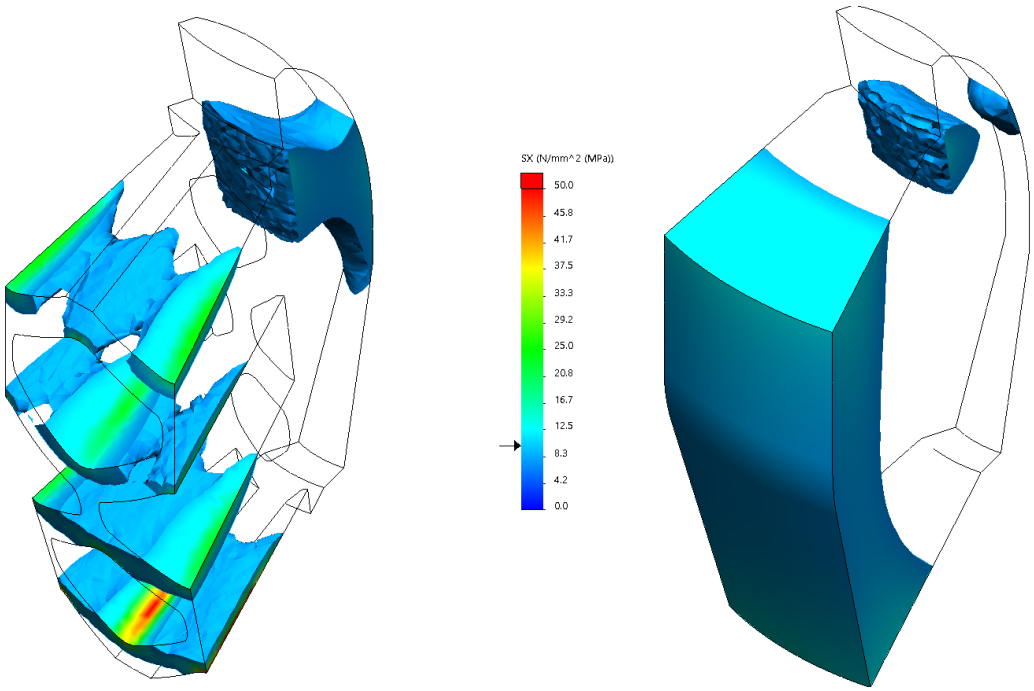

Figure 10-10: Circumferential stress σ_θ on the honeycomb and solid insulators. The plots are clipped to only show regions where the stress is $> 10\,\text{MPa}$. The maximum stress in the honeycomb insulator (left) is 65.2 MPa. The maximum stress in the solid insulator (right) is 17.9 MPa.

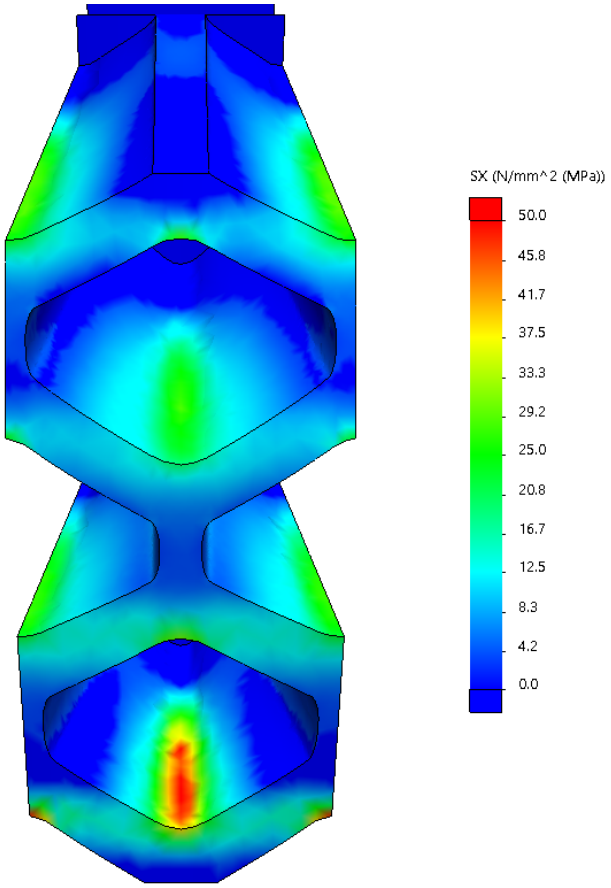

Figure 10-11: Circumferential stress σ_θ on the honeycomb insulator – view of outside surface. The stress is highest at the roots of the 'Y's where the almost-horizontal walls meet. This is where the bending moment in the walls is highest. These regions agree with the high-stress regions in the theoretical analysis in section 10.3.1, fig. 10-7.

10.3.3 Thermal conductivity of ceramic honeycomb insulation

Fully dense ($2.2\,\mathrm{g\,cm^{-3}}$) fused silica has a thermal conductivity of $1.38\,\mathrm{W\,m^{-1}\,K^{-1}}$ at 293 K, it increases to $2.7\,\mathrm{W\,m^{-1}\,K^{-1}}$ at 1220 K (fig. 10-12) [30, 16]. However, the Formlabs silica material is somewhat porous, with a density of $1.9\,\mathrm{g\,cm^{-3}}$. A similarly dense sintered silica material has a thermal conductivity of $1.0\,\mathrm{W\,m^{-1}\,K^{-1}}$ at room temperature [17]. This analysis will assume that the Formlabs silica has a thermal conductivity 1/1.38 times the values given in fig. 10-12.

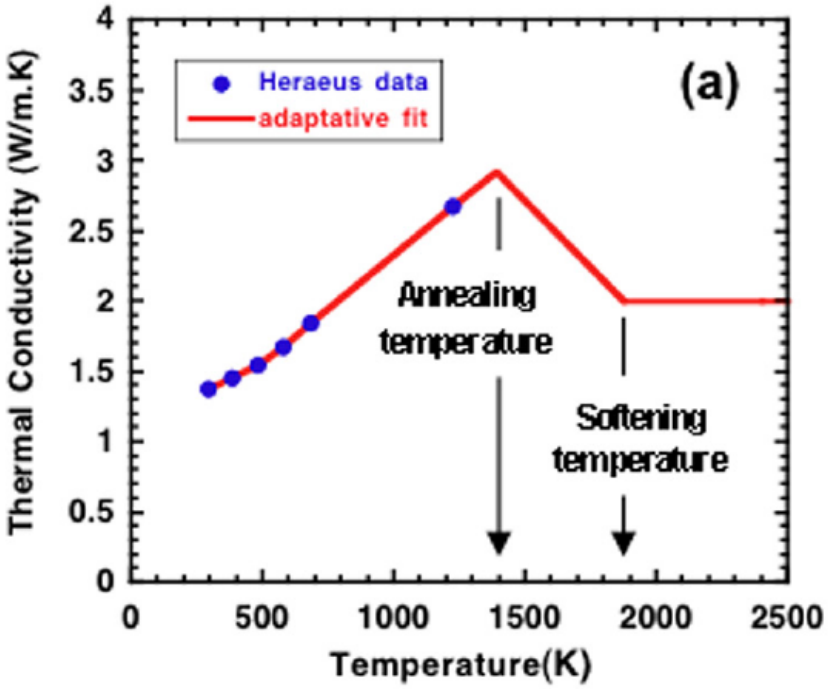

Figure 10-12: Thermal conductivity of full dense fused silica. The Formlabs silica is not fully dense, and probably has a thermal conductivity 1/1.38 times these values. Reprinted from [16].

In a honeycomb insulator, heat is transfered via three means [26]:

1. Conduction through the walls.

2. Radiation through the open cells.

3. Gas conduction though the open cells.

The effective thermal conductivity of the honeycomb (along the extrusion direction of the cells) is:

$$k^* = \underbrace{\left(\frac{\rho^*}{\rho_s}\right) k_s}_{\text{solid cond.}} + \underbrace{\left(1 - \frac{\rho^*}{\rho_s}\right) \left(\frac{\sigma_B (T_{hot}^4 - T_{cold}^4) l}{(\epsilon_{hot}^{-1} + \epsilon_{cold}^{-1} - 1)(T_{hot} - T_{cold})}\right)}_{\text{radiation}} + \underbrace{\left(1 - \frac{\rho^*}{\rho_s}\right) k_{gas}}_{\text{gas cond.}} \tag{10.13}$$

where

- ρ^*/ρ_s is the relative density of the honeycomb,
- k_s is the solid conductivity (which varies with temperature),
- σ_B is the Stefan-Boltzmann constant,
- T_{hot}, T_{cold} are the temperatures of the hot and cold sides of the insulation,
- l is the thickness of the insulation,
- $\epsilon_{hot}, \epsilon_{cold}$ are the emissivities of the surfaces on the hot and cold sides of the insulation,
- k_{gas} is the thermal conductivity of the gas within the cells.

The solid conduction and radiative heat transfer vary with temperature. Figure 10-13 shows the effective thermal conductivity of the insulator versus cold side (outside) temperature, for a fixed inside temperature of 1900 K. The black line represents a solid insulator. The dashed blue line represents a honeycomb without the radiation term; the solid blue line includes radiation. The solid fused silica is somewhat translucent, so there will be some radiation though the solid as well; this is not accounted for in fig. 10-13.

Radiation would be a significant source of heat transfer through the insulator. To reduce the radiation heat transfer, the cells of the insulator can be packed with ceramic fibers. This is shown in fig. 10-14; it blocks some, but not all, light passing through the insulator. With the fiber filling, the effective thermal conductivity of

the honeycomb is somewhere between the solid and dashed blue curves in fig. 10-13. Stuffing the cells with fibers is tedious and could be expensive in a mass-production application.

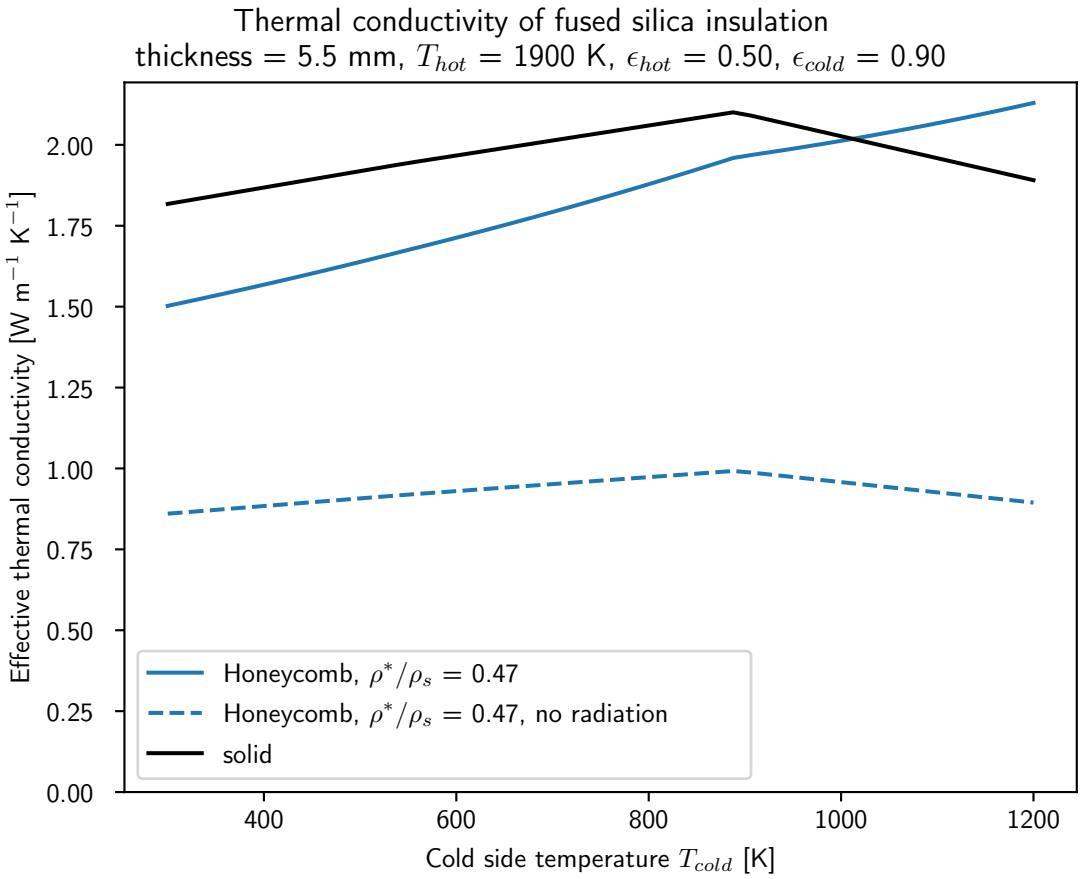

Figure 10-13: The effective thermal conductivity of the honeycomb depends on how much heat is transfered down the cells by radiation. The solid thermal conductivity is evaluated at $(T_{hot} + T_{cold})/2$.

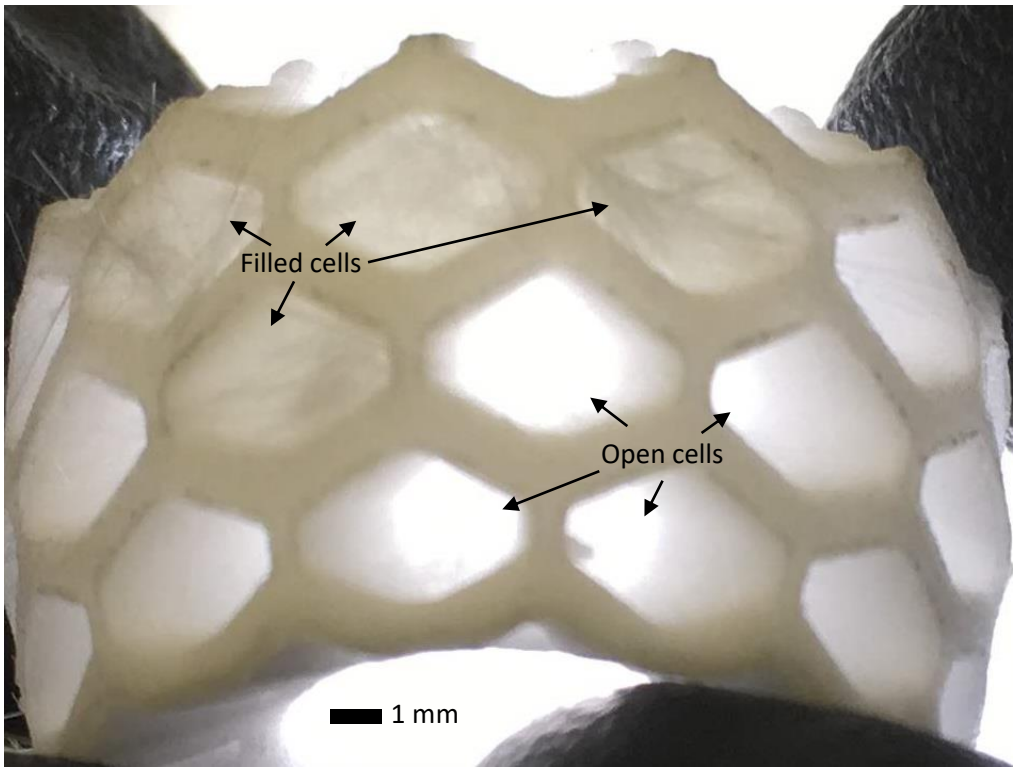

Figure 10-14: A honeycomb insulator, back-lit with a white light. Some of the cells are filled with ceramic (alumina) fibers; less light passes through the fiber-filled cells.

10.4 Producing cellular ceramic insulation

The process of printing the insulator and bonding it into the nozzle is shown in fig. 10-15. First, a green part is printed via vat photopolymerization (SLA printing) [10]. The green part consists of silica particles held together by a photopolymer binder. Then, the green part is fired in a kiln to burn out the binder and sinter the particles together. The temperature schedule of the sintering process has important effects on material properties, and is discussed further in section 10.4.1.

After firing, the fused silica insulation is bonded to the boron nitride nozzle insert. A silica ceramic adhesive is used for this bond. The insulation (and insert) are then bonded into the nozzle shell. Because the nozzle shell and insulation have different coefficients of thermal expansion, this bond is made with a flexible silicone adhesive.

[10] using the Form 2 printer from Formlabs.

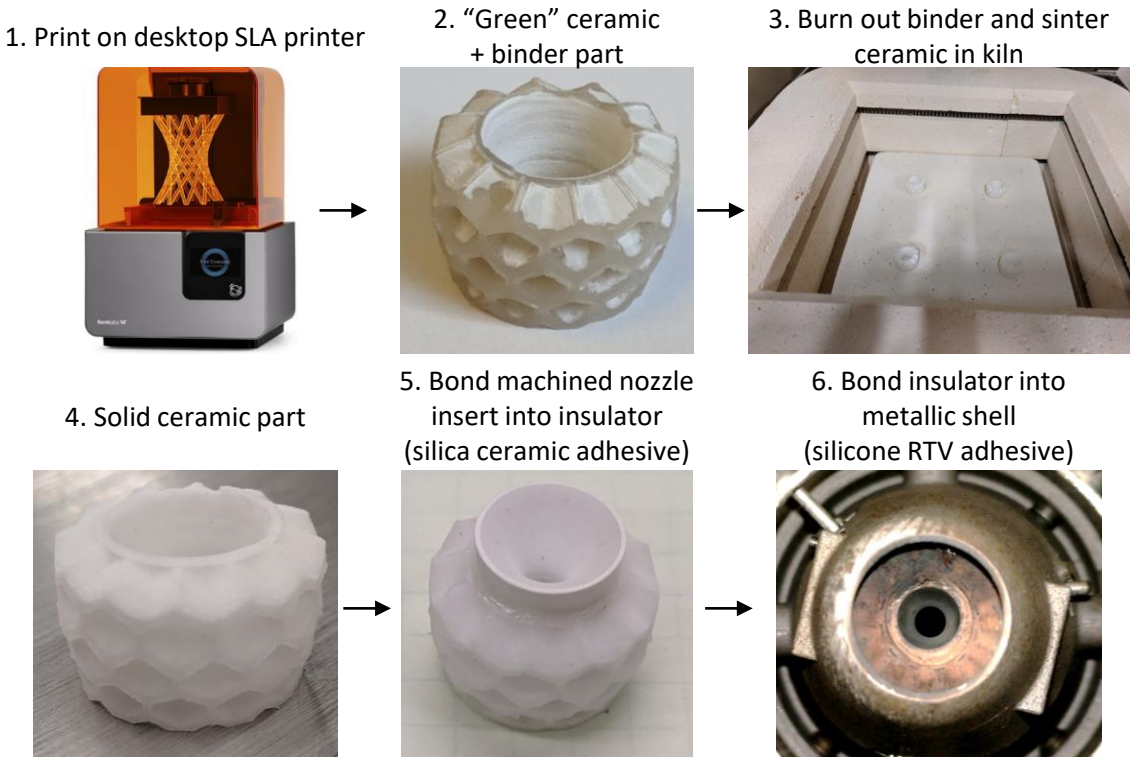

Figure 10-15: The complex honeycomb geometry is produced by 3d printing a 'green' ceramic+binder part.

10.4.1 Effect of sintering process on material properties of fused silica

Wan et al. [91] provides an excellent description of the effects of sintering temperature on the properties of fused silica. Wan et al. used fused silica ceramics produced via gelcasting, which is similar to the Formlabs process, except that the green polymer/ceramic powder part is cast, rather than SLA printed. They report that sintering temperatures of 1275 °C or higher (held for 4 h) cause the coefficient of thermal expansion at high temperatures to be 4-8 times higher (due to the formation of cristobalite). Such a large increase in the CTE would dramatically increase the thermal stresses in the insulator.

To avoid this issue, the material used in this work was sintered at temperature of 1271 °C, and held at the peak temperature for only 5 min. It is conceivable that further efforts to optimize the burn-out and sintering temperature schedule could

improve the mechanical properties of the insulation.

10.5 Nozzle insert material

The nozzle insert is made from boron nitride, which was selected for its high temperature tolerance, low thermal expansion, and machinability.

The requirements for the nozzle insert material are:

Machinability The insert requires a precise contour and smooth surface finish on its inside (gas-facing) surfaces. This can best be achieved by machining (lathe).

Temperature tolerance The insert could be exposed to temperatures up to 2200 K. This is the maximum propellant flame temperature with zero oxamide and no ablative film cooling.

Resistance to thermal shock and stresses The insert will be rapidly heated from about 250 K to 2000 K when the motor starts up. To avoid cracking due to thermal stresses, the insert material should have a low coefficient of thermal expansion, similar to that of the silica insulation.

Thermal conductivity It would be nice for the insert to also have low thermal conductivity, but this is not necessary.

Based on these requirements, boron nitride was selected; it appears to be the only widely available machinable ceramic with at CTE as low as that of silica.

Boron nitride has many different forms, so the material properties vary significantly between different vendor's formulations. The (single-crystal) hexagonal form is very anisotropic; but most pressed ceramics are polycrystalline with random orientations, so the bulk material can be vaguely isotropic (with some difference between the pressing direction and the perpendicular directions).

Our preferred grade of boron nitride is Aremco 502-1600-99. This is a 99% pure "binderless diffusion-bonded product" [3]. Its properties are:

- Thermal conductivity of $22\,\mathrm{W\,m^{-1}\,K^{-1}}$
- Coefficient of thermal expansion of 0.1 ppm/K parallel to the pressing direction, 0.3 ppm/K perpendicular to the pressing direction.
- Usable to 3300 K in an inert atmosphere (but may oxidize at lower temperatures).

In this work, some nozzles instead used a cheaper boron nitride grade, containing B_2O_3 binder. The gas-facing surfaces of these inserts became deeply pitted. The B_2O_3 binder melts at 723 K and is not suitable for high temperature applications.

The boron nitride was easily machinable, with similar machining characteristics to polycrystaline graphite. The boron nitide was bonded to the silica insulation with Aremco's 618-N silica adhesive (see fig. 10-16).

Earlier prototypes of the nozzle used a graphite insert instead of boron nitride. These prototypes cracked due to the thermal expansion mismatch between graphite and the silica insulation.

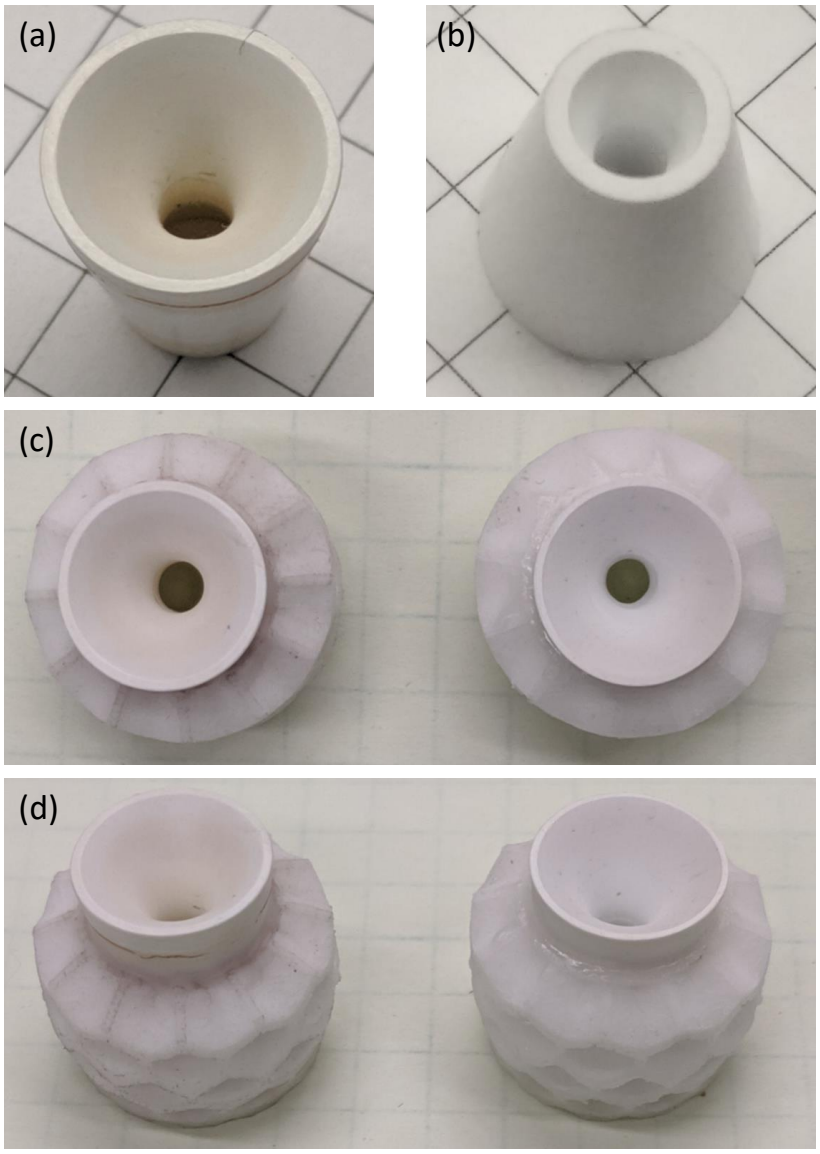

Figure 10-16: (a,b) A machined boron nitride nozzle insert. (c,d) Two sets of nozzle inserts and silica honeycomb insulators are bonded together with ceramic adhesive.

10.6 Tests of the ceramic insulation

10.6.1 Torch test method for preliminary evaluation of nozzle materials

For the first nozzle prototypes, resistance to thermal stresses was evaluated with torch tests. The torch test heats the inside of the nozzle prototype with an oxy-acetylene torch while cooling the outside with air jets (fig. 10-17). This creates extreme thermal gradients in the nozzle, similar to what would occur in a motor firing.

The nozzle samples were instrumented with two thermocouples: a type K thermocouple on the shell and a type C thermocouple at the inside of the insulation.

The samples were torched for 30 s. The nozzle shell reached a temperature of 600 K, and the temperature at the inside of the insulation was over 1600 K.

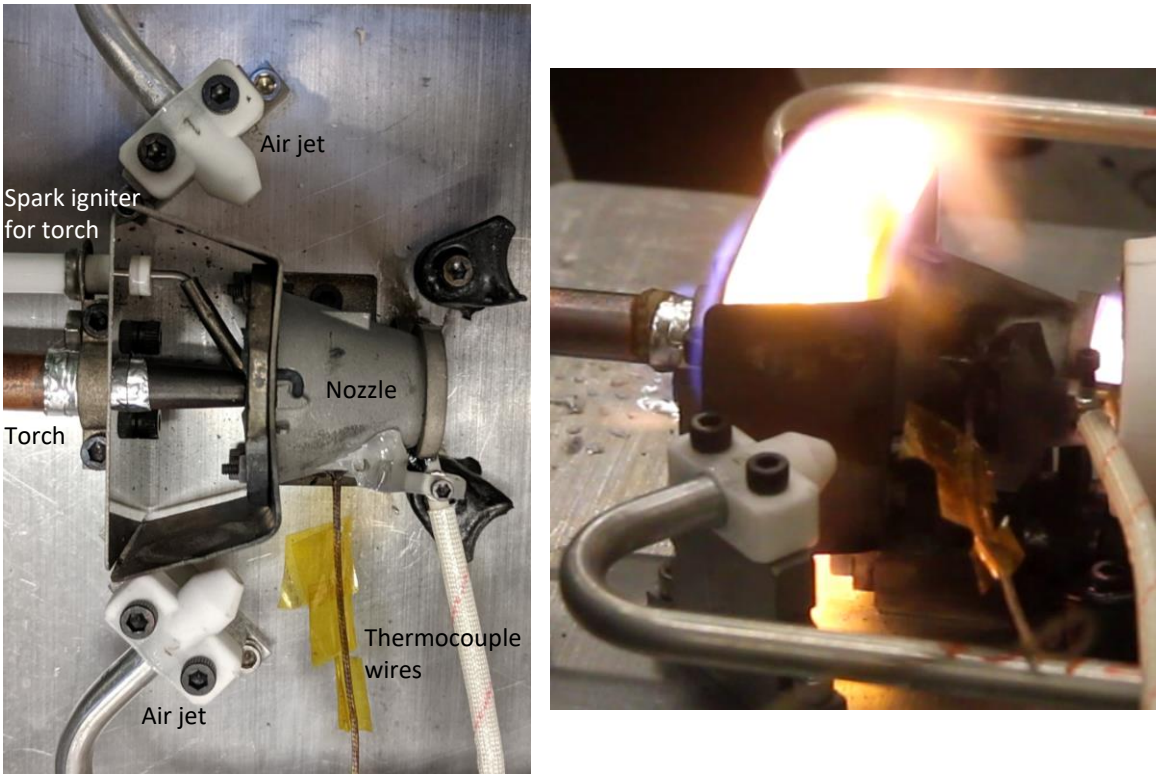

Figure 10-17: The torch test creates extreme thermal gradients in the nozzle prototype. A oxy-acetylene torch heats the inside of the nozzle while air jets cool the nozzle shell. Left: top-down view of test rig components. Right: the test rig in operation.

10.6.2 Failed tests with graphite nozzle inserts

The first nozzle prototypes used graphite, not boron nitride, as the nozzle insert material. These nozzles failed during torch tests. The failures were due to thermal stresses from the large thermal expansion mismatch between these materials: $4.6 \times 10^{-6}\,\mathrm{K}^{-1}$ for the grade of graphite used[11], vs. $0.6\,\mathrm{K}^{-1}$ for the Formlabs silica.

Several cracks were discovered in the silica insulation when the nozzle was inspected after the torch test. These cracks were on or emanated from the inside of the insulation (illustration in fig. 10-18, microscope images in fig. 10-19).

Cracking on the inside indicates that the cracks were due to thermal stresses arising from the thermal expansion mismatch between the silica insulation and the

[11] Superfine isomolded graphite, purchased from GarphiteStore.com, stock number GR001CC.

graphite insert – this would produce tensile stresses on the inside of the insulation (see fig. 10-20).

The adhesive bond between the graphite insert and the silica insulation also failed (see fig. 10-19(b)) due to the thermal expansion mismatch between these materials.

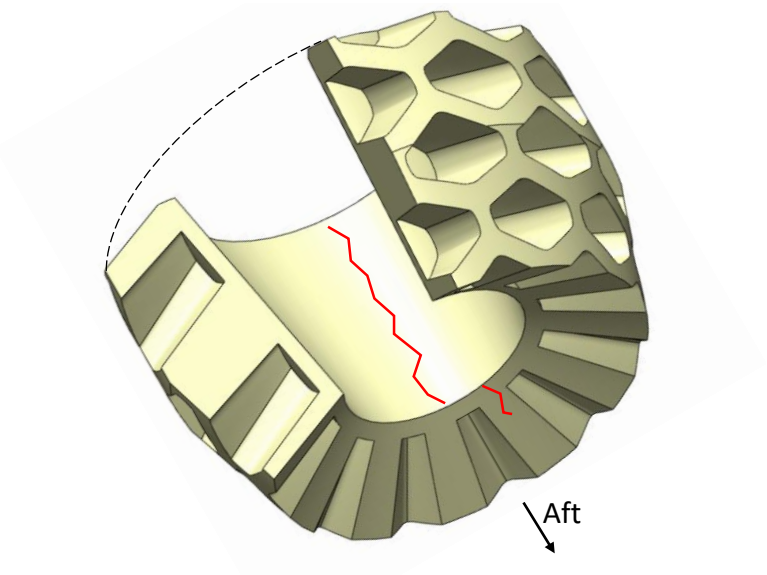

Figure 10-18: An illustration of the crack geometry observed after the torch test, showing that the cracks are on the inside of the insulation. The honeycomb geometry is simplified to clarify the illustration.

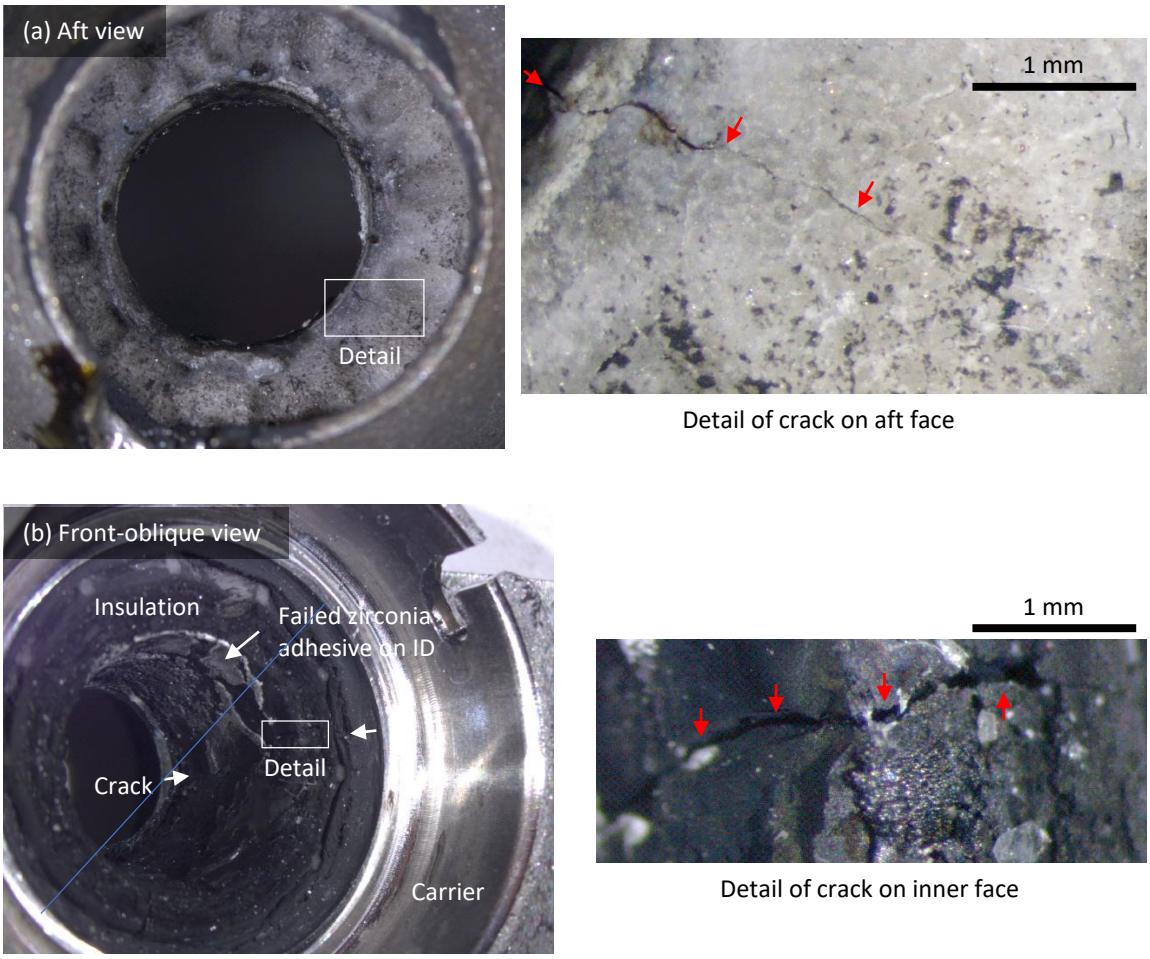

Figure 10-19: (a) A view from the aft end of the nozzle shows a radial crack emanating from the inside of the nozzle insulation. (b) An oblique view of from the front end of the nozzle shows a long crack on the inner face of the insulation.

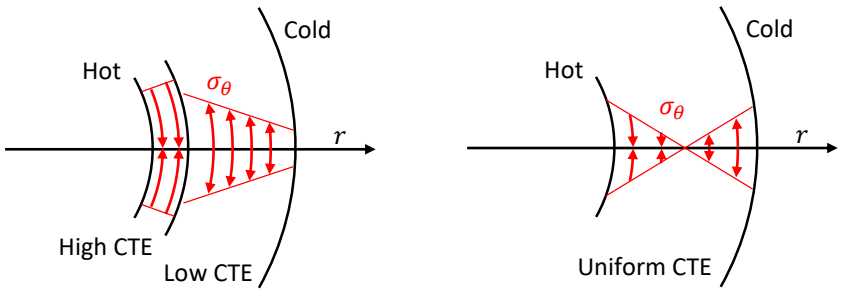

Figure 10-20: Notional circumferential stress distributions in internally heated cylinders with a high coefficient of thermal expansion (CTE) core (left) or with uniform CTE (right). Crack-producing tensile stresses exist on the inside of the insulation in the left case.

10.6.3 Successful test with boron nitride insert

The nozzle insulation survived without cracking when the insert material was changed to boron nitride. Boron nitride's thermal expansion closely matches that of silica, so the thermal stresses were much lower.

The nozzle for static fire SF9 used a honeycomb, silica ceramic insulator with a boron nitride nozzle insert. A photo from the firing is shown in fig. 10-21. The nozzle insulation survived the firing. After the firing, the insulation was inspected by microscope; no cracks were found in the insulation.

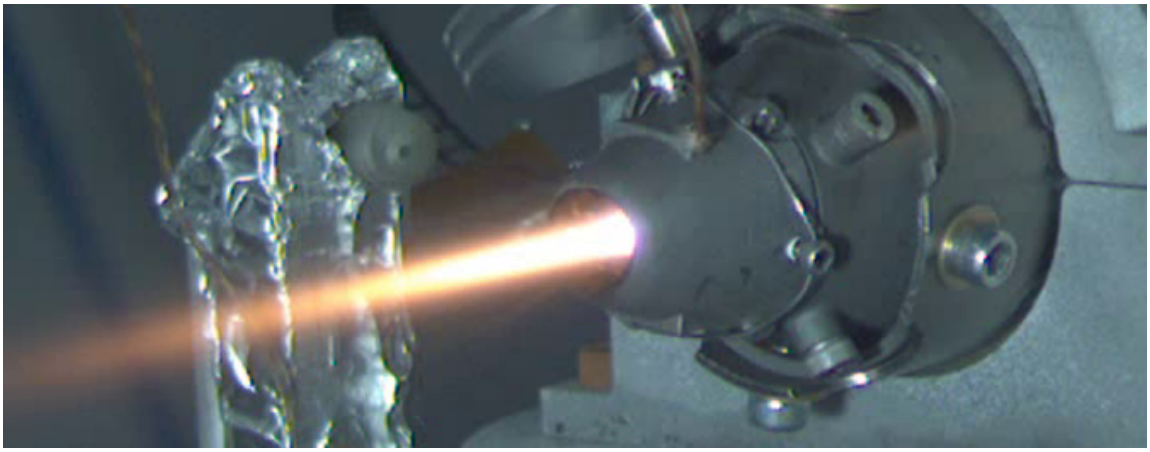

Figure 10-21: A ceramic-insulated nozzle was successfully fired for 39 s in static fire SF9. The nozzle used a silica honeycomb insulator.

10.7 Recommendations for further ceramic insulation development

This thesis has devised, analyzed and demonstrated silica ceramic insulation for small, long-burn-time nozzles, and identified boron nitride as a compatible nozzle insert material. These contributions enable the nozzle design described in chapter 9.

Future work should focus on making the insulation reliable and easier to produce. Currently, only a few tests have been conducted on the honeycomb insulation so its failure probability is not known (failure of stressed ceramic parts is typically

stochastic [42]). Also, it is not currently known whether the honeycomb or solid insulation structure gives a lower probability of failure. To determine this, either: 1) many tests must be conducted on both designs, or 2) the Weibull parameters of the sintered silica material must be measured.

Also, the solid design is simpler and easier to produce. In large production volumes it could be made by casting (which may be cheaper than additive manufacturing). By contrast, packing cells of the honeycomb with ceramic fibers is a tedious manual task (see section 10.3.3).

Chapter 11

Conclusion

This thesis addresses the need for miniature, yet powerful, propulsion systems for small, fast aircraft. Low thrust solid rocket motors can meet this need – a kilogram-scale solid rocket motor can produce 5–10 N of thrust for a few minutes. This would enable a small UAV, built around the motor, to fly at Mach 0.8.

However, such a motor is very different from conventional small solid rocket motors. The thrust level is orders of magnitude lower, and the burn time is 10-100 times longer. Major technology challenges arise from these changes. This work identifies and addresses these challenges, focusing on the propellant, motor design and operation, thermal protection, and nozzle design. These results enabled improvements to the design of Firefly, our group's concept for a small, fast UAV. The results will also be useful to future designers of small, fast aircraft. Most of these results are novel contributions to the field. Specifically, the contributions of this thesis are:

Design principles for small, low-thrust motors This work identifies low (thrust / burn area) ratio as a unique challenge of these motors (chapter 3). Low values of the F/A_b ratio reduce the motor's specific impulse, and very low F/A_b ratios are not possible. Inconveniently, the required thrust for steady level flight is quite low compared to the burn area, even with an end-burn grain. This works shows that low F/A_b requires a slow-burn propellant and low chamber pressure, and quantifies the

lower feasible limits on F/A_b.

Motor case design and materials are also considered (chapter 6). The key issues are stress from internal pressure loads, high temperature, and integration with the payload and aerodynamic surfaces. A baseline design is proposed, which is simple, lightweight, manufacturable, and has large structural margins.

Development and characterization of slow-burn propellants Low thrust and long burn time require a slow-burn propellant. This work developed a family of slow-burn propellants and a new model to quantify how the burn rate is reduced by adding oxamide to the propellant. This family of slow-burn ammonium perchlorate composite propellants employs two known techniques to reduce the burn rate: large AP particles and the burn rate suppressant oxamide (chapter 4). The propellant's burn rate is adjustable[1], so that a single family of propellants can accommodate a range of missions and aircraft concepts. The burn rate is adjusted by varying the oxamide content; propellants with oxamide contents of 0 to 20% were tested (chapter 5). The oxamide/burn rate model fits the experimental data well.

Although oxamide has been known as a burn rate suppressant for some time, this work is the first[2] to present a quantitative model of its effect on burn rate, and the first to test such a wide range of oxamide contents. Previous experiments only tested oxamide contents up to 10%, and measured the burn rate at higher pressures than are relevant for this work.

This work measured the propellants' burn rates at low pressures and measured the minimum pressure at which the propellants would burn. This is important because low thrust motors operate at unusually low chamber pressure (about 0.5 MPa).

Operation of small, low-thrust motors Motor test firings (chapter 7) demonstrated that the motor and propellant could operate at a F/A_b of only 2.4 kPa, near the lower limit for this propellant family. Low chamber pressure is necessary

[1] at the time of manufacture

[2] in the open literature, to the author's knowledge

to achieve low F/A_b; in these tests the chamber pressure was only 0.5 MPa. Some motors and propellants have combustion instabilities at low chamber pressure, so demonstrating stable operation of the research motor at only 0.5 MPa is significant.

Motor testing also revealed an unusually low thrust coefficient efficiency – only 85% – perhaps due to viscous losses in the small nozzle, and low characteristic velocity efficiency – again, about 85% – due to heat loss to the motor walls. These inefficiencies are unique features due to the motor's small size and low thrust. Measuring these inefficiencies is useful for accurate performance prediction. The ∼28% ($= 1 - 0.85 \cdot 0.85$) reduction in total impulse is important to account for, but does not significantly diminish the concept's usefulness.

This work also identifies nozzle clogging and pressure spikes as technical risks for these motors. In some tests, a solid deposit formed in the nozzle and interfered with the gas flow. This significantly reduced the nozzle's thrust coefficient. The exact cause of the clogging issue is not known. If the clogging issue were to occur in flight, the range of the aircraft would be significantly reduced. Thus, nozzle clogging remains a technical risk for small, low-thrust motors.

Further, occasional chamber pressure spikes of 0.1–1 MPa were observed due to solid particles passing through the small nozzle. This observation indicates a need for larger-than-typical structural margins on chamber pressure in the motor case design. Both these issues are related to the unusually small size (throat diameter of 3–5 mm) of the nozzles used in small, low-thrust motors.

Motor case thermal protection testing and modeling This work provides additional ablation measurements and heat transfer modeling under the unique conditions of these motors (chapter 8). Motor case thermal protection is difficult in these motors because the end-burn grain exposes a large area to hot combustion gas. Nonetheless, ablation measurements confirm that a reasonably thin (2–5 mm) ablative liner can protect the motor case. This work extends the preliminary thermal protection study by Spirnak [76]. It provides better empirical fits for the ablative

char depth, which are necessary to select the liner thickness for future motors.

This work revealed that heat is mostly transfered to the ablative liner by radiation from soot particles in the combustion gas, and the combustion gas is significantly cooled by this heat loss. The heat loss is predicted to reduce the motor's delivered impulse by 5-20%; this effect is corroborated by the low c^* efficiency measured in motor firings. These are unusual phenomena which occur due to the motor's small size and low thrust. These results enable better performance prediction for the Firefly motor, and suggest slightly modifying the propellant to reduce the amount of soot.

Steady-state nozzle design and testing The small size and long burn time pose unique challenges for the nozzle (chapter 9). Conventional nozzle designs – which rely on transient phenomena, e.g. ablative cooling or heat sinks – are not suitable. A new nozzle was designed using ceramic insulation, which can survive prolonged exposure to high temperatures in thermal steady state. To reduce thermal stresses, the ceramic insulation was carefully designed and made from low-expansion fused silica (chapter 10). The insulation has a honeycomb structure, which is produced via additive manufacturing. A nozzle using this insulation was successfully tested on the research motor. To predict the nozzle's temperature under flight conditions, a detailed heat transfer model was developed (chapter 9). The demonstration of this nozzle is a major technology risk reduction for small, low-thrust motors.

In summary, this work identifies and addresses technology challenges for the propellant, motor configuration, thermal protection, and nozzle design of low-thrust solid rocket motors. Feasibility has been demonstrated by motor firings with slow-burn propellant and a long-duration nozzle. Further, the experimental results and models will enable engineers to design and predict the performance of solid rocket motors for small, fast aircraft. By providing insight into the physics of these motors, this thesis may help to enable a new propulsion option for small, fast aircraft.

Appendix A

Methods of estimating burn rate from motor firings

One goal of motor firings is to measure the burn rate of the propellant, and its dependence on chamber pressure. Estimating the burn rate from motor firings is somewhat complicated because of the grain geometry used in the Ti Candle motor. In a perfectly end-burning grain, the burn rate and chamber pressure would be constant throughout the burn, and the burn rate could be measured by dividing the grain length by the burn time.

However, it was found that the higher-oxamide propellants could only be ignited by putting a star-shaped 'starter pocket' in the front face of the propellant grain and placing a few grams of faster-burning propellant within the pocket (see section 7.2.2.1). This startup technique was used in all static fires referenced in this work (SF4 onwards).

Thus, A_b, r and p_c have an initial peak as the burning surface blooms out from the star pocket. The burn surface becomes almost flat, and the burn rate and p_c pressure almost constant, after the burning surface advances 20–30 mm.

The motor is not equipped to measure the instantaneous burn rate or the intermediate progress of the burning surface. Thus, methods must be devised to estimate a representative burn rate and pressure. Some methods are described below.

A.1 Method 1: average burn rate and n-averaged chamber pressure

This method compares the average burn rate (over the entire firing) to an averaged chamber pressure. Let x be the distance the burning surface has advanced; the (instantaneous) burn rate is $r = \frac{\partial x}{\partial t}$. The average burn rate is:

$$\langle r \rangle = \frac{x_{end}}{t_{end} - t_{start}} = \frac{\int_{t_{start}}^{t_{end}} r dt}{t_{end} - t_{start}} \tag{A.1}$$

where x_{end} is the distance the burning surface must advance to completely burn the propellant grain. $\bar{r}$ is easy to measure: x_{end} is measured with calipers before loading the motor; $(t_{end} - t_{start})$ is measured from the thrust or pressure trace.

This burn rate needs to be compared at some average chamber pressure, $\langle p_c \rangle$. This average should have the property that $\langle r \rangle = a \left[\langle p_c \rangle \right]^n$. Thus, the point $(\langle r \rangle, \langle p_c \rangle)$ will fall on the curve $r = a p_c^n$, and a burn rate model of this form can be fit or compared to this point. Such an averaging formula is derived below:

$$r = a p_c^n \tag{A.2}$$

$$\int_{t_{start}}^{t_{end}} r dt = \int_{t_{start}}^{t_{end}} a p_c^n dt \tag{A.3}$$

$$\langle r \rangle = a \left(\frac{\int_{t_{start}}^{t_{end}} p_c^n dt}{t_{end} - t_{start}} \right) \tag{A.4}$$

$$\langle r \rangle = a \left[\left(\frac{\int_{t_{start}}^{t_{end}} p_c^n dt}{t_{end} - t_{start}} \right)^{1/n} \right]^n \tag{A.5}$$

$$\langle r \rangle = a \left[\langle p_c \rangle_n \right]^n \tag{A.6}$$

where

$$\langle p_c \rangle_n \equiv \left(\frac{\int_{t_{start}}^{t_{end}} p_c^n dt}{t_{end} - t_{start}} \right)^{1/n} \tag{A.7}$$

is the 'n-averaged' chamber pressure.

A.2 Method 2: c^*-based burn rate

The 'steady' burn rate is estimated using the measured $\langle c^* \rangle$, the pressure during the 'steady' portion of the burn, and equation 12-4 from [77]:

$$r_{steady,c*} \equiv \frac{A_t}{A_{b,steady}} \frac{p_{c,steady}}{\rho_s \langle c^* \rangle} \tag{A.8}$$

where $p_{c,steady}$ and $A_{b,steady}$ are the chamber pressure and burn area during the steady portion of the burn. $A_{b,steady}$ is the flat cross-section area of the propellant grain. c^* does not depend on pressure, so $\langle c^* \rangle$ should be the same as c^* during the 'steady' portion of the burn. The point for comparison to other burn rates is $(r_{steady,c*}, p_{c,steady})$.

Figure A-1 illustrates the 'steady' chamber pressure used in this method, and the 'n-averaged' chamber pressure used in the previous method.

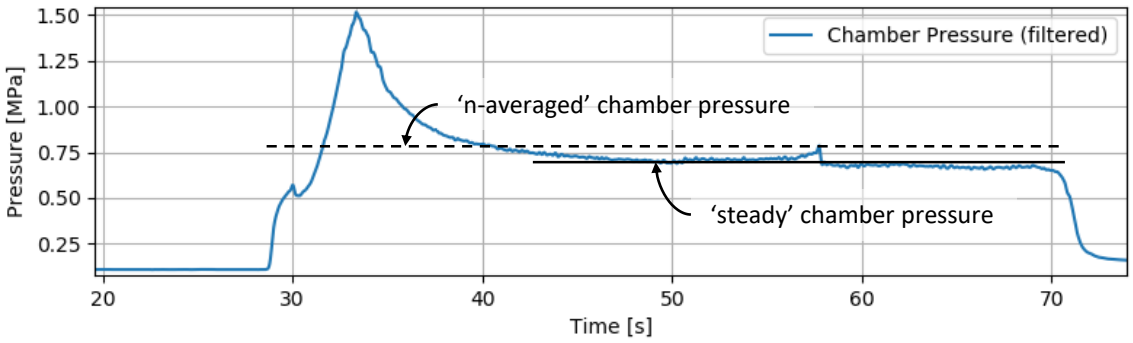

Figure A-1: Two methods are used to estimate a (burn rate, pressure) pair from a firing with varying chamber pressure. The 'n-averaged' chamber pressure $\langle p_c \rangle_n$ is comparable to the average burn rate (method 1). The 'steady' chamber pressure $p_{c,steady}$ is comparable to the c^*-based burn rate (method 2).

A.3 Fitting the pressure trace

Alternatively, the burn rate parameters a, n could be fit to the entire pressure vs. time curve from the firing. This method requires knowledge of the burn area evolution

throughout the burn, i.e. $A_b(x)$, where x is the distance that the burning surface has advanced. An advantage of this method is that it gives an estimate of both a and n, unlike the other methods.

If the burn surface is assumed to regress at the same rate everywhere, $A_b(x)$ can be calculated from simple surface offsets. A fit of the pressure trace form SF9 was attempted using a surface-offset $A_b(x)$ table, but the fits were poor and gave unrealistically low values for n (< 0.1).

Photographs of the star pocket after failed ignition attempts show that the burn surface does not regress equally everywhere; the inner corners of the star burn first. It appears that the $A_b(x)$ transition from the star pocket to the flat burning face is complicated and difficult to model. Thus, this method was abandoned.

Appendix B

Nozzle deposit SEM images and EDS maps

To investigate the composition and structure of the nozzle deposit, a piece of the nozzle deposit from static fire SF6 was imaged with a scanning electron microscope (SEM) and mapped with energy-dispersive X-ray spectroscopy (EDS). EDS creates maps of which chemical elements are present in the sample by identifying characteristic peaks in the sample's x-ray spectrum. The sample is shown with visible light in fig. B-1. It consisted of a black material covered in a fluffy orange material. The black material had a soft and flaky consistency. Some of the orange material was brushed off the sample to reveal the black material underneath.

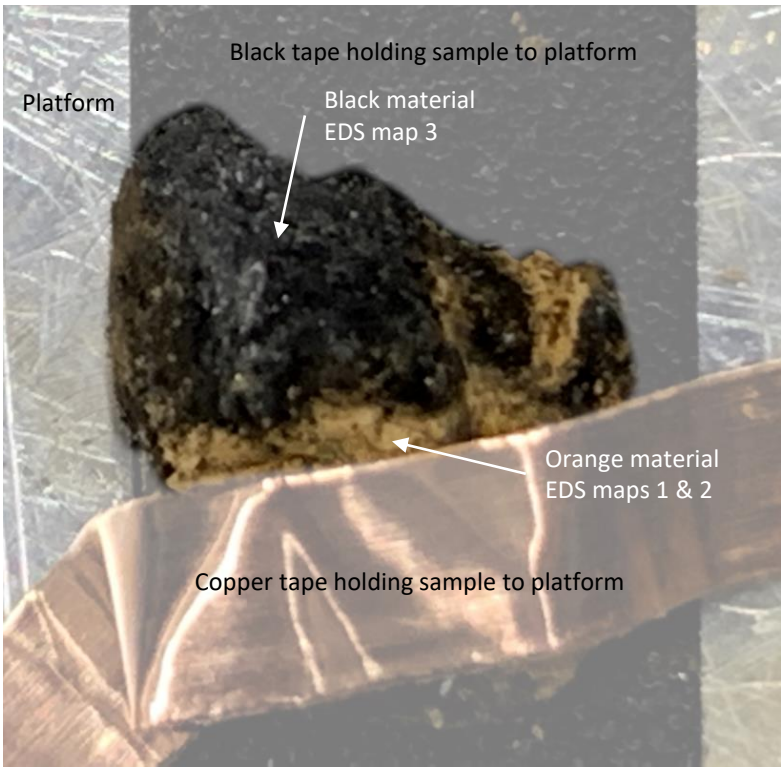

Figure B-1: Photograph of the nozzle deposit sample.

Figure B-2 shows a SEM image of the orange material. The inset photo at the top left shows where on the sample this image was taken. The orange material has a fluffy structure, reminiscent of wind-blown rime ice.

Figure B-3 is an EDS map showing the locations of carbon (top left), silicon (bottom left) and oxygen (bottom right) within the orange material. It appears that the orange material is mostly SiO_2 and some carbon. Trace amounts of chlorine were also detected; the chlorine likely originated from the propellant's ammonium perchlorate oxidizer. Iron was not detected – this rules out a hypothesis that the orange color was due to iron oxides or iron chlorides.

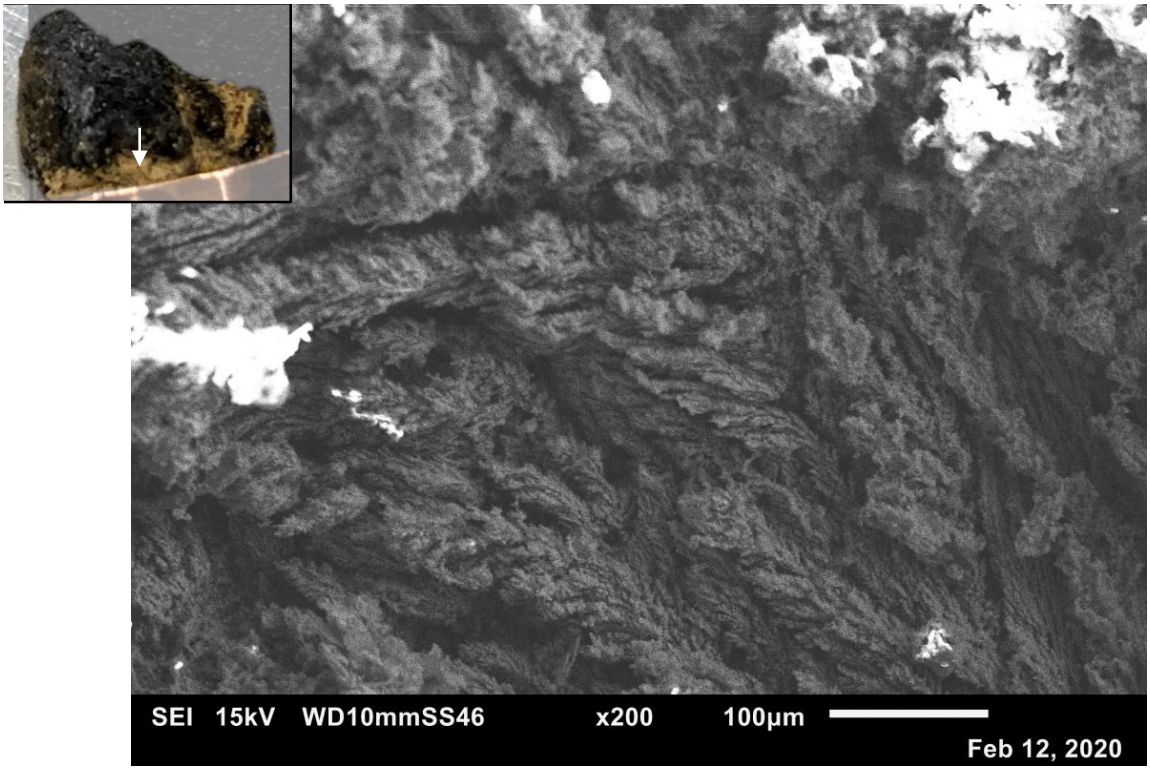

Figure B-2: SEM image of the orange material from the nozzle deposit.

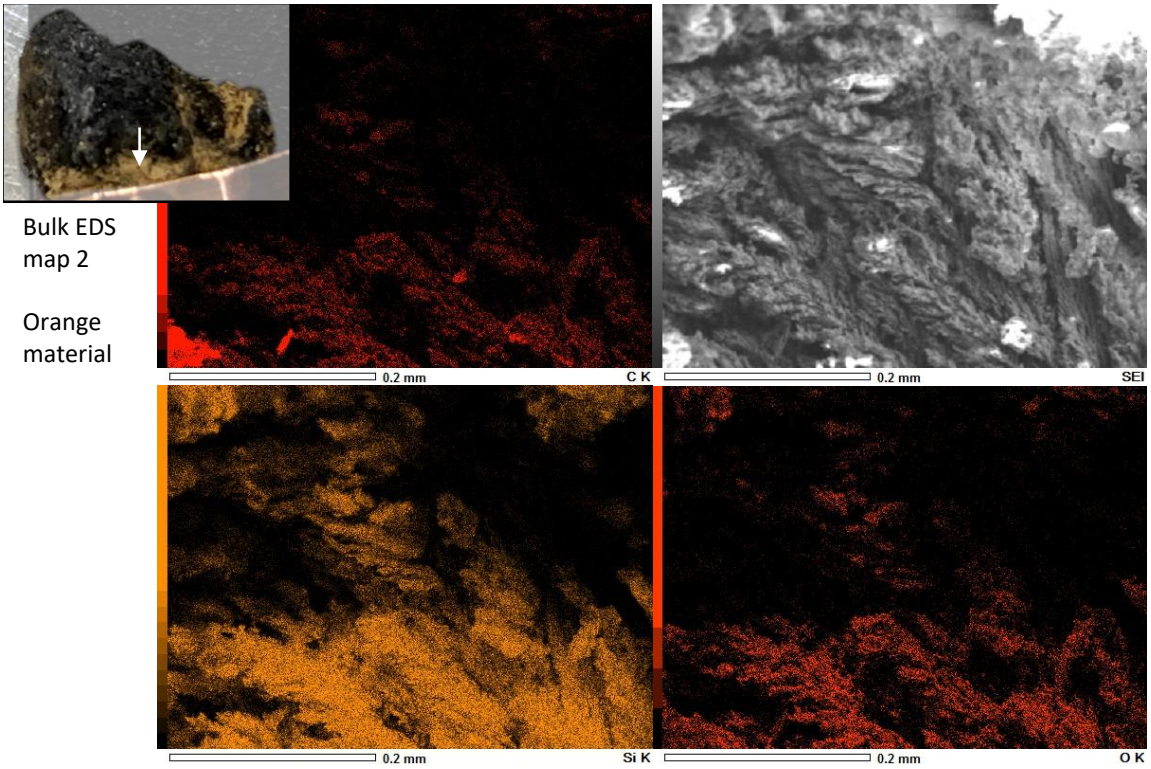

Figure B-3: EDS maps showing carbon, silicon and oxygen in the orange material from the nozzle deposit.

SEM images of the black material are shown in fig. B-4. The material is made of small flakes, which are layered in some regions and jumbled in others. The flakes are tens of micrometers across and a few micrometers thick.

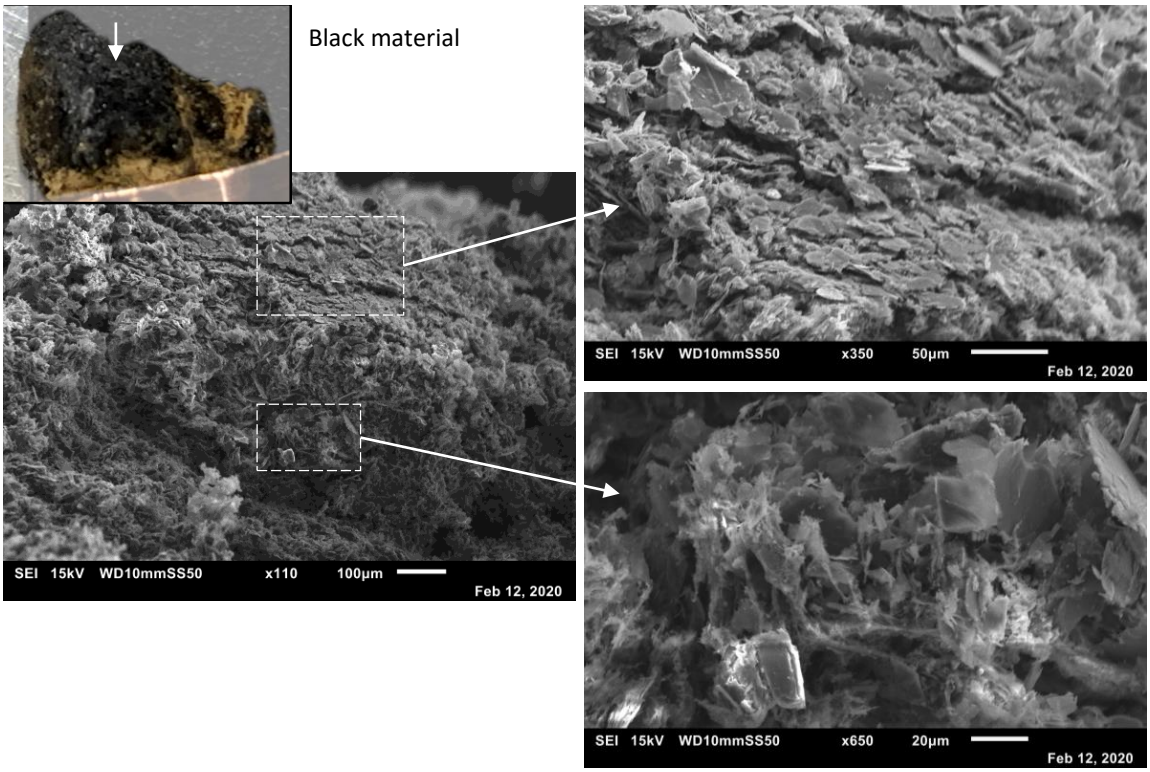

Figure B-4: SEM images of the black material from the nozzle deposit.

Figure B-5 is an EDS map of the black material. There were strong returns for carbon, silicon and oxygen – it appears that the black material also is mostly carbon and SiO_2. Trace amounts of chlorine and aluminum were detected. There were also trace amounts of calcium and phosphorus, which likely came from the tricalcium phosphate anti-caking agent in the ammonium perchlorate powder.

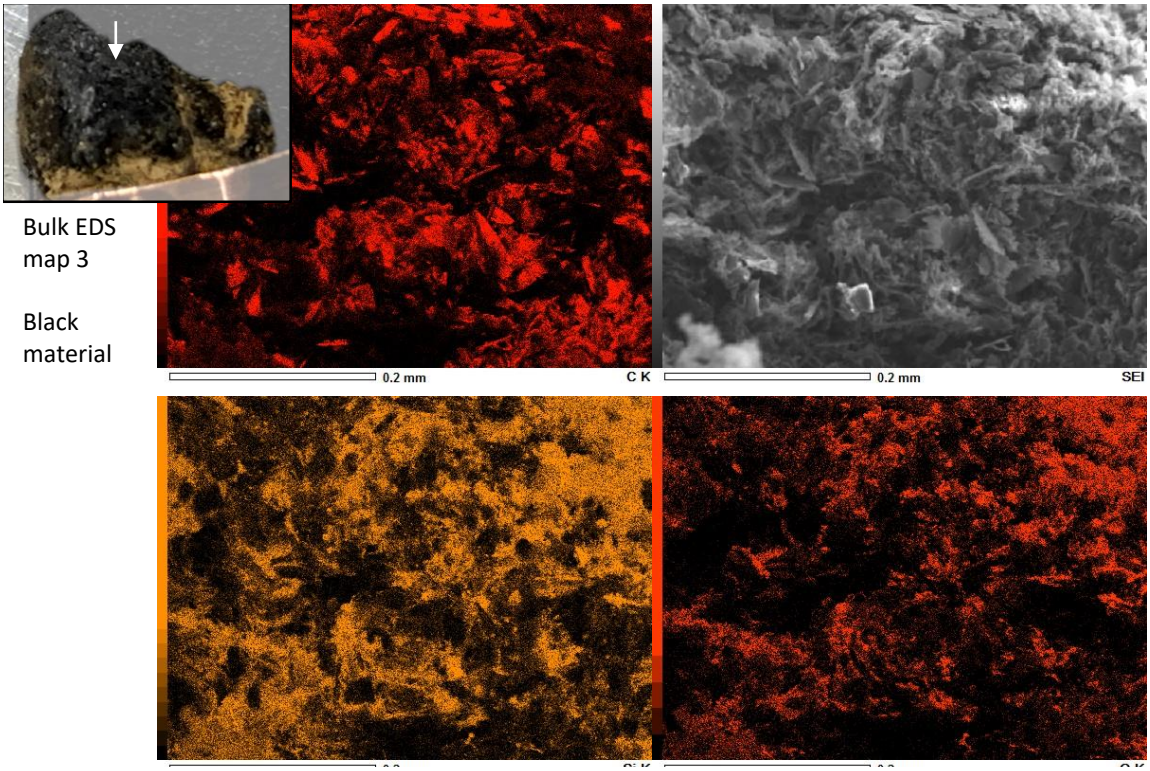

Figure B-5: EDS maps showing carbon, silicon and oxygen in the black material from the nozzle deposit.

Bibliography

[1] AeroVironment Inc. *AeroVironment Inc. | Unmanned Aircraft Systems*. 2016. URL: https://www.avinc.com/.

[2] Sourabh Apte and Vigor Yang. "Unsteady flow evolution and combustion dynamics of homogeneous solid propellant in a rocket motor". In: *Combustion and Flame* 131.1 (Oct. 1, 2002), pp. 110–131. ISSN: 0010-2180. DOI: 10.1016/S0010-2180(02)00397-8. URL: http://www.sciencedirect.com/science/article/pii/S0010218002003978 (visited on 11/17/2019).

[3] Aremco Products, Inc. *Machinable and Dense Ceramics*. Apr. 2015. URL: https://www.aremco.com/wp-content/uploads/2019/05/A01_19.pdf.

[4] Michael F. Ashby. *Material and Process Selection Charts*. Cambridge, UK: Cambridge University, Granta Design, Jan. 2010. URL: https://grantadesign.com/download/pdf/teaching_resource_books/2-Materials-Charts-2010.pdf.

[5] Randall F Barron and Brian R Barron. "Thick-Walled Cylinders and Spheres". In: *Design for Thermal Stresses*. John Wiley & Sons, Ltd, 2011, pp. 378–415. ISBN: 978-1-118-09318-4. DOI: 10.1002/9781118093184.ch9. URL: https://onlinelibrary.wiley.com/doi/abs/10.1002/9781118093184.ch9.

[6] David W. Blair. "The influence of diameter on the burning velocity of strands of solid propellant". In: *Combustion and Flame* 20.1 (Feb. 1, 1973), pp. 105–109. ISSN: 0010-2180. DOI: 10.1016/S0010-2180(73)81261-1. URL: http://www.sciencedirect.com/science/article/pii/S0010218073812611 (visited on 01/25/2020).

[7] N. W. Bressloff, J. B. Moss, and P. A. Rubini. "CFD prediction of coupled radiation heat transfer and soot production in turbulent flames". In: *Symposium (International) on Combustion* 26.2 (Jan. 1, 1996), pp. 2379–2386. ISSN: 0082-0784. DOI: 10.1016/S0082-0784(96)80067-1. URL: http://www.sciencedirect.com/science/article/pii/S0082078496800671 (visited on 12/19/2019).

[8] M E Brown and R A Rugunanan. "A Temperature-Profile Study of the Combustion of Black Powder and its Constituent Binary Mixtures". In: *Propellants, Explosives, Pyrotechnics* 14 (Apr. 1989), pp. 69–75. DOI: 10.1002/prep.19890140205. URL: https://doi.org/10.1002/prep.19890140205.

[9] L. W. Carlson and E. Talmor. "Gaseous film cooling at various degrees of hot-gas acceleration and turbulence levels". In: *International Journal of Heat and Mass Transfer* 11.11 (Nov. 1, 1968), pp. 1695–1713. ISSN: 0017-9310. DOI: 10.1016/0017-9310(68)90048-3. URL: http://www.sciencedirect.com/science/article/pii/0017931068900483 (visited on 11/17/2019).

[10] Fabiano Cassol et al. "Application of the weighted-sum-of-gray-gases model for media composed of arbitrary concentrations of H2O, CO2 and soot". In: *International Journal of Heat and Mass Transfer* 79 (Dec. 1, 2014), pp. 796–806. ISSN: 0017-9310. DOI: 10.1016/j.ijheatmasstransfer.2014.08.032. URL: http://www.sciencedirect.com/science/article/pii/S0017931014007194 (visited on 11/25/2019).

[11] L. H. Caveny et al. *Solid Propellant Flammability Including Ignitability and Combustion Limits*. Aberdeen: Ballistics Research Laboratories, 1974.

[12] William C Caywood, Robert M Rivello, and Louis B Weckesser. "Tactical Missile Structures and Materials Technology". In: *Johns Hopkins APL Techincal Digest* 4.3 (1983), pp. 166–174. URL: https://www.jhuapl.edu/TechDigest/Detail?Journal=J&VolumeID=4&IssueID=3 (visited on 12/06/2019).

[13] Cesaroni Technology Incorporated. *Rocket Motor Hardware and Accessories*. 2012. URL: http://www.pro38.com/products/pro38/hardware_pro38.php (visited on 11/24/2019).

[14] Y.-K. Chen and F. S. Milos. "Two-Dimensional Implicit Thermal Response and Ablation Program for Charring Materials". In: *Journal of Spacecraft and Rockets* 38.4 (2001), pp. 473–481. DOI: 10.2514/2.3724. URL: https://doi.org/10.2514/2.3724 (visited on 12/18/2019).

[15] Y.-K. Chen and Frank S. Milos. "Ablation and Thermal Response Program for Spacecraft Heatshield Analysis". In: *Journal of Spacecraft and Rockets* 36.3 (1999), pp. 475–483. DOI: 10.2514/2.3469. URL: https://doi.org/10.2514/2.3469 (visited on 12/18/2019).

[16] Patrick Combis et al. "Evaluation of the fused silica thermal conductivity by comparing infrared thermometry measurements with two-dimensional simulations". In: *Applied Physics Letters* 101.21 (Nov. 19, 2012), p. 211908. ISSN: 0003-6951. DOI: 10.1063/1.4764904. URL: https://aip.scitation.org/doi/full/10.1063/1.4764904 (visited on 11/16/2019).

[17] CoorsTek Corporation. *Porous Silica Material*. 2019. URL: http://www.coorstek.co.jp/eng/rd/detail_02.html (visited on 11/16/2019).

[18] Cotronics Corp. *Rescor Cer-cast ceramics*. URL: http://www.cotronics.com/vo/cotr/pdf/onepg700.pdf.

[19] Alain Davenas. *Solid Rocket Propulsion Technology*. Pergamon Press, 1993. URL: http://archive.org/details/A.DavenasEds.SolidRocketPropulsionTechnology (visited on 08/07/2019).

[20] Dow Corning. *Dow Corning 93-104 Ablative Material*. 10-1059A-01.

[21] R A Ellis and R B Keller. *SP-8115: Solid Rocket Motor Nozzles*. NASA-SP-8115. NASA, June 1, 1975. URL: https://ntrs.nasa.gov/search.jsp?R=19760013126.

[22] Estes Industries LLC. *Estes Model Rocket Engines*. 2019. URL: https://estesrockets.com/wp-content/uploads/Educator/Estes_Model_Rocket_Engines.pdf.

[23] Federal Aviation Administration and Battelle Memorial Institute. *Metallic materials properties development and standardization (MMPDS) : MMPDS-11*. Washington, DC: Federal Aviation Administration, July 2016. book. ISBN: 978-1-5231-0600-4.

[24] FormLabs. *Material Data Sheet: Ceramic*. Mar. 5, 2018. URL: https://archive-media.formlabs.com/upload/Technical_Data_Sheet_EN_-_Ceramic.pdf.

[25] Vishwas Govindrao Ghorpade et al. "Study of Burn Rate Suppressants in AP-Based Composite Propellants". In: *Propellants, Explosives, Pyrotechnics* 35.1 (2010), pp. 53–56. ISSN: 1521-4087. DOI: 10.1002/prep.200800046. URL: https://onlinelibrary.wiley.com/doi/abs/10.1002/prep.200800046 (visited on 10/27/2019).

[26] Lorna J. Gibson and Michael F. Ashby. *Cellular Solids: Structure and Properties*. 2nd ed. Cambridge Solid State Science Series. Cambridge University Press, 1997. DOI: 10.1017/CBO9781139878326.

[27] R. J. Goldstein, K. Y. Lau, and C. C. Leung. "Velocity and turbulence measurements in combustion systems". In: *Experiments in Fluids* 1.2 (June 1, 1983), pp. 93–99. ISSN: 1432-1114. DOI: 10.1007/BF00266261. URL: https://doi.org/10.1007/BF00266261 (visited on 11/17/2019).

[28] M. L. Gross and M. W. Beckstead. "Steady-State Combustion Mechanisms of Ammonium Perchlorate Composite Propellants". In: *Journal of Propulsion and Power* 27.5 (2011), pp. 1064–1078. URL: https://dx.doi.org/10.2514/1.B34053.

[29] Layton C. (Layton Carter) Hale. "Principles and techniques for designing precision machines". Thesis. Massachusetts Institute of Technology, 1999. URL: https://dspace.mit.edu/handle/1721.1/9414 (visited on 01/16/2020).

[30] Heraeus. *Quartz Glass for Optics: Data and Properties*. July 2019. URL: https://www.heraeus.com/media/media/hca/doc_hca/products_and_solutions_8/optics/Data_and_Properties_Optics_fused_silica_EN.pdf.

[31] Philip Hill and Carl Peterson. *Mechanics and Thermodynamics of Propulsion*. 2nd ed. Pearson, 1992.

[32] William Horton. "Status of The Space Shuttle Solid Rocket Booster". In: *The Space Congress® Proceedings* (Apr. 1, 1980). URL: https://commons.erau.edu/space-congress-proceedings/proceedings-1980-17th/session-1/3.

[33] J. R. Siegel Howell. *Thermal radiation heat transfer. Volume 3 - Radiation transfer with absorbing, emitting, and scattering media*. SP-164. Jan. 1, 1971. URL: https://ntrs.nasa.gov/search.jsp?R=19710021465 (visited on 11/23/2019).

[34] J. D. Hunley. "The History of Solid-Propellant Rocketry: What We Do and Do Not Know". In: *35th AIAA, ASME, SAE, ASEE Joint Propulsion Conference and Exhibit*. 1999.

[35] Dieter K. Huzel et al. *Modern Engineering for Design of Liquid Propellant Rocket Engines*. Ed. by D. K. Huzel and D. H. Huang. Washington, DC: AIAA, Jan. 1, 1992. 431 pp. ISBN: 978-1-56347-013-4.

[36] *Jane's All the World's Aircraft: Unmanned*. London: IHS Markit, 2016.

[37] *Jane's All the World's Aircraft: In Service*. London: IHS Markit, 2016.

[38] R. Jeenu, Kiran Pinumalla, and Desh Deepak. "Industrial Adaptation of Ultrasonic Technique of Propellant Burning Rate Measurement Using Specimens". In: *Journal of Propulsion and Power* 29.1 (2013), pp. 216–226. DOI: 10.2514/1.B34578. URL: https://doi.org/10.2514/1.B34578 (visited on 01/24/2020).

[39] Jim Dumoulin. *Solid Rocket Boosters*. NSTS 1988 News Reference Manual. URL: https://science.ksc.nasa.gov/shuttle/technology/sts-newsref/srb.html.

[40] John D. Anderson, Jr. *Aircraft Performance and Design*. McGraw-Hill, 1999. ISBN: 978-0-07-001971-3.

[41] Steven Kubiak. *Guidelines for Wall Thickness in Laser Sintering*. Additive Manufacuring Magazine. Apr. 5, 2017. URL: https://www.additivemanufacturing.media/blog/post/guidelines-for-wall-thickness-in-laser-sintering (visited on 11/02/2019).

[42] Jakob Kübler and L J Gauckler. *Material Properties of Ceramics, Parts 1-4*. 2010. URL: http://www.nonmet.mat.ethz.ch/education/courses/Materialwissenschaft_2/Downloads_FS_2010/LecETH_2010_P4_MechPropCeram_Kub.pdf.

[43] N. Kubota. *Propellants and Explosives: Thermochemical Aspects of Combustion*. Hoboken: John Wiley & Sons, Inc., 2015.

[44] W C Kuby and J L Richardson. *The Prediction of Heat Transfer and Ablation in the Aft-Closure of a Solid-Propellant Rocket Motor*. Ford Motor Company Aeronautic Division, 1962. URL: https://apps.dtic.mil/dtic/tr/fulltext/u2/282734.pdf.

[45] Kyocera Corporation. *Technical Data: Silicon Nitride*. URL: https://global.kyocera.com/prdct/fc/list/material/silicon_nitride/silicon_nitride.html.

[46] S.-T. Lee, E. W. Price, and R. K. Sigman. "Effect of Multidimensional Flamelets in Composite Propellant Combustion". In: *Journal of Propulsion and Power* 10.6 (1994), pp. 761–768.

[47] James G. Lucas and Richard L Golladay. *Gaseous-Film Cooling of A Rocket Motor with Injection Near the Throat*. NASA Lewis Research Center, Feb. 1967. URL: https://ntrs.nasa.gov/search.jsp?R=19670008176.

[48] Christopher Tucker Lyne. "Calibration and Testing of Rapid Prototyped Nozzles for Guidance and Control". PhD thesis. Nashville, Tennessee: Vanderbilt University, Dec. 16, 2017. URL: https://etd.library.vanderbilt.edu/available/etd-11252017-181933/unrestricted/Lyne.pdf.

[49] Manuel Martinez-Sanchez. *Ablative Cooling, Film Cooling*. 2005. URL: https://ocw.mit.edu/courses/aeronautics-and-astronautics/16-512-rocket-propulsion-fall-2005/lecture-notes/lecture_10.pdf.

[50] Kelly J. Mathesius. "Manufacturing Methods for a Solid Rocket Motor Propelling a Small, Fast Flight Vehicle". Masters. Cambridge, MA: Massachusetts Institute of Technology, June 2019.

[51] Terry McCreary. *Experimental Composite Propellant*. Murray, KY, 2014.

[52] C. B. Moyer and R A Rindal. *An analysis of the coupled chemically reacting boundary layer and charring ablator. Part 2 - Finite difference solution for the in-depth response of charring materials considering surface chemical and energy balances*. NASA-CR-1061. June 1, 1968. URL: https://ntrs.nasa.gov/search.jsp?R=19680017220 (visited on 12/18/2019).

[53] Roddam Narasimha. *Rockets in Mysore and Britian, 1750-1850 A.D.* Project Document DU 8503. Bangalore, India: National Aeronautical Laboratory and Indian Institute of Science, May 1985.

[54] NASA. *Orbiter Thermal Protection System*. 2006. URL: http://www.nasa.gov/centers/kennedy/pdf/167473main_TPS-06rev.pdf.

[55] NASA. *SP-8124: Liquid Rocket Engine Self-Cooled Combustion Chambers*. SP-8124. NASA, Sept. 1977. URL: https://ntrs.nasa.gov/search.jsp?R=19780013268.

[56] Maurizio Natali, Jose Maria Kenny, and Luigi Torre. "Science and technology of polymeric ablative materials for thermal protection systems and propulsion devices: A review". In: *Progress in Materials Science* 84 (Dec. 1, 2016), pp. 192–275. ISSN: 0079-6425. DOI: 10.1016/j.pmatsci.2016.08.003. URL: http://www.sciencedirect.com/science/article/pii/S0079642516300500 (visited on 12/12/2019).

[57] Matt Newville et al. *lmfit/lmfit-py 1.0.0*. Version 1.0.0. Dec. 2019. DOI: 10.5281/zenodo.3588521. URL: https://doi.org/10.5281/zenodo.3588521.

[58] Nickel Development Institute and American Iron and Steel Institute. *High-Temperature Characteristics of Stainless Steels*. 9004, p. 47. URL: https://www.nickelinstitute.org/en/TechnicalLibrary/AISI/9004_High_TemperatureCharacteristicsofStainlessSteel.aspx.

[59] Northrop Grumman. *AIM-9X (Mk139) Sidewinder Rocket Motor Factsheet*. Apr. 2015. URL: https://www.northropgrumman.com/Capabilities/PropulsionSystemsCo
Documents/AIM-9X_Factsheet.pdf.

[60] Nothrop Grumman Innovation Systems. *Propulsion Products Catalog*. Apr. 5, 2016. URL: https://www.northropgrumman.com/Capabilities/PropulsionSystems/Documents/NGIS_MotorCatalog.pdf.

[61] Achutananda Parhi et al. "Challenges in the development of a slow burning solid rocket booster". In: *Aerospace Science and Technology* 43 (June 1, 2015), pp. 437–444. ISSN: 1270-9638. DOI: 10.1016/j.ast.2015.04.001. URL: http://www.sciencedirect.com/science/article/pii/S1270963815001169 (visited on 10/27/2019).

[62] Achutananda Parhi et al. "Development of slow-burning solid rocket booster for RLV-TD hypersonic experiment." In: *Current Science (00113891)* 114.1 (Jan. 10, 2018), pp. 74–83. ISSN: 00113891. URL: https://search.ebscohost.com/login.aspx?direct=true&db=a9h&AN=127414385&site=eds-live&scope=site.

[63] Kihong Park et al. "Measurement of Inherent Material Density of Nanoparticle Agglomerates". In: *Journal of Nanoparticle Research* 6 (June 1, 2004), pp. 267–272. DOI: 10.1023/B:NANO.0000034657.71309.e6.

[64] Yury V Polezhaev. *Ablation*. Thermopedia. 2011. URL: http://dx.doi.org/10.1615/AtoZ.a.ablation.

[65] Alexander Ponomarenko. *RPA: Tool for Liquid Propellant Rocket Engine Analysis*. Neunkirchen-Seelscheid, Germany, May 2010. URL: http://www.propulsion-analysis.com/downloads/pub/RPA_LiquidRocketEngineAnalysis_II.pdf.

[66] E. W. Price and R. K. Sigman. "Combustion of Aluminized Solid Propellants". In: *Progress in Astronautics and Aeronautics: Solid Propellant Chemistry, Combustion, and Motor Interior Ballistics*. Reston: American Institute of Aeronautics and Astronautics, 2000, pp. 663–688.

[67] Ben Redwood, Filemon Schöffer, and Brian Garret. *The 3D Printing Handbook*. 3D Hubs, 2017. ISBN: 978-90-827485.

[68] Renishaw plc. *AlSi10Mg-0403 powder for additive manufacturing*. H-5800-1084-01-B. July 2015. URL: https://www.renishaw.com/media/pdf/en/0c48b4800c17480393f17pdf.

[69] Renishaw plc. *In718-0405 powder for additive manufacturing*. H-5800-1052-03-B. July 2017. URL: https://www.renishaw.com/media/pdf/en/b1296f200d6b415fa2c03bdc1da17f pdf.

[70] Renishaw plc. *SS 316L-0407 powder for additive manufacturing*. H-5800-3001-03-A. Apr. 2018. URL: https://www.renishaw.com/media/pdf/en/f8cba72a843440d3bd8a09fd502 pdf.

[71] Cheryl L Resch. "Ablation Models of Thermal Protection Materials". In: *Johns Hopkins APL Techincal Digest* 13.3 (1992), pp. 426–430. URL: https://www.jhuapl.edu/Content/techdigest/pdf/V13-N03/13-03-Resch.pdf.

[72] Sandvik Materials Technology. *Titanium tubing*. URL: https://www.materials.sandvik/en-us/products/tube-pipe-fittings-and-flanges/tubular-products/titanium-tubes/#tab-sizes-and-tolerances%20 (visited on 11/01/2019).

[73] Dennis J. Schumerth. "Thin-Wall Titanium Condenser Tubing: The Next Plateau". In: 2002 International Joint Power Generation Conference. American Society of Mechanical Engineers Digital Collection, Feb. 24, 2009, pp. 129–137. DOI: 10.1115/IJPGC2002-26121. URL: https://asmedigitalcollection.asme.org/IJPGC/proceedings/IJPGC2002/36177/129/292728 (visited on 11/01/2019).

[74] *SP-8025: Solid Rocket Motor Metal Cases*. NASA-SP-8025. NASA, Apr. 1, 1970. URL: https://ntrs.nasa.gov/search.jsp?R=19700020430.

[75] *SP-8064: Solid Propellant Selection and Characterization*. NASA-SP-8064. NASA, June 1, 1971. URL: https://ntrs.nasa.gov/search.jsp?R=19720006088.

[76] Jonathan R. Spirnak. "Development, modeling and testing of thermal protection systems in small, slow-burning solid rocket motors". Thesis. Massachusetts Institute of Technology, 2018. URL: https://dspace.mit.edu/handle/1721.1/118689 (visited on 10/20/2019).

[77] George P. Sutton and Oscar Biblarz. *Rocket Propulsion Elements*. 8 edition. Hoboken, N.J: Wiley, Feb. 2, 2010. 784 pp. ISBN: 978-0-470-08024-5.

[78] Tony Tao. "Design and development of a high-altitude, in-flight-deployable micro-UAV". Master's Thesis. Cambridge: Massachusetts Institute of Technology, 2012.

[79] John E Terry and Gus J Caras. *Transpiration and Film Cooling of Liquid Rocket Nozzles*. RSIC-535. Redstone Arsenal, Alabama, Mar. 31, 1966. URL: https://ntrs.nasa.gov/search.jsp?R=19660029438.

[80] The Raytheon Company. *Precision Weapons*. 2016. URL: http://www.raytheon.com/capabilities/precision/.

[81] D. Tingfa. "Thermal decomposition studies of solid propellant binder HTPB". In: *Thermochemical Acta* 138 (1989), pp. 189–197.

[82] *Titanium Grade 2*. ASM Material Data Sheet. URL: http://asm.matweb.com/search/SpecificMaterial.asp?bassnum=MTU020 (visited on 12/17/2019).

[83] Titanium Joe Inc. *Tubing*. 2019. URL: https://www.titaniumjoe.com/index.cfm/products/tubing/ (visited on 11/01/2019).

[84] D. Trache et al. "Effect of amide-based compounds on the combustion characteristics of composite solid rocket propellants". In: *Arabian Journal of Chemistry* (2015). URL: https://doi.org/10.1016/j.arabjc.2015.11.016.

[85] Djalal Trache et al. "Thermal behavior and decomposition kinetics of composite solid propellants in the presence of amide burning rate suppressants". In: *Journal of Thermal Analysis and Calorimetry* 132.3 (June 2018), pp. 1601–1615. ISSN: 1588-2926. DOI: 10.1007/s10973-018-7160-8. URL: https://doi.org/10.1007/s10973-018-7160-8.

[86] Philip D. Umholtz. "The history of solid rocket propulsion and Aerojet". In: (1999).

[87] United States Government Accountability Office. *Solid Rocket Motors: DOD and Industry are Addressing Challenges to Minimize Supply Concerns*. GAO-18-45. United States Government Accountability Office, 2017.

[88] Naor Elad Uzan et al. "High-temperature mechanical properties of AlSi10Mg specimens fabricated by additive manufacturing using selective laser melting technologies (AM-SLM)". In: *Additive Manufacturing* 24 (Dec. 1, 2018), pp. 257–263. ISSN: 2214-8604. DOI: 10.1016/j.addma.2018.09.033. URL: http://www.sciencedirect.com/science/article/pii/S2214860418302148 (visited on 11/02/2019).

[89] Matthew T. Vernacchia. "Development, modeling and testing of a slow-burning solid rocket propulsion system". Thesis. Massachusetts Institute of Technology, 2017. URL: https://dspace.mit.edu/handle/1721.1/112515 (visited on 10/20/2019).

[90] Mark Wade. *Solid Propellants*. 2019. URL: http://www.astronautix.com/s/solid.html.

[91] Wei Wan et al. "Effect of Sintering Temperature on the Properties of Fused Silica Ceramics Prepared by Gelcasting". In: *Journal of Electronic Materials* 43.7 (July 1, 2014), pp. 2566–2572. ISSN: 1543-186X. DOI: 10.1007/s11664-014-3112-7. URL: https://doi.org/10.1007/s11664-014-3112-7 (visited on 11/17/2019).

[92] Wikipedia contributors. *Wikipedia, the Free Encyclopedia*. 2016. URL: en.wikipedia.org.

[93] Jovan Zhang. *Titanium Candle Convection Study*. MIT, Aug. 23, 2019.